Charge Transport in Vanadia Oxidation Catalysts

vorgelegt von
Master of Science
Anna Maria Wernbacher
geb. in Graz/Österreich

von der Fakultät II - Mathematik und Naturwissenschaften
der Technischen Universität Berlin
zur Erlangung des akademischen Grades
Doktor der Naturwissenschaften
– Dr. rer. nat. –
genehmigte Dissertation

Promotionsausschuss:

Vorsitzender: Prof. Dr. rer. nat. Martin Lerch
Gutachter: Prof. Dr. rer. nat. Robert Schlögl
Gutachter: Prof. Dr. rer. nat. Peter Hildebrandt
Gutachter: Prof. Dr. rer. nat. Malte Behrens

Tag der wissenschaftlichen Aussprache: 08.02.2019

Berlin 2019

A very great deal more truth can become known than can be proven.

(Feynman, Richard P. "The Development of the Space-Time View of Quantum Electrodynamics" Nobel Lecture (11 December 1965).)

Acknowledgements

First of all, I express my sincere gratitude to Prof. Dr. Robert Schlögl, who gave me the opportunity to perform my PhD work at his Department of Inorganic Chemistry at the Fritz-Haber-Institute of the Max-Planck-Society. Without his guidance, invaluable advice, and scientific input throughout my PhD this work would never have been possible.

I am also deeply grateful to Prof. Dr. Maik Eichelbaum, former leader of the Charge Transport Group, who introduced me to the MCPT and the selective oxidation over vanadium-based oxides. His supervision and continual support were extremely helpful. Furthermore, I greatly thank Dr. Sébastien Cap, leader of the Electrochemistry Group, for his support and the suggestions, which advanced this work. I wish to extend special thanks to Dr. Annette Trunschke and Prof. Dr. Thomas Risse for their helpful advice, the reviewing of my work, and the discussions during our meetings which greatly improved this work.

I gratefully acknowledge Prof. Dr. Peter Hildebrandt and Prof. Dr. Malte Behrens, who invested their valuable time to review this thesis. In addition, I greatly thank Prof. Dr. Martin Lerch for taking the chair of the examination board.

I am particularly grateful to Dr. Michael Hävecker for his aid during the beam times at BESSY II and the many invaluable discussion about XPS and NEXAFS. In addition, I wish to thank Dr. Pierre Kube, who always found the time to help with all kinds of technical issues, and for the helpful discussions about catalysis and kinetics.

I would like to thank the following people without whose help this work wouldn't have been possible: Dr. Frank Girgsdies for the XRD measurements and Rietveld fits, the help with the gas cylinders, as well as for his explanations about crystallography, Dr. Walid Hetaba and Dr. Marc Willinger for the TEM measurements, Maike Hashagen for the BET measurements, Dr. Olaf Timpe for the XRF measurements.

I owe sincere gratitude to my colleagues of the former Charge Transport Group Dr. Maria Heenemann, Elisabeth Hannah Wolf and Dr. Christian Heine for their help throughout my work not only regarding the MCPT setup, but also for the many discussions and for their encouragement and support. It was a pleasure to work with you.

I thank my co-authors for their contributions to the manuscript and manuscript drafts included in this thesis, in alphabetical order: Dr. Sébastien Cap, Prof. Dr. Maik Eichelbaum, Dr. Michael Hävecker, Dr. Pierre Kube, Prof. Dr. Thomas Risse, Prof. Dr. Robert Schlögl, Dr. Annette Trunschke.

Moreover, I wish to thank Prof. Dr. Alexander Vinogradov, who gave valuable advice for the interpretation of the resonant photoelectron spectroscopy data. I address special thanks to Dr. Axel Knop-Gericke, Dr. Travis Jones, and Prof. Dr. Klaus Hermann for investing their valuable time to answer my questions and reading the XPS/NEXAFS work. Furthermore, I am grateful to Dr. Juan Velasco Vélez, Dr. Yuanqing Wang, Dr. Gregor Koch and Prof. Dr. Anne-Marie Kelterer for the highly valuable discussions.

I gratefully acknowledge the financial support given by the doctoral grant by the Max Planck Society. Furthermore, I thank the BasCat (UniCat BASF JointLab) project for the funding and for providing the samples. I am grateful to Dr. Frank Rosowski for the helpful advice during the BasCat meetings. Moreover, the staff of the HZB is gratefully acknowledged for their continuous support at the ISISS beam line at BESSY II. Thanks are also due to the electronics and mechanical workshops of the FHI.

I would like to thank the members of the AC department, in particular for conducting the routine measurements, for the good administrative work, and for creating this pleasant work environment and inspirational atmosphere. I especially want to mention Andrea Moebius, Dorothea Damm, Sabrina Wobring, Dr. Sabine Wrabetz and my fellow PhD students.

Last but not least, I am deeply indebted to my family and Thomas for their unyielding support and for their faith in me.

Abstract

An efficient direct functionalization of light alkanes is highly desirable to achieve a more sustainable raw material usage in chemical industry. Our knowledge of heterogeneous selective alkane oxidation catalysts is still largely based on empirical concepts. There is growing evidence that in addition to the traditional (local) concepts the underlying bulk electronic structure should be considered. The aim of this thesis is to further extend current understanding of the selective alkane oxidation over vanadium-based transition metal oxides. Within the framework of a redox mechanism, the role of charge transfer and charge transport in vanadia oxides was investigated under catalytic operation conditions.

For this reason, contact-free electrical conductivity or complex permittivity measurements based on the microwave cavity perturbation technique (MCPT) were performed, which enables the non-invasive and highly sensitive investigation of semiconducting powder catalysts under *operando* conditions. Complementary techniques like near-ambient pressure XPS and resonant photoemission spectroscopy, NEXAFS spectroscopy, or UV-Vis spectroscopy were applied to get additional information about the surface electronic structure and surface composition and the redox response of the catalysts to different gas atmospheres.

Non-stoichiometric V_2O_{5-x} showed reversible changes in the vanadium oxidation state in *n*-butane- and O_2-containing gas atmospheres, which were not restricted to the surface. A band gap peak caused by occupied V 3d levels adapted to the different gas feeds as was clearly demonstrated by resonant photoemission spectroscopy (resPES). This indicates that a redox mechanism is indeed operative over V_2O_{5-x}, but unlike in the selective catalysts VPP or MoVTeNb-oxide also deeper layers may contribute. Different decay channels contribute to the resPES spectra, which were likewise affected by the treatment of the sample in different gas feeds.

A comparative study on V_2O_{5-x} and VPP in the oxidation of *n*-butane to maleic anhydride was performed. The electrical conductivity was shown to be a sensitive function of the local chemical potential and closely linked to the catalytic reaction at the surface being also affected by the reactant conversion level. Although many factors are likely contributing to the selectivity or the activity of a partial oxidation catalyst, non-local electronic properties are part of the phenomenon. The following parameters were identified: (i) the conductivity of V_2O_{5-x} is $\sim$50 times higher compared to VPP under isothermal and iso-conversion conditions, (ii) the apparent activation energy of conduction (E_c) of V_2O_{5-x} is four to eight times lower than the one of VPP, (iii) the extent of the conductivity/permittivity change with varying conversion levels under isothermal conditions (i.e., with the number of exchanged electrons during the reaction) is much greater in V_2O_{5-x}. A stable catalytic performance retaining a high selectivity is related to low conductivity changes at various conversion levels and a "stable" surface layer.

These conclusions could further be extended to the mixed-metal MoV-oxide in the orthorhombic M1 phase, whose semiconducting properties were studied in the selective oxidation of ethane, propane, and *n*-butane. Furthermore, MoV-oxide was found to exhibit p-type semiconducting behavior contrary to MoVTeNb-oxide (M1)[1] as seen in a reversed conductivity response. The thus changed availability of either free holes or electrons may have an influence on their respective catalytic performance. The addition of steam to the propane oxidation feed leads to an enhanced acrylic acid formation. It further resulted in the modification of the surface termination and a significant decrease of the work function by 0.2 eV. This may rationalize the conductivity or permittivity decrease in the wet propane oxidation feed, which was observed at the same time and is probably not caused by a change in the charge carrier density. Also, the simultaneously changed chemical potential of the gas phase including the changed product distribution (increased selectivity) is suggested to be intricately linked to the conductivity/permittivity response.

Taken together, the findings of this thesis show the relevance of electronic properties for the catalytic performance of heterogeneous selective oxidation catalysts.

Zusammenfassung

Im Hinblick auf eine nachhaltige Nutzung von Rohmaterialien in der chemischen Industrie ist eine effiziente direkte Funktionalisierung von kurzkettigen Alkanen erstrebenswert. Unser Verständnis von heterogenen selektiven Oxidationskatalysatoren basiert großteils noch auf empirischen Konzepten. Zusätzlich zu den traditionellen (lokalen) Konzepten sollte auch die zugrundeliegende elektronische Struktur des Volumens („bulk“) berücksichtigt werden. Ziel dieser Arbeit ist es, das derzeitige Verständnis von der selektiven Oxidation von Alkanen über Vanadium-basierten Übergangsmetalloxiden zu verbessern. Die Rolle des Ladungstransfers und -transports (im Rahmen eines Redox-Mechanismus) wurde unter katalytischen Reaktionsbedingungen untersucht.

Kontaktlose elektrische Leitfähigkeits- oder komplexe Permittivitätsmessungen basierend auf der Mikrowellenresonator-Störungstechnik (MCPT) wurden durchgeführt, welche eine nichtinvasive und hochempfindliche Untersuchung von halbleitenden Pulverkatalysatoren unter *operando* Bedingungen ermöglicht. Ergänzend wurde Röntgenphotoelektronenspektroskopie nahe Umgebungsdruck (NAP-XPS) und resonante Photoelektronenspektroskopie (resPES), NEXAFS und UV-Vis Spektroskopie verwendet, um Informationen über die elektronische Struktur und Oberflächenzusammensetzung und über das Redox-Verhalten der Katalysatoren zu bekommen.

Nicht-stöchiometrisches V_2O_{5-x} hat reversible Änderungen des Vanadium-Oxidationszustands in *n*-Butan- und O_2-haltigen Gasatmosphären gezeigt, die nicht auf die Oberfläche beschränkt waren. Ein Peak in der Bandlücke (besetzte V 3d Niveaus) hat gasphasenabhängige Änderungen gezeigt, wie durch resPES verdeutlicht wurde. Das weist darauf hin, dass in der Tat ein Redox-Mechanismus über V_2O_{5-x} wirksam ist, aber im Gegensatz zu den selektiven Katalysatoren VPP oder MoVTeNb-Oxid auch tiefere Schichten beitragen können. Die resPES Zerfallskanäle wurden ebenfalls durch die Behandlung der Probe in verschiedenen Gasgemischen beeinflusst.

Es wurde eine Vergleichsstudie über V_2O_{5-x} und VPP in der Oxidation von *n*-Butan zu Maleinsäureanhydrid durchgeführt. Dabei wurde gezeigt, dass die elektrische Leitfähigkeit, die auch durch den Umsatzgrad der Reaktanden beeinflusst wurde, eine sensitive Funktion des lokalen chemischen Potentials ist und eng verbunden mit der katalytischen Reaktion auf der Oberfläche. Obwohl wahrscheinlich viele Faktoren zu der Selektivität oder Aktivität eines partiellen Oxidationskatalysators beitragen, sind nicht-lokale elektronische Eigenschaften Teil des Phänomens. Die folgenden Parameter wurden identifiziert: (i) die Leitfähigkeit von V_2O_{5-x} ist ∼50-mal höher als die von VPP unter isothermen Bedingungen und bei gleichem Umsatz, (ii) die scheinbare Aktivierungsenergie der Leitfähigkeit (E_c) von V_2O_{5-x} ist vier- bis achtmal kleiner als die von VPP, (iii) das Ausmaß der Leitfähigkeits-/Permittivitätsänderung bei verschiedenen Umsätzen unter isothermen Bedingungen (d.h. mit der Anzahl an ausgetauschten Elektronen während der Reaktion) ist viel größer in V_2O_{5-x}. Eine stabile katalytische Leistung unter Beibehaltung einer hohen Selektivität ist mit einer kleinen Leitfähigkeitsänderung bei verschiedenen Umsätzen verbunden und mit einer „stabilen“ Oberflächenschicht.

Diese Schlussfolgerungen konnten auf das Mischmetalloxid MoV-Oxid in der orthorhombischen M1 Phase erweitert werden, dessen Halbleitereigenschaften in der selektiven Oxidation von Ethan, Propan und *n*-Butan untersucht wurden. Zudem lässt die entgegengesetzte Leitfähigkeitsantwort von MoV-Oxid verglichen zu MoVTeNb-Oxid (M1)[1] den Schluss zu, dass MoV-Oxid ein p-Halbleiter ist. Die unterschiedliche Verfügbarkeit von entweder freien Löchern oder Elektronen kann sich auf deren jeweilige katalytische Leistung auswirken. Der Zusatz von Wasserdampf zu einem Propanoxidationsgemisch erhöht die Produktion von Acrylsäure. Des Weiteren führt er zu einer Modifikation der Oberflächenterminierung und zu einer signifikanten Abnahme der Austrittsarbeit um 0.2 eV. Das könnte die Abnahme der Leitfähigkeit in dem nassen Gasgemisch begründen, die wahrscheinlich nicht auf eine Änderung der Ladungsträgerdichte zurückzuführen ist. Das gleichzeitig veränderte chemische Potential der Gasphase inklusive der veränderten Produktverteilung (Selektivität) trägt ebenfalls zur Leitfähigkeits-/Permittivitätsänderung bei.

Zusammenfassend zeigen die Ergebnisse dieser Arbeit die Bedeutung von elektronischen Eigenschaften für die katalytische Leistung von heterogenen selektiven Oxidationskatalysatoren.

Contents

List of Figures

List of Tables

List of Abbreviations

AA	acrylic acid
AC	alternating current
AcA	acetic acid
AEY	Auger electron yield
BET	Brunauer-Emmett-Teller (surface area determination)
CB	conduction band
CBM	conduction band minimum
CT	charge transfer
DC	direct current
DFT	density functional theory
DOS	density of states
DR	diffuse reflectance
EDX	energy dispersive X-ray spectroscopy
EPR	electron paramagnetic resonance
FEM	finite element method
fwhm	full width at half maximum
GC	gas chromatograph
IR	infrared
LMCT	ligand-to-metal charge transfer
MA	maleic anhydride
MCPT	microwave cavity perturbation technique
MS	mass spectrometer
NAP	near-ambient pressure
NEXAFS	near edge X-ray absorption fine structure
NIR	near-infrared
OCM	oxidative coupling of methane
ODH	oxidative dehydrogenation

PTR-MS proton-transfer-reaction mass spectrometer

QMS quadrupole mass spectrometer

resPES resonant photoelectron spectroscopy

ROCIS restricted open shell configuration interaction singles

SEM scanning electron microscopy

TM transverse magnetic

TE transverse electric

TEM transverse electromagnetic

TEM transmission electron microscopy

TEY total electron yield

VB valence band

VBM valence band maximum

UHV ultra-high vacuum

UPS ultraviolet photoelectron spectroscopy

UV-Vis ultraviolet-visible

VNA vector network analyzer

VPO vanadium phosphorus oxide

VPP vanadyl pyrophosphate

WTY weight time yield

XPS X-ray photoelectron spectroscopy

XRD X-ray diffraction

XRF X-ray fluorescence

List of Symbols

Physical Constants

μ_0	Vacuum permeability	$4\pi \cdot 10^{-7}\,(\mathrm{V \cdot s})/(\mathrm{A \cdot m})$
ε_0	Vacuum permittivity	$8.854187817 \cdot 10^{-12}\,\mathrm{F/m}$
c	Speed of light	$2.99792458 \cdot 10^{8}\,\mathrm{m/s}$
e	Elementary charge	$1.6021766208 \cdot 10^{-19}\,\mathrm{C}$
h	Planck constant	$6.626070040 \cdot 10^{-34}\,\mathrm{J \cdot s}$
k	Boltzmann constant	$1.38064852 \cdot 10^{-23}\,\mathrm{J/K}$

Other Symbols

χ	Electron affinity
$\Delta\omega_{1/2}$	Half-power bandwidth of resonance peak
δ	Volume fraction factor
Γ_d	Detuned reflection coefficient
Γ_L	Loaded reflection coefficient at resonant frequency ω_L
κ	Coupling coefficient
λ	Wavelength
λ_0	Resonant wavelength
$\mathbf{B}$	Magnetic induction or magnetic flux density
$\mathbf{D}$	Electric displacement field
$\mathbf{E}$	Electric field
$\mathbf{H}$	Magnetic field
$\mathbf{P}$	Polarization vector
ω	Angular frequency, $\omega = 2\pi f$
ω_0	Angular resonant frequency
Φ	Work function
ρ_{crystal}	Crystallographic density
ρ_{powder}	Powder density
σ	Electrical conductivity
$\tilde{\Gamma}$	Complex reflection coefficient

$\tilde{\mu}$	Complex permeability
$\tilde{\varepsilon}$	Complex permittivity
A, B	MCPT calibration parameters (resonator mode constants)
a_{mn}	n-th root of m-th order Bessel function J_m
eV_s	Maximum band bending at the surface "s"
E_{CB}	Conduction band minimum
E_{D}	Donor level energy
E_{F}	Fermi level
E_{vac}	Vacuum level
E_{VB}	Valence band maximum
E_t	Surface state energy
f	Frequency
f_0	Resonant frequency
$J_m(x)$	Bessel function of the first kind of order m
m	Mass
N	Depolarization factor
N_{ss}	Density of surface states
P	Power
p	Pressure
P_L	Energy dissipation power
Q	Quality factor
Q_0	Unloaded Q factor
Q_L	Loaded Q factor
Q_{sc}	Space charge
Q_{ss}	Charge of surface states
T	Temperature
t	Time
V_c	Volume of the cavity resonator
V_s	Sample volume
V_s	Surface potential
W	Energy stored in the cavity resonator

Mathematics and Mathematical Operators

$\boldsymbol{\nabla}$	Differential operator del $\boldsymbol{\nabla} = (\frac{\partial}{\partial x}, \frac{\partial}{\partial y}, \frac{\partial}{\partial z})$
Δ	Laplacian, $\Delta = \nabla^2 = \frac{\partial^2}{\partial x^2} + \frac{\partial^2}{\partial y^2} + \frac{\partial^2}{\partial z^2}$
i	Imaginary unit, $i^2 = -1$

1. Introduction

The selective oxidation of alkanes plays an important role in chemical industry providing precursors for a great variety of products including solvents, additives, or, for example, polyester resins.[2–4] Nowadays basic organic chemicals are still mainly obtained from the oxidation of alkenes and aromatics, which can e.g. be obtained by steam cracking.[5] This is exemplified in Fig. 1.1 showing the dominant role of crude oil as feedstock for the German chemical industry. In view of the depletion of the oil reserves, the direct and efficient functionalization of light alkanes like propane or *n*-butane to alkenes and oxygenates is becoming increasingly important allowing for the replacement of aromatics and other refinery products of crude oil.[6] Key challenges include reducing the amount of waste products and increasing the product yields while running the reactions under mild conditions thus making the processes both economically and environmentally friendlier.[2,6,7] Therefore, considerable effort is invested in the development of efficient catalysts for the selective oxidation of alkanes.[2,6]

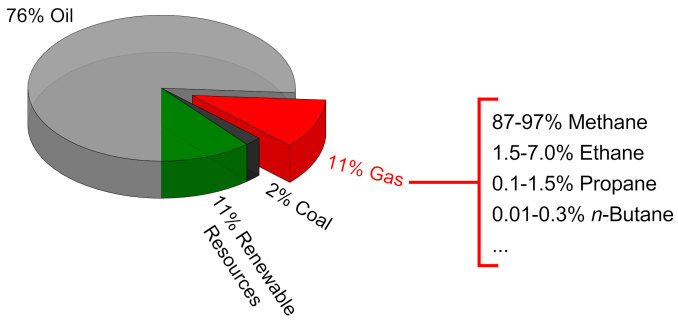

Figure 1.1.: Raw material usage in chemical industry in Germany (adapted from Ref. [8]).

An important class of catalysts for the direct functionalization of light alkanes are vanadium-based (mixed-metal) oxides.[9] Their application in selective oxidation reactions is shortly outlined in Section 1.1. Traditional concepts in heterogeneous selective oxidation research are introduced in Section 1.2 based on the so-called "seven pillars". In the last years, a growing body of literature has indicated the relevance of concepts from semiconductor physics and surface science taking the underlying band structure of the transition metal oxides into account.[10] Electronic properties should be considered in addition to the traditional concepts to better understand the mode of operation of selective oxidation catalysts. Sections 1.3 and 1.4 deal with semiconductor physics and surface science concepts applied to alkane oxidation reactions as well as with the charge transport and charge transfer in heterogeneous catalysts, respectively. Finally, an outline of the present thesis is given in Section 1.5. This work focused on the investigation of electronic properties and the role of charge transfer and charge transport in vanadia oxidation catalysts. Microwave conductivity or permittivity measurements were performed under catalytic operation conditions and complemented by techniques that characterize the (surface) electronic structure.

The oxidation of the light alkanes ethane, propane, and *n*-butane, which are present in natural gas, was examined.

1.1. Selective Oxidation of Alkanes

The heterogeneous selective oxidation of light alkanes typically involves a complex reaction network of consecutive and parallel steps requiring several functions of the catalysts.[10–13] In order to obtain a high product yield and avoid the formation of the waste products CO and CO_2, the catalyst should hinder the nonselective pathways while accelerating the steps towards the desired product.[10,12–14] These catalysts are usually sophisticated materials comprising a surface termination layer with a varying oxidation state of a redox-active metal ion.[2,10] Frequently, multi-component oxides of open d shell transition metals (e.g. vanadium or molybdenum) and main group elements like P or Te form the basis of these catalysts.[2,9,10] This is further complicated by the dynamic nature of the active surface layer, which may be only formed under catalytic operation conditions.[14] Correspondingly, it is difficult to quantitatively relate individual properties of these heterogeneous oxidation catalysts to their catalytic performance,[15] which contributes to the still limited understanding of these processes. It is unlikely that their mode of operation can be pinned down to a single descriptor such as a certain local active site structural motif without additionally considering their coupling to the bulk electronic structure.[10] Furthermore, the need for investigating the catalysts under catalytic operation conditions (*in situ* analysis or *in operando*) should be emphasized.[14]

1.1.1. Selective Oxidation of *n*-Butane

The oxidation of *n*-butane to maleic anhydride using vanadyl pyrophosphate $(VO)_2P_2O_7$ (VPP) as the bulk phase of the catalyst is one of the rare large scale industrially applied alkane oxidation reactions.[3,5,16–18] VPP is nowadays responsible for the majority of the maleic anhydride production,[3] which is in turn primarily used to produce polyester resins.[4] The functionalization of *n*-butane over VPP catalysts (or "**v**anadium **p**hosphorus **o**xides" VPO) has therefore been widely addressed in many review articles.[3,16,17,19–21]

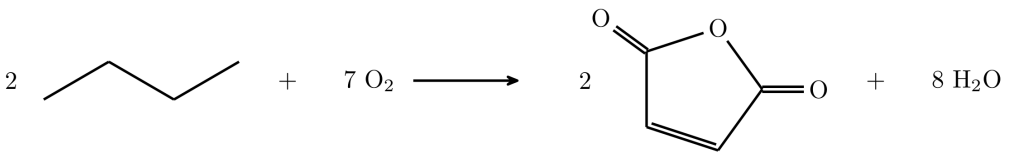

Scheme 1.1: Selective oxidation of *n*-butane to maleic anhydride.

The oxidation of *n*-butane to maleic anhydride requires multiple functions of the catalyst[22] involving the transfer of 14 electrons, the abstraction of 8 hydrogen atoms and the incorporation of three oxygen atoms. The surface layer of the active and selective VPP catalyst was shown to be different from the bulk composition with an average vanadium oxidation state and a P/V atomic ratio slightly exceeding the bulk values under steady-state operation conditions.[17,23–25]

Isotopic labelling studies have demonstrated the participation of "surface lattice oxygen" from the catalyst in the reaction according to a Mars–van Krevelen redox mechanism (V^{4+}/V^{5+} redox

couple).[25–30] Isolated V^{5+} sites were discussed to be responsible for the selective oxidation of *n*-butane[20,25] since the reaction is not possible on VPO catalysts containing vanadium only in the oxidation states +3 and +4,[31] whereas a higher V^{5+} content favours the combustion of *n*-butane.[17] Despite the research carried out in the past 50 years investigating VPP (or VPO)[32,33] with various methods,[23,24,26,27,29,31,34–63] the reaction mechanism and the nature of the active sites still remain under debate. Discrepancies in the literature were attributed to the investigation of fresh and "equilibrated" catalysts, respectively, which have different properties and structures.[17] Moreover, the catalyst surface often changes depending on the gas phase composition, therefore requiring the study of the catalyst under working conditions.[14,17,30] In recent years, theoretical studies on the mechanism of maleic anhydride formation over VPO have stressed the importance of the main group element phosphorus for the activation of *n*-butane.[64,65] The authors suggested a O=P–O–V^{5+}=O motif present on a metastable oxidized surface of VPO as being responsible for the homolytic C–H cleavage, which leads to the formation of a P–OH group and the reduction of V^{5+} to V^{4+}.[64,65]

1.1.2. Selective Oxidation of Propane

The production of propene from the oxidative dehydrogenation of propane might provide an alternative pathway substituting fluid catalytic cracking, steam cracking, or catalytic dehydrogenation in the future.[7] An efficient direct functionalization of propane to acrylic acid, which is an important intermediate chemical e.g. for the production of polyacrylates,[66,67] is likewise highly desirable. However, so far only the ammoxidation of propane to acrylonitrile has reached the commercial level.[6,68]

Complex mixed MoVTeNb-oxides in the orthorhombic M1 phase (ICSD 55097)[69,70] are well-known catalysts for the selective (amm)-oxidation of propane.[68] There are suggestions regarding the reaction network[10,71,72] and the active site motifs[15,68,73,74] for the oxidation of propane over $MoVTeNbO_x$. The activation of propane, i.e. the hydrogen abstraction as a kinetically relevant step, was proposed to occur in a quasi-simultaneous fashion.[71] The active surface of the catalyst is believed to be composed of vanadium oxide nanodomains, which are separated from each other by Mo_xO_y and Te_xO_y moieties, on top of the redox-active $MoVTeNbO_x$ bulk.[10,15,75] Similar to the findings for the VPP catalyst, DFT calculations suggest a critical role of the main group element tellurium in the vicinity of vanadium for the activation of propane.[74] A Te=O group was proposed to be responsible for the C–H cleavage, while the released electron reduces a V=O site.[74] This is in contrast to earlier studies, which proposed the hydrogen abstraction by a V^{5+}=O group.[15,76] The acrylic acid formation was found to correlate positively with the V^{5+} amount.[75] The activation of propane can also be achieved on MoV-oxide in the M1 phase, which shows, however, a low selectivity to the desired products propene or acrylic acid.[77]

1.2. Traditional Concepts in Heterogeneous Selective Oxidation

Grasselli [2] formulated "*seven pillars*" for heterogeneous selective oxidation reactions, which are summarized in Fig. 1.2. These in part interrelated empirical concepts[10] aided the design and improvement of complex mixed-metal oxide catalysts for selective alkane oxidation reactions.[2]

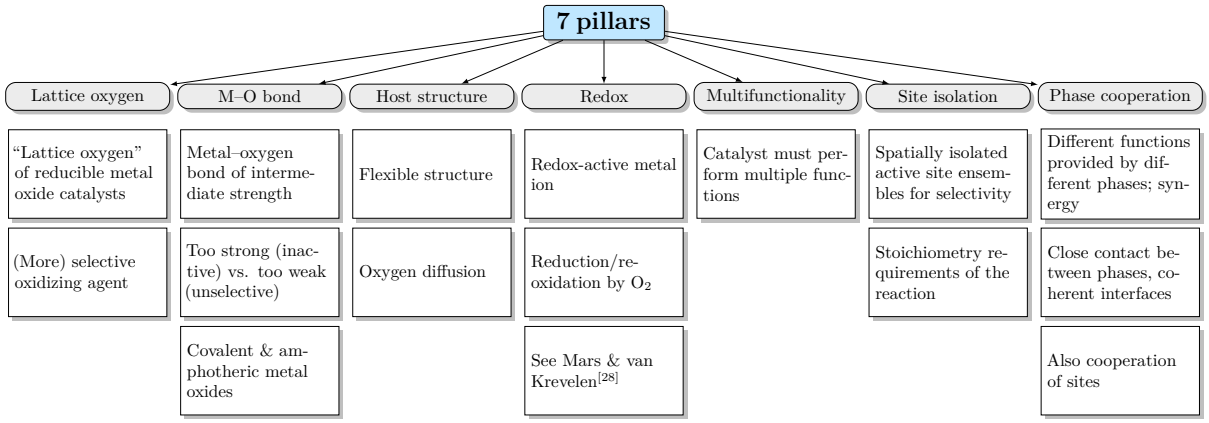

Figure 1.2.: "Seven pillars" of heterogeneous selective oxidation catalysts as described by Grasselli [2]. The individual concepts are discussed in the text.

One aspect is the "surface lattice oxygen" from the catalysts operating under a redox mechanism (see Mars & van Krevelen [28]), which was suggested to participate in the reaction.[2] The nature of the metal–oxygen bonds should be partially covalent,[2] which is satisfied by vanadium–oxygen bonds.[78–81] Here, the vanadyl V=O bond exhibits the highest degree of covalency.[79,80] It may be noted that the bonding character of V–O bonds (or similarly of Mo–O bonds) further varies with the formal oxidation state of the metal ion, where the highest oxidation state (d^0) is associated with the highest degree of covalency.[82] Concerning the redox properties, transition metal oxide catalysts like VPP are characterized by a varying oxidation state of the metal ion and reversible redox processes.[2,30,83] A sufficient oxygen mobility is likely to be required for the formation of the active surface layer.[10] The underlying crystallographic bulk structure of the catalysts is typically non-densely packed and flexible enabling the creation of defects (to a certain degree).[2,10,15] It should allow for the formation of a surface layer in structural similarity to the bulk,[84] which needs to avoid decomposing or transforming into an inactive state under catalytic operation conditions.[10,15]

An easy release of oxygen from the surface as well as a high oxygen mobility are believed to be key factors for these alkane oxidation catalysts.[2,10,83,85] The re-oxidation of the catalysts by O_2 might also be realized at a different site taking diffusion into account.[2,85] Both chemisorption of O_2 from the gas phase and oxygen diffusion from the subsurface region were discussed to lead to a filling of the oxygen vacancies.[2,12,85] It may be assumed that the diffusion from the bulk to the surface is rather slow compared to the processes occurring at the surface. Isotopic labeling studies on VPP suggest an oxygen exchange with the surface layer but only a limited participation of the subsurface region (of up to four layers).[26,27] Haber *et al.* [85] proposed an easy oxygen diffusion pathway through the non-densely packed V_2O_5 crystal structure (see Refs. [85, 86] and references therein). This is supported by low computed barriers for the inter-layer oxygen diffusion to a surface oxygen vacancy.[87] A contribution of subsurface oxygen was also suggested for δ-$VOPO_4$ by modeling the response of reduced catalysts to O_2 pulses, yet at time constants by a factor of ∼100 larger compared to the surface processes.[88] It should be noted that the operation of the catalysts may be different in the "catalytic mode" compared to the "stoichiometric mode".[10,89] In the catalytic mode an alkane/O_2 gas feed with an excess of oxygen at ambient pressure is usually applied.[10,89] In contrast, many investigations consider

a separate reaction with the alkanes and with O_2, apply O_2 pulses on a reduced catalyst, or work at low absolute pressures.[10,89] Here, it should be taken into account that these oxides like V_2O_5 are prone to oxygen loss under conditions of a low oxygen chemical potential (and elevated temperatures).[85,89,90] The simultaneous presence of an alkane (and oxygen) in the gas feed has a significant influence on the oxygen exchange properties of the sample as was recently demonstrated for V_2O_5.[91] As discussed above, a high oxygen mobility might rather be required for the formation of the active surface termination layer than indicate a direct participation of actual lattice oxygen (from bulk diffusion) in the reaction.[10]

The catalysts should accomplish both the activation of alkanes (reduction of the catalysts) and the activation of O_2 (re-oxidation).[83] The succesive transfer of electrons to adsorbed oxygen and finally the incorporation of oxygen into the metal oxide lattice may (transiently) create different species at the surface from the electrophilic O_2^-, O_2^{2-}, and O^-, to the nucleophilic O^{2-} species.[12,89] In addition, various lattice oxygen atoms (with a formal oxidation state of -2) can usually be distinguished in these selective oxidation catalysts. Differently coordinated oxygen atoms in the vanadium oxide-based crystal structure, which exhibit a more or less partial covalent bonding character, also show a different degree of nucleophilicity.[79,80] This may likewise be modified by the presence of different metal ions or metal ions in different formal oxidation states exhibiting more or less strong M–O interactions.[89] Both the function of "nucleophilic oxygen" and of "electrophilic oxygen" is required, the former for the hydrogen abstraction from the alkanes and the latter for the formation of oxygenated products (with carbon–oxygen bonds).[10,15] Controlling the availability of reactive oxygen species for the partial oxidation reactions is believed to be an essential factor for achieving a high selectivity and avoiding an over-oxidation of the alkanes.[10] Furthermore, the handling of OH groups or generally the "water management"[10] and the acid–base properties of the catalysts should be considered.[10,20,30,89]

As mentioned above, the active oxygen species should be restricted, which relates to the "site isolation pillar" as an important means for obtaining a high selectivity in oxidation reactions of alkanes.[2] The site isolation principle states that the availability of active oxygen species should be limited to one active site providing just enough reactive oxygens for the stoichiometry of the reaction.[2] Too many active site ensembles or centers containing too many reactive oxygen species would lead to a loss of selectivity (over-oxidation).[2] In contrast, fully isolated (single) active oxygen species would result in a lower activity or in a different pathway.[2] The site isolation was suggested to be achieved by separating the redox-active (transition metal ion containing) active centers via the insertion of usually main group elements[10,22,92,93] or the formation of defect structures or nanodomains[84] on the catalysts' surfaces.[10]

These "seven pillars" based on empirical concepts were shown to be highly valuable in the synthesis of heterogeneous selective oxidation catalysts for light alkanes.[2] Yet, there remain open questions e.g. regarding the selectivity limits[10] or why many of these selective oxidation catalysts are not effectively oxidizing CO to CO_2.[10,72] One of the main limitations in heterogeneous selective oxidation research is the lack of a comprehensive theory based on the physics of these complex systems.[10]

1.3. Alkane Oxidation over Semiconducting Bulk Oxides

It was shown that many of these catalysts are, in fact, (wide band gap) semiconductors that form surface termination layers differing from their bulk structure and adapting to the gas atmosphere.[10] In addition to traditional concepts discussing local active sites, electronic and semiconducting properties are likely to play a role for their catalytic performance, for instance the charge transfer between the catalyst and adsorbates, which can generate reactive species upon chemisorption.[94] At first glance, the picture of a catalyst as a semiconductor with a band structure enabling electron or hole transfer to the surface might raise the questions of how to accomplish isolated active sites[10] – a concept, which is very successful for explaining a high selectivity.[2,93] If there would be an unrestricted oxygen activation, the site isolation principle could hardly be realized. It should be emphasized, though, that both the localized molecular picture and the band structure picture of the catalyst–adsorbates system as described by a "rigid band model"*[95] represent boundary cases to the real situation.

Approaches for describing the working mode of selective oxidation catalysts including the bulk electronic structure modified by a surface termination layer have recently been addressed by Schlögl [10], together with a discussion of the "seven pillars" from Grasselli. Despite the relevance of semiconductor physics concepts for gaining understanding of selective oxidation catalysts,[42] there are still comparatively few studies in the literature. Figure 1.3 depicts the results of a literature search of keywords used in this context (ISI Web of Science `https://webofknowledge.com`) showing that the majority of studies are still conducted in the field of physics and less in the fields of chemistry and catalysis.

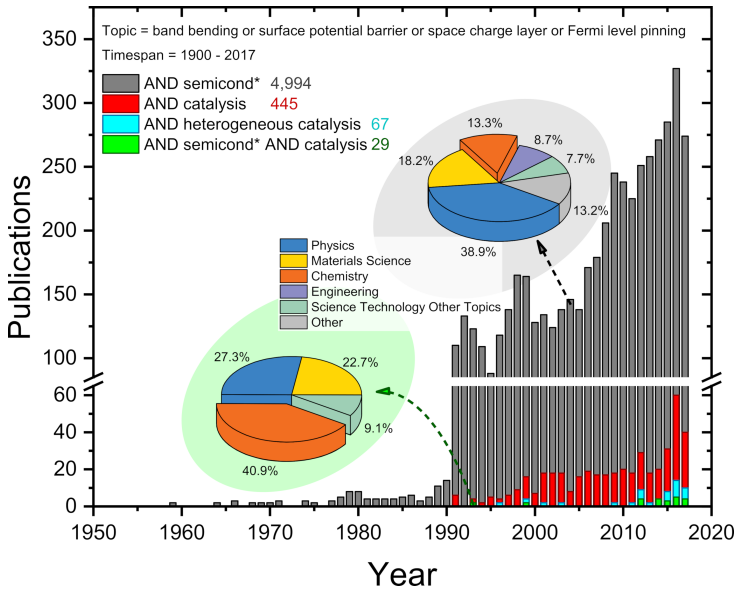

Figure 1.3.: Semiconductor physics publications in catalysis literature. ISI Web of Science literature search `https://webofknowledge.com` inspired by Zhang & Yates [96] (6th of September, 2017).

Besides local bonding interactions between reactants and active site ensembles, their coupling to the bulk electronic structure should be considered.[10] It should be remembered that such a

*Neglecting local bonding that e.g. leads to a shift and bonding/antibonding splitting of the involved energy levels.[95] Yet, the rigid band model is useful to describe charge transfer to surface species (surface states).[95]

coupling should not be unrestricted in terms of a free (unlimited) charge carrier "flow" to/from the surface (or an unrestricted supply of reactive oxygen species) with respect to the site isolation principle.[89] In the following, the concepts with which one is concerned in semiconducting catalysts will be shortly outlined.

Already about 50 years ago Vol'kenshtein [94] and others[97,98] introduced an *electronic theory of catalysis* on semiconductors. Haber's work also focused on these so-called *electronic factors* of catalysis with emphasis on (selective) alkane oxidation reactions.[11,83] It can be useful to describe a transition metal oxide catalyst in terms of a band scheme, see for instance Fig. 1.4 (a) for an n-type semiconductor with donor levels E_D. Here, also some quantities from solid state physics are defined such as the valence band and conduction band edges E_{VB} and E_{CB} and the band gap E_g, the Fermi level E_F and the vacuum level E_{vac}, the work function Φ and the electron affinity χ of the semiconductor. Two cases are illustrated, namely a situation with flat bands extending from the surface of the semiconductor at $x = 0$ into the bulk (Fig. 1.4 (a)) and a space charge layer formation due to surface states carrying a negative charge Q_{ss} (Fig. 1.4 (b)). This shifts the energetic quantities in the surface/subsurface region with respect to E_F, which will be briefly discussed below.

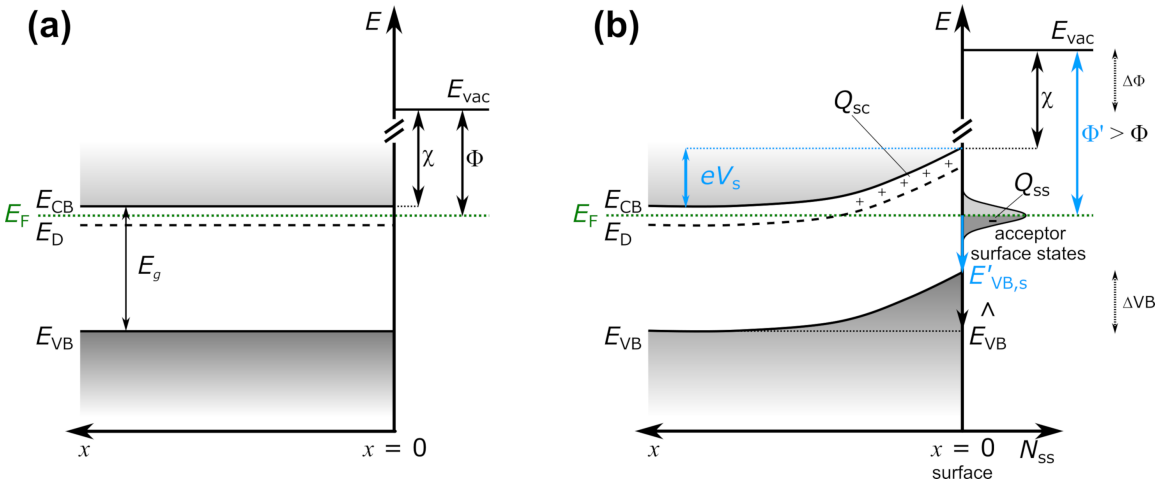

Figure 1.4.: Schematic representation of a space charge layer in an n-type semiconductor adapted from Lüth [99] and Morrison [95]: distance x pointing into the solid (surface at $x = 0$), filled or empty donor levels E_D, valence band and conduction band edges $E_{VB,CB}$, Fermi level E_F, density of surface states N_{ss} with charge Q_{ss}, space charge Q_{sc}, electron affinity χ, and work function Φ. The subscript "s" refers to the surface. **(a)** Flat band case, **(b)** depletion layer (upward band bending eV_s).

Initial studies often considered the "position" of the Fermi level E_F at the surface relative to the valence band maximum E_{VB} or conduction band minimum E_{CB} as descriptor,[83,94,95] which may affect the charge transfer across the bulk–surface–adsorbates interface and hence the activation of the reactants.[94] In a broader context, the reactivity of a catalyst's surface may be modified by shifting the energy levels at the surface relative to the Fermi level. This was also discussed to influence the selectivity of a reaction in certain cases, where it was distinguished between acceptor reactions that are accelerated by electrons and donor reactions that are accelerated by holes.[94] These reaction classes therefore favor a higher lying or a lower lying Fermi level, respectively.[94,95] Haber pointed out that a certain relative (matching) position of the energy

levels in the semiconducting catalysts and of the redox potential of the reactants is needed for the reaction to proceed, because the activation of both the alkane and of O_2 must be accomplished.[11,83] Also, a sufficient density of states is required for a high probability of charge transfer.[11,83]

Besides doping the bulk semiconductor, the chemisorption of molecules and the formation of the above-mentioned surface termination layer can shift the relative position of the energy levels at the semiconductor surface (valence band and conduction band onset, surface states) with respect to E_F.[98,100] Defect formation at the surface of vanadium oxide-based catalysts may lead to the creation of surface states which can readily interact with adsorbates.[11,83,99,101] Surface states represent localized electronic levels at the surface in the band gap and can be intrinsic or created by defects, impurities, a surface layer differing from the bulk, and adsorbates (extrinsic surface states).[95,99] For example, Fig. 1.4 (b) shows acceptor surface states of density N_{ss}. Charge carrier transfer to the surface creates a surface charge Q_{ss}, which is screened by the space charge Q_{sc} in the subsurface region of the semiconducting catalyst. This creates an electric field in the space charge region and leads to a bending of the bands with a maximum value of $|eV_s|$ at the surface (V_s being the potential at the surface "s").[95,99] This is illustrated in Fig. 1.4 (b) showing a depletion layer in an n-type semiconductor. However, the bulk–surface charge transfer is limited due to the built-up of the surface charge (see also Weisz limit[102]).[94] Considering an increase in band bending with increasing density of surface states N_{ss}, a limitation or saturation is reached where the Fermi level becomes pinned close to the surface state energy.[95,99,100] Importantly, the occupation of the valence and conduction band at the surface and of the surface states is affected by their "movement" relative to E_F.[95,99]

The subsurface region shown in Fig. 1.4 (b) is depleted of free electrons to the depth of the space charge region[95] (repulsive potential for electrons within the space charge layer[99]). Electrons in this range will experience a barrier for electron transfer.[95] In the context of selective oxidation reactions, the activation of oxygen (by transferring electrons to O_2(ads)) might be limited by the barrier height.[10,42] A recent application of such concepts to the industrial *n*-butane oxidation catalyst VPP was given by Eichelbaum *et al.* [42]. It should be kept in mind that the reactive gas atmosphere can modify or create surface states and affects the surface termination layer. Due to a change of the (adsorbate-modified) band bending, which adapts to the chemical potential of the gas phase, the relative positions of the valence band or conduction band edges and of the surface state energy can shift with respect to the Fermi level.[10,42,83] This dynamic surface potential barrier might provide a means of controlling the oxygen activation over selective semiconducting transition metal oxide catalysts like VPP or MoVTeNb-oxide.[10,42]

Thus, the catalytic properties of these catalysts may be influenced by shifting the energy levels in the solid (at the surface) with respect to E_F by the creation and filling of surface states due to defects, a surface termination layer ("interface"), chemisorption of reactants, or by doping the bulk.[83] Changes in band bending $e\Delta V_s$ can also affect the electrical conductivity since the charge carrier density in the space charge region is influenced. Furthermore, they can be monitored by changes in the work function $\Delta\Phi$, and in the valence band maximum ΔE_{VB} and core level binding energies (cf. Fig. 1.4), which can be obtained from near-ambient pressure X-ray photoelectron spectroscopy (NAP-XPS).

1.4. The Investigation of Charge Transport and Charge Transfer

Since it was realized that electronic properties may be relevant for the catalytic function of heterogeneous selective oxidation catalysts, the electrical conductivity and redox properties of the catalysts were studied with the aim of gaining a deeper understanding[11,30] that might pave the way to a rational design of new catalysts. Initial conductivity studies on VPP, which have been performed using contact methods on pressed powder samples, identified the catalyst as p-type semiconductor based on its conductivity response to more or less reducing or oxidizing gas atmospheres.[60] Within the concept of a redox catalyst, the charge carrier exchange between the reactants (i.e., alkane and oxygen) is mediated via the catalyst.[11] The catalyst can oxidize the alkane (starting with a C–H cleavage and reducing the catalyst) and activate O_2 (re-oxidation of the reduced catalyst to close the catalytic cycle).[11] The participation of charge carriers from the catalyst in the reaction might be monitored in changes in its electrical conductivity. Therefore, the study of the ease of charge transfer, of the electrical conductivity, and the charge carrier concentration and mobility[30] was advocated using "*operando* techniques" to obtain the charge carrier dynamics under catalytic operation conditions.[14] The information gained about the catalyst's behavior during the reaction could contribute to a better understanding that might lead to the identification of crucial parameters for their catalytic performance.

Operando and contact-free electrical conductivity measurements based on the microwave cavity perturbation technique (MCPT)[103] have been succesfully applied to study the electronic properties of semiconducting catalysts under operating conditions.[1,39,40,104,105] Changes in the complex permittivity $\tilde{\varepsilon} = \varepsilon' - i\varepsilon''$ (also called complex dielectric function) of the samples are addressed, where the imaginary part ε'' is related to the electrical conductivity of the catalysts.[103,106] The complex permittivity $\tilde{\varepsilon}(\omega)$ is a function of the frequency ($\omega = 2\pi f$) of the electric field or electromagnetic radiation. It describes the interaction with the electric field component, where the real part ε' is related to energy storage and the imaginary part ε'' to the dissipation of energy.[106] The interaction with the magnetic field is described by the complex permeability $\tilde{\mu}(\omega)$.[106] Complex permittivity and permeability investigations are mostly conducted in the field of materials science, for instance for nanostructured electromagnetic wave absorption materials (EM shielding etc.),[107–118] or in the characterization of ferroelectric materials (e.g. perovskites).[106,119–122] Fewer studies have been published on the complex permittivity of heterogeneous catalysts, besides the *operando* MCPT investigations in our group e.g. on selective oxidation catalysts,[1,39,40,104,105,123] or by Moos and co-workers in the study of the selective catalytic reduction of nitrogen oxides by ammonia[124,125] and the three-way-catalyst[126,127] as well as by Liu *et al.*, who investigated the coking of acid zeolite catalysts.[128]

The MCPT has several advantages over convential contact-methods, in particular over two-point methods, namely being a non-invasive and contact-free technique.[103,129] It allows for the characterization of catalysts under *operando* conditions at elevated temperatures in reactive gas atmospheres.[103] Furthermore, as resonant method a high sensitivity and accuracy is obtained.[106] The MCPT setup was recently refined using cylindrical resonators,[130] which enable the usage of TM_{0n0} modes for measuring the samples in the (highly uniform) electric field maximum along the cylinder axis.[106] The theoretical basis of the method is outlined in Chapter 2.

1.5. Aims and Outline of the Present Thesis

Research on heterogeneous selective oxidation catalysts has identified several important characteristics of these usually complex materials as outlined above in Sections 1.2 – 1.4. On the one hand, spatially isolated active site ensembles are recognized as being required for obtaining a high selectivity and limiting the formation of the waste products CO and CO_2, on the other hand, electronic properties like the charge carrier dynamics seem to be highly relevant for their catalytic performance.

The present thesis focused on investigating the role of charge transport and charge transfer between the catalysts and the adsorbates during the oxidation of light alkanes. To achieve this, contact-free conductivity measurements were performed under catalytic operation conditions and combined with other techniques that characterize the (surface) electronic structure. Vanadium oxide-based catalysts were selected with different catalytic properties. The series comprises non-stoichiometric vanadium pentoxide (V_2O_{5-x}) as reference material, which is an n-type semiconductor and exhibits a low selectivity for partial oxidation products. Furthermore, the moderately selective MoV-oxide in the orthorhombic M1 phase was studied, whose semiconducting properties are investigated for the first time in this thesis to the best of my knowledge. Finally, the highly selective industrial catalyst VPP for maleic anhydride production from *n*-butane was considered, whose bulk phase corresponds to the p-type semiconducting vanadyl pyrophosphate $(VO)_2P_2O_7$.

The results of this thesis are presented in Chapters 3 to 5.

In a first step, the influence of *n*-butane- and O_2-containing gas atmospheres on the electronic structure of V_2O_{5-x} was investigated. The aim was a comparison of the electronic structure response to the one of VPP, which might show differences that could be related to their respective catalytic performance. These data were in part published in Ref. [42], which addresses the question whether a dynamic gas-phase-dependent band bending acts as a means of controlling the bulk–surface–adsorbates charge transfer and hence the generation of reactive oxygen species. Chapter 3 presents a NAP-XPS and NEXAFS study on V_2O_{5-x}. Gas-phase-induced changes in the surface composition and oxidation state are shown both from a core level and from a V 3d band gap level analysis. NEXAFS spectroscopy was applied to study the local electronic structure of the unoccupied states from the V 2p and O 1s core level excitations. These measurements were complemented by resonant photoelectron spectroscopy, which enabled a detailed investigation of the valence band and band gap states of V_2O_{5-x} under the influence *n*-butane- and O_2-containing gas feeds.

Following this, the charge transfer and charge transport properties of V_2O_{5-x} and VPP were investigated in the oxidation of *n*-butane in Chapter 4. The aim was a quantitative and direct comparison of their semiconducting and charge transfer properties under catalytic operation conditions. For this purpose, *operando* microwave conductivity experiments were conducted. First, suitable experimental conditions had to be defined in terms of the microwave resonators and modes and the data analysis, in addition to the investigation under iso-conversion conditions. These measurements were complemented by diffuse reflectance UV-Vis spectroscopy, which is likewise related to the samples' permittivity (dielectric) function, but in a higher frequency range probing electronic transitions.

In Chapter 5 the (surface) electronic structure and semiconducting properties of the MoV-oxide catalyst (M1 phase) were studied under alkane oxidation conditions from ethane to *n*-butane. Furthermore, the influence of steam on the electronic properties and the surface electronic structure of MoV-oxide was investigated in the oxidation of propane. This chapter presents a thorough characterization of the mixed-metal oxide with *operando* MCPT conductivity/permittivity experiments, which were supported by NAP-XPS and NEXAFS spectroscopy.

Chapter 6 gives a general discussion of this "series" of vanadium-based transition metal oxide catalysts and a brief overview of their electronic structure under *n*-butane oxidation as determined with NAP-XPS and complemented by their semiconducting properties. This series comprises the oxides V_2O_{5-x} – MoVTeNb-oxide (M1 phase)[1] – MoV-oxide (M1 phase) – VPP[42].

A summary and the conclusions obtained in this thesis are presented in Chapter 7.

2. The Microwave Cavity Perturbation Technique

This chapter is intended to give an introduction to the physics behind the microwave cavity perturbation technique (MCPT), which is the basis for the contact-free and *operando* conductivity measurements applied in this work. To begin with, electromagnetic fields in cavity resonators will be discussed. The second part focuses on the principles behind the MCPT. In addition, the MCPT data analysis and an effective medium approach for obtaining bulk permittivity values from powder samples are briefly discussed.

2.1. Cavity Resonators and Cavity Modes

In a resonant cavity, a situation is created where a changing (time-varying) electric field gives rise to a changing magnetic field, which in turn produces an electric field etc.[131] For perfectly conducting cavity walls no energy is lost with time.[106] In the case of a cylindrical cavity, Maxwell's equations give the following solution for the oscillating electric field[131]

$$\mathbf{E} = \mathbf{E}_0 \, e^{i\omega t} \, J_0 \left(\frac{\omega r}{c} \right) \tag{2.1}$$

where $J_m(x)$ denotes Bessel functions of first kind of order m (see Fig. 2.1).[132] The angular frequency is given by $\omega = 2\pi f$. In this work the standard meaning of c (speed of light), t (time), i (imaginary unit $i^2 = -1$), ε_0 (vacuum permittivity), μ_0 (vacuum permeability) will be used, which can also be found in the "List of Symbols" on page xxi. The Bessel functions, which are needed to describe cylindrically symmetric waves, go through zero at characteristic values of x, for example $J_0(x)$ is zero at $x = 2.405, 5.52, \ldots$.[131] The resonant frequency ω_0 of the first mode Eq. (2.1) in a cylindrical cavity with radius r_c is given by $\omega_0 = 2.405 \ (c/r_c)$.[131] There are, however, other possibilities of oscillating electric and magnetic fields as well that are still concordant with Maxwell's equations, i.e. other cavity modes.[131]

The electromagnetic field in a cylindrical resonator can be split into an axial or longitudinal (z) component and into transverse components (r, ϕ).[106] It can then be distinguished between *transverse electric* TE ($E_z = 0$) and *transverse magnetic* TM ($B_z = 0$) waves.[106] It may be noted that transmission structures like coaxial lines can also support *transverse electromagnetic* TEM modes ($E_z = 0$ and $B_z = 0$).[106] The field distribution of a TM_{mnp} mode ($m = 0, 1, 2, \ldots$, $n = 1, 2, 3, \ldots$, and $p = 0, 1, 2, \ldots$) of a cylindrical resonator with radius r_c and height h, for

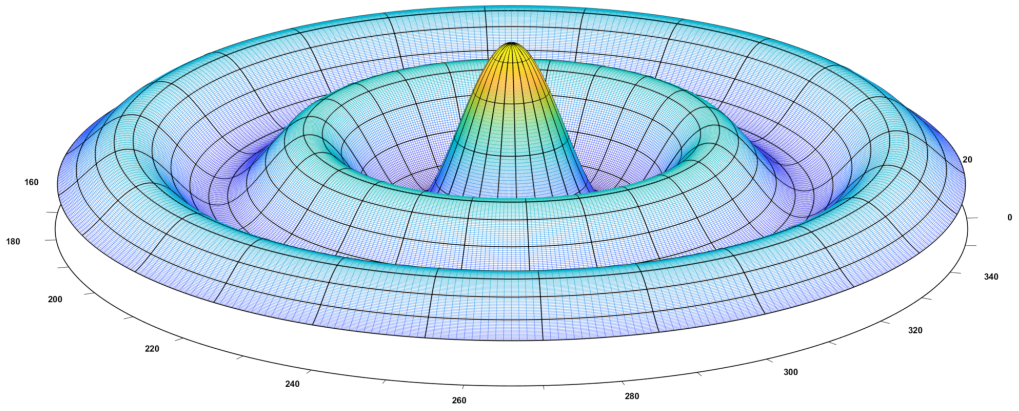

Figure 2.1.: Zeroth order Bessel function of the first kind $J_0(x)$ in polar coordinates.

example, is given by (in cylindrical coordinates r, z, ϕ)[103,106]

$$E_r = -\frac{a_{mn}}{r_c}\frac{p\,\pi}{h}\,J'_m\left(\frac{a_{mn}}{r_c}r\right)\,\cos\left(m\phi\right)\,\sin\left(\frac{p\,\pi}{h}z\right) \tag{2.2}$$

$$E_\phi = \frac{1}{r}\frac{m\,p\,\pi}{h}\,J_m\left(\frac{a_{mn}}{r_c}r\right)\,\sin\left(m\phi\right)\,\sin\left(\frac{p\,\pi}{h}z\right) \tag{2.3}$$

$$E_z = \left(\frac{a_{mn}}{r_c}\right)^2\,J_m\left(\frac{a_{mn}}{r_c}r\right)\,\cos\left(m\phi\right)\,\cos\left(\frac{p\,\pi}{h}z\right) \tag{2.4}$$

where E_r is the radial, E_ϕ the angular, and E_z the longitudinal component.[103,106] Here, the indices m and n are related to the (transverse) x and y directions (or to ϕ and r in cylindrical coordinates), whereas p is associated with the z direction and gives the number of changing cycles along the z direction.[103,106] J_m corresponds to the m-th order Bessel function with its first derivative J'_m and a_{mn} is the n-th root of J_m.[103,106] This TM_{mnp} mode has a resonant wavelength λ_0 of[103,106]

$$\lambda_0 = \frac{2}{\sqrt{(\frac{a_{mn}}{r_c\,\pi})^2 + (\frac{p}{h})^2}} \tag{2.5}$$

For a TM_{010} mode ($m = p = 0$, $n = 1$) with $a_{01} = 2.405$, which was used in this thesis, the electric field distribution simplifies to only one nonzero component E_z (generally for TM_{0n0} modes), i.e. $E_r = E_\phi = B_r = B_z = 0$. E_z only depends on the radius r_c of the cylindrical cavity but not on its height.[106]

$$E_z = \left(\frac{a_{01}}{r_c}\right)^2\,J_0\left(\frac{a_{01}}{r_c}r\right) \tag{2.6}$$

The resonant frequency of the TM_{010} mode in a cylindrical resonator is given by $f_0 = (c\,a_{01})/(2\,\pi\,r_c)$. Higher cavity modes can be used for measurements at increasing frequencies, for instance TM_{0n0} modes with $n > 1$, which exhibit higher resonant frequencies because of the greater roots of the zeroth-order Bessel function (e.g. $a_{02} = 5.52$[131]).

It should be noted that the above-derived equations describe an ideal resonant cavity, where the material of the cavity walls is a perfect conductor and which is filled with a lossless material. In

a real resonator, the stored energy in form of the oscillating electric and magnetic fields decreases with time due to the resistance of the wall material.[131] It is, however, possible to build resonant cavities with a high quality factor corresponding to a low energy dissipation by using materials with a high conductivity like silver.[131]

2.2. The Theory behind the MCPT

As a next step, a small semiconducting or insulating sample is inserted into a resonant cavity, which will be treated as a perturbation of the above-described ideal empty cavity. The following derivations correspond to the quasi-static approximation requiring a small sample size[133,134] and the depolarization regime assuming that the electric field penetrates the whole sample homogeneously and is close to the external field.[133,135] The microwave cavity perturbation technique (MCPT) was described by Slater [136] in 1946. It is based on a change of the resonant frequency ω and the quality factor Q of a microwave resonator caused by the introduction of a sample, which can be used to determine its permittivity.[106]

The microwave cavity perturbation formulas can be derived employing a complex angular frequency $\tilde{\omega}$ and using $\exp(i\tilde{\omega}t)$ for the time dependence of the fields inside the cavity resonator.[133] According to Maxwell's equations the curl of the electric and magnetic field, respectively, is given by[106,137]

$$\nabla \times \mathbf{E} = -\frac{\partial \mathbf{B}}{\partial\, t} = -i\,\tilde{\omega}\,\mathbf{B} = -i\,\tilde{\omega}\,\tilde{\mu}\,\mathbf{H} \tag{2.7}$$

$$\nabla \times \mathbf{H} = \frac{\partial \mathbf{D}}{\partial\, t} = i\,\tilde{\omega}\,\mathbf{D} = i\,\tilde{\omega}\,\tilde{\varepsilon}\,\mathbf{E} \tag{2.8}$$

$$\mathbf{B} = \tilde{\mu}\,\mathbf{H}$$

$$\mathbf{D} = \tilde{\varepsilon}\,\mathbf{E}$$

In the low conductivity region of the depolarization regime the following MCPT equations can be derived. Here, the perturbation of the empty cavity (subscript 1) by inserting a small sample with comparatively low permittivity $\tilde{\varepsilon}_r$ into the electric field antinode (subscript 2) will be described. Combing the curl expressions for the unperturbed and perturbed case and integrating over the cavity volume V_c the following equation is obtained.[106]

$$\underbrace{\iiint_{V_c} \nabla \cdot [(\mathbf{E}_1^* \times \mathbf{H}_2) + (\mathbf{E}_2 \times \mathbf{H}_1^*)]\, dV}_{=0 \quad \text{for perfectly conducting cavity walls}} = i \left[(\tilde{\omega}_2 - \tilde{\omega}_1) \iiint_{V_c} (\tilde{\varepsilon}_1\, \mathbf{E}_2 \cdot \mathbf{E}_1^* + \tilde{\mu}_1\, \mathbf{H}_2 \cdot \mathbf{H}_1^*)\, dV \right.$$

$$\left. + \tilde{\omega}_2 \iiint_{V_c} (\Delta\tilde{\varepsilon}\, \mathbf{E}_2 \cdot \mathbf{E}_1^* + \Delta\tilde{\mu}\, \mathbf{H}_2 \cdot \mathbf{H}_1^*)\, dV \right] \tag{2.9}$$

$$\text{with} \qquad \Delta\tilde{\varepsilon} = \tilde{\varepsilon}_2 - \tilde{\varepsilon}_1$$

$$\text{and} \qquad \Delta\tilde{\mu} = \tilde{\mu}_2 - \tilde{\mu}_1$$

Equation (2.9) can be rewritten giving an expression for the complex angular frequency shift.[106]

$$\frac{\tilde{\omega}_2 - \tilde{\omega}_1}{\tilde{\omega}_2} = -\frac{\iiint\limits_{V_c} \left(\Delta\tilde{\varepsilon}\,\mathbf{E}_2 \cdot \mathbf{E}_1^* + \Delta\tilde{\mu}\,\mathbf{H}_2 \cdot \mathbf{H}_1^*\right) dV}{\iiint\limits_{V_c} \left(\tilde{\varepsilon}_1\,\mathbf{E}_2 \cdot \mathbf{E}_1^* + \tilde{\mu}_1\,\mathbf{H}_2 \cdot \mathbf{H}_1^*\right) dV} \tag{2.10}$$

$$\approx -\frac{\iiint\limits_{V_s} \left(\Delta\tilde{\varepsilon}\,\mathbf{E}_2 \cdot \mathbf{E}_1^* + \Delta\tilde{\mu}\,\mathbf{H}_2 \cdot \mathbf{H}_1^*\right) dV}{\iiint\limits_{V_c} \left(\tilde{\varepsilon}_1\,\mathbf{E}_2 \cdot \mathbf{E}_1^* + \tilde{\mu}_1\,\mathbf{H}_2 \cdot \mathbf{H}_1^*\right) dV} \tag{2.11}$$

$$\approx -\frac{\iiint\limits_{V_s} \left(\Delta\tilde{\varepsilon}\,\mathbf{E}_2 \cdot \mathbf{E}_1^* + \Delta\tilde{\mu}\,\mathbf{H}_2 \cdot \mathbf{H}_1^*\right) dV}{2\iiint\limits_{V_c} \left(\tilde{\varepsilon}_1\,\mathbf{E}_2 \cdot \mathbf{E}_1^*\right) dV} \tag{2.12}$$

The integral in the numerator of Eq. (2.10) needs to be carried out only over the sample volume V_s.[137] It is assumed that the electromagnetic field is unchanged in the region outside of the sample.[106] With the assumption that $\tilde{\mu}_1 = \tilde{\mu}_2 = \mu_0$ and $\tilde{\varepsilon}_1 = \varepsilon_0$, μ_0 and ε_0 being the vacuum permeability and vacuum permittivity, as well as $\tilde{\varepsilon}_2 = \tilde{\varepsilon}_r\,\varepsilon_0$, Eq. (2.12) can be expressed as[106]

$$\frac{\tilde{\omega}_2 - \tilde{\omega}_1}{\tilde{\omega}_2} = -\left(\frac{\tilde{\varepsilon_r} - 1}{2}\right) \underbrace{\frac{\iiint\limits_{V_s} \mathbf{E}_2 \cdot \mathbf{E}_1^*\, dV}{\iiint\limits_{V_c} |\mathbf{E}_1|^2\, dV}}_{C} \tag{2.13}$$

Using $\tilde{\omega} = \omega(1 + i/2Q)$ for the complex angular frequency and assuming a *small* real frequency shift ($\omega = 2\pi f$) upon inserting the sample, i.e. $\omega_1 \approx \omega_2$, as well as $\omega/2Q \ll \omega$ and $Q_2 \gg 1$, the complex frequency shift can be further simplified to[106]

$$\frac{\tilde{\omega}_2 - \tilde{\omega}_1}{\tilde{\omega}_2} \approx \left(\frac{f_2 - f_1}{f_2}\right) + i\left(\frac{1}{2\,Q_2} - \frac{1}{2\,Q_1}\right) \tag{2.14}$$

Inserting this expression into Eq. (2.13) and separating into real and imaginary parts ($\tilde{\varepsilon}_r = \varepsilon_r' - i\varepsilon_r''$) leads to the cavity perturbation equations used in the present work.

$$\frac{f_2 - f_1}{f_2} = -\frac{1}{2}\left(\varepsilon_r' - 1\right)\, C$$

$$\frac{f_1 - f_2}{f_2} = \frac{1}{2}\left(\varepsilon_r' - 1\right)\, C \tag{2.15}$$

$$\frac{1}{Q_2} - \frac{1}{Q_1} = \varepsilon_r''\, C \tag{2.16}$$

Substituting the parameter $C = B \cdot (V_s/V_c)$, which is sometimes called "filling factor", with the resonator mode constants A and $B = 2\,A$, which in a strict treatment depend on the sample and resonator geometry* and cavity mode, but can be determined by calibration using samples of

*The field $\mathbf{E}_2$ in the sample depends on geometric factors and the sample's permittivity.[106]

known permittivity,[103] the following equations are obtained

$$\frac{f_1 - f_2}{f_2} = A\ \left(\varepsilon_r' - 1\right)\ \frac{V_s}{V_c} \tag{2.17}$$

$$\frac{1}{Q_2} - \frac{1}{Q_1} = B\ \varepsilon_r''\ \frac{V_s}{V_c} \tag{2.18}$$

which relate the real frequency shift upon insertion of a sample to the real part of the relative permittivity ε_r' (Eq. (2.17)) and the change in the Q factor to the imaginary part of the sample's relative permittivity ε_r'' (Eq. (2.18)).

In summary, the main assumptions behind the microwave cavity perturbation equations (2.17) and (2.18) are that (i) the electromagnetic field distribution is essentially unchanged outside the sample[106,137] and the change of the frequency is small $\Delta\omega \ll \omega$,[137] (ii) the sample is small (compared to the cavity) and homogeneous,[106,137] (iii) the cavity walls are perfect conductors[106,137] and the empty cavity is filled with a lossless medium.[106]

The measurements in this thesis are assumed to be in the low-conductivity region of the depolarization regime according[138]

$$\frac{f_1 - f_2}{f_1} \ll A\frac{V_s}{V_c}\frac{1}{N} \tag{2.19}$$

with a small frequency shift for samples placed along the electric field antinode in a cylindrical resonator operating at the TM_{010} mode and assuming a maximum depolarization factor of $N =$ 0.1 to 0.2 (approx. cylindrical sample shape with a height of 7 mm and radius of 1.5 mm). The sample placement in the electromagnetic field inside the cylindrical cavity (TM_{010} mode) will be shown later in Fig. 2.2 (b). The ratio of the sample radius to the cavity radius was between $r_s/r_c = 0.04$ and 0.07 throughout this work, i.e. $r_s \ll r_c$, in which case the external electric field is highly uniform in the center of the cavity where the sample is placed.[106,139]

2.2.1. Electrical Conductivity Determination and Effective Medium Theory

The complex permittivity $\tilde{\varepsilon}$ of a sample is related to its complex electrical conductivity $\tilde{\sigma}(\omega) = \sigma'(\omega) - i\sigma''(\omega)$. The real part of the conductivity is related to the imaginary part of the permittivity (loss current), whereas the imaginary part of the conductivity (charging current) can be compared to the real part of the permittivity.[106,140] The real part of the conductivity may comprise both contributions from free charge carriers (ohmic loss) and from dielectric loss due to bound charges, where the contribution of the former should dominate for semiconductors investigated in the microwave frequency range.[106] This holds true for low frequencies of the electromagnetic field,† where the charge carrier collision frequency ω_0 of the semiconductor is much higher than the angular frequency of the microwaves ω ($\omega_0^2 \gg \omega^2$).[106,141,142] The real part

†Compared to e.g. optical frequencies.

of the electrical conductivity can be calculated according to[106]

$$\sigma' = \omega\, \varepsilon'' = \omega\, \varepsilon_0\, \varepsilon_r'' \tag{2.20}$$

i.e. using the resonant angular frequency (ω) and the imaginary part of the permittivity (ε'').

In the case of powder samples, Eqs. (2.17) – (2.18) and (2.20) give the conductivity of the powder. The complex permittivity of the solid or bulk (subscript s) can be determined from the measured complex permittivity of the powder samples (subscript p) by using an "effective medium theory". Several approximations were derived in the literature for obtaining bulk permittivity values, for example by Bruggeman,[143] Böttcher,[144,145] or by Maxwell Garnett.[146] In the present thesis the formula by Landau, Lifshitz and Looyenga[147,148] was used because it was shown to yield accurate values for semiconducting or insulating powder samples investigated in the microwave range and can be applied for various particle shapes.[104,148,149] The formulas are given in Eqs. (2.21) and (2.22) with the volume fraction factor $\delta = \rho_{\text{powder}}/\rho_{\text{crystal}}$.[149] The crystallographic density ρ_{crystal} can be determined from a Rietveld analysis of the XRD pattern of the sample and the powder density is given by $\rho_{\text{powder}} = m/V_s = \text{mass}/(\text{sample volume})$.[104]

$$\varepsilon_{r,p}'^{\,1/3} - 1 = \delta \cdot \left(\varepsilon_{r,s}'^{\,1/3} - 1\right) \tag{2.21}$$

$$\varepsilon_{r,s}'' = \frac{\varepsilon_{r,p}''}{\delta} \left(\frac{\varepsilon_{r,s}'}{\varepsilon_{r,p}'}\right)^{2/3} \tag{2.22}$$

2.3. Experimental Considerations of the *Operando* MCPT Setup

The *operando* MCPT setup in our group was developed by Eichelbaum *et al.* [103] for investigating the electrical conductivity of catalytically active solid samples. The instrument was designed in order to measure sieve fractions of powder samples in a thin-walled quartz tube fixed-bed reactor with a continuous gas flow and online gas analytics at elevated temperatures (e.g. room temperature to 450 °C). The current setup, which was used in this thesis, is schematically depicted in Fig. 2.2.

In practice, the measurements are realized by coupling energy from a source into the electromagnetic field in the resonator and analyzing the reflection coefficient (ratio of reflected wave and incoming wave voltages V_-/V_+[106,150]). The core of the apparatus is shown in Fig. 2.2 (a) consisting of a cylindrical microwave resonator connected to a vector network analyzer (VNA) as external source and detector via semi-rigid coaxial cables. In the present work a coupling loop was used (inductive coupling mechanism). The electric and magnetic field distribution of the TM_{010} mode and the sample positioning in the electric field antinode along the cylinder axis[106] is illustrated in Fig. 2.2 (b).

The *operando* measurements are realized as indicated in Fig. 2.2 (c), where the thin-walled quartz reactor tube and the heating system are shown. The sample is heated by a preheated nitrogen flow, while a quartz dewar connected to a vacuum pump as thermal insulation and Peltier elements mounted on the resonator keep the cavity at a constant temperature. The cavity resonator was cooled to 20 °C during the *operando* measurements and a constant flow of dried N_2 through the cavity was applied in order to avoid water condensation. The MCPT

setup is equipped with a gas supply system using Bronkhorst mass flow controllers and a gas chromatograph (GC) to measure the effluent gas feed composition and to obtain the catalytic performance data. Further details on the setup can found in the experimental sections of the following chapters and in Refs. [103, 130, 151]. The MCPT data analysis will be described in the next section.

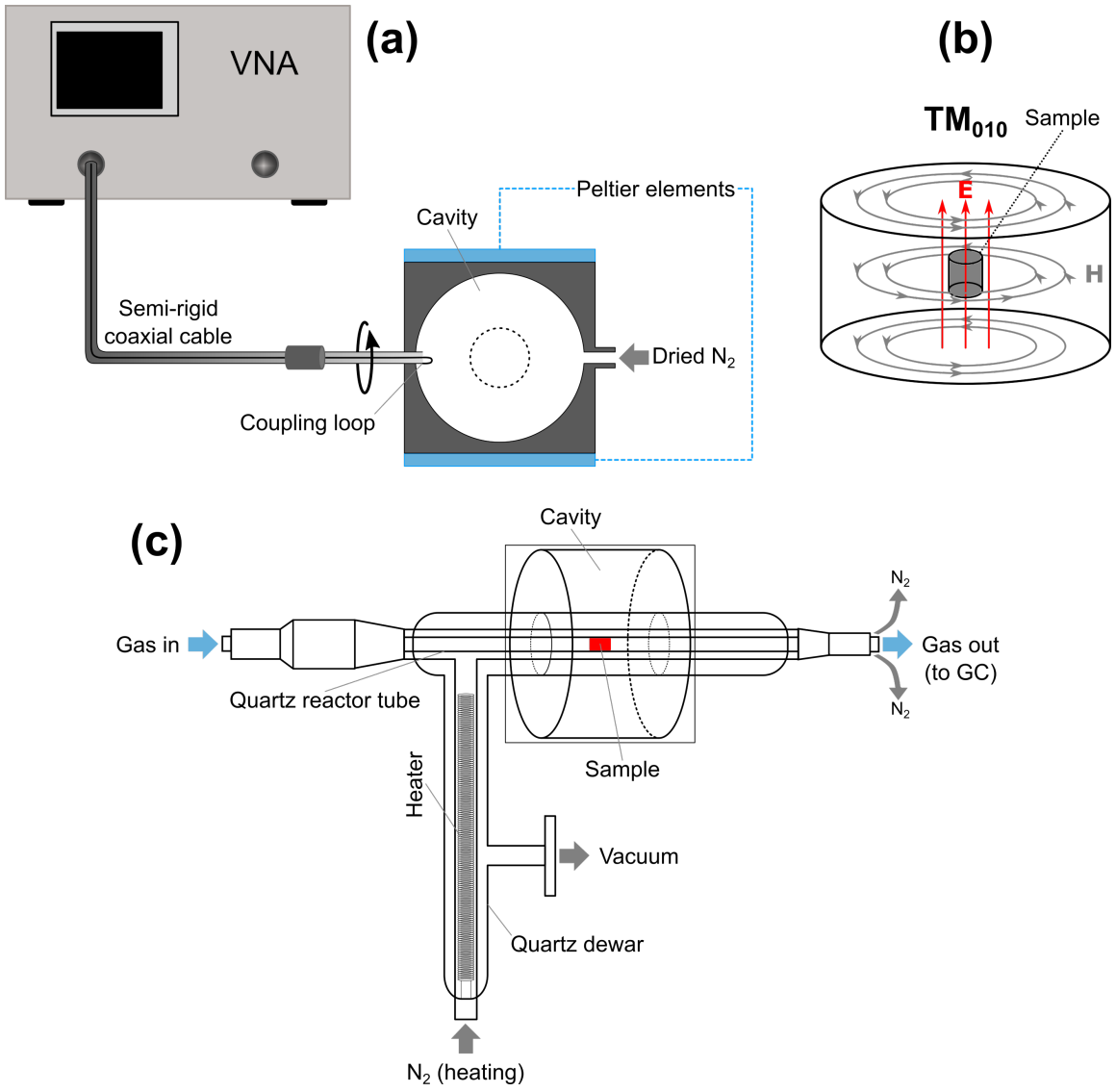

Figure 2.2.: Scheme of the MCPT setup: **(a)** cylindrical cavity resonator connected to a vector network analyzer (VNA) via semi-rigid coaxial cable and applying a coupling loop; **(b)** TM_{010} mode and sample positioning (adapted from Ref. [106]); **(c)** reactive or inert gas flow through quartz reactor tube heated by a nitrogen flow; the heater is placed outside of the resonator in a quartz dewar connected to a vacuum pump for thermal insulation.

2.4. Reflection Coefficient and Q Factor Determination

To obtain the permittivity of a sample, the MCPT equations ((2.17) and (2.18)) require the cavity Q factor and resonant frequency of the empty resonator and the sample-loaded resonator. The quality factor Q of a cavity is given by the resonant frequency ω divided by the half-power

bandwidth $\Delta\omega_{1/2}$ and is related to the energy storage (W) and loss (P_L).[106,133]

$$Q = \frac{\omega}{\Delta\omega_{1/2}} = \omega\,\frac{W}{P_L} = \omega\,\frac{\text{time-averaged energy stored}}{\text{energy loss / cycle}} \tag{2.23}$$

The energy dissipation power P_L is related to resistive losses of the cavity walls and the dielectric loss due to the medium inside the cavity.[106]

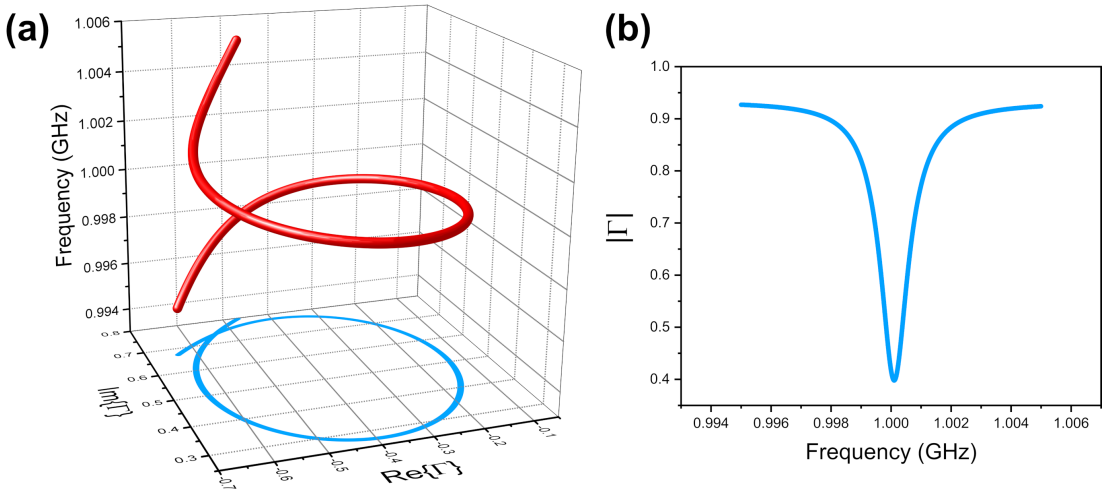

Figure 2.3.: **(a)** Complex reflection coefficient $\tilde{\Gamma}(\omega)$ as a function of the microwave frequency (in red) for a cavity resonating at ∼1 GHz and projection onto Re{Γ}–Im{Γ} plane (in blue); **(b)** amplitude (magnitude) of $|\Gamma| = [(\mathrm{Re}\{\Gamma\})^2 + (\mathrm{Im}\{\Gamma\})^2]^{1/2}$ (simulated data with MATLAB).

The experiments in this thesis correspond to reflection-type measurements, i.e. changes in the complex reflection coefficient $\tilde{\Gamma}(\omega)$ as a function of the frequency around the resonance were monitored with a vector network analyzer (VNA). A simulated reflection coefficient $\tilde{\Gamma}(\omega)$ is presented in Fig. 2.3. The effects of introducing a small sample into a microwave resonator on $\tilde{\Gamma}$ are schematically shown in Fig. 2.4 in terms of a shift of the resonant frequency and a peak broadening (increase in the bandwidth), which leads to a decrease of the cavity Q factor according to Eq. (2.23). The data shown in Figures 2.3 and 2.4 were simulated with MATLAB as described by Kajfez [152].

The recorded Q factor of the entire system is a "loaded" Q factor, Q_L, which includes both the effects of the external circuit (the VNA as external source, the transmission line, and the coupling mechanism) and the resonator, i.e. it includes the additional energy dissipation (P_{ext}) which can be summarized in an external Q_{ext}.[106,152] The unloaded Q_0 can be obtained from the measured Q_L if the coupling coefficient κ is known.[106,152]

$$\frac{1}{Q_L} = \frac{1}{Q_0} + \frac{1}{Q_{\mathrm{ext}}} = \frac{1}{\omega}\,\frac{(P_0 + P_{\mathrm{ext}})}{W} = \frac{(1+\kappa)}{Q_0} \tag{2.24}$$

The coupling coefficient describes the ratio of power dissipated in the external circuit to the power dissipated in the resonator.[106,152] For a *critical coupling* ($\kappa = 1$) this ratio is equal to one, whereas for *under-coupling* ($\kappa < 1$) the power dissipation in the resonator is greater than the one in the external circuit and vice versa for $\kappa > 1$ (*over-coupling*).[106] In order to extract the

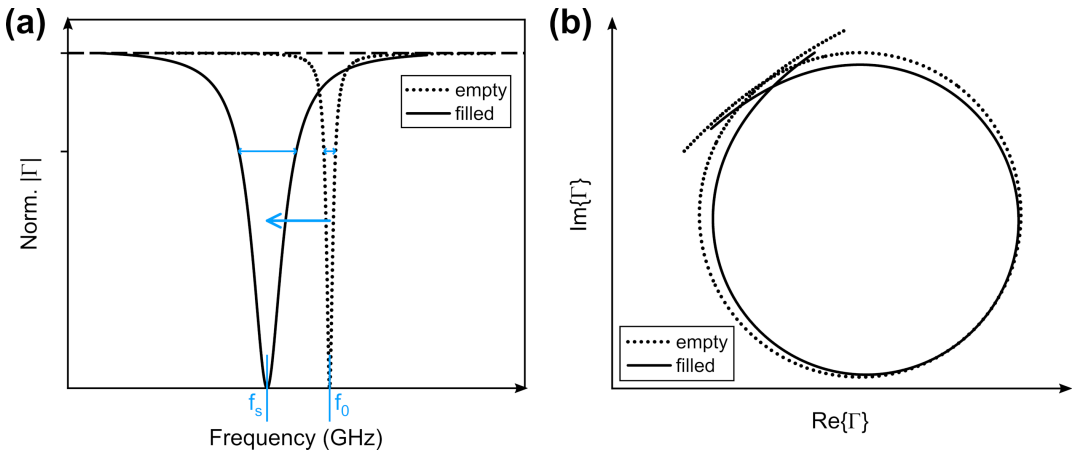

Figure 2.4.: Schematic representation of effects of introducing a sample into a microwave resonator on the complex reflection coefficient $\tilde{\Gamma}(\omega)$ with empty = empty cavity, filled = sample-loaded cavity; **(a)** normalized amplitude of reflection coefficient $|\Gamma|$ vs. frequency, **(b)** $\mathrm{Re}\{\Gamma\}$ vs. $\mathrm{Im}\{\Gamma\}$ (simulated data with MATLAB).

unloaded Q_0 and resonant frequency from the measured complex reflection coefficient, which are required in the MCPT equations ((2.17) and (2.18)), the data were fitted with the Q0REFL MATLAB program,[152] which was modified in the present thesis to automatically select the fitting range and subsequently perform the fit for all data points recorded during the *operando* MCPT measurements. The data analysis is based on an iterative fitting of the complex reflection coefficient $\tilde{\Gamma}$ to the ideal "Q circle" in the Smith chart, which is depicted in Fig. 2.5, weighted around the resonant frequency.[153,154] The quantities needed for the Q circle analysis are also defined in Fig. 2.5. If no coupling losses are present, the Q circle touches the perimeter of the Smith chart in the point Γ_d (the detunded reflection coefficient far from the resonance) and a line from the center of the Smith chart to Γ_d also goes through the center of the Q circle and through $\Gamma_L(\omega_L)$ (the loaded reflection coefficient at the loaded resonant frequency ω_L), which lies furthest from Γ_d (at $\max|\Gamma - \Gamma_d|$).[153] In this case, the coupling coefficient κ can be directly determined from the diameter d of the Q circle $\kappa = 1/[(2/d) - 1]$.[153] However, if coupling losses are present an auxiliary circle ("loss circle"[106]) is needed (cf. Fig. 2.5). This loss circle has a diameter d_2 and is tangential to both the perimeter of the Smith chart (at $\Gamma = 1$) and the Q circle (at Γ_d).[153]

$$d_2 = 2\frac{1 - |\Gamma_d|^2}{1 - |\Gamma_d|\cos\varphi} \tag{2.25}$$

In the presence of coupling losses, the coupling coefficient is determined from[153]

$$\kappa = \frac{1}{(d_2/d) - 1} \tag{2.26}$$

It is now possible to obtain the unloaded Q_0 from Eqs. (2.24) and (2.26), which can then be used for the MCPT permittivity calculation in Eq. (2.18).

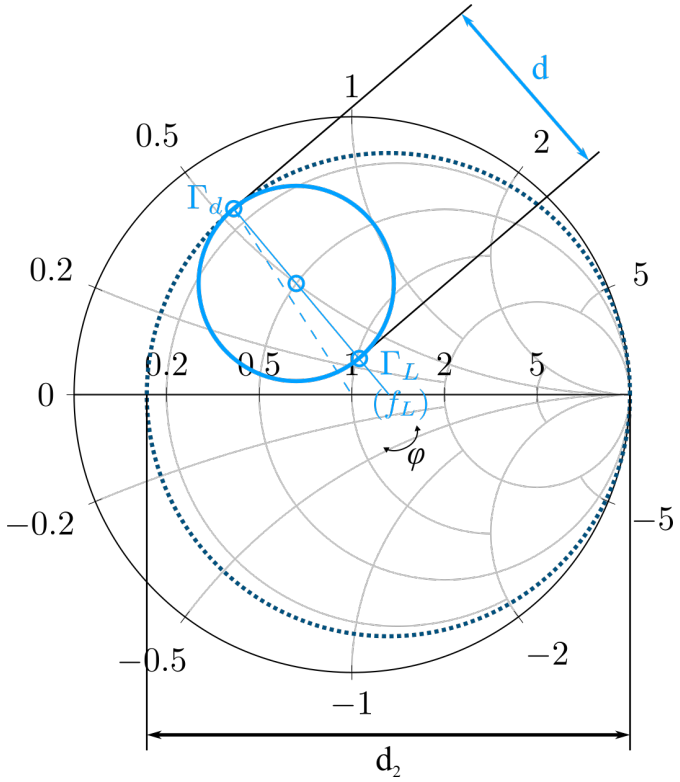

Figure 2.5.: Characteristic points of "Q circle" (solid line in blue) in Smith chart used for Q factor determination: detunded reflection coefficient Γ_d, loaded reflection coefficient Γ_L, diameter d of Q circle and d_2 of auxiliary circle (dotted line) (adapted from Refs. [106] and [153]).

3. The Influence of Alkane Oxidation Gas Feeds on the Electronic Structure of V_2O_{5-x} Studied by NEXAFS and Photoelectron Spectroscopy

3.1. Abstract

The response of the surface electronic structure of non-stoichiometric vanadium pentoxide to *n*-butane- and oxygen-containing gas atmospheres was investigated with a combination of NAP-XPS and NEXAFS spectroscopy as well as normal and resonant valence band photoelectron spectroscopy. The redox activity of the sample was demonstrated. The adaption of a band gap peak caused by occupied V 3d levels to the different gas feeds was clearly shown by resonant photoelectron spectroscopy. Furthermore, the effect of the gas feeds on the different decay channels in the resonant measurements was monitored.

3.2. Introduction

The heterogeneous selective oxidation of light alkanes to alkenes and oxygenates over (semiconducting) vanadium oxide-based catalysts[9] plays an important role allowing for the usage of natural gas as feedstock for chemical industry.[5] An efficient direct functionalization of the alkanes like *n*-butane is highly desirable, which is usually discussed to proceed via a complex reaction network operating under a (Mars–van Krevelen)[28] redox mechanism with the incorporation of oxygen from the catalyst surface into the alkane molecule and a re-oxidation by O_2.[2,10,26,27,30,83,85] In such redox materials, the catalyst is believed to play an important role in the charge carrier exchange during the reaction.[11,155] Despite the interest in the heterogeneous selective oxidation of light alkanes, the underlying fundamental physical concepts are still not entirely understood in terms of a comprehensive theory.[10] For example, a facile change of the oxidation state of the metal ion (e.g. V^{4+}/V^{5+} redox couple), an easy release of oxygen from the surface and high oxygen mobility, and partially covalent metal–oxygen bonds of intermediate strength in a non-densely-packed bulk structure were identified as important properties of selective oxidation catalysts.[2,10,26,30,83] The latter is fulfilled by V-O bonds,[78,79,81,156] where the vanadyl V=O(1) bond exhibits the highest degree of covalency.[79] It is challenging to obtain quantitative structure–function relationships given the complexity of both the catalyst and the reaction network. Many studies have dealt with the investigation of local concepts of isolated active sites at the catalyst surface,[2,64,65,157,158] however, their coupling to the bulk electronic structure

should be considered as well. Since the active surface is usually formed under reaction conditions, investigations should be carried out under *in situ* conditions using complementary methods. Such methods include X-ray photoelectron spectroscopy and X-ray absorption spectroscopy, which can be used to characterize the surface and subsurface region of the catalysts in reactive gas atmospheres.

In the present study the binary oxide V_2O_5 was chosen as model catalyst with a reduced complexity compared to e.g. the industrial $(VO)_2P_2O_7$-based VPP catalyst. It is active in alkane oxidation reactions, however at a significantly reduced selectivity compared to VPP. Even though the redox properties of bulk V_2O_5 have been investigated by initial surface science experiments, *in situ* studies addressing the influence of alkane oxidation gas feeds on the redox properties are not available. There are approaches of "pseudo *in situ*" XPS, where the samples are pre-treated in reaction cells attached to the XPS spectrometer and subsequently transferred to the analysis chamber, which was for example applied to supported V_2O_5 catalysts studied in the selective catalytic reduction of nitrogen oxides[159] or in the CO and methanol oxidation.[160,161] The advent of near-ambient pressure photoemission spectroscopy allowed for the investigation of the electronic structure and the redox properties of catalysts in reaction gas atmospheres of comparatively high pressures and at high temperatures. This was for instance used to study the VPP catalyst in alkane oxidation reactions.[38,39,42,123] In the last few years, experiments on monolayer V_2O_5/TiO_2 catalysts in alcohol oxidation reactions were conducted as well.[162–164]

Valuable insight into the electronic structure of materials can furthermore be obtained from the study of the de-excitation of resonantly excited core level states.[78,165–169] The two processes forming the basis of the resonant enhancement of valence band features, for instance features of V 3d character in vanadium oxides, are outlined below.[78]

$$2p^6 3d^n + h\nu \longrightarrow 2p^6 3d^{n-1} + e^- \tag{3.1}$$

$$2p^6 3d^n + h\nu \xrightarrow{\text{V L-edge}} \left[2p^5 3d^{n+1}\right]^* \longrightarrow 2p^6 3d^{n-1} + e^- \tag{3.2}$$

Equation (3.1) gives the direct photoemission process, where in the case of vanadium oxides an electron from the O 2p–V 3d valence band is emitted. The second excitation pathway that results in the same final state is shown in Eq. (3.2),[168,170] i.e. the excitation of a V 2p electron to unoccupied 3d states at the vanadium $L_{2,3}$-edge (the star indicates the intermediate excited state) which is followed by an Auger-like decay. This second pathway can interfere with Eq. (3.1)[168,170] leading to an intensity enhancement thus making the assignment of V 3d contributions to the valence band possible. Strong resonant enhancement of photoemission features is observed in the case of a similar character of the involved occupied and unoccupied states and a high degree of localization resulting in large transition matrix elements,[78,165,169,171] e.g. both a strong V 3d contribution to the valence band and a dominant V 3d character of the unoccupied states in the X-ray absorption final state ($2p^5 3d^{n+1}$).

In this work we investigated the response of the electronic structure of non-stoichiometric vanadium pentoxide (V_2O_{5-x}) to *n*-butane- and oxygen-containing gas feeds using NEXAFS spectroscopy at the V L-edge and O K-edge and valence band photoelectron spectroscopy at elevated temperatures and pressures, which were shown to be suitable methods for the

investigation of both the occupied and the unoccupied states. Detailed information about the influence of *n*-butane oxidation gas feeds on the valence electronic structure was obtained from resonant photoelectron spectroscopy by tuning the photon energy across the V 2p and O 1s core level excitation energies thus enhancing e.g. states of V 3d character.

3.3. Experimental Section

Near-ambient pressure X-ray photoelectron spectroscopy (NAP-XPS), valence band photoelectron spectroscopy (both resonant and non-resonant), and near edge X-ray absorption fine structure (NEXAFS) spectroscopy were conducted at the ISISS (Innovative Station for In Situ Spectroscopy) beamline at the synchrotron radiation source BESSY II in Berlin, Germany. The beamline is equipped with a plane grating monochromator based on the Peterson type design. For the resonant photoelectron spectroscopy, the monochromator was set to a higher diffraction order suppression mode with a fix focus constant c of 1.40. The experimental setup was described by Bluhm *et al.*[172] and Vass *et al.*[173] A pressed powder pellet of about 10 mg α-V_2O_5 (internal ID 18433, purchased from Merck Millipore) on a SiC plate and a sapphire sample holder was heated with 5 K/min to 400 °C. The measurements were carried out under isothermal conditions at 400 °C and 25 Pa in 1:10 (0.5 N ml/min, 5 N ml/min) mixtures of helium/oxygen, *n*-butane/oxygen and *n*-butane/helium ($He/O_2 \rightarrow C_4H_{10}/O_2 \rightarrow C_4H_{10}/He \rightarrow C_4H_{10}/O_2$).

The core level binding energies were calibrated with an internal graphite standard using the C 1s level, which was set to 284.3 eV.[174] The peaks were fitted with Gaussian-Lorentzian product functions after a Shirley background correction with the CasaXPS software (Neal Fairley, Version 2.3.15, © 1999 – 2009 Casa Software Ltd.). The V/O atomic ratio ($V/O = A_V/A_O$) was determined based on a quantitative analysis of the O 1s and the V $2p_{1/2}$ and V $2p_{3/2}$ core levels using atomic subshell photoionization cross sections σ and asymmetry parameters β from numerical calculations.[175,176] The areas A correspond to the total peak areas of the respective core levels after a Shirley background correction. In the case of vanadium, the sum of the V $2p_{1/2}$ and V $2p_{3/2}$ areas was used. The electron inelastic mean free path lengths λ_{IMFP} were determined using calculated values based on the predictive formula by Tanuma, Powell and Penn[177,178] (NIST Electron Inelastic-Mean-Free-Path Database Version 1.2).[179]

NEXAFS measurements were carried out in the total electron yield (TEY) and Auger electron yield mode (AEY) with the kinetic energy set to 365 eV and a pass energy of 50 eV as described in Ref. [180]. The energy of the NEXAFS spectra was calibrated using the π^* resonance of molecular O_2 at 530.8 eV[181,182] (see the TEY spectra in the SI, Fig. A.6 (b)) and the spectra were normalized to the pre- and post-edge at 510 eV and 560 eV, respectively. The first moment of the V L_3-edge was determined in the energy range of 505 to ∼521 eV (minimum between the V L_3- and L_2-edge determined from the first derivative of the spectra) according to Ref. [183].

The sample characterization with XRD (Fig. A.1), BET (Fig. A.2), and EPR spectroscopy (Fig. A.3) can be found in the Supporting Information (SI).

3.4. Results

3.4.1. Redox Response of V_2O_{5-x} in Alkane Oxidation Feeds

The redox response of the non-stoichiometric V_2O_{5-x} sample to *n*-butane- and oxygen-containing gas atmospheres at 400 °C was investigated with respect to changes in the vanadium oxidation state or V 3d occupation. Core level spectra as well as valence band spectra were recorded in the different gas feeds. Furthermore, NEXAFS spectroscopy was applied as sensitive probe of the local electronic structure of the unoccupied states.

Core Levels and Valence Band Spectra

Gas-phase-induced changes in the vanadium oxidation state and surface composition of the sample were monitored in the core level spectra at different probing depths. The V $2p_{3/2}$ peak was deconvoluted using a fitting procedure described in the SI (Table A.1 and Figure A.4) to obtain the average vanadium oxidation state and the V/O atomic ratio was determined from the O 1s and V 2p core levels. In addition, the valence band spectra (see SI in Figure A.5) were analyzed in the different gas feeds focusing on a band gap peak with a maximum at a binding energy of ∼1 eV, which is ascribed to filled V 3d levels in the non-stoichiometric sample as will be discussed below. The probing depths of the "surface sensitive" core level measurements at $E_{h\nu}$ of 680 eV and of the valence band and V 3d level measurements at $E_{h\nu}$ of 100 eV are slightly different with inelastic mean free path lengths of 0.8 nm (E_{kin}(V $2p_{3/2}$) ≈ 163 eV) and of 0.6 nm (E_{kin}(V 3d) ≈ 99 eV), respectively.
Figure 3.1 presents the results from the core level analysis in terms of the average vanadium oxidation and the V/O ratio as a function of time on stream in the different gas feeds. The band gap peak area ("V 3d area") is shown in Figure 3.1 (c). Moreover, the times at which the NEXAFS spectra ("N") and the resonant photoelectron spectra ("resPES") were recorded are indicated in Figure 3.1 at the top.

The redox response of the V_2O_{5-x} sample is clearly shown with respect to gas-feed-induced changes in the average vanadium oxidation state or the V 3d occupation, in particular the reduction of the sample in the C_4H_{10}/He gas feed. A lower vanadium oxidation state is associated with a higher V/O ratio, which can be explained by an oxygen loss from the sample, and a greater band gap peak area, which is ascribed to filled V 3d levels. These changes were dominated by the oxygen partial pressure, whereas the O_2-containing gas feeds (He/O_2 and C_4H_{10}/O_2) showed essentially the same vanadium oxidation state. This is in contrast to the response of V_2O_{5-x} to these gas feeds at p_{tot} of 100 kPa, where for example the electrical conductivity significantly changes between C_4H_{10}/O_2/inert and O_2/inert gas atmospheres,[104] which is likely due to the still comparatively low pressure of the NAP-XPS experiments. Measurements at higher photoelectron kinetic energies showed that not only the surface and subsurface region is redox active (λ_{IMFP} = 0.8 nm), but interestingly also deeper layers with an inelastic mean free path length of 1.8 and 2.3 nm were reduced in the C_4H_{10}/He feed (cf. Figure 3.1 (a)). Similar findings were reported for V_2O_5 subject to heating in UHV or treated in H_2 at elevated temperatures with respect to a reduction of the surface and of deeper layers.[184] In contrast, a NAP-XPS investigation on the selective catalyst vanadyl pyrophosphate (VPP) under *n*-butane

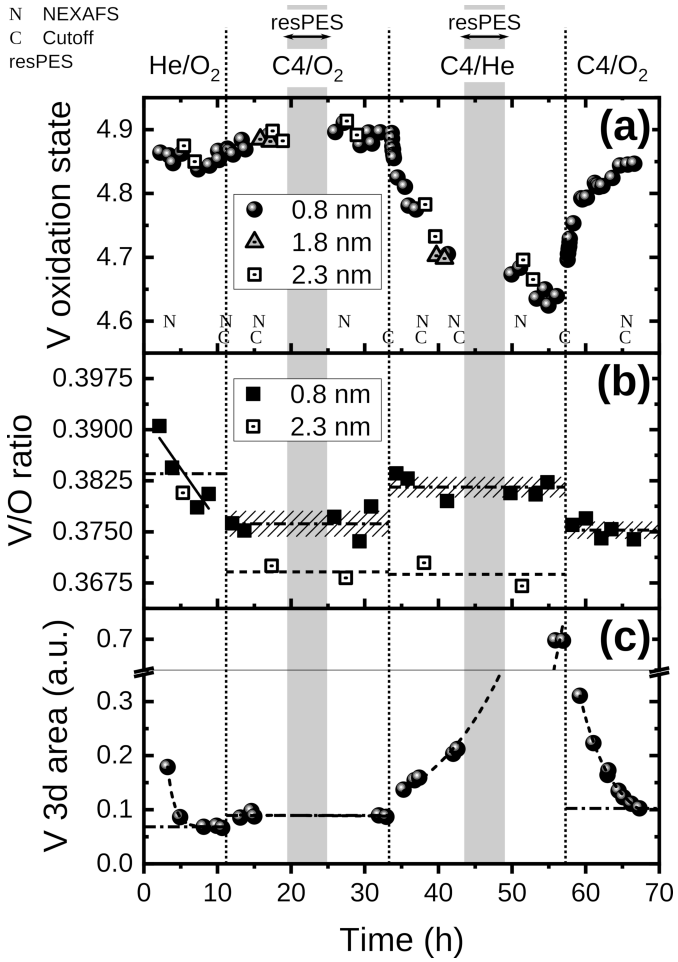

Figure 3.1.: **(a)** Vanadium oxidation state at different probing depths $\lambda_{\mathrm{IMFP}} = 0.8 - 2.3$ nm; **(b)** V/O ratio together with average values (dash-dotted and dotted lines) and one standard deviation is indicated for 0.8 nm (dashed area); **(c)** V 3d area from Gaussian fit in different gas feeds at 400 °C and 25 Pa. The times at which the NEXAFS spectra "N" and the resonant photoemission spectra were recorded are indicated at the top.

oxidation conditions showed that only the surface region is redox-active in VPP.[39]

Figure 3.1 (a) and (c) furthermore illustrate the redox kinetics of the V_2O_{5-x} sample under the experimental conditions (25 Pa, 400 °C). No steady state was reached in the reducing C_4H_{10}/He gas feed and the sample was likewise not fully re-oxidized by the subsequent treatment in the reaction gas feed C_4H_{10}/O_2. The latter observation can be explained by a rather strong reduction of the sample at the end of the C_4H_{10}/He gas feed therefore requiring a longer time to re-establish the previously observed degree of reduction in the reaction gas feed C_4H_{10}/O_2. Also, there seems to be a still ongoing oxidation in the beginning in the He/O_2 feed (Figure 3.1 (c)). The sample reduction or re-oxidation is probably slower at a low pressure ($p_{\mathrm{tot}} = 25$ Pa) than at atmospheric pressure (100 kPa).

As for the absolute values of the V/O ratio, even though close to the nominal value of 0.4, small deviations were observed, which can be explained by uncertainties in the numerically calculated cross sections,[175] also because atomic photoionization cross sections were used for V_2O_5, as well as in the Shirley background correction and in the determination of the area of the core levels. The O 1s core level was not deconvoluted, because of the high complexity

of the peak caused by many overlapping species which occur in this (rather narrow) binding energy region. Besides the main peak from the oxide, satellites from the V $2p_{3/2}$ and V $2p_{1/2}$ core levels are expected,[78,185,186] together with possible "surface oxygen" species with a slightly different binding energy, hydroxyl groups or adsorbed oxygen-containing carbon species.[78,185] When integrating the peak at ∼530 eV this error due to different overlapping species additionally contributes to the total error of the O 1s area determination. This could also be the reason for the differences observed in the time dependence of the evolution of the V oxidation state and V 3d area on one side and of the V/O ratio showing a rather constant value in the C_4H_{10}/He feed on the other side.
The intensity of the band gap peak increased in the reducing C_4H_{10}/He gas feed and decreased in the oxidizing He/O_2 feed compared to the reaction gas atmosphere, which is interpreted as changes in the vanadium 3d occupation. A detailed investigation of the nature of the valence states in V_2O_{5-x} and the effect of the different gas atmospheres will be given in the resonant photoelectron spectroscopy section. The profile of the (V 3d) band gap peak area vs. time (Figure 3.1 (c)) resembled the evolution of the vanadium oxidation state closely (Figure 3.1 (a)) and hence strongly supports the core level analysis. In fact, even the small changes between the He/O_2 and the reaction gas feed C_4H_{10}/O_2 could be resolved by analyzing the band gap peak area, in contrast to the V $2p_{3/2}$ core level analysis, where the oxidation states in the O_2-containing gas feeds could not be distinguished.

NEXAFS Spectroscopy

Near edge X-ray absorption spectroscopy was shown to be a useful method to study the local electronic structure of the unoccupied states providing information about e.g. oxidation state changes.[37,187] The vanadium L_3-edge is sensitive to changes in the stoichiometry of the vanadium oxide and can hence be used for analyzing the redox response in different gas feeds.[183,188] Both the V-O bond lengths and the structure of the V-O polyhedra, as well as the V 3d occupation affect the relative intensities and positions of the fine structure peaks of the V L_3-edge.[37,183,189] Auger electron yield NEXAFS spectra were recorded at the vanadium $L_{2,3}$-edge and oxygen K-edge of the vanadium pentoxide sample probing the unoccupied states in *n*-butane- and oxygen-containing gas feeds.
Figure 3.2 summarizes the NEXAFS spectra at the V L_3-edge and O K-edge of the V_2O_{5-x} sample in different gas feeds (see Fig. A.6 in SI for additional information). The discussion of the vanadium L-edge will be restricted to the L_3-edge, corresponding to transitions from the V $2p_{3/2}$ core level to unoccupied 3d states, because of the less informative lifetime broadened structure of the L_2-edge (Coster-Kronig decay of the $2p_{1/2}$ core hole).[190,191] The V L_3-edge AEY NEXAFS spectra (Figure 3.2) of the sample allow distinguishing about six features either as distinct peaks or as shoulders. To highlight the effect of the He/O_2, C_4H_{10}/O_2, and C_4H_{10}/He gas feeds on the V L_3-edge, difference spectra are shown at the bottom of Figure 3.2 (a).

The spectra taken in He/O_2 and in C_4H_{10}/O_2 nearly coincided, which indicates that the oxidation state of the V_2O_{5-x} sample is not significantly affected by the addition of *n*-butane under the experimental conditions (p_{tot} of 25 Pa, 400 °C). It seems likely that the oxidation state is controlled by the partial pressure of oxygen. The V L_3-edge shifted to lower energies upon

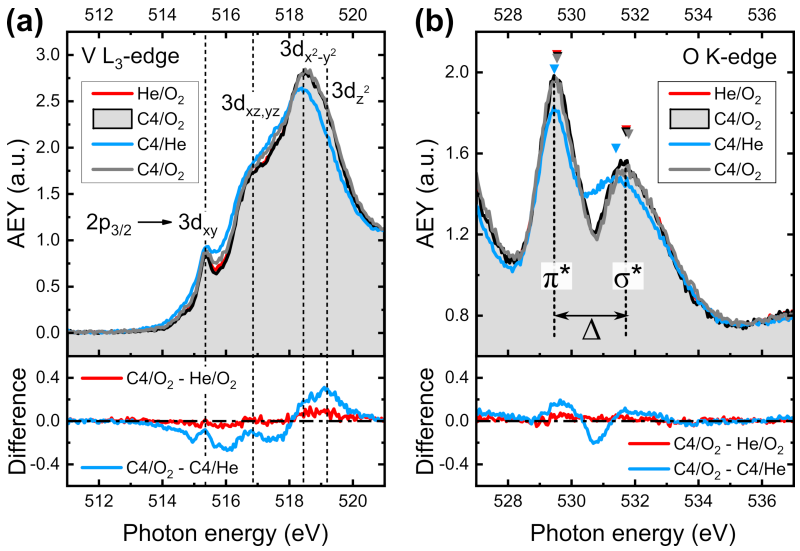

Figure 3.2.: **(a)** Normalized V L_3-edge NEXAFS spectra of V_2O_{5-x} (Auger electron yield, AEY) in different gas feeds and assignment of fine structure (top) and difference spectra (bottom): spectra in He/O_2 (red) and in C_4H_{10}/He (blue) subtracted from spectrum in C_4H_{10}/O_2; **(b)** changes in O K-edge with doublet peak separation Δ are indicated.

reduction of the sample in C_4H_{10}/He (blue spectrum, Figure 3.2 (a)). The overall position of the V L_3-edge was shown to depend on the stoichiometry of the vanadium oxide due to changes in the electrostatic potential at the V absorption site (changes in the effective nuclear charge),[189] which can be quantified by determining changes in the first momentum of the V L_3-edge.[183] The average first momenta of the V L_3-edge of the sample were found to be 518.1 – 518.2 eV in the two O_2-containing gas feeds He/O_2 and C_4H_{10}/O_2 and it decreased to 517.9 eV in C_4H_{10}/He showing the reduction of V_2O_{5-x}. The difference between the V L_3 and V L_2 first momenta was found to be 6.5 ± 0.1 eV irrespective of the gas feed. In addition, the fine structure of the blue spectrum is less distinct, which is typical for a partly reduced V_2O_{5-x} surface, where some of the individual features of the V L_3-edge are only visible as broad shoulders. In lower vanadium oxidation states there are more final states over which the intensity is distributed, which leads to a loss of fine structure.[189] A redistribution of spectral weight was clearly observed in V_2O_{5-x} in the C_4H_{10}/He gas feed, which can be seen in an intensity decrease of the peak maximum and at the high energy side, which are dominated by transitions to V $3d_{x^2-y^2}$ and $3d_{z^2}$ orbitals participating in the σ-bonds with O 2p.[192] By contrast, a higher intensity was observed in the low energy region of the V L_3-edge and the position of the peak around 515.4 eV was hardly affected. According to literature, the intensity in the low energy region of the V L_3-edge (around the first distinct peak and below) was attributed to a mixed contribution of neighboring vanadium atoms together with the main V absorption center.[193] The assignment of the fine structure to the different $3d^1$ final states in the one electron picture shown in Figure 3.2 (a) is based on DFT/ROCIS (Restricted Open Shell Configuration Interaction Singles) calculations on embedded vanadium oxide clusters by Maganas *et al.*[192] (splitting of the d-orbitals in approximate C_{4v} symmetry of vanadium in the order of $3d_{xy}$ (b_2 symmetry), $3d_{xz,yz}$ (e), $3d_{x^2-y^2}$ (b_1), and $3d_{z^2}$ (a_1) with increasing energy; compare also to Ref. [194]). It should be noted that the origin of the detailed fine structure of the V L-edge is more complex, arising from multiplet effects (due to

electron correlation), ligand field interactions, and spin–orbit splitting.[192] In addition, vanadium oxides in different oxidation states might contribute to the overall experimental V L-edge. This makes the interpretation of spectral changes in the V_2O_{5-x} V L_3-edge challenging. Still, the data show that the changes in the spectra of V_2O_{5-x} were reversible, which can be seen in the second C_4H_{10}/O_2 gas feed that was applied after the reducing C_4H_{10}/He feed. Hence, it may be assumed that the surface and subsurface region of the sample is subject to reversible changes in the reducing C_4H_{10}/He feed.

Figure 3.2 (b) presents the AEY O K-edge NEXAFS spectra of the V_2O_{5-x} sample in the different gas feeds, which exhibit two peaks centered at 529.5 eV and 531.4-531.7 eV, respectively. It may be noted that the spectra were recorded in the Auger electron yield mode in such a way as to suppress the contribution from gas phase signals as described in the Experimental Section. The total electron yield spectra (Fig. A.6 (b)) are in fact dominated by the π^* transition of O_2(g) at 530.8 eV. In the following, the AEY spectra will be discussed. The gas-phase-induced changes can clearly be seen in the difference spectra at the bottom, which demonstrate an overall reduced intensity of the O K-edge as well as a higher intensity in the photon energy region between the two distinct peaks for the spectrum recorded in the C_4H_{10}/He gas feed (shown in blue). As a consequence of the hybridization between V 3d and O 2p in vanadium pentoxide, which was mentioned in the Introduction, also the O K absorption edge (O 1s $\rightarrow$ O 2p transition) is sensitive to changes of the vanadium oxidation state in different gas feeds. The peak centered around $\sim$530 eV is split due to ligand field interactions causing the V 3d orbitals to divide into states mixing with O $2p_{\mathbf{x},\mathbf{y},z}$ via a weak π-overlap (π^* peak) and into states mixing with O $2p_{x,y,\mathbf{z}}$ in a strong σ-overlap (σ^* peak).[192,194] Changes in the double peak separation Δ of the O K-edge can reflect changes in the V 3d ligand field splitting.[188,195] There are three differently coordinated oxygen atoms in the vanadium pentoxide crystal structure, which contribute to the O K-edge spectrum. The π^* peak was shown to be dominated by the vanadyl oxygens O(1), whereas the σ^* peak exhibits contributions from all oxygens.[192,194,196,197] The O K-edge π^* peak in the V_2O_{5-x} sample was centered at 529.54 eV in the O_2-containing gas feeds He/O_2 and C_4H_{10}/O_2, and the center of the σ^* peak was found to be at 531.74 – 531.75 eV leading to an O K-edge peak splitting $\Delta E_{\text{center}}(\sigma^* - \pi^*)$ of 2.2 eV. This is in good agreement with the literature value for V_2O_5 of $\Delta = 2.2$ eV.[195] A seeming decrease of the splitting Δ was observed in the C_4H_{10}/He gas feed to $\sim$2.0 eV.

In summary, the NEXAFS spectra recorded in different *n*-butane- and O_2-containing gas feeds support the oxidation/reduction of the sample observed in the core level spectra and in a band gap peak.

3.4.2. Resonant Photoelectron Spectroscopy (resPES)

Taking valence photoelectron spectra at photon energies corresponding to core level excitation energies enables an intensity enhancement of certain features, in this case of features of V 3d character in the valence electronic structure of V_2O_{5-x}. The resPES measurements of the sample in the C_4H_{10}/O_2 and C_4H_{10}/He gas feeds are shown in Fig. 3.3 normalized to the O 2s level after a Shirley background correction. The photon energies that were used to record the valence band spectra (labeled with the letters "A–K") are compared to the NEXAFS spectrum of V_2O_{5-x}

in C_4H_{10}/O_2, which is shown on the right. It can be seen that the band gap peak at a binding energy of ∼1 eV as well as the high binding energy region of the valence band below ∼5.3 eV were particularly affected with an increase in intensity upon resonant excitation at the V L-edge. Qualitatively the same trends were observed in both gas feeds. However, the increase in intensity in the valence band region and in the band gap peak was more pronounced in the reducing C_4H_{10}/He gas feed and differences were also observed in the features between the valence band and the O 2s level of the sample.

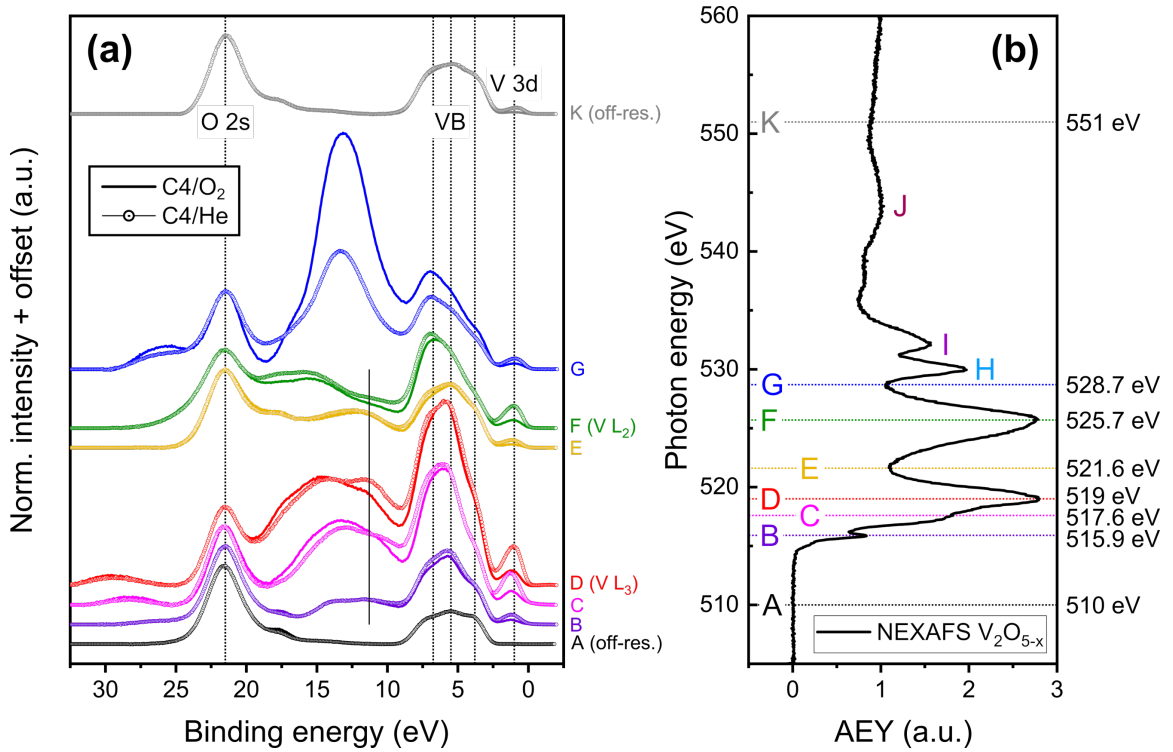

Figure 3.3.: **(a)** Valence band spectra of V_2O_{5-x} recorded at photon energies corresponding to the vanadium L-edge from 510 to 551 eV (resPES) normalized to the O 2s level after a Shirley background correction in C_4H_{10}/O_2 (lines) and in C_4H_{10}/He (symbols) (25 Pa, 400 °C); **(b)** NEXAFS spectrum of the sample in C_4H_{10}/O_2.

An increased intensity was also observed between the valence band and the O 2s level of the sample upon resonant excitation at the V L-edge, which not only change in intensity but also exhibit significant shifts in binding energy. The latter points to Auger electron emission channels exhibiting constant kinetic energy which are superimposed onto the resPES spectra.[78] An assignment of signals belonging to Auger processes is easiest for spectra plotted as a function of kinetic energy shown in Fig. 3.4. The valence band and O 2s spectra hence shift on the kinetic energy scale depending on the used photon energy, which is shown by the dashed lines in Fig. 3.4. The constant kinetic energy features at ∼489 eV and between 502 and 510 eV are probably mainly caused vanadium Auger electrons. They are marked with symbols in Fig. 3.4 and are highlighted in the inset of the figure. Based on a comparison with an Auger electron study on a V_2O_5 single crystal,[198] the peak at $E_{kin} \approx 489$ eV is ascribed to the V-L_{23}–O-L_1L_{23} Auger transition, which exhibits a rather low intensity due to the partly interionic nature. In addition, two to three peaks appeared in the kinetic energy range between 502 and 507 eV upon excitation at the V L_3-edge, which are marked by arrows and a straight line in Fig. 3.4. When the photon

energy was scanned across the V L_2-edge (spectra "E" and "F"), peaks between the valence band and the O 2s level at $E_{kin} \approx 509 - 510$ eV became visible marked by an asterisk in Fig. 3.4. These peaks are probably caused by V-$L_3M_{45}M_{45}$ and V-$L_2M_{45}M_{45}$ Auger transitions, respectively. When the photon energy no longer coincides with a core level X-ray absorption edge, only normal Auger peaks and direct photoemission peaks can be observed. The two off-resonance valence band spectra of V_2O_{5-x} ("A" and "K" in Fig. 3.3 (a) or in Fig. 3.4) indeed resembled each other closely.

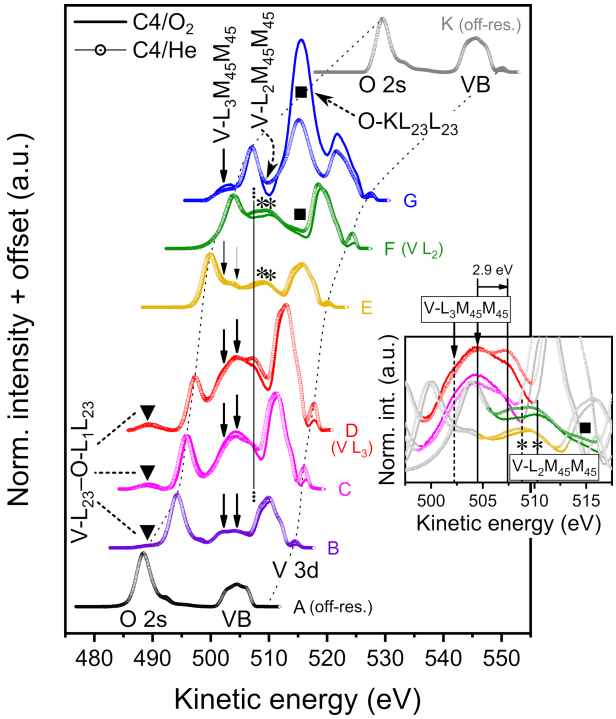

Figure 3.4.: Normalized resPES spectra of V_2O_{5-x} in C_4H_{10}/O_2 and in C_4H_{10}/He: valence band spectra as a function of photoelectron kinetic energies and indicated Auger lines. The spectra C, D, E, and F are plotted again in the inset in the kinetic energy region between 497.5 and 517.5 eV, where the constant kinetic energy peaks are highlighted and the constant binding energy valence band and O 2s features of the sample are shown in light gray.

In Figure 3.5 (b) the area of the band gap peak ascribed to V 3d at $E_{bind} \approx 1$ eV is plotted as a function of the incident photon energy (indicated by the letters "A – K") and is compared to the NEXAFS spectrum of the sample in C_4H_{10}/O_2 (Fig. 3.5 (a)). The band gap peak area was determined from a Gaussian fit of the raw data. The similarity of the photon energy dependence of the V 3d level and the valence band features to the vanadium L-edge is apparent from Fig. 3.5. It should be noted that an error is introduced due to the normalization to the O 2s level in the analysis presented in Fig. 3.5, because the O 2s level overlaps with vanadium Auger peaks in spectrum "F" (maximum of the V L_2-edge; see Fig. 3.4). The background correction and normalization are generally not straightforward in the resPES spectra of vanadium oxides[78,199] due to the occurrence of several processes covering the whole recorded binding energy region (namely resonant enhancement of valence band features, normal and spectator Auger electrons; for details see the Discussion section or the SI). Figure 3.5 therefore serves as a qualitative picture of the contribution of V 3d states to the valence states in V_2O_{5-x}. In addition to the band gap level, an intensity enhancement of valence band features at E_{bind} of 5.9 and 6.75 eV can be seen,

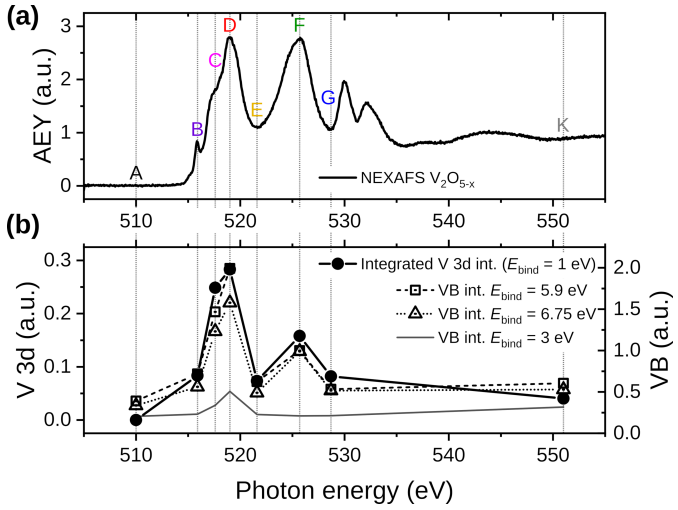

Figure 3.5.: Resonant photoelectron spectroscopy of V_2O_{5-x} in C_4H_{10}/O_2: **(a)** Auger electron yield NEXAFS V $L_{2,3}$-edge and O K-edge spectrum; **(b)** integrated peak area of V 3d level from Gaussian fit of raw data and valence band intensities at E_{bind} of 6.75, 5.9, and 3 eV as a function of photon energy.

whereas only minor effects were found in the valence band region around 3 eV. These findings for V_2O_{5-x} agree with the literature on vanadium pentoxide, where bonding interactions of V 3d and O 2p states followed by non-bonding O 2p states that form the valence band maximum of V_2O_5 were reported.[78,156,186,200,201] The V 3d–O 2p mixing in the valence band region is particularly pronounced in the partly reduced V_2O_{5-x} sample in the reaction gas feed C_4H_{10}/O_2 and the C_4H_{10}/He feed. The partial reduction of the sample or increased V 3d occupation in the *n*-butane-containing gas feeds can be clearly seen in the growing V 3d peak above the valence band edge, especially upon resonant excitation at the V L-edge which enhances this feature.

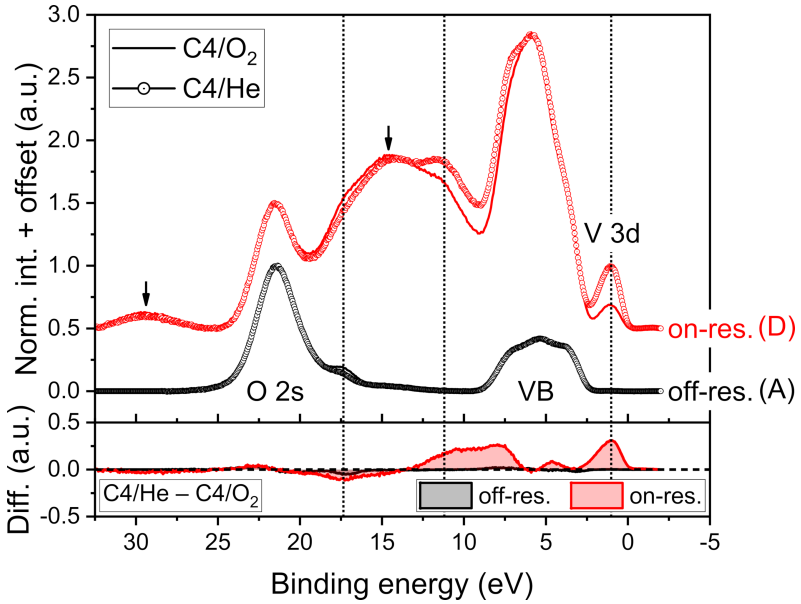

Figure 3.6.: Comparison of V_2O_{5-x} resPES spectra in C_4H_{10}/O_2 (lines) and in C_4H_{10}/He (symbols) normalized to the O 2s level after a Shirley background correction and their difference spectra. The off-resonance spectra ($E_{h\nu} = 510$ eV) are shown in black and the on-resonance spectra in red ($E_{h\nu} \approx 519$ eV, maximum of V L_3-edge). (A) and (D) refer to energy positions as used in Fig. 3.3 (b). The arrows indicate the positions of the Auger peaks from Fig. 3.4.

Figure 3.6 presents a comparison of the resPES spectra of V_2O_{5-x} in the two gas feeds C_4H_{10}/O_2 and C_4H_{10}/He. Both the off-resonance ($E_{h\nu}$= 510 eV) and the on-resonance spectra, which were recorded at photon energies corresponding to the maximum of the V L_3 absorption edge at ∼519 eV, are shown normalized to the intensity of the O 2s peak after a Shirley background correction. The positions of the main vanadium Auger peaks determined from Figure 3.4 are indicated by the arrows. The spectra in the two gas feeds followed the same qualitative trends upon resonant excitation at the V L-edge. The effect of the different gas atmospheres becomes apparent from the difference spectra (spectra taken in C_4H_{10}/O_2 subtracted from the spectra in C_4H_{10}/He) for both the on- and the off-resonance situation shown at the bottom of Figure 3.6. The off-resonance spectra in the two gas feeds resembled each other very closely. Yet, differences were observed in the on-resonance spectra. In the C_4H_{10}/He gas feed, corresponding to a more reduced situation, an increased intensity of the resPES spectrum was found compared to the other gas feed C_4H_{10}/O_2. The increase of signal intensity is most pronounced at low binding energy corresponding to a band gap state and on the high binding energy side of the valence band above $E_{\text{bind}} \approx 6.4$ eV extending to $E_{\text{bind}} \approx 14$ eV. Importantly, differences between the two gas feeds were also observed in the binding energy region between the valence band and the O 2s level showing a feature of a higher intensity in the C_4H_{10}/He gas feed.

3.5. Discussion

3.5.1. Gas-Phase-Induced Response of V_2O_{5-x} Electronic Structure

The redox response of non-stoichiometric vanadium pentoxide was investigated in different *n*-butane- and oxygen-containing gas feeds at 400 °C. The core levels, V 3d band gap level, and NEXAFS spectra consistently showed the oxidation and reduction of the sample adapting to the chemical potential of the gas atmospheres. The small changes of the vanadium oxidation state between the two oxygen-containing gas feeds He/O_2 and C_4H_{10}/O_2 were difficult to observe, but slight changes in the V 3d peak area could still be detected. Gas-phase-induced changes in the local structure of the V–O polyhedra and in the vanadium oxidation state of V_2O_{5-x} are reflected in the NEXAFS spectra in the V L-edge position and relative intensities. The decreased resonance position in the reduced vanadium oxide sample indicates an increase in the V-O bond lengths and hence weakening of the bonds or a change of the electrostatic potential at vanadium.

Changes of the O K-edge doublet in different gas feeds were observed accompanying the changes of the vanadium L-edge in the V_2O_{5-x} sample. A seeming decrease in the peak separation and a slight downward shift of the peak maxima were found, together with an apparent broadening of the σ^* peak. The position and width of the π^* peak were only marginally altered, with a downward shift by ∼70 meV and a slight narrowing, but its intensity decreased. The presence of O_2 in the gas phase was shown to affect the AEY O K-edge spectra of a V_2O_5 powder sample in the literature due to a reduced photon transmission at the position of the O_2(g) absorption at 530.8 eV.[180] It may therefore be assumed that the majority of the observed changes in the O K-edge spectra of V_2O_{5-x} between the O_2-containing gas feeds and the C_4H_{10}/He feed in the present study are caused by the oxygen in the gas feed. The smaller intensity of the O K-edge in the reducing C_4H_{10}/He feed (Figure 3.2) can be explained by the occupation of V 3d states related

to the creation of oxygen vacancies, because of the decreased number of available unoccupied d levels hybridized with O 2p orbitals. This explanation is consistent with the NEXAFS study on transition metal oxides by de Groot *et al.*[202] Recent experiments on defect-rich V_2O_5 thin films suggest a lower π^*/σ^* intensity ratio of the O K-edge in reduced vanadium oxide films that have a higher amount of V^{4+} and oxygen vacancies.[203] Similarly, changes in the VO_2 O K-edge NEXAFS spectra in ordered and disordered thin films were observed in terms of a decreased splitting Δ with a higher disorder in the VO_2 samples, which was mainly caused by a downward shift of the σ^* peak along with a peak broadening.[204] The greater effect on the σ^* peak was attributed to the better σ-orbital overlap between V 3d and O 2p orbitals, which facilitates the observation of changes.[204] A change in the relative contributions of the differently coordinated oxygen atoms in the V_2O_5 crystal structure to the O K-edge might in part account for the seeming decrease of the peak separation Δ. Since the shape of the O K-edge is to a large extent determined by the contribution of the vanadyl oxygens O(1), in particular the π^* O K-edge peak,[192,196] changes in the V=O(1) bonding should be readily seen in the spectral shape of the O K-edge. Yet, no significant effect was observed in the π^* peak in the present study upon reduction of the sample in C_4H_{10}/He. It may be concluded that the dominant influence on the O K-edge spectra comes from the presence of O_2 in the gas atmosphere affecting the X-ray transmission. Furthermore, the data show that the sample is reduced in the C_4H_{10}/He feed as observed in a shift of the V L_3-edge to lower photon energies (reduction of effective nuclear charge) and in the reduced intensity of the NEXAFS spectra. These findings support the response of the V_2O_{5-x} surface electronic structure as determined from NAP-XPS demonstrating reversible changes in the V 3d occupation induced by the treatment in different *n*-butane- and O_2-containing gas feeds.

3.5.2. ResPES: V_2O_{5-x} Valence Band Spectra

The resPES spectra of V_2O_{5-x} in C_4H_{10}/O_2 and C_4H_{10}/He showed an intensity enhancement in the band gap peak and at the high binding energy side of the valence band upon excitation at the V L-edge due to the V 3d character of the involved states. This increase in intensity was more pronounced in the more reduced sample in C_4H_{10}/He, in particular in the band gap peak at $E_{\text{bind}} \approx 1$ eV due to a greater V 3d occupation. An unambiguous assignment of the peaks in the V_2O_{5-x} resPES spectra is challenging due to many overlapping processes. The intensity enhancement of valence band features of V 3d character in the photon energy range of 515.9 to 525.7 eV ("B–F") in V_2O_{5-x} are pronounced due to the rather localized character of the involved states and a similar character of these (valence band) features and the unoccupied levels in the intermediate excited state.

Remarkably, differences in the resPES spectra between the two gas feeds were also observed in the region between the valence band and the O 2s level. A comparison of the resPES spectra recorded in C_4H_{10}/O_2 and in C_4H_{10}/He showed an additional increase in intensity, which was particularly pronounced in the more reduced V_2O_{5-x} sample in the C_4H_{10}/He gas feed. This peak occurred at a binding energy of ∼11.6 eV in the on-resonance spectra "D" (corresponding to the maximum of the V L_3-edge) or at a kinetic energy of ∼507.4 eV, which was highlighted by a line in Figure 3.3 (a), Figure 3.4, and Figure 3.6. Further studies which take different gas feeds

into account with and without *n*-butane will be performed in order to assign this feature, where also adsorbed hydrocarbon species might contribute. This feature further makes the discussion of Auger peaks necessary.

Besides the resonant photoemission or participant autoionization process, the intermediate excited state $2p^5 3d^{n+1}$ can also decay via an Auger transition leading to a different (double hole) final state. Indeed, an overlap with Auger electrons was observed for many vanadium oxide compounds measured at the V L-edge.[78,205–207] It should be noted that shifts in the kinetic energy of the Auger electrons are likely to occur, which complicates the assignment of the different features. If the excited electron remains in the previously unoccupied state comparatively localized at the absorption center, a "double hole–one electron" final state is reached where the energy is modified by screening effects caused by the presence of the electron in an excited bound state.[166,167,169] The kinetic energy of the emitted "spectator" Auger electron is higher than that of a normal Auger electron because of this spectator screening.[166,167,169] In addition, also shake up and shake off loss features can occur at a lower kinetic energy than the main Auger line, as well as shake down features at higher kinetic energy,[166,167] which would lead to additional peaks in the spectra.

The feature in the on-resonance resPES spectra of the more reduced V_2O_{5-x} sample at $E_{\mathrm{bind}} \approx 11.6$ eV or $E_{\mathrm{kin}} \approx 507.4$ eV may be caused by a V-$L_3M_{45}M_{45}$ Auger peak shifted in kinetic energy from the main line or by an additional contribution of adsorbed hydrocarbon species. The higher intensity of the feature in the more reducing C_4H_{10}/He gas feed could be due to a greater contribution of V-$L_{2,3}M_{45}M_{45}$ Auger electrons in case of a greater V 3d occupation (more reduced V_2O_{5-x} sample), which is a reasonable assumption. The position does not entirely agree with the Auger lines determined in Figure 3.4, but there are several reasons for shifts in the Auger electron kinetic energies. At photon energies corresponding to the vanadium 2p excitation contributions of V-$L_{2,3}M_{45}M_{45}$ Auger electrons occurred mainly between the valence band and the O 2s region, but there might also be an overlap with valence band features in the spectra "B–D", in agreement with the observations for a V_2O_5 single crystal.[78] A spectator Auger decay channel can explain the two peaks marked with arrows in Figure 3.4 at $E_{\mathrm{kin}} \approx 502.25$ eV and 504.5 eV as due to normal and spectator V-$L_3M_{45}M_{45}$ Auger peaks. These kinetic energies lie within the reported range of 501 to 510 eV for V_2O_5,[198] yet it should be emphasized that these vanadium Auger transitions are masked by the dominant O-$KL_{23}L_{23}$ peak in the normal Auger electron spectra of vanadium oxides,[82] which makes the determination of the (precise) kinetic energy difficult. The identification of the V-$L_2M_{45}M_{45}$ Auger peak is even more challenging due to the expected lower intensity of the Auger transition originating from the filling of the V $2p_{1/2}$ core hole.[82] In V_2O_5 it was reported at kinetic energies of 508 to 517 eV even closer to the main O-$KL_{23}L_{23}$ peak and separated by ∼7 eV from the V-$L_3M_{45}M_{45}$ transition.[198] In the resPES spectra of V_2O_{5-x} using excitation energies close to the V L_2-edge (spectra "E" and "F") two peaks around 509 and 510 eV were observed, which are probably caused by V-$L_2M_{45}M_{45}$ Auger transitions, the first peak being ∼6.8 eV above the first V-$L_3M_{45}M_{45}$ line.

3.6. Conclusions

This work presented an analysis of the influence of *n*-butane- and oxygen-containing gas atmospheres on the electronic structure of oxygen-deficient V_2O_{5-x} at elevated temperatures. Gas-phase-induced changes in the V L_3-edge and O K-edge NEXAFS spectra were interpreted as reduction of the sample by the treatment in the C_4H_{10}/He gas feed, whereas no significant influence of the other gas atmospheres was detected. The V 3d occupation was shown to reversibly adapt to the different gas feeds demonstrating the redox activity of the sample. An analysis of the V 3d peak area could even resolve changes in the 3d occupation between the two O_2-containing gas feeds He/O_2 and C_4H_{10}/O_2.

The influence of the *n*-butane-containing gas feeds on the valence electronic structure of V_2O_{5-x} was further investigated with resonant photoelectron spectroscopy. The partial covalency of the oxide could be shown in the enhancement of valence band features (at the high binding energy onset) and the band gap level due to the V 3d character of both the intermediate excited state and the valence states. An unambiguous assignment of the peaks in the resPES spectra of V_2O_{5-x} is challenging given the partial overlap of different processes. In addition to the resonant photoemission (participant autoionization) decay channel, the contribution of mainly V-$L_{2,3}M_{45}M_{45}$ Auger electrons to the spectra was observed when scanning the photon energy across the V L-edge. A comparison of the resPES spectra recorded in C_4H_{10}/O_2 and in C_4H_{10}/He showed a greater intensity enhancement in the more reduced V_2O_{5-x} sample, not only in the V 3d peak and the valence band, but also between the valence band and the O 2s level. This may be due to an increased contribution of V-$L_3M_{45}M_{45}$ Auger electrons (at higher kinetic energies) in the more reduced V_2O_{5-x} sample, but also adsorbed hydrocarbon species may need to be considered. Research into assigning this feature is in progress. Using resonant photoelectron spectroscopy, even a small band gap peak caused by occupied V 3d levels in the non-stoichiometric oxide can clearly be shown due to the intensity enhancement.

4. *Operando* Electrical Conductivity and Complex Permittivity Study on Vanadia Oxidation Catalysts*

Anna M. Wernbacher, Maik Eichelbaum, Thomas Risse, Sébastien Cap, Annette Trunschke, and Robert Schlögl

4.1. Abstract

The electrical conductivity and its real and imaginary permittivity parameters were studied over two vanadium-containing catalysts for the selective oxidation of *n*-butane to maleic anhydride. Parameter variation under isothermal conditions allowed determining multiple steady-state conditions for catalytic performance and charge carrier dynamics. One sample was the n-type semiconductor V_2O_{5-x} with low selectivity and the other sample was the p-type semiconductor vanadyl pyrophosphate (VPP) with high selectivity for the target product. Well-resolved conductivity parameters supported by *in situ* UV-Vis studies allowed correlations between performance and charge carrier dynamics. A concept for interpreting the trends is presented and consequences for further analytical work as well as for material design are derived.

4.2. Introduction

Vanadium oxide-based catalysts are widely applied in heterogeneous hydrocarbon oxidation, for instance vanadyl pyrophosphate $(VO)_2P_2O_7$ (VPP), which is used in maleic anhydride production from *n*-butane.[3,18] Concerning their electronic structure, many of the selective oxidation catalysts are (wide bandgap) semiconductors that contain vanadium as redox active metal ion, usually in the oxidation states +5 and +4.[9,10] The identification of quantitative structure–function relationships is challenging given the complexity of the materials, which are often characterized by the formation of a dynamic surface termination layer under catalytic operation conditions.[14] The catalysts may be considered as multi-functional materials that ideally accelerate the steps towards the partial oxidation product and inhibit unselective pathways.[10]

The electrical conductivity of VPP catalysts was investigated *in operando* during the oxidation of *n*-butane.[25,39,40,60,208,209] Conductivity studies on pressed VPP powder samples using contact-methods revealed p-type conductivity, i.e., the majority charge carriers are holes.[60] The observed

*Reprinted with permission from Wernbacher, A. M.; Eichelbaum, M; Risse, T.; Cap, S.; Trunschke, A.; Schlögl, R. Operando Electrical Conductivity and Complex Permittivity Study on Vanadia Oxidation Catalysts. *J. Phys. Chem. C* **123**, 8005–8017 (2019), DOI: 10.1021/acs.jpcc.8b07417. Copyright 2018 American Chemical Society.

conductivity changes in different gas feeds are in line with the proposed redox mechanism of the reaction via a V^{4+}/V^{5+} redox couple,[25–27,30] i.e., a redox-active layer on VPP with an average vanadium oxidation state slightly above +4 that adapts to the chemical potential of the gas atmosphere.[39,40,60]

The idea of conductivity studies is to link the catalytic performance with charge carrier properties. Under the widespread assumption that *n*-butane oxidation follows a Mars–van Krevelen[28] mechanism, it would be conceivable to relate the availability of unbound electrons to the activity of the catalyst and the control of their number to the selectivity of the catalyst. In this way the qualitative concept of "site isolation" on the basis of the "seven pillars" by Grasselli[2,10,30] would obtain a physical basis.

V_2O_5 is an active oxidation catalyst, however with low selectivity to partial oxidation products of hydrocarbons. It has been studied extensively as model system with regard to its surface termination and defects by surface science techniques and theory.[210–216] Electrical transport measurements of vanadium pentoxide single crystals identified V_2O_5 as a n-type semiconductor with low mobility electrons as majority carriers.[217–222] Above 77 to 97 °C a hopping of free polarons was proposed as the conduction mechanism.[218,219,222,223] Other authors focused on V_2O_5 glasses[224] and thin films,[217] also applying Mott's polaron conduction model.[225] Few studies, however, have addressed the semiconducting properties of vanadium pentoxide under alkane oxidation conditions. Heine *et al.*[104] performed an *in situ* microwave conductivity study on V_2O_5 during *n*-butane oxidation, where reversible conductivity changes were found as a function of the applied gas feeds like for VPP (V^{4+}/V^{5+} redox couple), which could be related to the occupation of V 3d states and the formation of oxygen vacancies.[104]

The concept of the present work is to compare two vanadium-based oxidation catalysts in the same reaction and determine their charge carrier characteristics under *operando* conditions applying the same parameters in terms of temperature and alkane conversion. The results may give hints to the way of involvement of the catalyst in the catalytic conversion. It is noted that a complex reaction network is operative in *n*-butane oxidation, where, despite extensive scientific effort, only limited experimental insight[226–229] into the mode of operation is available. The two catalysts were chosen such as to allow also the elucidation of a possible role of the main group element phosphorus and thus to verify the simplification that for fundamental insight into selective oxidation the binary oxide may be sufficient. Recent work[65] suggests that this simplification may be incorrect and that the main group element has a critical function in catalysis other than creating[10,230,231] the structural motif of a non-densely packed crystal structure.

The present study relies on true operando analysis of the electrical properties applying the contactless microwave cavity perturbation technique (MCPT) without compromising the kinetic conditions of the experiment; if the reaction is related to the charge carrier properties, their observation will critically depend on the exact local chemical potential. As it is not clear what is the information depth of the here employed MCPT measurement, a truly bulk sensitive complementary observation of the two systems using optical absorption spectroscopy was applied. It is realized that optical absorption and microwave absorption both probe the permittivity of the material albeit under different boundary conditions of the transition energies involved.

4.3. Experimental Section

4.3.1. Catalysts

We investigated vanadium pentoxide V_2O_5 (internal ID 22054) and vanadyl pyrophosphate $(VO)_2P_2O_7$ (VPP, internal ID 12831), which were analyzed with XRD (Figs. B.1–B.2), XRF, and TEM (Fig. B.3) shown in the Supporting Information. The BET surface areas are 3.4 m^2/g (V_2O_5) and 28.1 m^2/g (VPP), respectively. The VPP sample was prepared as previously described by Eichelbaum *et al.*[39] (see SI for details) and both samples were pre-treated at 400 °C in the respective gas feeds (*n*-butane oxidation gas feed in case of the contact time variation and redox response experiments and in the three different gas feeds, *n*-butane/O_2/N_2, O_2/N_2, and N_2, for the temperature dependent measurements) in the MCPT setup prior to the conductivity and permittivity measurements.

4.3.2. Microwave Cavity Perturbation Technique and Catalytic Testing

The contactless *operando* conductivity measurements of catalysts based on the microwave cavity perturbation technique (MCPT)[136] were described by Eichelbaum *et al.*[103] It is based on a perturbation of the resonator properties of a microwave cavity by a semiconducting sample, which leads to a decrease of the resonator Q factor and resonant angular frequency ω. This can be related to the relative complex permittivity $\tilde{\varepsilon} = \varepsilon' - i\varepsilon''$ of the sample according to Eqs. (4.1) – (4.2).[103,106]

$$A\ \left(\varepsilon'_p - 1\right)\ \frac{V_s}{V_c} = \frac{(\omega_0 - \omega_s)}{\omega_s} \tag{4.1}$$

$$B\ \varepsilon''_p\ \frac{V_s}{V_c} = \frac{1}{Q_s} - \frac{1}{Q_0} \tag{4.2}$$

Here, ε' and ε'' correspond to the real and the imaginary part of the relative complex permittivity, respectively, A and B denote calibration constants of the resonator and microwave mode, and V_s and V_c are the sample and the cavity volumes.[106] The subscript "s" refers to the resonator with sample and the subscript "0" to the empty resonator. The powder permittivities (subscript "p") were subsequently transformed to bulk values using the Landau-Lifshitz-Looyenga formulas based on an effective medium theory.[147–149]

The complex permittivity $\tilde{\varepsilon}$ describes the response of the samples to the electric field component of the microwave field, where the real part is related to energy storage and polarization effects and the imaginary part to energy dissipation, which may comprise ohmic loss from free charge carriers and dielectric loss from bound charges, where the former should dominate for semiconductors investigated in the microwave frequency range.[106] It is related to the complex conductivity of the samples according to $\tilde{\sigma}(\omega) = i\ \omega\ \varepsilon_0\ \tilde{\varepsilon}(\omega)$,[104,106] where the discussion will be restricted to the real part of the conductivity associated with the loss caused by the free (or bound) charge carriers. In the low frequency limit the complex conductivity is reduced to the DC conductivity. The real part of the conductivity, σ, was determined from the imaginary part of the relative permittivity, ε'', and the resonant frequency ω_s of the resonator with sample according to Eq. (4.3). The

vacuum permittivity is given by ε_0.

$$\sigma = \varepsilon_0 \, \omega_s \, \varepsilon'' \tag{4.3}$$

The MCPT measurements were carried out in a cylindrical silver- and gold-plated resonator (radius 34 mm, height 20 mm) using the microwave modes TM_{010} ($\approx$ 3 GHz) and TM_{020} ($\approx$ 7 GHz). The resonator was connected to an Agilent PNA-L N5230C vector network analyzer via a semi-rigid coaxial cable. Catalyst beds (100 to 200 μm sieve fraction) with a height of 10 mm were placed in a fixed-bed thin-walled quartz reactor in the electric field maximum in the center of the resonator. The samples were heated by a preheated nitrogen flow, while the temperature of the resonator was kept at 20 °C. Water condensation in the resonator was avoided by a constant flow of 15 ml/min dried N_2 through the resonator.

The recorded reflection coefficient $\Gamma(\omega)$ was fitted with a modified version of the Q0REFL program by Kajfez[152] in order to obtain the unloaded Q factor and the resonant frequency. The Q0REFL program accounts for the external circuit, which consists of the vector network analyzer, the transmission line, and the coupling loop.[152]

Contact time (W/F) variation experiments were conducted in a reaction gas feed consisting of 2% *n*-butane and 20% oxygen in nitrogen with total gas flows F of 2 to 30 ml/min controlled by Bronkhorst mass flow controllers and catalyst mass W of 61 mg V_2O_5 and 66 mg VPP. The redox response of the catalysts was investigated by sequentially applying the reaction gas feed and oxidizing/inert/reducing gas feeds ($C_4H_{10}/O_2/N_2$, O_2/N_2, N_2, $C_4H_{10}/O_2/N_2$). Online gas chromatography (Agilent 7890 GC) was used for the analysis of the reactant and product gases. The temperature dependence of the electrical conductivity σ was evaluated in order to determine an apparent activation energy of conduction E_c according to Eqs. (4.4) – (4.6),[60,103,222] k being the Boltzmann constant and T the temperature. Here, the subscripts "ion" and "polaron" refer to ionic and polaron conduction, respectively. A polaron corresponds to a quasiparticle formed by an electron or hole and a polarization field associated with a rather strong electron–phonon coupling leading to an increased effective mass of the charge carrier.[142] It can be distinguished between large and small polarons (small radius comparable to the lattice constant), where the latter are rather localized and have a larger effective mass, in which case the conduction mechanism is usually described by a hopping process.[142,225]

$$\sigma = \sigma_0 \, \exp\left(-\frac{E_c}{k\,T}\right) \tag{4.4}$$

$$\sigma_{\text{ion}} = \frac{\sigma_{\text{ion},0}}{T} \, \exp\left(-\frac{E_c}{k\,T}\right) \tag{4.5}$$

$$\sigma_{\text{polaron}} = \frac{\sigma_{\text{polaron},0}}{T^{3/2}} \, \exp\left(-\frac{E_c}{k\,T}\right) \tag{4.6}$$

The conductivities were measured in the temperature range of 30 to 450 °C. The samples were first heated to 425 °C in the respective gas feed and kept at this temperature for 30 to 60 min to desorb water, and then cooled down to 30 °C. Details on the experimental procedure are described in the Supporting Information (SI).

4.3.3. Diffuse Reflectance UV-Vis Spectroscopy

Diffuse reflectance (DR) UV-Vis measurements were carried out using the Agilent Cary 5000 UV-Vis spectrometer equipped with a Harrick Praying Mantis diffuse-reflectance attachment (DRP-P72) and a reaction chamber (HVC-VUV). The *in situ* cell was connected to a gas-delivery system for operation under flow conditions. Spectralon was used as a white standard. The samples were heated to 400 °C under a gas flow of 5 ml/min 2% C_4H_{10} / 20% O_2 in He, 20% O_2 in He, 100% He, 2% C_4H_{10} / 20% O_2 in He. The reflectance was then converted to the Kubelka-Munk function F(R).

4.4. Results

4.4.1. Catalytic Behavior

The experimental conditions were chosen such that a substantial conversion of *n*-butane was reached for both systems. In order to encode chemical information into the conductivity measurement, the flow rate was varied giving rise to changes in conversion and selectivity. It was avoided using the temperature as variable, as the conductivity itself is a strong function of temperature in a semiconductor, which may well mask the sought relation between conductivity and catalysis. The temperature level of 400 °C was chosen as it is close to practical conditions and it allows observing substantial conversions for both catalyst systems.

In Figure 4.1 the catalytic behavior of the two systems under study are compared. With increasing *n*-butane conversion the binary oxide exhibits a strongly decaying selectivity to the target product maleic anhydride (MA) in favor of more combustion to CO_2. The selectivity to the decarbonylation product CO that cannot be further oxidized by the catalyst to CO_2 is high and constant with conversion. This behavior is indicative to the existence of a complex reaction network with several pathways and intermediates.

The behavior of the high performance catalyst is significantly different with almost no dependence of the product distribution on alkane conversion. Also here the decarbonylation activity is higher than the combustion reaction, albeit on a much reduced level than in the binary oxide.

4.4.2. Correlations between Permittivity/Conductivity and Catalytic Performance

In a previous study of the selective oxidation of *n*-butane over VPP, a linear correlation between the MCPT conductivity at 9 GHz (TM_{110} mode) and the maleic anhydride yield was found.[39] The present experiments expand the range of experimental parameters substantially and observe the conductivity response of the binary model oxide under comparable conditions. In order to further investigate the relation between electrical conductivity and reactant conversion as well as product yield, contact time variation experiments were performed for the two vanadium oxide catalysts V_2O_5 and VPP, the former being an n-type semiconductor and leading mainly to the formation of carbon oxides in the oxidation of *n*-butane, the latter being a p-type semiconductor with a high selectivity to maleic anhydride.

The measurements at a constant temperature of 400 °C are presented in Figure 4.2 as time on stream plots of the conductivity σ and complex permittivity $\tilde{\varepsilon} = \varepsilon' - i\varepsilon''$ as well as of the

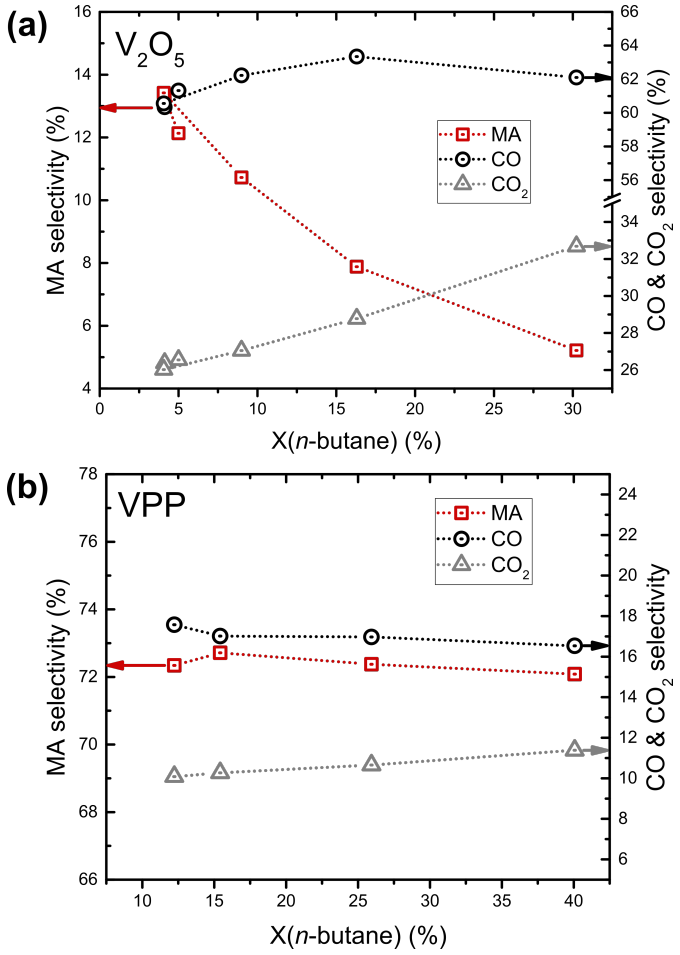

Figure 4.1.: Conversion (X) – selectivity (S) plots for the two catalysts studied. The data were measured *in operando* during recording of the electrical conductivity reported in Figure 4.2. Note the changes in ordinate scales.

n-butane conversion and product selectivity (maleic anhydride (MA), CO, and CO_2). The conductivity changes of VPP at different *n*-butane conversions were less pronounced than the corresponding response of V_2O_5 (compare Figure 4.2 (a) and (b)), which required the usage of the more sensitive TM_{020} mode and a smaller resonator (i.e., with higher resonant frequency) with a greater sample/cavity volume ratio for the study of VPP, whereas the other measurements were conducted in a bigger resonator (3 GHz, TM_{010}) due to the greater perturbation caused by V_2O_5. The VPP catalyst was tested in three resonators of different size using both the TM_{010} and the TM_{020} mode and two different sample batches (Supporting Information, Figures B.5–B.7). The conductivity of VPP was found to be about $2{\cdot}10^{-2}$ S/m in the *n*-butane oxidation gas feed at 400 °C at various frequencies from 3 to 10 GHz, which is much smaller than the conductivity of V_2O_5 of about 1 S/m under the same conditions at 3 GHz. In this frequency range no significant influence of the frequency on the conductivity of VPP was detected, hence not only the relative changes, but also the absolute conductivity can be compared with V_2O_5.

The observed conductivity and permittivity changes at different conversions were small. Still, it was possible to resolve them in the *operando* MCPT measurements. It is pointed out here that for mechanistic studies it seems highly relevant to perform true *operando* studies as the response of the electronic structure of an oxide catalyst is strong enough to detect the rather minor change

in local chemical potential associated with the W/F range used here. The result further shows that the electronic structure of such catalysts is indeed sensitive to flow conditions and will thus be by no means constant over a typical plug flow reactor. The rather generous statements about "*operando* experimentation" found in the literature may thus be taken with some reservation. It is on the other hand evident that the MCPT method is a sensitive probe to the electronic structure of almost free charge carriers being likely most relevant to redox reactions involving the charge carrier reservoir of the catalyst. This holds equally for electrons and holes as majority charge carriers. The drift in the MCPT signal can either be related to the instrumentation (e.g. temperature drift of the resonator) or to continuous slight changes of the catalyst, yet it should be emphasized that this drift is only observed because of the very small absolute changes of the conductivity at different conversions, which are nevertheless real as can be clearly shown by the reproducibility of the conductivity response using different batches of VPP (Supporting Information, Figure B.5).

It can be seen that both the conductivity and the complex permittivity of V_2O_5 increased with increasing *n*-butane conversion (Fig. 4.2 (a)). In contrast to this, VPP showed a decrease of the conductivity and of ε'' at higher conversions (Fig. 4.2 (b)). This indicates that the catalysts' surfaces are sensitively adapting to the local chemical potential of the gas atmosphere revealing that the degree of catalyst reduction is affected by the reactant conversion level, which will be discussed later. Interestingly, the real part of the permittivity ε' of VPP showed no changes to the different *n*-butane conversions as opposed to the response of ε' of V_2O_5 (cf. Figure 4.2). This was confirmed in contact time variation experiments of VPP in different microwave cavities and modes (Supporting Information, Figure B.6) and is in agreement with the previously mentioned study of VPP using a 9 GHz resonator (TM_{110} mode).[39]

4.4.3. Response of Conductivity to Reversible Redox Reaction

To gain further insight into the charge carrier response against changes in chemical potential, more drastic changes than executed by the variation in feed flow rate were realized. The response of the electrical conductivity and complex permittivity of the two oxides towards an increase in the oxidation potential of the gas feed is shown in Figure 4.3 together with the catalytic performance in the oxidation of *n*-butane. The samples were investigated at the same *n*-butane conversion of approx. 15%, because the conversion of the reactants influences the conductivity of the catalysts, which was shown in the previous section. This required an adjustment of the contact time to 0.73 g·s/ml for V_2O_5 and to 0.12 g·s/ml for VPP.

The typical conductivity response of the two samples to different gas feeds can be seen in parts (a) and (b) of Figure 4.3 at the top with a decreasing conductivity of V_2O_5 in the more oxidizing gas feed (20% O_2 in N_2) and likewise an increased conductivity of VPP, in agreement with the literature.[40,60,104] Both samples exhibited a stable conductivity in the reaction gas feeds and a slow oxidation in O_2/N_2. The catalytic activity was fully reversible following the reverse of the gas composition.

The permittivity changes of the two oxides are shown in the center of Figure 4.3 (a) and (b) and the simultaneously recorded catalytic data can be found at the bottom. Both the real part and the imaginary part of the permittivity qualitatively followed the same response like the

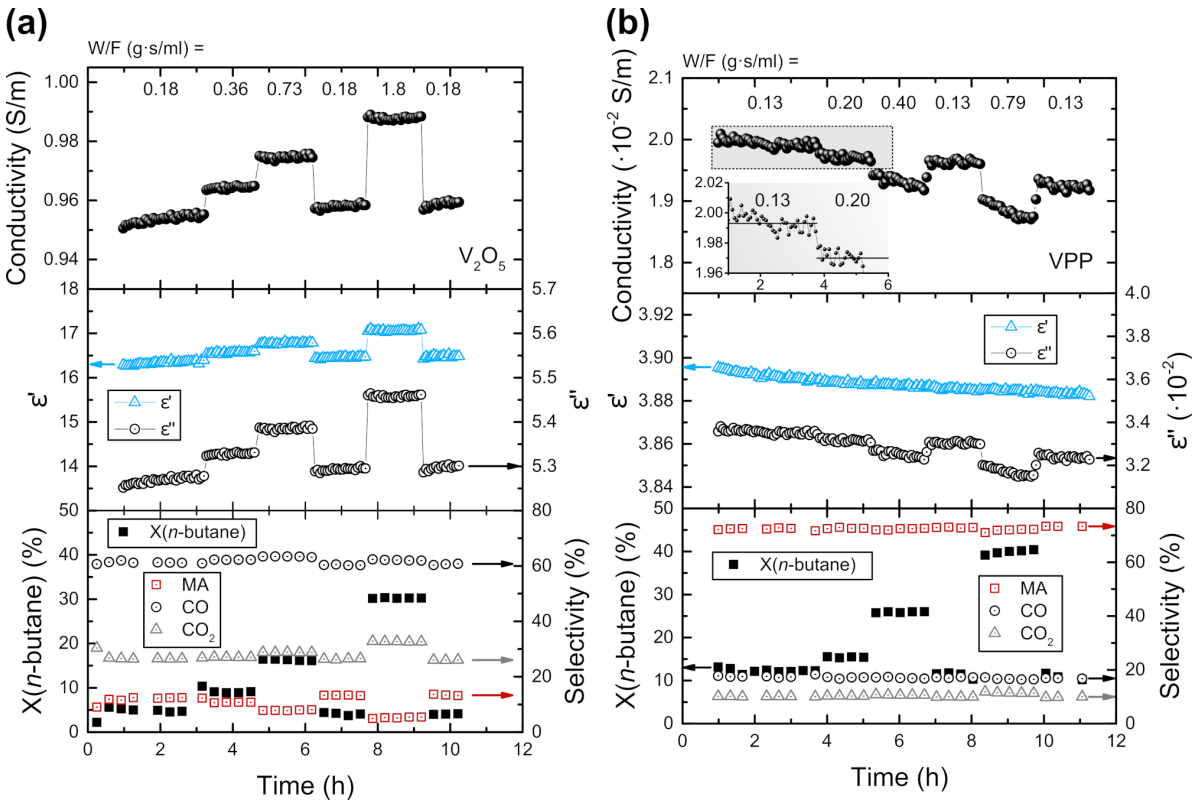

Figure 4.2.: MCPT conductivity and complex permittivity changes and corresponding *n*-butane conversion and product selectivity at 400 °C in 2% *n*-butane / 20% O_2 in N_2 at different W/F (contact time 0.18 – 0.76 g s ml^{-1} for V_2O_5 and 0.13 – 0.79 g s ml^{-1} for VPP) to vary *n*-butane conversion over the two catalysts in the same range between 0 and 40%: **(a)** V_2O_5 at 3 GHz (TM_{010} mode), **(b)** VPP at 10 GHz (TM_{020} mode).

conductivity of V_2O_5 or VPP, which suggests that they are correlated or that these changes have a common reason like a change in the charge carrier concentration that influences the conductivity and ε'', but also affects the dielectric relaxation or ε'. Yet, the relative response of the imaginary part of the permittivity, and hence of the conductivity, is much more pronounced than the response of ε'.

The microwave conductivity of V_2O_5 at 3 GHz and 400 °C in 2% *n*-butane / 20% O_2 in N_2 amounts to about 1 S/m. Under these conditions a selectivity of 9% towards maleic anhydride and of 28% and 63% towards CO_2 and CO, respectively, was observed. For VPP a conductivity of $\sim 2 \cdot 10^{-2}$ S/m was found under the same conditions, which is roughly 50 times lower than the conductivity of V_2O_5, together with a selectivity of 74% towards maleic anhydride and of 9% and 17% towards CO_2 and CO, respectively. The conductivity of VPP is in good agreement with the reported $1.7 \cdot 10^{-2}$ S/m at 400 °C in a 3% propane / 6% O_2 in N_2 recorded in a microwave resonator at about 5 GHz (TM_{010} mode).[123]

Both V_2O_5 and VPP follow the suggested criteria for (selective) oxidation catalysts[40] with respect to a stable conductivity under reaction conditions as well as reversible conductivity changes adapting to the gas atmosphere. Yet, the third proposed criterion of a low absolute conductivity in the reaction gas feed, compared to other gas feeds,[40] is only met by VPP. It may be noted that the observation that many p-type semiconducting oxides show a rather good performance in selective oxidation reactions[95] and the suggestion that holes might be required

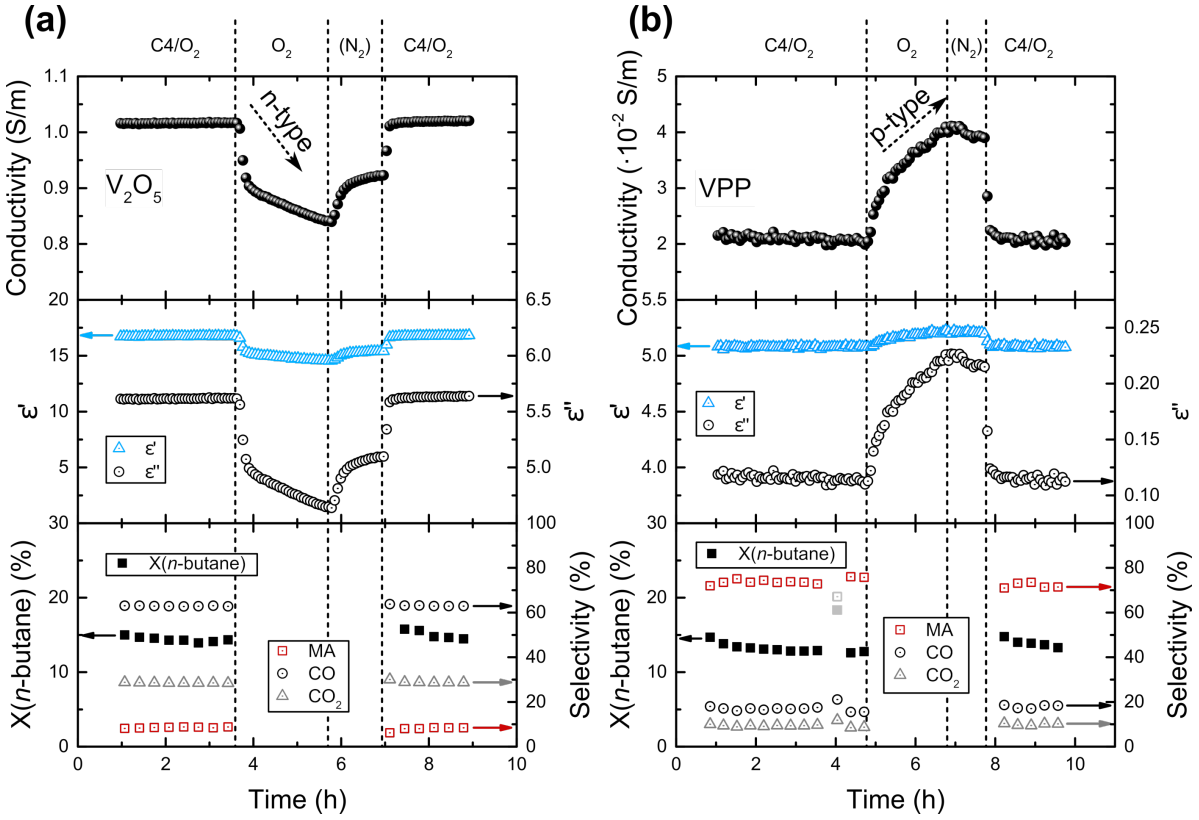

Figure 4.3.: MCPT conductivity, permittivity change and catalytic performance (*n*-butane conversion and product selectivity) of **(a)** V_2O_5 and **(b)** VPP at 3 GHz (TM_{010} mode), 400 °C, in 2% C_4H_{10} / 20% O_2 in N_2, 20% O_2 in N_2, N_2, 2% C_4H_{10} / 20% O_2 in N_2.

in the oxidation of *n*-butane,[25,60] at least in oxides containing only vanadium as transition metal ion, also hold true for VPP.

Diffuse reflectance (DR) UV-Vis measurements were carried out following the experimental protocol from the MCPT measurements shown in Figure 4.3. It is assumed here that these measurements exhibit such a large depth of information that pure surface modifications caused by changes in gas feed composition should not be detected. A comparison of conductivity and UV-Vis response should thus allow a comparison of bulk and surface responses of the MCPT technique. It is noted that the physical nature of the optical absorption experiment covers a much broader range of charge carrier energies than the MCPT experiment resulting in a possible error when comparing the two responses. Similarities in response between the two methods are taken here as indication of a non-surface process as origin of the response. Heine *et al.*[104] performed similar DR-UV-Vis experiments on V_2O_5 in *n*-butane- and O_2-containing gas atmospheres and found an increase in the intensity at about 800 nm in the reducing gas feeds, which the authors correlated to the conductivity response of the sample.

The results of V_2O_5 and VPP are presented in Figure 4.4 (a) and (b) in terms of a comparison of the MCPT conductivity (at the top) with the DR-UV-Vis response (at the bottom) in the different gas feeds at 400 °C. In the case of V_2O_5 the Kubelka-Munk function F(R) at 775 nm is shown as a function of time on stream (in 2% C_4H_{10} / 20% O_2 in He, 20% O_2 in He, 100% He, 2% C_4H_{10} / 20% O_2 in He) and for VPP the value of F(R) at 385 nm was used. For V_2O_5 the increase in absorption at 775 nm is related to an increased V 3d occupation, whereas V^{5+}-related

transitions contribute to the absorption of VPP at 385 nm.

This methodical inconsistency (it should have been possible to use the d-d transitions in both samples as measure) is caused by the fact that close inspection of the whole spectra indicate a contribution of an unknown species to the UV-Vis spectrum of VPP with absorptions in the visible range and below ca. 320 nm but not in the absorption window of the ligand-to-metal charge transfer band of O^{2-}–V^{5+}. The original data are presented in the Supporting information as Figures B.8–B.11.

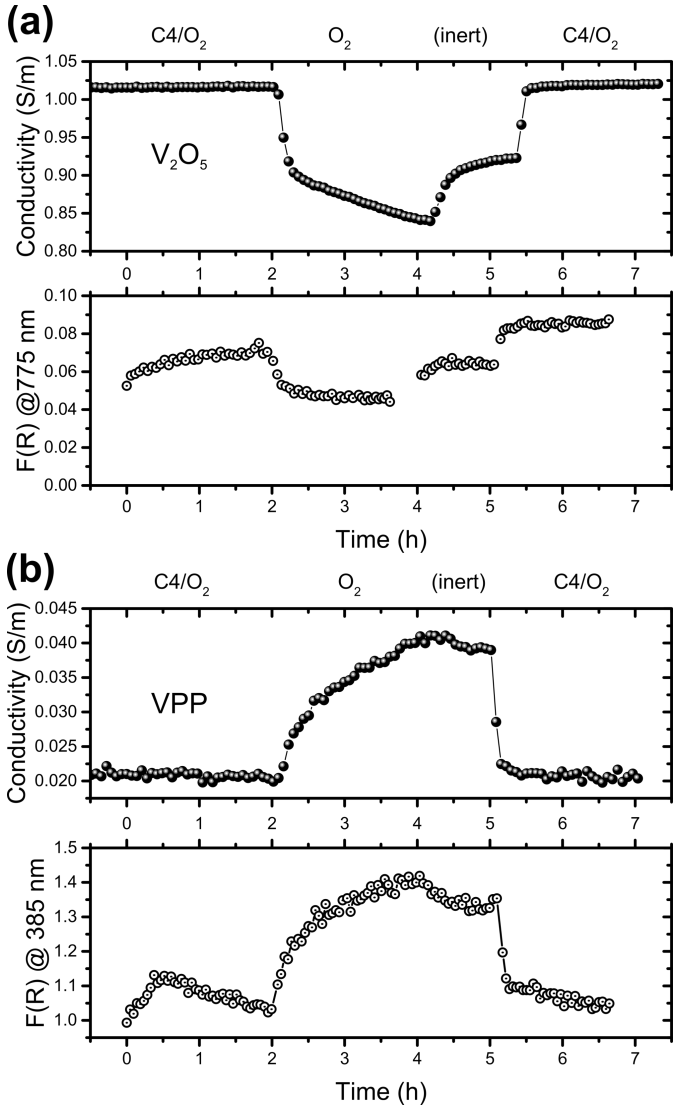

Figure 4.4.: Comparison between MCPT conductivity and DR-UV-Vis redox response in different gas feeds at 400 °C: **(a)** V_2O_5 conductivity (at the top) and Kubelka-Munk function F(R) at 775 nm (at the bottom) and **(b)** VPP conductivity and Kubelka-Munk function F(R) at 385 nm.

In Figure 4.4 (a) the similarity of the MCPT conductivity changes of V_2O_5 to the changes in the intensity at 775 nm in the DR-UV-Vis spectra can be seen. The absorption at 775 nm is caused by transitions from V^{4+} ($3d^1$).[232,233] In the reducing reaction gas feeds an increase of the absorption before the charge transfer edge was observed, while in the oxidizing O_2/He gas feed a decrease of the intensity in this region was found. This indicates a changing number

of V^{4+} centers adapting to the gas atmosphere. Even the conductivity changes in the inert gas feed were captured by the response of the absorption at 775 nm. Hence, both the increased absorption (Kubelka-Munk function F(R)) and the MCPT conductivity are likely caused by the same effects, i.e. an increased reduction of the V_2O_5 sample leading to a higher electrical conductivity of the n-type semiconductor in the reaction gas feed. This correlation between the DR-UV-Vis measurements and the MCPT experiments strongly supports the interpretation of the response of the conductivity and of ε'' as due to a change in the number of charge carriers.

The DR-UV-Vis experiments were also performed with the p-type VPP, which is shown in Figure 4.4 (b). Here, the absorption of VPP at 385 nm (in terms of the Kubelka-Munk function) is compared to the MCPT conductivity redox response. In this energy range O^{2-}–V^{5+} charge transfer transitions were reported.[234–236] Therefore the response of F(R) at 385 nm should be correlated with an increased sample oxidation or decreased V 3d occupation. It can be seen in Figure 4.4 (b) that the Kubelka-Munk function at 385 nm indeed increased upon oxidation of VPP in the 20% O_2 in He gas feed indicating a higher amount of V^{5+}. The subsequent 100% He feed was found to slightly change the response. The redox response of VPP was found to be reversible as seen by the decrease of F(R) at 385 nm upon returning to the reaction gas feed.

These observations from DR-UV-Vis spectroscopy are in good agreement with the MCPT conductivity changes of VPP in different gas feeds. It is therefore concluded that both measurements have a common reason, which are reversible changes in the V 3d occupation. The close similarity of the response signals is taken as indication for mainly the sub-surface regime of the catalysts being the location of these redox changes. The responses from oxygen to pure inert indicate, however, that the sub-surface regime quickly reacts upon the surface chemical potential and diffusion of lattice oxygen towards the oxygen-free surface sets in. The complex temporal evolution of the responses is not further analyzed respecting the unclear physical basis of the observation that could either lead to a distribution of transport processes or of the nature of charge carriers in terms of energy effective mass.

4.4.4. Temperature Dependence of Conductivity and Permittivity

V_2O_5 and VPP were further characterized in terms of the temperature dependence of their conductivity and permittivity. As semiconductors, their charge carrier density is expected to increase exponentially with temperature. The investigation of the temperature dependence of the MCPT resonant frequency shift and the change in the reciprocal Q factor may also provide information about the conductivity regime of the samples and the vicinity of the so-called depolarization peak.[40,138] The detailed experimental procedure showing for instance the effect of increasing the temperature on the MCPT raw data as well as the initial conductivity and permittivity values upon reaching the respective temperatures can be found in the SI (Figures B.12–B.16).

Figure 4.5 shows semi-logarithmic plots of the conductivity of V_2O_5 and VPP (steady-state values) as a function of inverse temperature from 30 to 450 °C in the different gas feeds 2% *n*-butane / 20% O_2 in N_2, 20% O_2 in N_2, and 100% N_2. The room temperature conductivity of V_2O_5 of about 0.1 to 0.2 S/m (30 °C, 3 GHz) falls within the range of reported literature values, compare for instance to the room temperature DC conductivities of 0.37 S/m for a V_2O_5 single

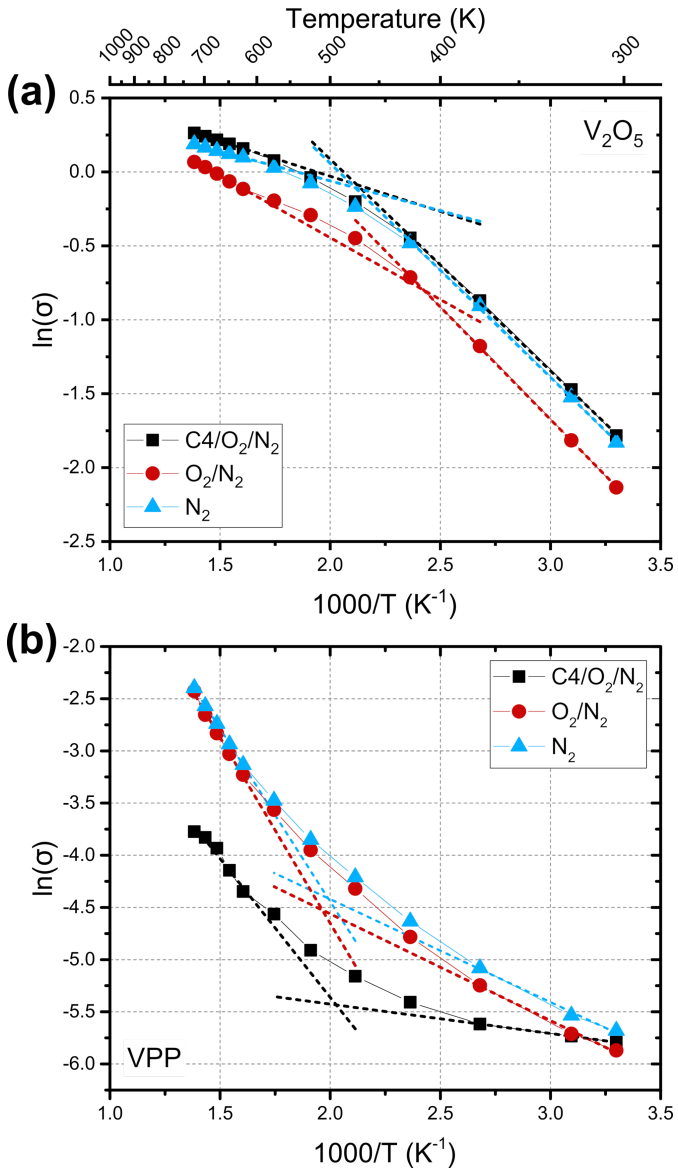

Figure 4.5.: The Arrhenius-type plots of $\ln(\sigma)$ vs. $1/T$ of **(a)** V_2O_5 and **(b)** VPP in the different gas feeds. Analysis was performed in low and high temperature regimes. The dashed lines correspond to linear fits.

crystal,[222] or to 0.01 – 0.1 S/m for a polycrystalline V_2O_5 pressed powder.[237]

Inspection of Figure 4.5 reveals clear differences in the temperature dependence of the conductivities of V_2O_5 and VPP. Two temperature regimes with different slopes can be distinguished for both samples, which show opposite trends. While V_2O_5 exhibited an initial steep increase in conductivity below 200 °C, which leveled off at higher temperatures, the conductivity of VPP started to increase significantly only above ∼200 °C. Similar findings of two linear regimes were reported in literature for the DC conductivity of V_2O_5 single crystals at lower temperatures,[222,238] and were also found for (doped) VPP powders.[60,103] The origin of the changes may be associated with the loss of structural water occurring in vanadia-containing materials in that temperature regime.[239] This type of water is not hydrating the parent structure, but is part of the structure often in dissociated form. Its release causes the formation of defective lattice sites and has thus a marked influence on the conductivity. It is noted that also redox phase transitions between

trivalent and pentavalent vanadium oxide can occur[240] in this temperature regime.

Moreover, a comparison of the effects of different gas feeds on the temperature dependence of the conductivity showed significant responses for VPP between the reaction gas feed and the other gas environments. Whereas the increase in conductivity in VPP may be associated with a generation of hole states, this process is leveling off in the reaction feed. The onset of reaction injecting electrons from *n*-butane into the catalyst seems to equilibrate the thermally induced loss of oxygen. In V_2O_{5-x} a similar yet weaker phenomenon of changed temperature dependence of the conductivity was observed. The moderating effect of reactivity is not observed. The lower conductivity in oxygen plus the earlier onset of the conductivity change in temperature both point to the ability of the catalyst to activate adsorbed oxygen by using electrons from its defect structure.

In order to get a better understanding of the charge transport in the V_2O_5 and VPP samples, the temperature dependence of the conductivity σ was analyzed in terms of the apparent activation energy of conduction E_c according to Eq. (4.4). The apparent activation energies from a linear fit of the data are summarized in Table 4.1. They reflect the two temperature regimes for V_2O_5 and VPP that were discussed above. The activation energies determined with different conduction models (Eqs. (4.4) – (4.6)) and the corresponding semi-logarithmic plots are shown in the SI (Figures B.17–B.18). Table 4.1 further presents the apparent activation energies of *n*-butane oxidation as determined from an Arrhenius plot of the *n*-butane consumption rates (Fig. B.19).

V_2O_5 exhibited an apparent activation energy of conduction of ∼0.12 to 0.13 eV in the range of 30 to 150 °C, which decreased to ∼0.04 to 0.07 eV between 350 and 450 °C. Generally, the highest activation energy in both temperature regions was observed in the oxidizing gas feed, O_2/N_2, where the n-type semiconductor V_2O_5 has the lowest conductivity. Still, these differences in the activation energies between different gas feeds were not pronounced. The same results were found using other conduction models; see SI (Figure B.18). Sanchez *et al.*[222] reported an activation energy of 0.22 eV for the DC conductivity of a V_2O_5 single crystal from about 100 to 150 °C according to the small polaron model (Eq. (4.6)). This value is similar to the one found for the V_2O_5 powder in the present study, particularly given that our measurements were carried out in the microwave frequency range, which is expected to decrease the apparent activation

Table 4.1.: Apparent activation energies of *n*-butane oxidation E_a (300 to 450 °C) and comparison to apparent activation energies of conduction E_c of V_2O_5 and VPP determined from the data of Figure 4.5. Low temperature regime: 30 to 150 °C (V_2O_5) or to 100 °C (VPP); high temperature regime: 350 to 450 °C.

	$\mathbf{E_a}$ **(eV)**	$\mathbf{E_c}$ **(eV)**		
	C4/O$_2$/N$_2$	**C4/O$_2$/N$_2$**	**O$_2$/N$_2$**	**N$_2$**
		Low temperature		
V_2O_5		0.12	0.13	0.12
VPP		0.024	0.088	0.085
	High temperature	High temperature		
V_2O_5	0.63	0.041	0.072	0.035
VPP	0.88	0.23	0.31	0.29

energy of conduction compared to DC measurements.[103]

For VPP, none of the Equations (4.4) – (4.6) yielded a line over the whole temperature range. The transition between the low temperature regime ($\leq$ 100 °C) with a small activation energy of conduction of about 0.02 to 0.09 eV to the high temperature regime ($\geq$ 350 °C) with E_c of $\sim$0.23 to 0.31 eV using the Arrhenius equation (4) occurred at 220 to 236 °C. It was reported in literature that this "threshold temperature" depends on the sample preparation and pretreatment and was reported to lie between 121 to 348 °C.[60,103] In the literature, the activation energy of conduction of VPP was measured under different conditions and in different setups thus making the direct comparison of the values difficult. The literature values range from E_c of 0.14 eV for Nb-doped VPP in an *n*-butane oxidation gas feed above 200 °C measured in an MCPT setup at 9 GHz,[103] to DC activation energies in vacuum above the threshold temperature from 0.76 eV to 1.4 eV depending on the sample pretreatment,[60] and to E_c of 1.6 eV in O_2/N_2 and of 1.2 eV in N_2 gas feeds in the temperature range of 445 to 545 °C.[208]

A comparison of the apparent activation energies of conduction (E_c) and of *n*-butane oxidation (E_a) reveals much higher values of E_a compared to E_c, in particular for V_2O_5 (cf. Table 4.1). For the binary oxide the activation energy of the reaction is by a factor of 15 higher than E_c, whereas for VPP it is only by a factor of 4 higher than E_c.

In summary, the temperature dependence effects of the two systems support the findings from the catalysis study, namely that the charge carrier dynamics is sensitive to the gas environment at the surface of the bulk powders. The strong change of the dependence of the conductivity on temperatures where defect induction through loss of structural water should occur underlines the sensitivity of the conductivity on these defects. This sensitivity is in line with the dependence of absolute values of the conduction activation energy on the pre-history of the samples. In a more general sense the data from Table 4.1 suggest that the charge carriers are available for chemical reaction outside of their solids at temperatures where reactions are observed. It is noted that the selective catalyst VPP exhibits an activation energy of conduction larger than an order of magnitude as compared to the non-selective catalyst. Remarkable in this context is the property of the defective binary oxide to activate oxygen in the whole temperature range studied here.

4.5. Discussion

4.5.1. General Remarks to Conductivity and Selective Oxidation

The initial idea to use electrical conductivity as a proxy for charge carriers in a catalyst that are available for the activation of an adsorbate stems from the concept of the function of a redox catalyst that activates oxygen by its electrons that are given back to it by oxidizing the hydrocarbon in a proton-coupled electron transfer or homolytic C-H cleavage reaction. Determination of the electrical conductivity understood as the effect of free carriers available in a solid substance could then serve as a descriptor for the ability of a catalyst to activate oxygen and hence to perform redox reactions. The practical realization of a DC conductivity experiment using electrodes fixed to pressed pellets of a polycrystalline catalyst leads to multiple problems associated with contact and grain resistances of the material.

Hence the microwave cavity perturbation technique was introduced[39] overcoming these

problems. The price to be paid for this advantage is however the much more complex interpretation of the term "conductivity". First, the experiment is designed such that the microwave measurement penetrates the whole sample and is thus a bulk-sensitive technique. The skin effect as surface conductivity was deliberately excluded to allow quantification of the perturbation signals. Second, the observed effect is a combination of energy losses similar to Ohmic resistance as in DC conductivity measurements and to charging losses to fixed carriers in covalent bonds occurring due to polarization effects of the high frequency electromagnetic field. This applies as well to bulk charge carriers and their polarons as to surface adsorbates such as water or strongly bound organic intermediates. The result is a complex permittivity quantity. Its relation to the quantity of interest in the present context is associated with many unknown influences as described in the literature quoted in the Introduction. In the present context, the analysis in terms of Equation (4.3) reduces the conductivity data to a quantity mainly associated with energy losses of mobile charge carriers to the catalyst bulk. In this way, the MCPT conductivity comes close to the intended proxy for the available charge carriers for catalytic action. The separation between static and dynamical factors affecting imaginary and real part of the permittivity is nevertheless rather crude. The present work looks separately at both quantities and finds indeed striking differences between the catalysts as shown in Figure 4.2.

As a result of this complex situation, the present discussion can only be fragmentary with respect to the question about the participation of catalyst charge carriers in the catalytic process. The rather rigorous measurement approach illustrated here follows a first pathfinder study[39,42] and needs extension to other catalyst systems in order to attain relevant quantifications. A key observation made in the present study is that the charge carriers of the catalyst solid experience well-measurable influences from the catalytic processes at its surface. This in its own right is an important result as it excludes the notion that the electronic structure of the bulk catalyst is not relevant for catalysis. The local electronic structure of an "active site" as a molecular entity as treated in theory and experiment of modern catalysis science is certainly an important and critical contribution, but is incomplete to describe as a whole the catalyst mode of operation. Non-local phenomena are likewise important as they were discussed under the term "electronic factor"[42] of catalysis as indicated in the Introduction. This is fully recognized by the addressees[241–243] of the present special issue, but not likewise common understanding in the whole community as exemplified with the term "innocent support".

4.5.2. Relation between Catalytic Performance and Conductivity

The performance of the two catalysts is complicated to combine into a single figure of merit that may be correlated to the conductivity. The underlying concept is that electrons are given to the catalyst into the conduction band of the surface termination layer through proton-electron transfer of homolytic C-H cleavage[155] from *n*-butane and are donated out of the partly filled valence band to oxygen molecules forming the various types of electrophilic and nucleophilic reactive oxygen species.[9] Surface states in the bandgap of the semiconducting catalysts can facilitate the charge transfer.[11] In an ideal case representing perfect site isolation in Grasselli's nomenclature,[244] this process would not change the conductivity at all as under steady-state reaction conditions exactly the desired number of electrons is exchanged between *n*-butane and

oxygen to arrive at the desired product.

The type of product being maleic anhydride (MA) and the decarbonylation product (CO formation) or the combustion product CO_2 will be regulated by the extent of electron transfer between organic adsorbate and oxygen molecules. This regulation may occur in redox catalysis through the surface band dispersion creating an energetic barrier for electron flow through the catalyst interface. This barrier is zero for a metal or a semiconductor in the hypothetical flat band case and it will reach finite values for redox-active semiconductors such as the present catalysts and can be so high that the electron flow is inhibited when the semiconductor is a wide bandgap material. The present work is not concerned with these energetic quantities that are accessible[42] through *operando* electron spectroscopy.

The relevant descriptor for the present study is how much the conductivity changes for a given flow of electrons. This can be evaluated by comparing the conductivity change for various levels of conversion under isothermal conditions. The well performing system should exhibit a small change, whereas large conductivity changes indicate modifications in the nature of active material with changing conversion levels. Well performing catalysts should, in addition, exhibit finite kinetic barriers for electron transfer through their surface in order to avoid leakage of charge carriers arising from other processes than the catalytic transformation (i.e., the stoichiometric reduction of oxides or electrons from thermal defects). The two studied systems show both situations with a high barrier in VPP and a low barrier in V_2O_{5-x} leading to continuous oxygen activation (see Figure 4.5 and Table 4.2).

Structural changes of active sites with performance levels are undesired as they affect the ratio of selective to unselective pathways by influencing the energetic barrier for charge carrier dynamics. It is noted as caveat that this interpretation assumes the concept of a redox catalyst to be operational whereby the charge carriers between oxygen and *n*-butane are exchanged through the action of the catalyst. The hypothetical case that charges are exchanged directly between oxygen and *n*-butane as it is exemplified in the OCM case over non-reducible wide bandgap semiconductors would not be accounted for by this descriptor. The fact that all observations in this work indicate a response of the catalyst electronic structure is taken as argument to exclude this case.

The relevant figure of merit is the total number of electrons exchanged under steady-state operation. Thanks to the *operando* conditions of the experiment, this number can be exactly evaluated by considering the selective and unselective reaction pathways.

$$C_4H_{10} + \frac{13}{2}\ O_2 \longrightarrow 4\ CO_2 + 5\ H_2O \qquad \text{(formally 26 } e^- \text{ transferred)} \tag{4.7}$$

$$C_4H_{10} + \frac{9}{2}\ O_2 \longrightarrow 4\ CO + 5\ H_2O \qquad \text{(formally 18 } e^- \text{ transferred)} \tag{4.8}$$

$$C_4H_{10} + \frac{7}{2}\ O_2 \longrightarrow C_4H_2O_3 + 4\ H_2O \qquad \text{(formally 14 } e^- \text{ transferred)} \tag{4.9}$$

In Figure 4.6 the respective correlations are given between the conductivity and the total number of electrons transferred for the two catalyst systems calculated according to Equations (4.7) – (4.9) based on the performance data. At first glance the data reveal that there is indeed a relation between the two quantities. Different majority charge carriers being electrons for vanadium oxide and holes for the pyrophosphate system explain the different slopes for the two systems.

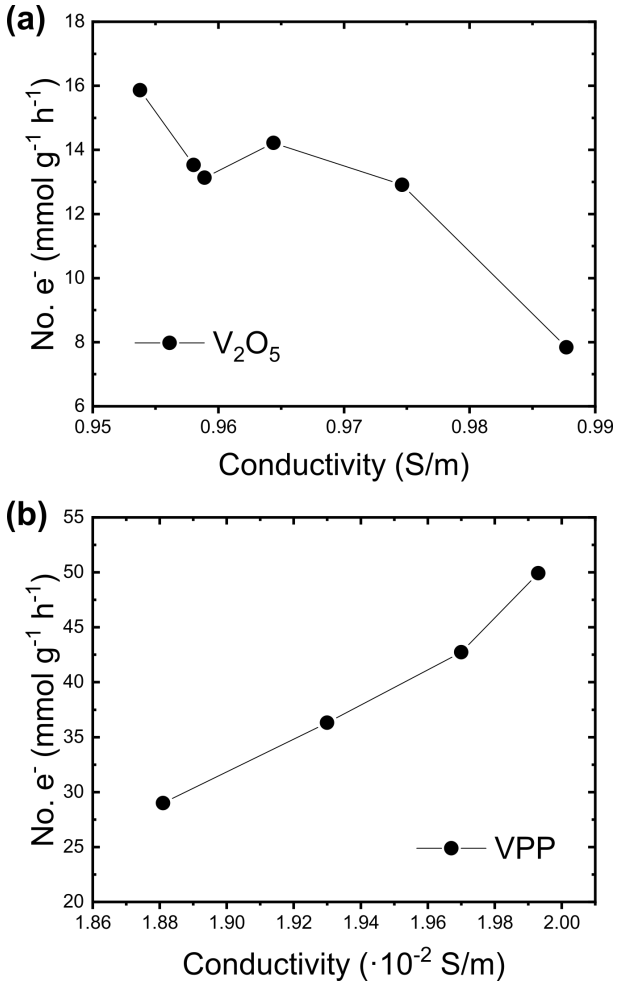

Figure 4.6.: Comparison of the total electron flow during *n*-butane oxidation with the change in conductivity as observed by the MCPT technique. All data are measured at 400 °C.

Table 4.2 summarizes the observations to facilitate further discussion.

It is apparent that VPP is the by far more active catalyst. From inspection of Figure 4.1 it further occurs that it is the by far more selective catalyst in full agreement with the low conductivity change observed here and postulated above. The increase in conductivity with high conversion may be understood as donation of electrons to the then limiting oxygen activation. It is instructive to see that the real part of the permittivity describing polarization effects is unchanged during this experiment. The changing conversion levels seem not to change the type of active sites and their relative coverage levels. The catalyst is "sealed off" against the changing local chemical potential coming with the flow changes. The fact that the real part of the permittivity (Figure 4.2) does not change with the flow rate is taken as indication that the catalyst has retained the ability to buffer the increased demand for electrons from its bulk without a respective change of its surface, where one expects the location of the unchanged polarization. Such behavior requires inhomogeneity both lateral at the surface[65] (locations of adsorption/activation of *n*-butane and of attaching of activated oxygen) and as gradient into the bulk (electron withdrawal from the V^{4+} reservoir of the VPP structure to the V_xO_y/P sites of *n*-butane conversion).

The behavior of V_2O_{5-x} is complementary to that of VPP. A much smaller number of electrons

Table 4.2.: Characteristic relations of the two vanadium-containing catalysts during *n*-butane oxidation at various gas velocities and 400 °C.

Property	$\mathbf{V_2O_{5-x}}$	**VPP**
Change in electron transfer (mmol g^{-1} h^{-1})	8	20
Change in conductivity (S/m)	$3{\cdot}10^{-2}$	$1{\cdot}10^{-3}$
High conversion limit	High conductivity	Low conductivity
Low conversion limit	Low conductivity	High conductivity
Majority charge carriers	Electrons	Holes

exchanged gave rise to a much larger change in conductivity. From Figure 4.2 it occurs that both contributions to the permittivity change in line with the local chemical potential and indicate the proportional response of the catalyst in its electronic structure both at the surface (active sites) and in the bulk. The missing buffer function seems to be a poor property for a high performance selective oxidation catalyst. From comparison with the UV-Vis data this response is related to a chemical reduction of the pentoxide to multiple possible arrangements of point defects or ordered sub-oxides. The kink in the data of Figure 4.6 (a) may be taken as indication of a transformation into a different ordering that was not sensed by the UV-Vis data (no change in local symmetry around the V species). The changing local chemical potential affected the nature of the surface termination and its ability to adsorb species and to activate oxygen. From Figure 4.1 it is clear that this was detrimental for the selectivity of the process. Notably the combustion activity increased with increasing conductivity. The low kinetic barrier of electron transfer through the surface to oxygen as seen from the temperature dependence study (Table 4.1) is supporting the combustion activity of the system.

4.6. Conclusions

Operando MCPT is a tool that allows probing the electronic structure of a working redox catalyst in fine detail. Above all it verifies that charge carrier properties beyond a local approximation are important and critical for catalytic function. The method gives access to quantitative observables that are, however, difficult to relate to single structural properties as multiple factors of static and dynamical charge carrier motion are convoluted in the single number “conductivity”. The limited number of sufficiently resolved case studies precludes at present the deconvolution of these factors. The discussion of the limited results gained here reveals that the phenomenon of selectivity requires, besides the analysis of the conductivity, in addition the knowledge of the absolute position of the energy levels with respect to the vacuum level at which the charge carrier dynamics occurs. It is thus unlikely that the single physical quantity “conductivity” may serve as descriptor for the complex phenomenon of selective oxidation. It is clear, however, that this observable is a valuable and sensitive component of such a descriptor.

The present work shows that the qualitative concept of site isolation can be put into a physical observable by studying the excess of charge carriers generated in a multiple steady-state catalysis experiment. This approach seems viable when comparing catalysts with similar local chemical bonding as done in the present work, but will clearly require more care when wider libraries

of systems are to be studied. Correction factors for the relative sensitivity of the method that account for the different static and dynamical loss factors may be needed.

The results give hints to the chemical design concept of a high performance catalyst. VPP reveals the property of a "buffer" for charge carriers in its bulk that can be transported to the active sites when the delivery of redox equivalents between adsorbates is too slow. Likewise, the surface layer containing the active sites is robust against chemical changes induced by the lack of redox equivalents leading to chemical oxidation or reduction of the sites. The Grasselli pillar[244] of "multifunctionality" becomes a structural reality by assuming that a rigid bulk structure tolerates changes in its charge carrier content (redox reactions without much structural changes in non-densely packed framework structures). This bulk can exchange charge carriers with a dynamical surface structure reversibly generating active sites by structural fluctuation that can couple in their electronic structure to the charge carrier supply of the bulk. One envisages a structurally loose surface geometry allowing, e.g., redox tautomery of vanadyl (V^{5+}=O $\leftrightarrow$ V^{4+}-O^{-}) and exchange of redox equivalents by the coupling through a transfer agent that itself may not participate in the catalytic process. The covalent main group element modifiers being always constituents or promoters of well-performing redox catalysts may take on this function. The successful material is thus a fully reversible redox buffer providing the correct absolute energy of its Fermi level with respect to the adsorbing reactants that carries an electronically decoupled dynamical (fluctuating) surface termination layer that is coupled through a redox transfer agent to the bulk. The typical system may thus contain a minimum of three structurally and chemically different volume elements in a suitable distribution. This would be a function of "inhomogeneous" catalyst materials that one identifies so often in practical realizations of working redox catalysts.

It will be left to the future to see, for example, if catalyst chemistry continues to rely on the cleverly enabled autogenous formation of such complex multi-functional systems during activating and steam addition, or if technologies of nanostructuring can generate optimized versions of such systems in simpler and more controllable operating environments. In any case, the *operando* control of these processes of catalyst operation will be needed and to this end the present work may serve as one tool. With respect to model studies in theory and experiment, the present observations give hints to the level of detail that is required for generating insight that is causally related to the catalytic phenomena under study.

5. Electronic and Dielectric Properties of MoV-Oxide (M1 Phase) under Alkane Oxidation Conditions*

Anna M. Wernbacher, Pierre Kube, Michael Hävecker, Robert Schlögl, and Annette Trunschke

5.1. Abstract

MoV-based oxides are an important class of selective oxidation catalysts of light alkanes. We investigated possible relations between the semiconducting properties and (surface) electronic structure of MoV-oxide in the orthorhombic M1 phase and its catalytic performance in the oxidation of ethane, propane, and *n*-butane. *Operando* conductivity and permittivity measurements were performed and complemented by near-ambient pressure XPS. Interestingly, MoV-oxide showed p-type semiconducting behavior. The electronic properties of the sample were found to be a sensitive function of the chemical potential of the surrounding atmosphere adapting not only to the different alkane chain lengths, but also to different reactant conversion levels. The addition of steam to a propane oxidation feed had a significant influence on the surface termination layer on MoV-oxide and lead to a decrease of its conductivity or permittivity. The modification of this overlayer is suggested to be related to the steam-induced changes in the conductivity and is likely affecting the catalytic performance as well.

5.2. Introduction

Complex mixed oxides like $MoVTeNbO_x$ in the orthorhombic M1 phase (ICSD 55097)[69,70] have attracted much interest as promising catalysts for selective oxidation reactions, in particular for the (amm)-oxidation of propane.[68,245,246] The active surface layer of $MoVTeNbO_x$ is believed to be composed of vanadium oxide nanodomains, which are separated from each other by Mo_xO_y and Te_xO_y moieties, on top of the redox-active bulk.[15,75] This termination layer is likely adapting its (electronic) structure and composition to the chemical potential of the surrounding atmosphere.[10,15,75] Indeed, changes in the surface layer on $MoVTeNbO_x$ were observed under reaction conditions together with a change in band bending, which also affects the electrical conductivity of the n-type semiconductor.[1] The acrylic acid formation over $MoVTeNbO_x$ is enhanced by the addition of water vapor to the gas feed.[72] Steam was shown to modify the valence band spectra and the work function as well, and it causes a higher average vanadium oxidation state and a decreased electrical conductivity.[105]

Recently, the tellurium- and niobium-free MoV-oxide in the M1 phase was shown to be able to produce acrylic acid as well, in spite of the diminished selectivity compared to $MoVTeNbO_x$.[77,245]

*Reprinted (adapted) with permission from Wernbacher, A. M.; Kube, P.; Hävecker, M.; Schlögl, R.; Trunschke, A. Electronic and Dielectric Properties of MoV-Oxide (M1 Phase) under Alkane Oxidation Conditions. *J. Phys. Chem. C*, Just Accepted Manuscript, DOI: 10.1021/acs.jpcc.9b01273.

Differences in the occupation of the hexagonal channels in the M1 crystal structure between the two mixed-metal oxides are also reflected in differences in the surface layer formed under catalytic operation conditions, where an accumulation of vanadium is observed on MoV-oxide and of tellurium on MoVTeNb-oxide.[77] There are still open questions regarding the semiconducting properties of MoV-oxide and the influence of steam on its surface electronic structure and electrical conductivity. Microwave cavity perturbation techniques (MCPT) provide a sensitive and non-invasive tool to study the dielectric properties (complex permittivity) and the electrical conductivity of semiconductors[103,106] under *operando* conditions and in a contact-free fashion thus avoiding erroneous results caused by electrode-sample contact problems.[103,129,247]

In this study we investigated the electronic properties of MoV-oxide (M1 phase) and their possible relation to its catalytic performance. The complex permittivity and electrical conductivity of MoV-oxide were studied under catalytic operation conditions in the oxidation of light alkanes from ethane to *n*-butane based on the MCPT. These measurements were complemented by synchrotron-based NAP-XPS and near edge X-ray absorption fine structure (NEXAFS) spectroscopy in the same gas feeds, which give information about the surface electronic structure and surface composition. Moreover, the effect of steam not only on the catalytic performance, but also on the conductivity or permittivity of MoV-oxide and its surface (electronic) structure was analyzed.

5.3. Experimental Section

5.3.1. Catalyst

The MoV-oxide sample in the orthorhombic M1 phase (internal ID 18075) was prepared by a hydrothermal synthesis method using a specially built reactor from Premex Reactor AG, Lengnau, Switzerland, as described in Ref. [77]. In brief, the hydrothermal reactor was loaded with 9.18 g of $(NH_4)_6Mo_7O_{24}{\cdot}4H_2O$ (AHM, Merck, 52 mmol Mo) in 230 g Milli-Q water (Merck) mixed with 3.30 g $VOSO_4$ (Acros Organics, 12.9 mmol V) in 30 g water. The mixture was subsequently heated to 200 °C with 1 K/min under a stirring rate of 100 rpm and kept for 17 h at the final temperature. A black solid was obtained by filtration (pore 5 glass frit) after cooling to room temperature, which was washed twice with distilled water and then dried for 16 h at 80 °C. The dried powder was further washed with 25 ml of oxalic acid solution (0.25 M, Acros Organics) under stirring for 30 min at 60 °C. The solid was isolated by centrifugation (30 min, 5000 rpm), washed two times with 25 ml of water, and dried overnight at 80 °C. The sample was obtained after a final thermal treatment in a rotary tube furnace (Xerion, Freiberg, Germany) under an argon flow of 100 ml/min for 2 h at 400 °C (heating rate of 10 K/min).

The sample exhibits total surface area of 27.9 m^2/g determined from the isothermal adsorption of nitrogen at -196 °C (Quantachrome Autosorb-6-B) with a micropore surface area of 18.1 m^2/g and external surface area of 9.8 m^2/g. Detailed structural information based on a single crystal structural analysis and complemented by scanning electron microscopy and scanning transmission electron microscopy can be found in the previous study in Ref. [77] showing the high crystallinity and phase purity of the sample. The sample characterization with XRD (Fig. C.1) and TEM (Fig. C.2) is shown in the SI. Energy-dispersive X-ray spectroscopy (Hitachi S-4800, EDAX detector at 15 kV) showed a metal content of 29.5 at-% V and 70.5 at-% Mo.

5.3.2. Microwave Cavity Perturbation Technique (MCPT)

Contact-free and *operando* electrical conductivity and permittivity measurements of MoV-oxide in the orthorhombic M1 phase (internal ID 18075) were performed based on the microwave cavity perturbation technique (MCPT).[103,136] The MCPT relies on a perturbation of the resonator properties of a microwave cavity (cylindrical resonator with a radius of 22.5 mm and height of 20 mm; TM_{010} mode at 5 GHz) by the semiconducting sample.[103,133] The sample was placed in the electric field antinode in the center of the resonator. In order to obtain the unloaded quality factor Q of the cavity, the measured reflection coefficient $\Gamma(\omega)$, which was recorded with an Agilent PNA-L N5230C vector network analyzer, was fitted with the Q0REFL program.[152] The perturbation was be related to the relative complex permittivity $\tilde{\varepsilon} = \varepsilon' - i\varepsilon''$ of the sample[103,106] as described in Ref. [248]. The Landau-Lifshitz-Looyenga effective medium approach was used to obtain the bulk permittivity values.[147–149] Finally, the electrical conductivity σ was obtained from the imaginary part of the permittivity ε'' and the angular resonant frequency ω according to[103,106]

$$\sigma = \varepsilon_0 \, \omega \, \varepsilon'' \tag{5.1}$$

where ε_0 denotes the vacuum permittivity. Online gas chromatography (Agilent 7890 GC) was used for analysis of the reactant and product gases.

The dielectric properties given by the (frequency-dependent) permittivity or dielectric function describe the response of a sample to the driving electromagnetic field, which stems from the displacement of bound and free charges or dipole alignment.[106] The present study is concerned with the interaction with the electric field component of the microwave analyzing changes in $\tilde{\varepsilon}$ of MoV-oxide. In the frequency-domain the permittivity is a complex function, where the real part (ε') is associated with energy storage and the imaginary part (ε'') with energy dissipation or loss.[106] While both a dipolar response and the response of mobile charge carriers contribute to the dielectric behavior,[249] it is assumed that the imaginary part of the permittivity or the electrical conductivity (i.e., the dissipative contributions; Eq. (5.1)) are dominated by charge carriers in case of semiconductors investigated in the microwave frequency range.[106]

MoV-oxide was investigated in the oxidation of light alkanes with a gas feed composition of 3% alkane (ethane, propane, *n*-butane) and 6% O_2 in N_2 at 270 °C (heating rate 2 K/min). The influence of water was analyzed by adding 5% steam to the propane oxidation feed. The catalyst was measured at contact times (W/F) ranging from 0.13 to 1.63 g·s/ml (W = 44 – 54 mg $MoVO_x$, total gas flows F = 2 – 20 ml/min) and at temperatures from 200 to 290 °C. The apparent activation energy of conduction was determined as described in Ref. [248].

5.3.3. NAP-XPS and NEXAFS

Near-ambient pressure X-ray photoelectron spectroscopy (NAP-XPS) and near-edge X-ray absorption fine structure (NEXAFS) measurements were performed at the ISISS (Innovative Station for In Situ Spectroscopy) beam line at the synchrotron radiation source BESSY II in Berlin, Germany. A pressed powder pellet of 13 mg MoV-oxide (ID 18075) was measured at 270 °C (heating rate 5 K/min) and 25 Pa in 1:2 mixtures of alkane/O_2 (1 N ml/min, 2 N ml/min,

alkane = ethane, propane, *n*-butane) and in a wet propane oxidation feed (0.37 N ml/min propane / 0.74 N ml/min O_2 / 4.9 N ml/min H_2O). The gas phase was monitored using a Varian CP-4900 Micro gas chromatograph (Micro-GC) and a IONICON proton-transfer-reaction mass spectrometer (PTR-MS).

The core level spectra were deconvoluted using Gaussian-Lorentzian product functions after subtracting a Shirley background with the CasaXPS software (Neal Fairley, Version 2.3.15, © 1999 – 2009 Casa Software Ltd.). The measurements were carried out at different photoelectron kinetic energies probing the "surface" region with an approximate electron inelastic mean free path length λ_{IMFP} of 0.6 nm ($E_{\mathrm{kin}} \approx 144$ to 163 eV using photon energies $E_{h\nu}$ of 380 eV (Mo 3d) and of 680 eV (V 2p, O 1s)) and at greater probing depths with λ_{IMFP} of 1.7 nm ($E_{\mathrm{kin}} \approx 744$ to 763 eV using photon energies $E_{h\nu}$ of 980 eV (Mo 3d) and of 1280 eV (V 2p, O 1s)). The values of λ_{IMFP} were estimated using the predictive TPP-2M formula by Tanuma, Powell and Penn[177,178] (NIST Electron Inelastic-Mean-Free-Path Database Version 1.2).[179] For the quantitative analysis of the core levels atomic subshell photoionization cross sections and asymmetry parameters from numerical calculations by Yeh and Lindau[175,176] were used taking the photon energy dependent photon flux into account.

In order to determine the work function Φ of the sample, the secondary electron cutoff was measured with a bias of -17.8 V applied to the sample at a photon energy of 100 eV and a pass energy of 2 eV. The position of the cutoff was determined by a linear extrapolation between 20% and 80% of the maximum intensity. The valence band onset was likewise evaluated by a leading-edge extrapolation using a photon energy of 100 eV.

The NEXAFS spectra were recorded in the photon energy range of 500 to 560 eV at the V $L_{2,3}$-edge and O K-edge in the total electron yield (TEY) mode and in the Auger electron yield (AEY) mode using a kinetic energy of 385 eV and pass energy of 50 eV in order to minimize the contribution of the gas phase O_2 signal to the AEY spectra (see Ref. [180] for details). The plane grating monochromator was operated in the continuous driving mode ("on the fly") with a speed of 0.25 eV/s combining a quick data acquisition with a small energy interval between adjacent data points. The spectra were normalized to the pre-edge at 500 eV and the post-edge at 560 eV and the energy was corrected using the π^* resonance of molecular O_2 from the gas phase, which was set to 530.8 eV[181,182] (see the total electron yield TEY spectra in Fig. C.23 in the SI).

5.4. Results

5.4.1. MCPT Permittivity and Conductivity

Conductivity Response under Alkane Oxidation Conditions

To investigate the semiconducting properties of MoV-oxide and their possible relation to its catalytic performance, the electrical conductivity was monitored during the oxidation of light alkanes. Figure 5.1 (a) presents the conductivity response to ethane (C2), propane (C3), and *n*-butane (C4) oxidation gas feeds at 270 °C and the simultaneously recorded catalytic data are shown in Fig. 5.1 (b). The total gas flow was adjusted in order to measure the conductivity at similar alkane conversions of ∼4%.

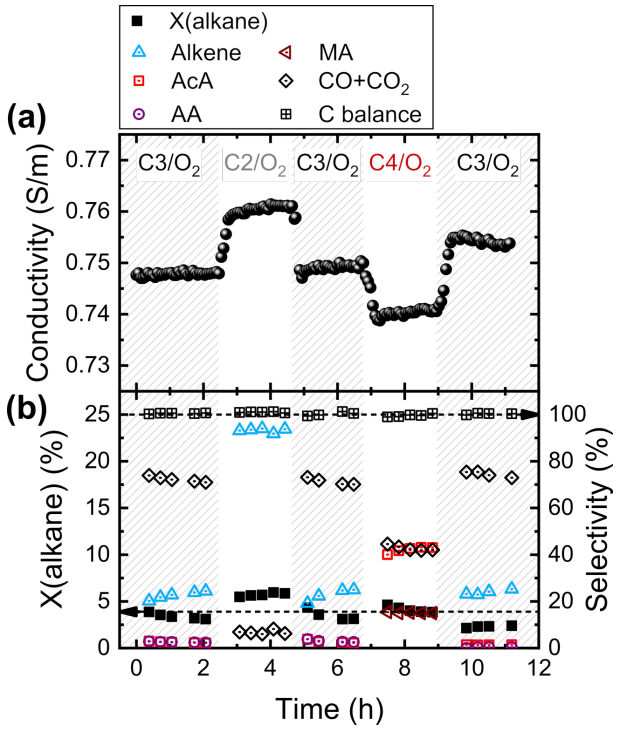

Figure 5.1.: **(a)** MCPT conductivity of MoV-oxide in 3% ethane/propane/*n*-butane, 6% O_2 in N_2 at 270 °C and similar alkane conversions (W/F = 0.18 g·s/ml (C2), 0.57 g·s/ml (C3), 1.3 g·s/ml (C4)); **(b)** catalytic data (alkane conversion, selectivity to alkenes = propene or ethene, acetic acid AcA, acrylic acid AA, maleic anhydride MA, sum of CO and CO_2 selectivities, and carbon balance).

MoV-oxide exhibited a high selectivity towards ethene in the C_2H_6/O_2 gas feed, whereas in the propane oxidation and *n*-butane oxidation gas feeds more of the waste products CO and CO_2 were formed (see Fig. 5.1 (b)). The conductivity decreased with increasing alkane chain length in the order of ethane > propane > *n*-butane, i.e. with an increased number of exchanged electrons during the reactions. The conductivity response of MoV-oxide to more or less reducing gas atmospheres was further investigated by switching from 6% propane / 3% O_2 to 3% propane / 6% O_2 in N_2 at the same contact time showing likewise a conductivity decrease in the more reducing gas feed, which is depicted in the Supporting Information (Fig. C.3). MoVTeNb-oxide showed an opposite behavior with an increase in conductivity from ethane to *n*-butane oxidation gas feeds and also with an increased reduction potential of gas feeds with different propane/O_2 ratios, which was interpreted as n-type semiconducting behavior.[1] The finding of an opposite conductivity response suggests that MoV-oxide is a p-type semiconductor with holes being the majority charge carriers. Even though it crystallizes in the same structure like $MoVTeNbO_x$, i.e. in the orthorhombic M1 phase, the substitution of tellurium by vanadium and of niobium by molybdenum has an impact on the electronic structure. It may be noted that the conductivity response, i.e. the gas-phase-induced conductivity changes, can have different origins as will be discussed later.

The Influence of Steam

The addition of steam to the gas feed has beneficial effects for the propane oxidation to acrylic acid over MoV-based oxides, since both the propane conversion and the selectivity to acrylic acid

are increased.[72] The effect of steam on the semiconducting properties of MoV-oxide was analyzed by switching between "dry" (3% C_3H_8 / 6% O_2 in N_2) and "wet" (3% C_3H_8 / 6% O_2 / 5% H_2O in N_2) propane oxidation gas feeds and monitoring the MCPT conductivity and permittivity and the catalytic performance at 270 °C. The total gas flow was adjusted to investigate the response of MoV-oxide at similar propane conversions of 3.2 to 4.8%. Furthermore, a reference experiment was conducted by switching between dry and wet O_2/N_2 gas feeds in order to determine the effect of steam on the MCPT results without an additional conversion of propane over MoV-oxide. The conductivity and permittivity (ε' and ε'') response is shown in Fig. 5.2 (a), (c), (d) and the catalytic data are summarized in Fig. 5.2 (b).

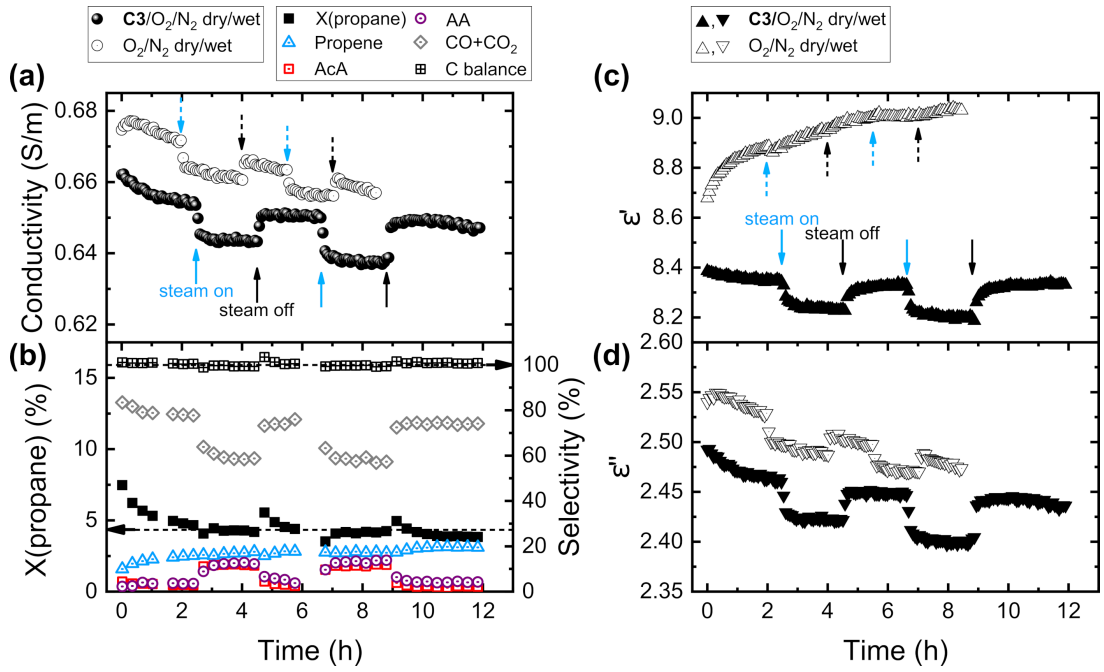

Figure 5.2.: MoV-oxide in 3% propane, 6% O_2, 0 or 5% H_2O in N_2 at 270 °C and similar propane conversions with W/F = 0.80 g·s/ml (dry) and 0.28 g·s/ml (wet) (filled symbols) and reference experiment in 6% O_2 and 0 or 5% H_2O in N_2 (open symbols): **(a)** conductivity changes, **(b)** catalytic performance (propane conversion; selectivity to propene, acetic acid AcA, acrylic acid AA, sum of CO and CO_2 selectivities, and carbon balance), **(c)** response of real part of permittivity ε' and **(d)** response of imaginary part of permittivity ε''.

The conductivity and permittivity of MoV-oxide decreased in the presence of steam. Part of the effect of steam on the conductivity (or ε'') is caused by MoV-oxide and water vapor alone; see the reference experiment in Fig. 5.2 (a) and (d). However, the response of the real part of the permittivity ε' to the addition of steam was only observed in the reaction gas feed, while ε' steadily increased in the reference experiment without any pronounced drop when introducing H_2O(g) (Fig. 5.2 (c)). It should be mentioned that the measurement of the empty reactor using the same experimental protocol, which is always required for determining the "unperturbed" quality factor Q_0 and resonant frequency ω_0 of the microwave cavity, showed no response to the dry/wet cycles thus excluding gas phase H_2O to be the reason for the observed MCPT response.

A slight deactivation was observed during the dry/wet cycles and a small change in the product selectivities (Fig. 5.2 (b)), which could explain the not entirely reversible changes of the conductivity. The influence of steam on the catalytic performance of MoV-oxide from

the *operando* MCPT experiments is in agreement with the literature in terms of an increased selectivity to the acids mainly at the expense of CO and CO_2, as well as an increased activity,[77] which is qualitatively similar to the findings for MoVTeNb-oxide.[72]

Correlations between Conductivity and Catalytic Performance

Previous *operando* MCPT measurements showed a positive correlation between the reactant conversion and the conductivity for the n-type semiconductor V_2O_5[248] and a negative correlation for the p-type vanadyl pyrophosphate[39,248] associated with an increased degree of reduction at higher conversions. Figure 5.3 presents the conductivity response of MoV-oxide to different contact times (W/F of 0.13 to 1.6 g·s/ml) in ethane, propane, and *n*-butane oxidation gas feeds at 270 °C, as well as in a wet propane oxidation gas feed with 5% steam. Further details on the contact time variation experiments including a repetition of the experiments with MoV-oxide (ID 27353) can be found in the SI (Figures C.4–C.9).

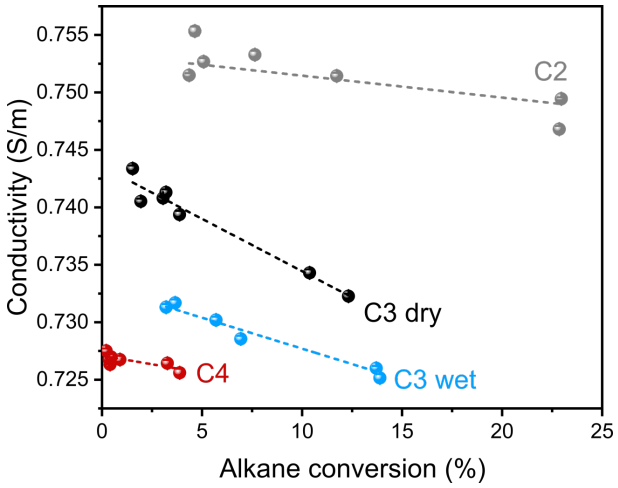

Figure 5.3.: Conductivity of MoV-oxide vs. alkane conversion in 3% ethane/propane/*n*-butane, 6% O_2, 0% (dry) or 5% (wet) H_2O in N_2, 270 °C, at different contact times (0.13 – 1.6 g·s/ml).

The conductivity of MoV-oxide decreased at higher conversions. The previous results with respect to a decrease of the conductivity in the order of σ(ethane) > σ(propane) > σ(*n*-butane) could be confirmed, as well as the lower conductivity in a wet propane oxidation gas feed compared to the dry feed. The catalytic performance is summarized in Fig. 5.4 in terms of selectivity–conversion (S-X) plots.

MoV-oxide was most active in ethane oxidation and least active in *n*-butane oxidation. In ethane/O_2 the oxidative dehydrogenation product ethene was formed with a high selectivity ($\geq$ 90%) over a wide range of conversions, whereas the catalyst was less selective in the oxidation of propane, where the propene selectivity significantly decreased at higher conversions. The addition of steam to the propane oxidation feed lead to a higher activity and a larger amount of the acids with a decreased formation of CO and CO_2. The rather flat S-X curve in the oxidation of ethane may be reflected in the small conductivity changes in this gas feed (cf. Fig. 5.3), i.e. a stable catalytic performance seems to be related to a rather stable conductivity over a wide range of conversions. On the contrary, the product distribution changed considerably in the dry

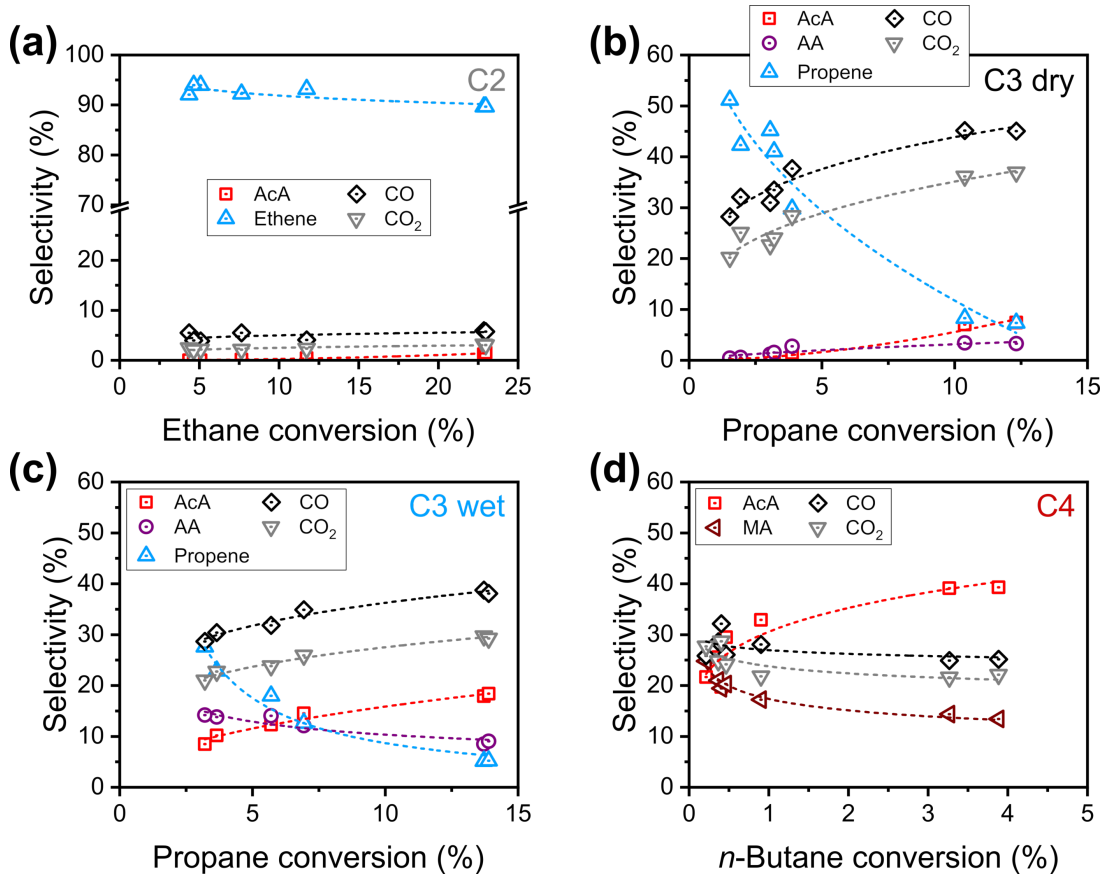

Figure 5.4.: Catalytic data of MoV-oxide from MCPT contact time variation experiments (Fig. 5.3) as selectivity–conversion (S-X) plots at 270 °C in 3% alkane, 6% O_2 in N_2: **(a)** ethane oxidation, **(b)** propane oxidation, **(c)** propane oxidation with 5% steam, **(d)** *n*-butane oxidation. The products were ethene, propene, acrylic acid AA, acetic acid AcA, maleic anhydride MA, CO, and CO_2.

propane oxidation feed, where also the steepest decrease of the conductivity as a function of the alkane conversion was observed.

Temperature Dependence of Conductivity

In order to further investigate the electrical transport mechanism in MoV-oxide, the temperature dependence of the conductivity was measured from 200 to 290 °C in different gas feeds, which corresponds to the catalytically relevant temperature regime, but below 300 °C to avoid catalyst decomposition. The sample was first heated to 270 °C in the respective gas feed and kept for 1 h at this temperature and then it was cycled between low and high temperatures (270 °C (no. 1) → 200 °C → 290 °C → 230 °C → 270 °C (no. 2) → 250 °C). Details on the experimental procedure and the cooling curves can be found in the SI (Figures C.10–C.13). In the following, the steady-state values at the respective temperatures will be shown. Figure 5.5 presents the logarithm of the conductivity of MoV-oxide as a function of the reciprocal temperature and the inset shows the apparent activation energies of conduction E_c in the different gas feeds from the slope of the Arrhenius-type plot. The values recorded at 270 °C, which was measured twice, were found to coincide.

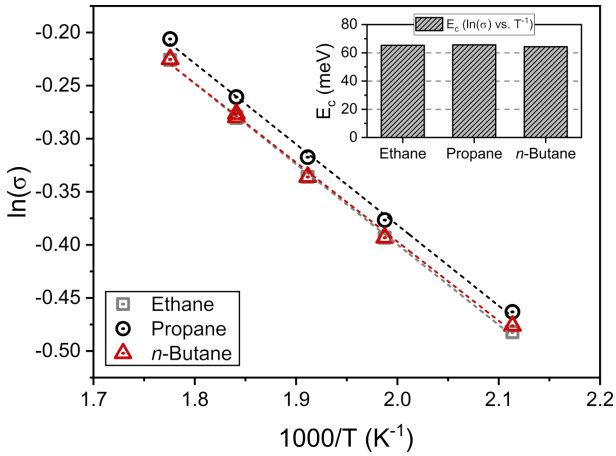

Figure 5.5.: Temperature dependence of conductivity of MoV-oxide (3% ethane/propane/*n*-butane, 6% oxygen in N_2). The inset shows the Arrhenius-type apparent activation energy of conduction.

The conductivity of MoV-oxide increased approximately linear with temperature in the investigated range. The offset of the conductivity in the propane oxidation gas feed could be caused by a difference in the microwave coupling since the temperature-dependent measurements correspond to individual measurements on subsequent days. The Arrhenius-type apparent activation energy of conduction E_c, shown in the inset of Fig. 5.5, was similar in the different gas feeds and amounts to about 0.060 eV. The small activation energy indicates a barrier of an (activated) hopping conduction mechanism or an excitation to(/from) a defect level in the band gap of the semiconductor. In the literature on MoO_3, a theoretical activation energy of 0.08 eV was found for an intralayer hopping conduction[250] and an experimental value of 0.06 eV (1 MHz, 77 to 120 °C),[251] which is in good agreement with MoV-oxide. In other vanadia oxidation catalysts, apparent activation energies of conduction of 0.024 eV for vanadyl pyrophosphate (VPP) and of 0.12 eV for V_2O_5 were found from 30 to 100-150 °C and of 0.23 eV (VPP) and 0.041 eV (V_2O_5) in the high temperature regime 350 to 450 °C (in 2% *n*-butane / 20% O_2 in N_2, TM_{010} mode at ∼3 GHz).[248]

5.4.2. NAP-XPS and NEXAFS

Redox Properties and Surface Composition of MoV-Oxide under Alkane Oxidation Conditions

The redox response and the surface composition of MoV-oxide under different alkane oxidation conditions (ethane, dry and wet propane, *n*-butane oxidation feeds) was investigated with NAP-XPS and NEXAFS spectroscopy. The catalytic performance of MoV-oxide during the NAP-XPS measurements is summarized in Table 5.1. The alkane conversion was below 1% in all gas feeds. MoV-oxide showed a high selectivity towards ethene and propene under the experimental conditions (270 °C, 25 Pa). The product selectivities are similar to the S-X curves from the *operando* MCPT measurements at atmospheric pressure (Fig. 5.4) when extrapolating to lower conversions.

Table 5.1.: Catalytic performance of MoV-oxide recorded with a Micro-GC during the NAP-XPS and NEXAFS measurements in the dry alkane oxidation gas feeds (product selectivities). The alkane conversions were below 1%. Maleic anhydride formation in the *n*-butane oxidation gas feed could be confirmed by the PTR-MS.

Gas feed	Selectivity (%)		
	Alkene	CO	CO_2
C_2H_6/O_2	100	0	0
C_3H_8/O_2	93.1	4.6	2.3
C_4H_{10}/O_2	0.6	92.0	7.4

The core level spectra were measured at two probing depths with estimated inelastic mean free path lengths λ_{IMFP} of 0.6 and 1.7 nm (for additional information see SI, Figures C.14–C.15). Changes in the vanadium oxidation state in different gas feeds were evaluated by fitting the V $2p_{3/2}$ core level with Gaussian-Lorentzian functions representing V^{4+} and V^{5+} components and analyzing their relative contributions to the overall peak area. A constrained fit model was applied that was developed for MoV-oxide (M1) in a previous work by Trunschke *et al.*[77] using one 4+ component and two 5+ components (as described in Table C.1 in the SI), where the second V^{5+} (II) species was ascribed to surface vanadium species originating from the migration out of the hexagonal channels in the M1 crystal structure (M12 position).[77] The results of the V $2p_{3/2}$ core level analysis in terms of gas-phase-induced changes in the average vanadium oxidation state and in the relative contributions of the different vanadium species (V^{4+}, V^{5+} (I), and V^{5+} (II)) to the overall V $2p_{3/2}$ peak are presented in Figure 5.6 as time on stream plot. It may be noted that for an estimated inelastic mean free path length of 1.7 nm most of the photoelectrons are released from this depth which includes, of course, the photoelectrons originating from the surface region.

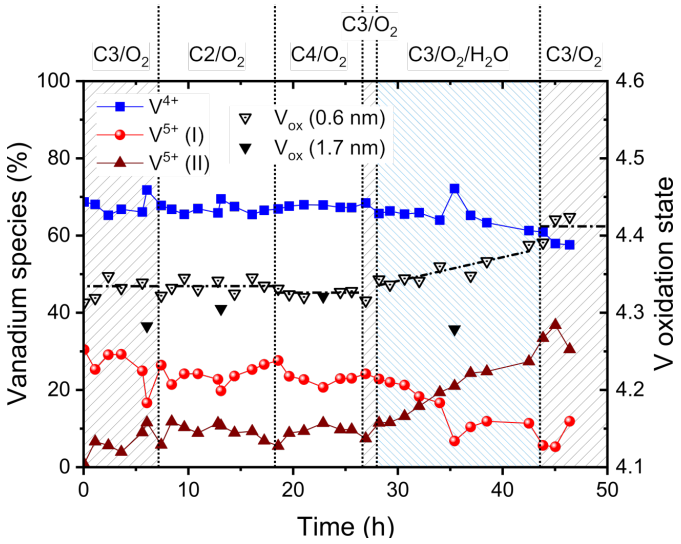

Figure 5.6.: Relative amount of V species determined from a fit of the V $2p_{3/2}$ core level with one 4+ and two 5+ components and vanadium oxidation state V_{ox} at λ_{IMFP} = 0.6 and 1.7 nm.

In the dry alkane oxidation feeds the average vanadium oxidation state was ~4.3 and it increased to 4.4 by the treatment of MoV-oxide in the steam-containing gas feed in the surface

sensitive V $2p_{3/2}$ measurements. In contrast to this, the oxidation state in deeper layers (λ_{IMFP} of 1.7 nm) remained rather constant at 4.3 in all gas feeds. Most notably, the addition of steam lead to a change of the relative amounts of the two V^{5+} components with the V^{5+} (II) species becoming the prominent 5+ species. This agrees with findings in the literature for MoV-oxide (M1),[77] MoVTeNb-oxide (M1),[77] and vanadyl pyrophosphate.[123] The influence of the gas atmospheres on the surface composition of MoV-oxide was investigated based on a quantitative analysis of the V 2p and Mo 3d core levels at similar photoelectron kinetic energies (λ_{IMFP} of 0.6 and 1.7 nm). Figure 5.7 depicts the evolution of the vanadium and molybdenum atom-% on the basis of the metal concentration. At the beginning ~24% V and ~76% Mo were found, while after the treatment in the wet propane oxidation feed 33% V and 67% Mo were observed. The different alkanes exhibited only a minor influence on the surface composition.

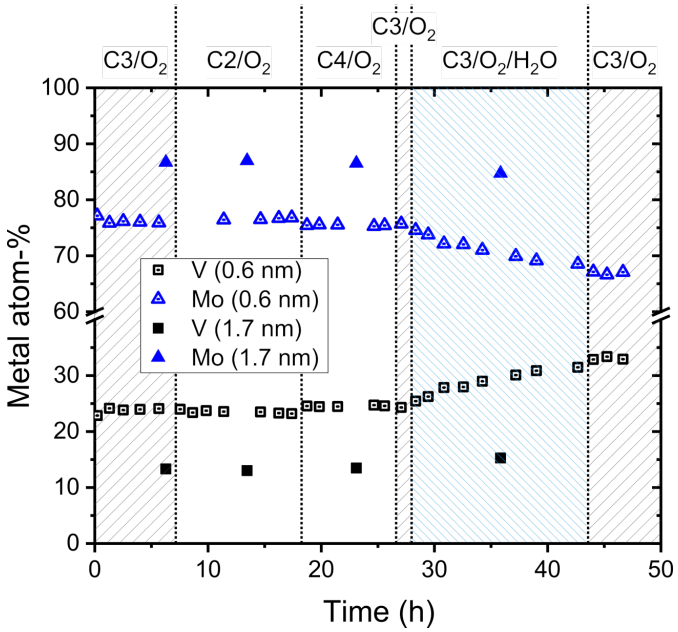

Figure 5.7.: Vanadium and molybdenum atom-% at two probing depths (λ_{IMFP} = 0.6 and 1.7 nm) from quantitative analysis of V 2p and Mo 3d core levels.

Major changes in the average vanadium oxidation state and in the surface composition of MoV-oxide were only observed by the addition of steam to the gas feed, which lead to an enrichment of V^{5+} on the surface and a decrease of the relative Mo content (Fig. 5.7). The changes in the core level spectra were irreversible, i.e. re-applying the dry propane oxidation gas feed did not decrease the V^{5+} (II) contribution, in agreement with the findings by Trunschke *et al.*[77] In the last dry propane oxidation gas feed, the ongoing surface changes that were observed in the wet feed came to a halt and MoV-oxide exhibited a higher V/Mo ratio than before. There might also be small changes of the surface composition in the different dry alkane oxidation feeds with a higher V/Mo ratio with increasing alkane chain length in the order ethane < propane < *n*-butane, even though these changes were rather small. Vanadium atom-% of 24.0 ± 0.1% in C_3H_8/O_2 (1), of 23.5 ± 0.3% in C_2H_6/O_2, of 24.6 ± 0.1% in C_4H_{10}/O_2, and of 24.3% in C_3H_8/O_2 (2) were observed (average value ± one standard deviation). Deeper layers of MoV-oxide responded less sensitive to the gas atmospheres including the wet feed.

The effect of the different gas atmospheres on a peak above the valence band onset at

$E_{\text{bind}} \approx 1.6$ eV was investigated (see Fig. 5.8 (b)), which was analyzed by fitting the peak with a Gaussian curve. The results of the fit are presented in Fig. 5.8 (a) as time on stream plot of the peak area.

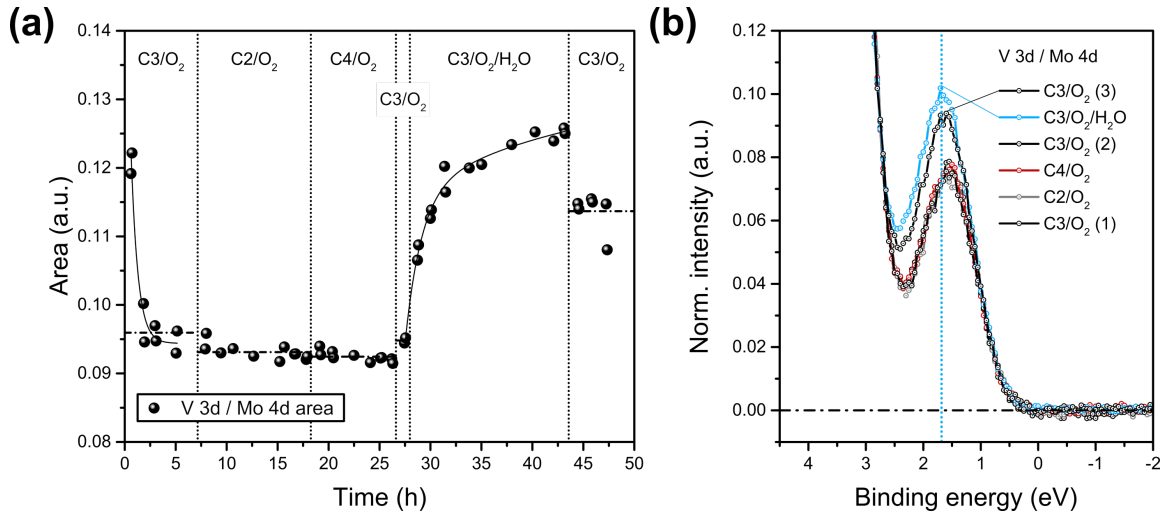

Figure 5.8.: **(a)** Evolution of V 3d peak area of MoV-oxide as a function of time on stream (25 Pa, 270 °C) in different gas feeds; **(b)** example spectra.

The peak at $E_{\text{bind}} \approx 1.6$ eV is characteristic for occupied V 3d states, see vanadium oxides with 3d electrons including non-stoichiometric V_2O_{5-x},[156,184] vanadyl pyrophosphate,[42] and $MoVTeNbO_x$.[1,105,252] Additionally, also Mo 4d states can contribute to the peak, e.g. in defective MoO_{3-x}.[252–255] Given the major contribution of V^{4+} with an average V oxidation state always below 4.5 and the dominant contribution of Mo^{6+} as seen in the core level spectra, it may be assumed that this peak is mainly caused by occupied V 3d levels (henceforth named "V 3d"). It can be seen from Figure 5.8 that the V 3d peak area increased in the steam-containing $C_3H_8/O_2/H_2O$ gas feed pointing towards an increased occupancy of the d states. This is an interesting observation since the core level analysis showed an overall surface *oxidation* in this gas feed (cf. Fig. 5.6). It may be noted that steam mainly led to a surface enrichment of the V^{5+} (II) species, which was ascribed to extra-framework vanadium originating from the migration out of the hexagonal channels to the surface,[77] whereas the concentration of the V^{5+} (I) species even decreased. The relative amount of V^{4+} (compared to the other V species from the V $2p_{3/2}$ fit as seen in Figure 5.6) was not significantly affected by the different gas feeds. Hence, the increase in the average vanadium oxidation state in the wet propane oxidation gas feed was mainly associated with the enrichment in the V^{5+} (II) species.

The Influence of Steam on the Surface Electronic Structure

In the following, the influence of steam on the surface electronic structure of MoV-oxide will be discussed in more detail. The work function Φ of MoV-oxide was analyzed in different gas feeds. The linear extrapolation of the secondary electron cutoffs is shown in Figure 5.9 (a) on an "apparent" binding energy scale for the last cutoff measurements in the respective gas feeds and the work function is presented in Figure 5.9 (b) as time on stream plot.

The work function of MoV-oxide was found to be about 6.7 eV in the dry alkane oxidation gas

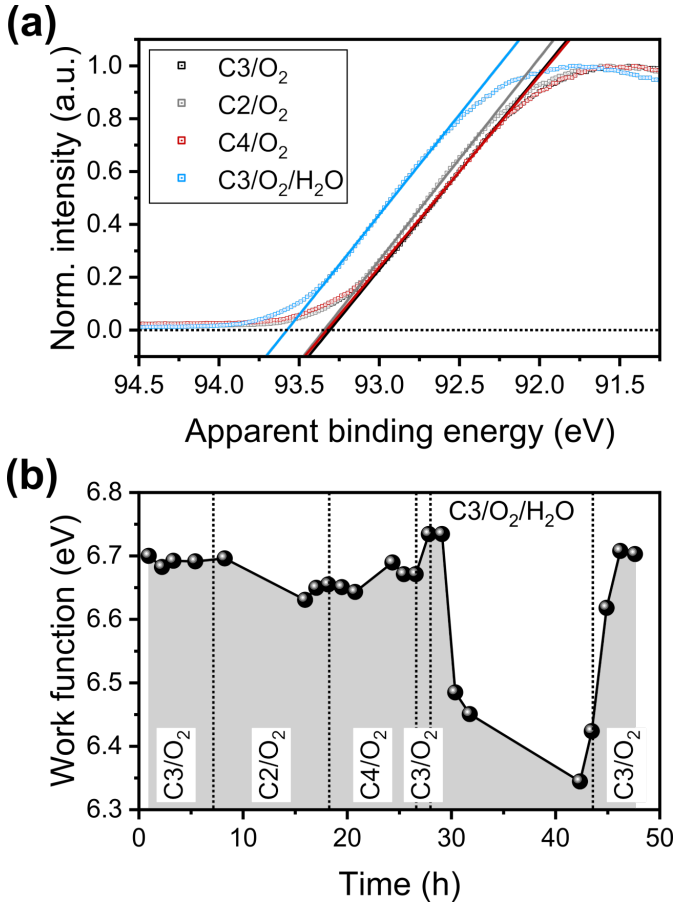

Figure 5.9.: **(a)** Secondary electron cutoff of MoV-oxide at $E_{h\nu} = 100$ eV in different gas feeds and leading-edge extrapolation (last measurements in respective feed); **(b)** work function as a function of time on stream (25 Pa, 270 °C).

feeds. This is similar to the work functions of $MoVTeNbO_x$ (M1) (6.3 to 6.7 eV),[1,105] of vanadyl pyrophosphate (6.8 to 6.9 eV),[42,123] and of V_2O_5 (6.5 to 6.6 eV) determined in the same way, or of MoO_3 (6.86 eV) determined with UPS measurements.[256] In the dry ethane/propane/*n*-butane oxidation gas feeds only small changes of the work function of MoV-oxide were observed, e.g. a small shift of the cutoff to higher energies in the C_2H_6/O_2 gas feed (gray curve). However, significant changes were found in the presence of steam (blue curve in Fig. 5.9) showing a decrease of the work function in the order of 200 meV between the dry C_3H_8/O_2 feed and the wet $C_3H_8/O_2/H_2O$ feed. The valence band onset and the core level binding energies did not shift to the same extent, which would be the case for a change in band bending ($e\Delta V_s$). Hence, it is assumed that the work function changes in the steam-containing gas feed are dominated by changes of the electron affinity ($\Delta\chi$) according to $\Delta\Phi = \Delta\chi - e\Delta V_s$ due to a changed surface dipole.

Figure 5.10 compares the valence band spectra recorded in the dry propane oxidation gas feed and in the wet propane oxidation gas feed, which were normalized to the background at 30 eV. The changes are clearly shown in the difference spectrum at the bottom of Figure 5.10.

Given the expected partial covalent bonding character and the contribution of metal d states to the high binding energy range of the valence band,[78,81,105,156] an increased covalency could play a role in the observed changes in the valence band spectra. This may be related to an enrichment

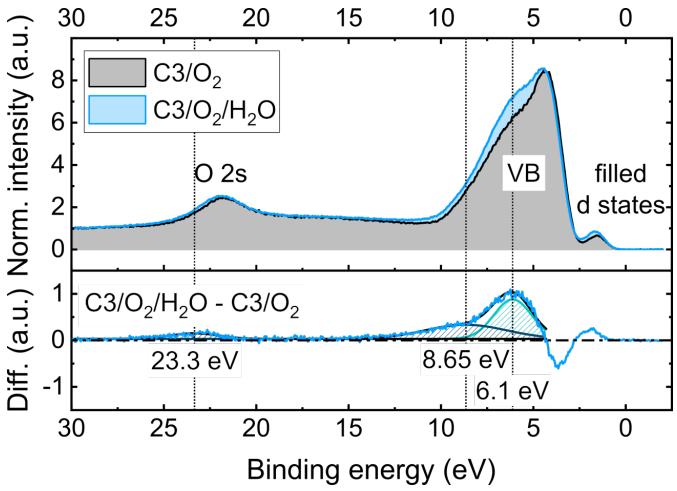

Figure 5.10.: Valence band spectra of MoV-oxide in dry and wet propane oxidation gas feeds and difference spectrum Int($C_3H_8/O_2/H_2O$) – Int(C_3H_8/O_2) (270 °C, 25 Pa, $E_{h\nu}$ = 100 eV).

in a V^{5+}-oxide on the surface of MoV-oxide in view of the increased covalency in vanadium oxides with a higher V oxidation state.[78,82,257] Another explanation is the chemisorption of water on MoV-oxide and an increased coverage with OH groups. The peak positions in the valence band difference spectrum in Figure 5.10 (∼6.1, 8.65, and 23.3 eV) are in good agreement with literature values for the surface hydroxylation of various metal oxides.[258–263] This could also well be responsible for the decrease of the work function of MoV-oxide.

Figure 5.11 presents the O 1s core level spectra of MoV-oxide in different gas feeds at two probing depths (λ_{IMFP} of 0.6 and 1.7 nm), which were fitted with two components O(1) and O(2) (at 1.2 eV higher binding energies; for details see Table C.2 in SI). The high binding energy shoulder "O(2)" of the main peak increased in the steam-containing gas feed.

When interpreting the intensity increase in the valence band region and at the high binding side of the O 1s core level in the steam-containing feed as due to an increased surface hydroxylation, one has to be careful because of an overlap with other features. An unambiguous assignment of this shoulder O(2) of the O 1s peak is in many cases not possible because of overlapping contributions from "surface oxygen" species and adsorbed oxygen-containing carbon species,[264–266] in addition to satellite lines from V $2p_{1/2}$ and V $2p_{3/2}$.[78,185,186,257] In the present study a C 1s signal appeared in the wet propane oxidation feed (see Fig. C.16 in the SI). Adsorbed H_2O is usually reported at larger chemical shifts (higher binding energies),[264–268] which was not observed on MoV-oxide. The intensity increase in the O 2s region of MoV-oxide at about 23.3 eV should not overlap with satellites and is thus supporting the interpretation of an increased coverage with hydroxyl groups. Hence, it is likely that the increase in intensity in the steam-containing propane oxidation gas feed in the valence band region between 4.3 to 14 eV, in the O 2s region at ∼23.3 eV, and at the high binding energy side of the O 1s core level peak at ∼531.8 eV is due to the formation of or increasing coverage with OH groups on the MoV-oxide surface.

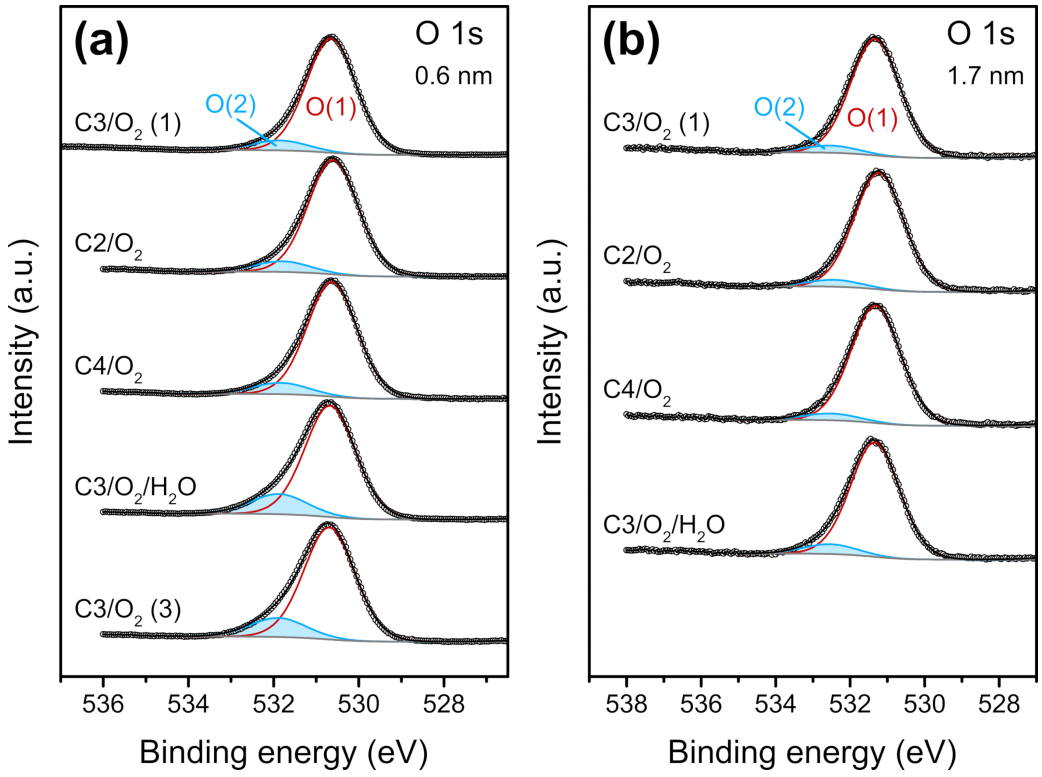

Figure 5.11.: Changes in MoV-oxide O 1s core level in different gas feeds fitted with two components O(1) and O(2): **(a)** $\lambda_{\mathrm{IMFP}} = 0.6$ nm, **(b)** $\lambda_{\mathrm{IMFP}} = 1.7$ nm.

5.5. Discussion

5.5.1. On the Origin of the Conductivity or Permittivity Response

The data clearly show that the electrical conductivity of MoV-oxide, determined with an *operando* MCPT method, responded sensitively to changes in the gas phase, even to the small changes associated with different contact times and hence reactant conversions and product selectivities. It may be assumed that there is no simple relation between e.g. the conductivity and the partial pressure of oxygen, which is frequently observed for semiconducting metal oxide gas sensors. The conductivity is rather a function of the chemical potential of the surrounding atmosphere, which affects the surface overlayer on MoV-oxide and surface oxidation states. Hence, the charge carrier density (or the degree of reduction) is influenced by (i) the alkane chain length, (ii) the reactant conversion with an increased catalyst reduction at higher conversions, and (iii) the selectivities to the different reaction products. The product distribution depends both on the reaction, i.e. it is different for the oxidation of ethane, propane (dry/wet), and *n*-butane, and on the reactant conversion, where an increased formation of the undesired oxidation products acetic acid, CO, and CO_2 occurs at higher conversions. A reasonable explanation for the largest conductivity changes in the dry propane oxidation feed is the associated largest change in the product distribution and hence in the number of exchanged electrons at different contact times; compare to the S-X plots in Fig. 5.4. Not only is the higher propane conversion itself related to an increased reduction of the catalyst, but also the decrease of the selectivity to propene and the increased formation of CO and CO_2 (and of the acids) (Eqs. (5.2) – (5.4)). This is suggested to be the reason for the conductivity decrease of the p-type semiconductor MoV-oxide at higher

reactant conversions and enhanced carbon oxide formation.

$$2\ C_3H_8 + \ O_2 \longrightarrow 2\ C_3H_6 + 2\ H_2O \qquad \text{(formally 4 } e^- \text{ transferred)} \tag{5.2}$$

$$2\ C_3H_8 + \ 7\ O_2 \longrightarrow 6\ CO + 8\ H_2O \qquad \text{(formally 28 } e^- \text{ transferred)} \tag{5.3}$$

$$2\ C_3H_8 + \ 10\ O_2 \longrightarrow 6\ CO_2 + 8\ H_2O \qquad \text{(formally 40 } e^- \text{ transferred)} \tag{5.4}$$

In the oxidation of ethane over MoV-oxide the main product was ethene even at high conversions. The rather flat S-X curve can likewise serve as explanation for the small conductivity changes at different contact times in this gas feed.

Concerning the origin of the changes of the permittivity ($\tilde{\varepsilon} = \varepsilon' - i\varepsilon''$) or electrical conductivity (σ) in MoV-oxide, changes in the conductivity are likely caused by a change in the number of charge carriers n or in their mobility μ, i.e. $\Delta\sigma = e\ (\mu\ \Delta n + n\ \Delta\mu)$. It is usually assumed that the charge carrier concentration plays a major role in the conductivity change ($\Delta\sigma \propto \Delta n$).[40] The first and kinetically relevant step in the oxidation of propane, the abstraction of a hydrogen atom, for instance, may be associated with a consumption of holes explaining the observed conductivity decrease at higher conversions. The conductivity is related to the imaginary part of the permittivity ε'' (cf. Eq. (5.1)), which represents the energy loss.[106] A significant contribution of ionic conductivity to ε'' in the microwave frequency range is unlikely to occur, because of the higher mass of the ions compared to electrons or holes.[39] Changes in the charge carrier concentration can also occur in the surface or subsurface region. In case of a space-charge-layer-modified conductivity response e.g. due to changes in the surface termination layer, the charge carrier density in the subsurface space charge region is affected. The conductivity as a function of the coordinate x pointing away from the surface (at $x = 0$) into the bulk then changes according to Eq. (5.5), where $eV(x)$ denotes the band bending at position x with e being the elementary charge and k and T are the Boltzmann constant and temperature, respectively.[99]

$$\sigma(x) \approx e\,\mu_h\,n_h(x) = e\,\mu_h\,n_h(\text{bulk})\,\exp\left(-\frac{eV(x)}{kT}\right) \tag{5.5}$$

When it comes to the methodology, i.e. to the microwave cavity perturbation measurements, care must be taken when interpreting the response of ε'. In the vicinity of the depolarization peak, which is observed for higher conductivities and large conductivity changes, the MCPT frequency shift would be related to both ε' and ε'' as well as to geometric factors of the sample[138] and considerable changes of the frequency shift are expected.[269] It should be kept in mind that the interpretations are made under the assumption that the change of the frequency shift is dominated by the response of ε' of the sample. The real part of the permittivity ε' describes the energy storage.[106] The contribution surface dipoles is generally recognized as being an important factor for the response of ε' in transition metal oxides.[104,108,110,118] Additionally, defects as polarization sources, for instance oxygen vacancies,[121,270] and their influence on ε' have frequently been discussed.[108,110,112,118] Another contribution to ε' may arise from dielectric relaxation via a dipole reorientation by "discrete jumps" associated with mixed-valent metal ions.[140,270,271] In a similar way, one could think of a contribution of V^{4+}/V^{5+} pairs in MoV-oxide to the dielectric relaxation ($V^{4+} + h^+ \leftrightarrows V^{5+}$), also to the energy storage. Such a hopping process of course also contributes to the loss and hence to ε''. It is assumed that the most important

mechanisms leading to the changes in ε' in MoV-oxide e.g. between the dry and the wet propane oxidation gas feed or with increasing reactant conversion are reaction- or adsorption-induced changes in the surface dipole (changes in the surface termination layer, surface oxidation states, coverage with different adsorbates or OH groups) or in the number of V^{4+}/V^{5+} centers. It should be stressed that a *decrease* of ε' of MoV-oxide was observed e.g. at higher reactant conversions, which renders the interpretation in terms of less defects unlikely, but a decrease of the surface dipole might still occur. Since the changes in ε' and in ε'' were always found to be in the same direction, it is concluded that they are correlated and have a common origin in MoV-oxide.

5.5.2. Comparison of MoV-Based Oxide Catalysts

In this section, differences in the (electronic) structure and the semiconducting properties of MoV-oxide and MoVTeNb-oxide will be discussed in view of their opposite conductivity response, which may be explained by a p-type behavior of the former and an n-type behavior of the latter. Besides MoVTeNb-oxide (M1 phase),[1] also MoVTeNb-oxide (M2 phase)[272] and MoVSbNb-oxide (M1 phase)[273] were found to exhibit n-type conduction behavior. This indicates that the additional elements, Te or Sb and Nb, have an impact on the electronic structure.

First of all, there are the differences in the chemical composition of these mixed-metal oxides. In the orthorhombic M1 structure (ICSD 55097)[69,70] of MoVTeNb-oxide, Nb^{5+} substitutes molybdenum in the pentagonal bipyramids (M9 position), and $Te^{4+}(Te^{6+})$ partly occupies the hexagonal channels (M12 position) under the formation of tellurium oxide chains.[68–70,274] In these hexagonal channels extra-framework vanadium was observed in MoV-oxide.[77] In the distorted octahedral linker positions (M1, M3, M4, M7 sites) a mixed Mo and V occupancy was found, while the other "octahedral" sites (M2, M5, M6, M8, M10, M11) are occupied by Mo in both $MoVTeNbO_x$ and in $MoVO_x$.[68–70,77,275]

At first glance, no major differences are observed between the p-type MoV-oxide (M1) and the n-type MoVTeNb-oxide (M1)[105] regarding their valence band structure. Still, the conduction band structure, for instance, might be different to some extent. The n-type semiconducting behavior of many transition metal oxides is believed to be caused by an oxygen deficit (non-stoichiometry) and the related formation of shallow donor levels close to the conduction band minimum.[276–281] Conversely, the opposite factors should be favorable for p-type metal oxide semiconductors, in particular the formation of shallow acceptor levels close to the valence band onset,[279,282] which is favored by a low ionization potential of the semiconductor.[280,282] P-type behavior is frequently observed for oxides where there exists a stable higher oxidation state of the metal ion or a (partially) filled d shell which lies close to the O 2p energy,[276,277,279,282] for instance V^{4+} in MoV-oxide, which can be readily oxidized to V^{5+}. Vanadium is considered here as an important element, because it is the main redox-active cation in these catalysts. Both MoVTeNb-oxide and MoV-oxide have a mixed vanadium oxidation state, however, in MoV-oxide V^{4+} is the main surface (or near-surface) vanadium species (oxidation state < 4.5 like in the p-type VPP catalyst[39,42,123]). The formation of V^{5+} in MoV-oxide could be related to the creation of acceptor states leading to the p-type behavior by introducing holes in the valence upon thermal emission, in line with the suggestions for vanadyl pyrophosphate.[39,60] In MoVTeNb-oxide, on the other hand, vanadium occurs mainly in its highest oxidation state

5+ at the surface (V oxidation state > 4.5).[1] This may be compared to the n-type V_2O_5 (or V_2O_{5-x}), where defect levels introduced by the non-stoichiometry and the related V^{4+} formation can form donor levels close to the conduction band.[85] Other V^{5+} compounds like the different vanadyl phosphates $VOPO_4$ are likewise n-type semiconductors.[283] Similarly, MoO_3 exhibits n-type behavior due to oxygen vacancies associated with partially occupied Mo 4d states (non-stoichiometric MoO_{3-x}).[284–287] For both binary oxides a polaron conduction mechanism was suggested.[218,219,222,223,250] An activated mobility is also likely to occur in MoV-oxide, which was shown by the apparent activation energy of conduction. Furthermore, the partial covalent bonding character in MoV-oxide should be favorable for the charge carrier mobility in view of the smaller effective mass of charge carriers upon an enhancement of the covalency.[278–281,288]

Regarding the overall surface composition, the vanadium content is higher in MoV-oxide (∼24% V; V/Mo ratio of 0.32) than in MoVTeNb-oxide (∼15% V; V/Mo ratio of 0.27[1]), which could be related to the lower selectivity of MoV-oxide. In particular an accumulation of vanadium in its highest oxidation state 5+ might enhance combustion reactions. A comparison of the V^{5+} surface content of the catalysts shows however a slightly lower amount of V^{5+} on MoV-oxide (∼7.9% V^{5+} on $MoVO_x$ compared to 8.7% V^{5+} on $MoVTeNbO_x$[1]) due to the lower average surface vanadium oxidation state. Both oxides show a (slight) decrease in the average vanadium oxidation state with increasing alkane chain length from ethane to *n*-butane,[1] which is in line with the increased number of electrons transferred in the oxidation of longer chain alkanes.

Tellurium was suggested to be an essential component of the selective MoVTeNb-oxide catalyst taking part in the alkane activation[74] or in consecutive steps of the reaction.[68,289] Furthermore, surface Te species may be important for achieving an efficient site isolation and may hence be crucial for the selectivity of the multi-component catalyst.[15,77] These factors can contribute to the inferior catalytic performance of MoV-oxide compared to MoVTeNb-oxide. In addition, the occupation of the hexagonal channels by either vanadium or tellurium can have implications for their respective electronic properties. Besides the application of tellurium compounds in heterogeneous catalysis, tellurides are frequently used in electronic applications (e.g., solar cells, thermoelectric materials, and optical storage media).[290,291] There are reports of n-type semiconducting mixed-metal tellurium oxides[292] and of Te-doped n-type In_2O_3, which leads to an altered conduction band structure but with a poor doping effectiveness.[293] Tellurium-doping was also applied to enhance the p-type conductivity[294] of other metal oxides when substituting oxygen, e.g. in $CuAlO_2$, where it leads to a decrease of the band gap and increased covalency.[295,296] Recently, it was proposed that the reduction and subsequent emission of tellurium from the hexagonal channels in the M1 structure in the course of the oxidation reaction creates reactive O^- species which are involved in the alkane activation (similar to the vanadyl species $V^{5+}{=}O \leftrightarrow V^{4+}{-}O^-$).[297] Importantly, the authors indicated that the removal of Te might ultimately change the semiconducting properties from n-type (with Te) to p-type (without Te) based on DFT calculations.[297] The present study can be taken as first experimental evidence which verifies the opposite semiconducting properties of M1 catalysts with and without tellurium. While the localization of a hole creating an electrophilic O^- species may contribute to the reactivity of the catalyst, the p-type conductivity of MoV-oxide does not seem to be favorable for the catalytic performance, in particular for the selectivity. Yet, other factors as mentioned

above (e.g., the site isolation concept) may contribute to the lower selectivity. The different semiconducting properties of MoV-oxide compared to MoVTeNb-oxide can have implications for their respective catalytic properties, for instance regarding the oxygen activation or alkane activation. It is thought that the oxygen activation is facilitated on n-type transition metal oxide catalyst, i.e. is favored by a high-lying Fermi level, while the C-H activation might require a low-lying Fermi level.[95] Generally, the availability of free electrons or holes will be different, which may influence their catalytic properties. In this context it is interesting to note that the catalytic performance of MoV-oxide in the dry and wet propane oxidation is more similar to the one of vanadyl pyrophosphate[123] than to MoVTeNb-oxide; the latter showing a higher selectivity towards propene in the dry propane oxidation feed and a higher selectivity to acrylic acid in the wet feed.[72]

As was discussed above (with the MCPT being taken as highly sensitive integral method), the opposite conductivity response of MoV-oxide and MoVTeNb-oxide to different alkane oxidation gas feeds could originate from changes in the surface–subsurface region or in the bulk conductivity. In case of a gas-phase-induced change of the surface charge or surface termination layer, it is likely that a change in band bending occurs shifting the relative positions of the valence band and conduction band onset and of surface states with respect to the Fermi level. This would affect the electron distribution (occupation of valence band, conduction band, and surface states) and the barrier height for bulk–surface charge transfer. In the NAP-XPS experiments, a change in band bending would manifest itself in an energy shift of the entire photoelectron spectrum, i.e. in a consistent shift of the valence band and core level binding energies as well as of the work function.[101] These experiments revealed another important difference between MoV-oxide and MoVTeNb-oxide. The negligible effect of the alkane chain length on the work function or valence band onset of MoV-oxide leads to the conclusion that no change in band bending occurred between the different dry alkane oxidation gas feeds. This is in contrast to MoVTeNb-oxide, where energy shifts of 0.08 to 0.2 eV for $\Delta\Phi$ and of up to 0.08 eV for the valence band onset and core level binding energies were reported between ethane and *n*-butane oxidation feeds.[1] The observed linear correlation between conductivity and work function strongly supported the interpretation of a space-charge-layer-modified conductivity response in the case of MoVTeNb-oxide.[1] On the other hand, there is no correlation between work function changes and electrical conductivity changes in MoV-oxide. This result further strengthens the hypothesis that selective catalysts like MoVTeNb-oxide or VPP exhibit a dynamic gas-phase-dependent surface potential barrier, which is thought to control the charge transfer between the catalyst bulk and the adsorbed reactants.[42] The behavior of MoV-oxide is similar to that of the unselective V_2O_5, which also showed only small effects of the gas phase on the electronic structure.[42] The missing "control function" for charge transfer via a band bending (surface potential barrier) that sensitively adapts to the chemical potential of the surrounding atmosphere may be linked to the rather low selectivity of MoV-oxide.

5.5.3. The Influence of Steam

The permittivity response of MoV-oxide in the dry/wet propane oxidation cycles can be understood in terms of water chemisorption and changes of the catalyst surface such as changes in the

oxidation states and the surface composition including surface hydroxylation. Furthermore, the chemical potential of the gas phase changes between the dry and the wet propane oxidation gas feeds also due to a different product distribution (different selectivities). This will probably affect the conductivity of MoV-oxide as well. Neither dielectric relaxation from mobile multilayers of water, nor proton conduction are likely to play a role in MoV-oxide, first of all because a *decrease* of the conductivity and of ε' was observed in a wet propane oxidation feed. In addition, a higher real part of the permittivity would only be expected for more or less mobile physisorbed multilayers of water[298] that can re-orient with the microwave field and a significant contribution of proton conductivity was only observed on metal oxides at room temperature and below, because of the desorption of water a higher temperatures.[272,299–303]

The additional chemical modification of the surface of MoV-oxide, which was shown by NAP-XPS, complicates the interpretation of the conductivity response. The addition of steam lead to the formation of a surface termination layer enriched in V^{5+} and hence to a semiconductor- or insulator-semiconductor heterostructure between the MoV-oxide (M1) bulk and this interface. A growing shoulder in the valence band spectra, like in the present study, was also observed for MoVTeNb-oxide (M1).[105] The binding energy of this shoulder below ∼6 eV agrees well with the formation of OH groups, which is supported by an increase in the O 2s emission and at the high binding energy side of the O 1s core level. Hence, also an increased surface hydroxylation and modified acid-base properties may play a role in the formation of the active surface layer, but also, for instance, for the modified surface polarity, which is suggested to be the reason for the decrease of the work function and the real part of the permittivity of MoV-oxide. The changes in the surface termination layer and in the occupation of the V 3d level are likely to affect the electrical conductivity as well. In contrast to the irreversible changes in the core level spectra, the work function changes were found to be reversible and the V 3d area at least partly decreased by the subsequent treatment in a dry propane oxidation feed.

The conductivity or permittivity changes of MoV-oxide in the dry/wet cycles were found to be rather reversible, although a slight decrease of the conductivity (and ε'') with time on stream was observed. Since a decrease of the MCPT conductivity in a steam-containing propane oxidation feed was not only observed for MoV-oxide, but also for the n-type MoVTeNb-oxide (M1 phase)[105] and for the p-type vanadyl pyrophosphate,[123] a change in the charge carrier density is unlikely to play a dominant role. Hence, the charge carrier mobility μ could be decreased. The conductivity changes of MoV-oxide were also observed in the reference experiment without propane in the gas feed. A hydrolysis of the V–O bonds in the hexagonal channels of MoV-oxide (M12 position in the M1 phase) followed by the migration to the surface and the creation of a V^{5+}-enriched termination layer might also occur in the $O_2/H_2O/N_2$ gas feed at 270 °C. Likewise, also an increased hydroxyl coverage of the MoV-oxide surface seems reasonable. Hence, it is not surprising that ε'' or the conductivity also show a response to the dry/wet cycles in the reference experiment. It is interesting, though, that this is not the case for the real part of the permittivity, which showed a response only to dry/wet cycles in a propane oxidation feed (cf. Fig. 5.2 (c)).

5.6. Conclusions

We have presented electrical conductivity and permittivity investigations of MoV-oxide (M1 phase) under dry and wet alkane oxidation conditions based on an *operando* MCPT method, which were complemented by the characterization of the electronic structure and surface composition with NAP-XPS.

It is suggested that MoV-oxide behaves as a p-type semiconductor. The conductivity is a sensitive function of the chemical potential of the surrounding atmosphere, which is also affected by the conversion level. Temperature-dependent measurements showed a small apparent activation energy of conduction, which is indicative for an activated hopping conduction mechanism or for the excitation from the valence band to acceptor levels in the band gap of MoV-oxide.

Despite the similarity between MoV-oxide and the multi-component MoVTeNb-oxide, which both crystallize in the orthorhombic M1 structure, the partial substitution of vanadium by tellurium and of molybdenum by niobium leads to changes in the electronic structure of the two catalysts and ultimately to reversed conduction properties. This is likely to affect their catalytic properties as well via a changed availability of either free electrons or holes. It appears that the occupation of the d states and their relative position with respect to the valence band maximum or conduction band minimum plays an important role in determining the semiconducting properties of these oxides. The changed occupation of the hexagonal channels by either tellurium or vanadium may be related to the n-type or p-type conductivity, respectively. Unlike MoVTeNb-oxide,[1] no change in band bending depending on the alkane chain length was observed in MoV-oxide and hence no indication of a space-charge-layer-modified conductivity response. The lack of a dynamic (gas-phase-dependent) surface potential barrier in unselective oxidation catalysts may be related to their (poor) catalytic performance due to an insufficient control of charge transfer to adsorbed reactants.

The addition of steam to a propane oxidation feed lead to a decrease of the MCPT conductivity of MoV-oxide, which is not entirely reaction-induced. Yet, the real part of the permittivity, ε', only showed a response to the dry/wet cycles in reaction gas feeds. NAP-XPS showed an irreversible formation of a V^{5+}-enriched surface termination layer in addition to an increased surface hydroxylation. Surprisingly, also an increased occupancy of the d states was observed. Furthermore, a major decrease of the work function by about 0.2 eV was found, which is proposed to be primarily caused by a modification of the surface dipole in line with the decrease in the real part of the permittivity. The formation of the surface termination layer may be described by a semiconductor- or insulator-semiconductor heterostructure between the MoV-oxide (M1) bulk and this interface. An increased selectivity towards acrylic acid was observed upon creation of this termination layer. Taken together, our results show that changes in the surface termination play an important role in the gas-phase-induced conductivity changes of MoV-oxide and are likely affecting its catalytic performance.

6. Overview of Vanadia Oxidation Catalysts

In the following, the electronic structure of four vanadia oxide catalysts (V_2O_{5-x}, vanadyl pyrophosphate VPP, MoVTeNb-oxide (M1), and MoV-oxide (M1)) will be compared under alkane oxidation conditions. The aim is to get a better understanding of differences in their electronic structure and to elucidate possible implications for the selective oxidation of light alkanes. These differences could also be linked to their respective semiconducting properties (the former two being p-type semiconductors, the latter two n-type semiconductors). This work is based on results from previous investigations of VPP[42] and MoVTeNb-oxide[1] in our group, in combination with the results from the present thesis on the electronic structure (from NAP-XPS) and the semiconducting properties (MCPT) of V_2O_{5-x} and MoV-oxide. Figure 6.1 shows the valence band spectra of the samples in *n*-butane/O_2 gas feeds at elevated temperatures measured with NAP-XPS. A continuous shift of the valence band onset and of the peak of the filled d states to higher binding energies is observed as well as an increased occupation of the metal d levels in line with the decreased average vanadium oxidation state.

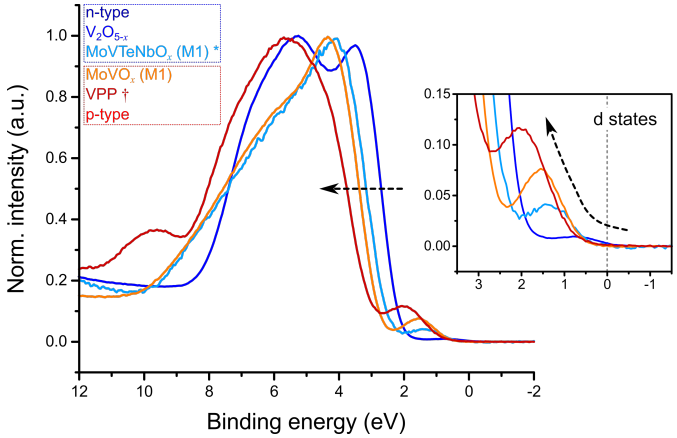

Figure 6.1.: Valence band spectra of V_2O_{5-x}, MoVTeNb-oxide (M1), MoV-oxide (M1), and VPP recorded with NAP-XPS. Conditions: $E_{h\nu}$ = 100 eV; 25 Pa; 400 °C and 270 °C ($MoVO_x$); gas feed: *n*-butane/O_2 1:10 (V_2O_{5-x} and VPP) and *n*-butane/O_2 1:2 ($MoVTeNbO_x$ and $MoVO_x$). References: $MoVTeNbO_x$ Heine *et al.*[1]* and VPP Eichelbaum *et al.*[42]†.

There are numerous similarities between these semiconducting transition metal oxide catalysts. To begin with, there are common features in their bulk crystal structure, namely in the local coordination environment around vanadium, which consists of distorted [VO_5] square pyramids,

*Reprinted (adapted) with permission from Heine, C.; Hävecker, M.; Sanchez-Sanchez, M.; Trunschke, A.; Schlögl, R.; Eichelbaum, M. Work Function, Band Bending, and Microwave Conductivity Studies on the Selective Alkane Oxidation Catalyst MoVTeNb Oxide (Orthorhombic M1 Phase) under Operation Conditions. J. Phys. Chem. C, 2013, 117, 26988–26997. Copyright 2013 American Chemical Society.

†Reprinted (adapted) with permission from Eichelbaum, M.; Hävecker, M.; Heine, C.; Wernbacher, A. M.; Rosowski, F.; Trunschke, A.; Schlögl, R. The Electronic Factor in Alkane Oxidation Catalysis. Angew. Chem. Int. Ed., 2015, 54, 2922–2926. Copyright 2015 Wiley-VCH Verlag GmbH & Co. KGaA, Weinheim.

which can also be viewed as distorted [VO_6] octahedra.[50,70,77,275,304] The V–O polyhedra form a layered network[304] or are interlinked by other moieties.[50,70,77,275] Furthermore, their valence band is mainly formed by O 2p states as generally observed in metal oxides, yet there is a partial covalent bonding character leading to a mixing of O 2p and metal d states (V 3d and Mo 4d) in the valence band region.[2,78,81,105,156,252] Still, the valence band maximum is usually formed by nonbonding O 2p states.[78,87,105,156] The oxides exhibit a mixed vanadium oxidation state with a certain [V^{4+}]/[V^{5+}] ratio in the near surface region, which adapts to the chemical potential of the gas atmosphere.[1,42,85] In some cases, the average oxidation state between +4 and +5 is due to the structure of the catalyst[68–70,275,297] and in other cases due to non-stoichiometry[85] or the formation of a surface overlayer differing from the bulk composition (under catalytic operation conditions).[39] Also, vanadium is thought to be the main redox-active component in these (selective) oxidation catalysts.[1,75,77] For the mixed-metal oxides MoVTeNb-oxide and MoV-oxide, also molybdenum is suggested to occur in the two oxidation states Mo^{5+} and Mo^{6+}.[68–70,275,297] The filled d states form a V 3d(/Mo 4d) level above the valence band maximum.[1,42,105,156,184,252]

Nonetheless, there are also differences both in their electronic properties and in their catalytic performances. Whereas V_2O_{5-x} and MoVTeNb-oxide are n-type semiconductors and exhibit an average surface vanadium oxidation state above 4.5,[1,222] MoV-oxide and VPP[39,60] behave as p-type semiconductors and have an average surface V oxidation state below 4.5. Interestingly, Eichelbaum *et al.* also remarked in a study on V^{3+}, V^{4+} and V^{5+} phosphorus oxides that the oxides with a mainly V^{5+} oxidation state showed n-type semiconducting behavior and the oxides with a mainly V^{4+} oxidation state were found to be p-type semiconductors.[40]

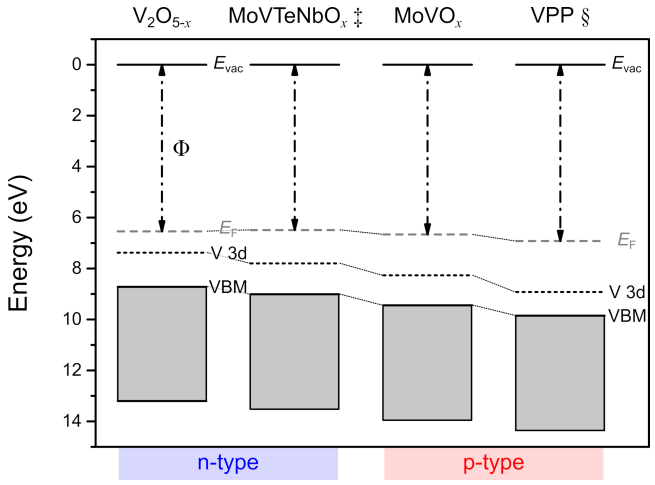

Figure 6.2.: Band scheme of vanadia oxidation catalysts (based on Fig. 6.1): work function Φ, valence band maximum VBM, and V 3d (Mo 4d) peak maximum. References: $MoVTeNbO_x$ Heine *et al.*[1]‡ and VPP Eichelbaum *et al.*[42]§.

‡Adapted with permission from Heine, C.; Hävecker, M.; Sanchez-Sanchez, M.; Trunschke, A.; Schlögl, R.; Eichelbaum, M. Work Function, Band Bending, and Microwave Conductivity Studies on the Selective Alkane Oxidation Catalyst MoVTeNb Oxide (Orthorhombic M1 Phase) under Operation Conditions. J. Phys. Chem. C, 2013, 117, 26988–26997. Copyright 2013 American Chemical Society.

§Adapted with permission from Eichelbaum, M.; Hävecker, M.; Heine, C.; Wernbacher, A. M.; Rosowski, F.; Trunschke, A.; Schlögl, R. The Electronic Factor in Alkane Oxidation Catalysis. Angew. Chem. Int. Ed., 2015, 54, 2922–2926. Copyright 2015 Wiley-VCH Verlag GmbH & Co. KGaA, Weinheim.

Figure 6.2 presents a band scheme of the four vanadia oxide catalysts. Here, the valence band onset (VBM) and the maximum of the V 3d(/Mo 4d) level determined with NAP-XPS is plotted with respect to E_F (from Fig. 6.1), as well as the work function Φ from the secondary electron cutoff measurements. The most remarkable finding from Fig. 6.2 is a trend in this series of oxides with a continuous downward shift of the valence band onset and particularly a shift of the V 3d(/Mo 4d) level. This peak of the filled d states is rather close to the valence band onset in VPP, but closer to E_F in V_2O_{5-x}. In MoVTeNb-oxide and MoV-oxide, intermediate situations were observed. In other words, a continuous decrease in the energy difference $\Delta\left(E_{\text{d states}} - E_{\text{VB}}\right)$ occurs in the order of V_2O_{5-x} > MoVTeNb-oxide > MoV-oxide > VPP and at the same time a "transition" from n-type to p-type semiconducting behavior is observed. This indicates that the partially filled d states (or a narrow d band) in the band gap of these vanadia oxide catalysts act as either donor levels close to the conduction band minimum (n-type) or as acceptor levels close to the valence band maximum (p-type) and are hence essential for determining the semiconducting properties. Theoretical studies investigating the semiconducting properties of these samples taking the real (defective) structure into account are highly desirable to get a better understanding of their physical origin and also of the implications for the interaction with the reactants.

Regarding alkane oxidation reactions over these oxides, the differences in their electronic structure are likely also reflected in their respective catalytic performance. The selective oxidation of light alkanes over transition metal oxides is frequently discussed in terms of a redox mechanism. Hence, the semiconducting properties of the catalysts, which might provide charge carriers for the reaction, were investigated.[30,60] The absolute (p- or n-type) electrical conductivity itself, however, is certainly insufficient as a sole descriptor for selective oxidation catalysts. Yet, valuable information can be obtained in the study of the conductivity response as a function of the catalytic reaction at the surface. In this context it was suggested that the conductivity of the catalysts should be low under reaction conditions compared to other reducing/oxidizing gas feeds.[40] In the last decades it was also realized that the amount of highly active oxygen species should be limited as described in the "site isolation principle" to avoid an over-oxidation.[93] A certain electronic structure of the catalysts is required, which is given by a bulk semiconductor modified by defects and (possibly) a surface termination layer, which may create surface states in the band gap of the oxides.[10] The surface (electronic) structure is furthermore dependent on the chemical potential of the surrounding atmosphere.[10] Moreover, the catalysts should be able to control the bulk–surface–adsorbates charge transfer (in particular to control the oxygen activation) and to adapt to the course of the reaction ("dynamic active site")[10] or to various performance levels.[10,89] Here, gas-phase-dependent changes in band bending were observed over selective oxidation catalysts, which may provide a means to control the charge transfer to adsorbates (e.g., oxygen).[42] The present thesis contributes to this picture of semiconducting selective oxidation catalysts. Using the MCPT conductivity as highly sensitive probe it is possible to monitor this response of the catalysts even to varying reactant conversion levels. Returning to the electronic structure of this series of oxides, the relative energetic position of the partially occupied d states with respect to the valence band or conduction band onset (Fig. 6.2) is certainly highly relevant for the interaction with adsorbates and the charge transfer properties. These electronic states being more or less close to the Fermi level could be involved in the activation

of the reactants. A well-performing selective oxidation catalyst should enable the exchange of electrons between the alkane molecules and oxygen. While a homolytic C–H cleavage leads to a reduction of the catalyst (electron transfer to the catalyst), the catalyst is re-oxidized by oxygen from the gas feed (electron transfer to oxygen). By providing the "correct" surface electronic structure with respect to the absolute position of the energy levels of the catalyst in relation to the redox potential of the reactants,[83] the oxygen and the alkane activation can be decoupled, which may be beneficial for the selectivity of the partial oxidation reaction. In addition, the surface potential barrier (band bending) should provide a means to regulate the charge carrier transfer to the surface. These oxides differ both in the relative energetic position and occupation of the d states and in their ability to regulate[42] the bulk–surface charge transfer. These factors may contribute to their different performance in selective alkane oxidation reactions.

7. Thesis Summary and Final Conclusion

The selective oxidation of light alkanes plays an important role in heterogeneous catalysis applying in many cases vanadium-based (mixed-metal) oxides. The "seven pillars" of heterogeneous selective oxidation provide a useful framework for the development of complex selective oxidation catalysts. In the last years, a number of studies has indicated that the investigation of the bulk electronic structure and its coupling to the surface layer of transition metal oxide catalysts yields valuable insight. Hence, electronic properties need to be considered in addition to local interactions between the reactants and the active site ensembles at the surface to better understand the mode of operation of selective oxidation catalysts. The present thesis investigated the electronic structure and the charge transfer and charge transport in vanadium oxide-based catalysts during the oxidation of light alkanes.

The starting point of this thesis was an investigation of the response of the electronic structure of V_2O_{5-x} to *n*-butane oxidation feeds as reference material exhibiting a low selectivity towards partial oxidation products and with a reduced complexity compared to VPP or mixed-metal oxides. In fact, vanadium pentoxide shows already a certain degree of complexity due to the ease of oxygen loss and the formation of mixed-valent non-stoichiometric compounds. The electronic structure and surface composition of the sample were investigated with NAP-XPS and NEXAFS spectroscopy in *n*-butane- and O_2-containing gas atmospheres.

It was shown that a redox-active surface layer adapting to different gas atmospheres is formed, but also deeper layers of the sample were reduced/oxidized. This is in contrast to the redox response of the selective benchmark catalyst VPP, which is restricted to the surface or near-surface region.[39] The changes in the V_2O_{5-x} sample were dominated by changes in the oxygen chemical potential. Yet, an analysis of a V 3d band gap level showed slight changes in the 3d occupation even between the reaction gas feed *n*-butane/O_2 and the He/O_2 feed. Despite the same qualitative trends that were observed for V_2O_{5-x} and VPP with respect to gas-phase-dependent changes in the oxidation state, the work function, and the valence band onset, a (dynamic) surface potential barrier which might control the bulk–surface–adsorbates charge transfer like in VPP was not observed to the same extent in V_2O_{5-x}.[42] To better elucidate the electronic structure of V_2O_{5-x} in *n*-butane oxidation feeds, resonant photoemission spectroscopy was performed showing the V 3d–O 2p mixing in the valence band region (partial covalent bonding character) as well as an enhancement of a band gap peak ascribed to occupied V 3d states. Clear differences were observed in the valence electronic structure of V_2O_{5-x} in the *n*-butane/O_2 feed compared to *n*-butane/He in terms of a greater intensity of the band gap peak and in the high binding energy region of the valence band. This is attributed to an increased V 3d occupation in the latter gas feed. Furthermore, gas-phase-induced differences in the region between the valence band and the O 2s level were observed, which may be due to an enhanced V-$L_{2,3}M_{45}M_{45}$ Auger electron contribution in case of a higher V 3d occupation, but also a contribution of carbonaceous

adsorbates should be considered.

Following this, a comparative study of the charge transport and charge transfer in vanadium pentoxide and VPP was conducted with the aim to investigate their possible interrelation with the catalytic performance. To achieve this, *operando* and contact-free MCPT conductivity (complex permittivity) measurements were carried out during the oxidation of *n*-butane, which were complemented by UV-Vis spectroscopy under the same experimental parameters. Suitable conditions had to be defined, which enabled the direct and quantitative comparison of both samples. This entailed measuring the samples with very different conductivities and catalytic performances in the same microwave resonator and at the same *n*-butane conversion level. Furthermore, isothermal measurements at various contact times and hence reactant conversion levels (and product selectivities) as well as temperature-dependent measurements were chosen to identify relevant performance properties and their relation to electronic properties.
This study has demonstrated a sensitive response of the electronic structure of V_2O_{5-x} and VPP to changing conversion levels or to a changing chemical potential of the gas phase. UV-Vis spectroscopy supported the interpretation of the MCPT conductivity response as due to changes in the V 3d occupation adapting to the different gas feeds. Non-local properties like available charge carriers are important factors contributing to their respective catalytic performance. The hypothesis[10,42] is that controlling the charge carrier transfer across the bulk–surface interface via providing a finite surface potential barrier under reaction conditions is essential for limiting the formation of CO and CO_2. The extent to which the conductivity is affected by varying conversion levels was monitored. It was found that the highly selective benchmark catalyst VPP exhibits only small conductivity changes and the real part of its permittivity describing polarization effects was not affected at all. This indicates that the surface is "stable" against chemical modification or accumulation of excess charge. In contrast to this, a smaller number of exchanged electrons (determined from the catalytic performance data) has led to greater conductivity or permittivity changes in the quite unselective V_2O_{5-x} sample. In case of an increased sample reduction both in the surface and subsurface region at higher reactant conversions, the changed surface termination may also affect the catalytic performance. A tentative link between changes in the product distribution and the conductivity/permittivity changes as a function of the *n*-butane conversion is suggested, where greater changes in the selectivities are reflected in greater changes of ε' or of the conductivity. The binary oxide further exhibited a comparatively low activation energy for charge transport, which was four to eight times lower than the one of VPP. This may have implications for the charge transfer and could be linked to the higher selectivity of VPP. To sum up, relevant factors for selective oxidation catalysts are low conductivity or permittivity changes and a "stable" surface at different conversion levels as well as a sufficient kinetic barrier for charge transfer in order to control the abundance of reactive oxygen species. These factors can complement traditional concepts like the site isolation.

The n-type semiconducting complex MoVTeNb-oxide in the orthorhombic M1 phase has previously been investigated owing to its promising performance in the direct functionalization of propane. In this thesis, the less complex mixed-metal MoV-oxide catalyst in the M1 phase was studied, whose semiconducting properties have not been investigated so far. This work further explored possible relationships between electronic properties and the catalytic function following

the experimental approach of the study on V_2O_{5-x} and VPP. To begin with, the electrical conductivity (complex permittivity) of MoV-oxide was investigated in the *operando* MCPT setup in the oxidation of ethane, propane, and *n*-butane. These measurements were complemented by NAP-XPS and NEXAFS spectroscopy.

Notably, the conductivity of MoV-oxide decreased both with increasing alkane chain length and with increasing propane/O_2 ratio suggesting a p-type semiconducting behavior, which is in contrast to the reported observations[1] for MoVTeNb-oxide. Since the availability of free electrons or holes will be different in the two oxides, differences in their catalytic performance could partly be related to their respective semiconducting properties. MoV-oxide exhibits a lower selectivity than MoVTeNb-oxide[72] in the oxidation of propane. It should be noted that also the main group element tellurium was suggested to be essential for the higher selectivity of the latter multi-component mixed-metal oxide.[77] Like VPP, MoV-oxide showed a negative relation between conductivity and reactant conversion. In addition, the extent of the conductivity/permittivity changes at various conversion levels was correlated with the changes in the product distribution. A stable catalytic performance retaining a high selectivity over a wide conversion range (e.g. in the oxidative dehydrogenation of ethane) was also seen in very small conductivity changes with increasing reactant conversion. The apparent activation energy of conduction of MoV-oxide was found to be in between the one of VPP and the one of V_2O_{5-x}, but closer to the unselective V_2O_{5-x}. Generally, these findings strengthen the assumption of a broader validity of the above-drawn conclusions for V_2O_{5-x} and VPP.

As a next step, the influence of water vapor, which enhances the acrylic acid formation, on the semiconducting properties and on the surface electronic structure of MoV-oxide was analyzed. A decrease of the conductivity or permittivity was observed in a steam-containing propane oxidation feed. It is concluded that a change in the charge carrier density does not play a dominant role in the conductivity change, because steam was generally found to lead to a decrease of the MCPT conductivity also for the n-type semiconductor MoVTeNb-oxide[105] and for the p-type VPP.[123] In addition, the simultaneously observed change in the product distribution and chemical potential of the gas phase (compared to a dry propane oxidation feed) is likely to affect the conductivity as well. Interestingly, ε' showed a response only to dry/wet reaction gas feed cycles, in contrast to the conductivity changes, which were also observed in a reference experiment applying dry/wet cycles without propane in the gas feed. This indicates that the changes in ε' are reaction-induced. It further supports the notion that relevant information can also be obtained from the study of the real part of the permittivity, even though the disentanglement of the different factors contributing to the energy storage (i.e., to ε') in these complex samples in the microwave frequency range is difficult. NAP-XPS showed an irreversible surface enrichment in V^{5+}, yet also an increased occupancy of the d states was observed, as well as an increased surface hydroxylation. It is a reasonable assumption that the conductivity or permittivity of the sample is influenced by the formation or modification of this termination layer, which may correspond to a semiconductor heterojunction between the MoV-oxide (M1) bulk and an overlayer enriched in V_xO_y nanodomains with an increased average vanadium oxidation state, as well as by changes in the V 3d(/Mo 4d) occupancy. The modified surface layer could well affect the bulk–surface–adsorbates charge transfer and presumably also has an effect on the catalytic

performance in conjunction with the increased surface hydroxylation.

In conclusion, this thesis provides insight into the role of charge transfer and charge transport in vanadium-based transition metal oxide catalysts in (selective) alkane oxidation reactions. Non-local electronic properties as probed by *operando* and contact-free conductivity or permittivity measurements were demonstrated to be sensitively adapting to the catalytic reactions occurring at the surface. Partially occupied d states in these oxides seem to be highly relevant e.g. for their semiconducting properties, but they may also need to be considered in the interaction with adsorbates. This work has indicated some requirements for well-performing catalysts. Key parameters for selective high performance oxidation catalysts like VPP are a stable conductivity or permittivity at various conversion levels, which may be linked to the prevention of a modification of the surface layer, and the control of the charge transfer. Such factors are lacking in V_2O_{5-x}. The concepts were further extended to the low to moderately selective mixed-metal MoV-oxide. The findings obtained in this thesis support the picture[10,42] of a selective oxidation catalyst which features a surface layer on top of a semiconducting bulk and is able to transfer charge carriers across the bulk–surface–adsorbates interface in a controlled way. A correlation between the number of exchanged electrons during the reactions and the conductivity changes was observed for vanadium oxide-based catalysts. The need for investigating the catalysts not only under catalytic operation conditions, but also under iso-conversion conditions in order to obtain a quantitative comparison is highlighted. The experimental approach from this work could serve as a base for future studies testing a range of selective oxidation catalysts. Complementary techniques including photoelectron spectroscopy or other (spectroscopic) techniques that give access to the surface termination layer and the energetic quantities at the catalyst's surface (valence electronic structure, surface potential barrier) or the redox properties provide support for the interpretation of the MCPT experiments. These results can contribute to a better understanding of the working mode of vanadia oxidation catalysts.

Appendices

A. Supporting Information – The Influence of Alkane Oxidation Gas Feeds on the Electronic Structure of V_2O_{5-x} Studied by NEXAFS and Photoelectron Spectroscopy

A.1. Vanadium Pentoxide Sample Characterization

A.1.1. X-ray Diffraction

XRD measurements were performed on a STOE STADI P transmission diffractometer equipped with a primary focusing germanium monochromator (Cu Kα_1 radiation) and DECTRIS MYTHEN 1K position sensitive solid-state detector. The sample was mounted in the form of small amounts of powder sandwiched between two layers of polyacetate film and fixed with a small amount of X-ray amorphous grease. Figure A.1 shows the powder diffractogram of the V_2O_5 sample (ID 18433) corresponding to the α-V_2O_5 crystal structure, where the main reflections are indexed.

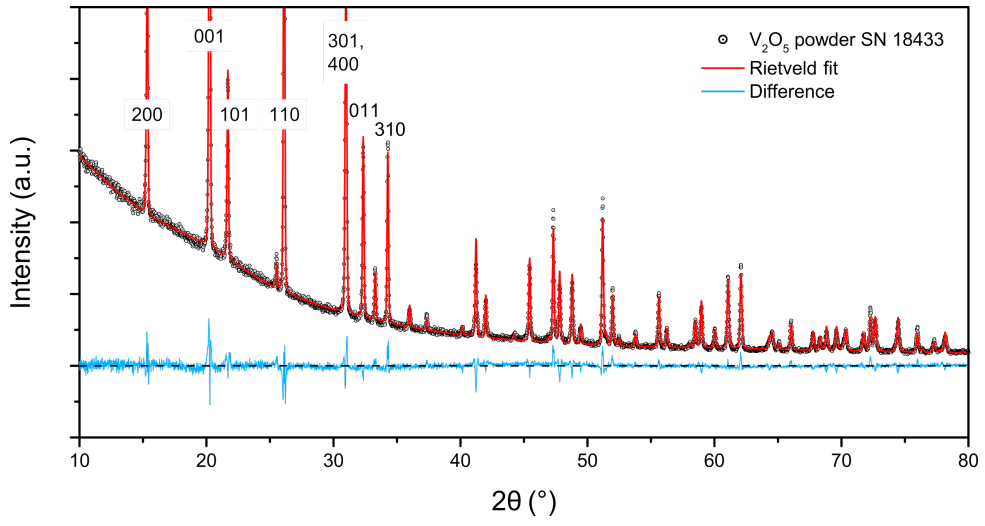

Figure A.1.: Powder diffractogram of V_2O_5 sample (black) and Rietveld fit (red) based on the α-V_2O_5 crystal structure (ICSD entry 60767). The difference between measured data and the fit is shown below (blue) and the main reflections are indexed.

The signals seen in the difference curve of the Rietveld fit (magnified in Figure A.1) are mainly caused by anisotropic (hkl-dependent) peak broadening, which was not successfully modeled in the fit.

A.1.2. BET Surface Area Determination

The specific surface area of the V_2O_5 sample was determined with isothermal nitrogen adsorption, which is presented in Figure A.2. It was found to be 3.4 m^2/g.

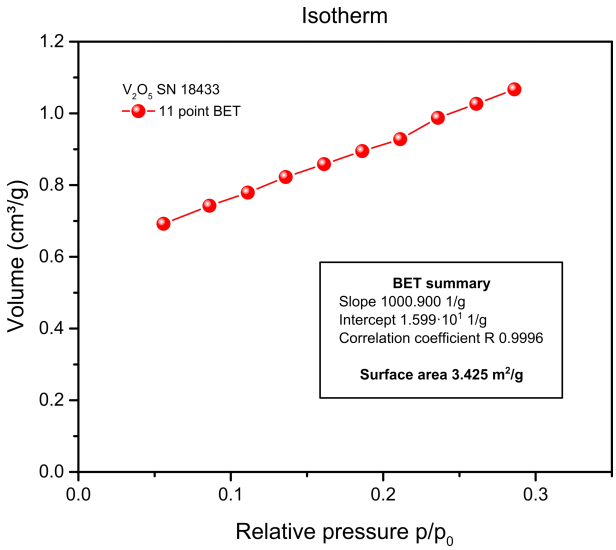

Figure A.2.: Specific surface area determination of V_2O_5 powder sample: adsorption isotherm of nitrogen at -196 °C and Brunauer-Emmett-Teller (BET) surface area of 3.43 m^2/g.

A.1.3. EPR Spectroscopy

Electron paramagnetic resonance (EPR) spectra of the V_2O_5 powder (Figure A.3) were recorded on a Bruker ESP 300 E spectrometer with a Bruker ER 4116 DM resonator (TE_{102} mode) and a Bruker ER 042 MRH E microwave bridge. The sample was measured in a Sigma-Aldrich Wilmad® quartz (CFQ) EPR tube (o.d. 4 mm) at -196 °C (liquid nitrogen cooling) in the X-band frequency range (9.63 to 9.64 GHz) using microwave powers ranging from 20 to 0.02 mW, a modulation frequency of 100 kHz and a modulation amplitude of 0.537 mT.

The oxidation state of the V_2O_5 sample was estimated from the EPR measurements based on the number of spins N_S, which is proportional to the double integral of the continuous wave

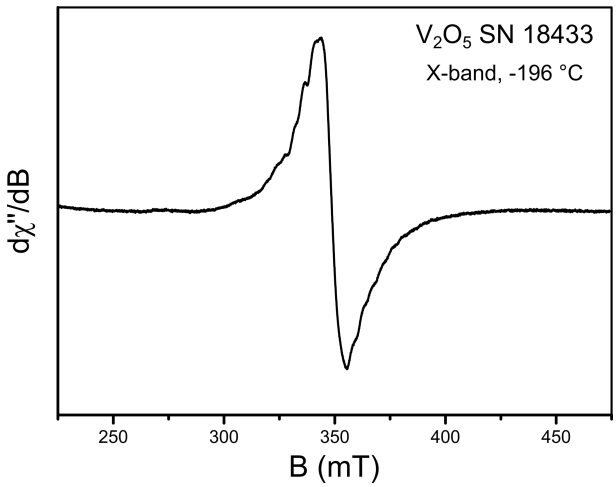

Figure A.3.: EPR spectrum of V_2O_5 sample showing V^{4+} defect centers (X-band, 2 mW, -196 °C).

EPR (first derivative) signal.[305]

$$\text{Double integral} = \text{const} \cdot (G_R \cdot C_t \cdot n) \cdot \left[\frac{\sqrt{P}\ B_m\ Q\ n_B\ S\,(S+1)\,N_S}{f(B_1, B_m)} \right]$$

Here, $n_B = \exp(-\Delta E/kT)$ is the Boltzmann factor, S is the total electron spin, and $f(B_1, B_m)$ denotes the spatial distribution of the microwave field B_1 and the modulation field B_m. The absence of power saturation at -196 °C was checked for. The number of spins of V_2O_5 was estimated by a comparison of the double integral with the one of an MgO/Cr^{3+} sample (internal ID 18729) with known number of spins, $N_S = 59$ mol/m^3, recorded at the same conversion time C_t, number of scans n, microwave power P, modulation amplitude B_m, and using approximately the same sample volume. The double integrals were corrected for the receiver gain G_R and quality factor Q using the relations Double integral $\propto \sqrt{\text{Receiver gain factor}}$ and Double integral $\propto$ Q factor. In this way, $N_S = 7.0 \cdot 10^{19}$ spins/g were found for the V_2O_5 sample.

The number of spins can be transferred to an estimation of the oxidation state under the assumption that all spin centers can be identified with V^{4+} centers ($3d^1$, $S = 1/2$) and the residual vanadium is in the 5+ oxidation state ($3d^0$, $S = 0$). The EPR spectra of the V_2O_{5-x} sample taken at atmospheric pressure under air suggest a vanadium oxidation state of about 4.99, which is very close to the nominal value of the stoichiometric compound, i.e. ∼1% V^{4+} were found instead of ∼10% V^{4+}, which were determined by NAP-XPS, see below. Yet it should be mentioned that there also exists an error due to the background correction required for the double integration of the EPR signal, besides the above-mentioned assumptions.

A.1.4. Near-Ambient Pressure XPS

The V_2O_{5-x} sample was characterized with near-ambient pressure X-ray photoelectron spectroscopy (NAP-XPS) in He/O_2, C_4H_{10}/O_2, and C_4H_{10}/He gas feeds (1:10, 25 Pa) at 400 °C. Details on the experimental conditions can be found in the main part of this work.

Core Level and Valence Band Spectra: Surface Composition and Redox Response

In order to monitor changes in the average vanadium oxidation state of the sample in different gas feeds, the V $2p_{3/2}$ core level was fitted with Gaussian-Lorentzian functions after a Shirley background correction. Only the V $2p_{3/2}$ peak was used for the oxidation state analysis, because the V $2p_{1/2}$ peak overlaps with a satellite of the V $2p_{3/2}$ level therefore complicating the fitting.[78] A good fit was possible using only two Gaussian-Lorentzian curves, termed 5+ and 4+ components, whose relative area contributions to the overall V $2p_{3/2}$ peak were evaluated. The average vanadium oxidation state was calculated based on their relative contributions assigning the main component to V^{5+} and with the assumption that the lower binding energy component corresponds to V^{4+}, which will be discussed below. Example fits of the V $2p_{3/2}$ core level are presented in Figure A.4. The corresponding fit parameters and constraints are listed in Table A.1. The main V^{5+} component "V(1)" was observed at $E_{\text{bind}}(V^{5+}\ 2p_{3/2}) \approx 517$ eV and a growing shoulder occurred at the low binding energy side in the reducing gas atmospheres. The low binding energy component ascribed to a lower vanadium oxidation state was fixed at 1.45 eV

below the main V^{5+} peak (V(1)) and with a 1.2 times greater full width half maximum than the main V(1) peak, which gave the best agreement between experimental curve and fit. The greater peak width (fwhm) is justified, since the V $2p_{3/2}$ linewidth is generally found to be higher for lower vanadium oxidation states[306] due to the coupling of the (2p) core hole and (3d) valence electrons.[78,82] Also, the measurements at higher photoelectron kinetic energies corresponding to greater probing depths (cf. Figure A.4 (b) and Table A.1) require greater linewidths due to the monochromator resolution at higher photon energies.

Table A.1.: Fit parameters for V $2p_{3/2}$ core level using two Gaussian-Lorentzian product functions V(1) (V^{5+}) and V(2) (V^{4+}) as shown in Figure A.4: peak positions, full width at half maximum (fwhm), and relative Lorentzian contributions; constraint fit with position(V(2)) = position(V(1)) – 1.45 eV and fwhm(V(2)) = fwhm(V(1))·1.2. A Shirley background was used.

V $2p_{3/2}$	**Surface sensitive (0.8 nm)**		**Deeper layers (2.3 nm)**	
	V(1)	**V(2)**	**V(1)**	**V(2)**
Position (eV)	516.98 – 517.04	515.53 - 515.59	516.96 – 517.00	515.51 - 515.55
fwhm (eV)	1.23 – 1.44	1.48 – 1.72	1.44 – 1.60	1.73 – 1.92
Lorentzian contribution	60% L			

An unambiguous assignment of the peaks contributing to the V $2p_{3/2}$ core level in (defective) mixed-valent vanadium oxides is often not straightforward. A range of V $2p_{3/2}$ binding energies was reported in the literature for different vanadium oxidation states depending on the used energy reference, the sample pretreatment, etc.[306,307] Furthermore, the oxides VO_2 and V_2O_3 exhibit metal-insulator transitions and distinct changes in their core level spectra (esp. in the linewidth) depending on whether they are investigated in their metallic or insulating (semiconducting) phase.[82] In these cases, also an asymmetric line shape was applied.[308,309] For example, V $2p_{3/2}$ binding energies of V_2O_5 were reported to lie between 516.2 eV (polycrystalline V_2O_5 with a V_6O_{13} surface),[306] 517 eV for polycrystalline V_2O_5,[306] and 517.2 eV for a V_2O_5 single crystal,[185] respectively, and the binding energy difference between V^{5+} and V^{4+} was found to be 1.3 – 1.4 eV.[185,306] A number of studies have also found binding energy differences between V^{5+} and V^{4+} of 1.2 – 1.3 eV.[184,307,308,310] Some of the XPS fit parameters of vanadium oxides were summarized in Ref. [307], where V^{5+} $2p_{3/2}$ binding energies of 516.90 – 517.50 eV were reported and of 515.50 – 516.40 eV for V^{4+}. The V $2p_{3/2}$ binding energy in oxides with a V^{3+} oxidation state was reported in the range of 514.9 to 515.85 eV[82,184,185,306–308] close to the V^{4+} positions. It may be noted that a three-component fit describing 5+, 4+, and 3+ oxidation states yielded the same qualitative results for the V_2O_{5-x} sample, but with a lower overall oxidation state. Given the spread in the reported binding energies, an estimation of the vanadium oxidation state using the energy difference Δ between O 1s and V $2p_{3/2}$ was also suggested.[306] For the V_2O_{5-x} sample, Δ(O 1s – V^{5+} $2p_{3/2}$) values of ∼12.87 eV were found, which is in good agreement with literature values of vanadium pentoxide ($\Delta \approx 12.8$ eV[185,306,307]). The peak at a lower binding energy exhibited a greater energy difference of $\Delta \approx 14.3$ eV in the V_2O_{5-x} sample, which is close to the values reported for VO_2 of 14.1 to 14.35 eV.[185,306]

Taken together, the V $2p_{3/2}$ binding energies and the energy difference between the V(1) and

V(2) components (Table A.1) agree with the literature values for formal 5+ and 4+ oxidation states. Therefore, the main V $2p_{3/2}$ component is assigned to V^{5+} and the second component is assumed to be V^{4+}. The gas phase-induced changes in the vanadium oxidation state of the sample from the V $2p_{3/2}$ core level analysis were supported by the V 3d band gap level, whose area correlated with the average vanadium oxidation state.

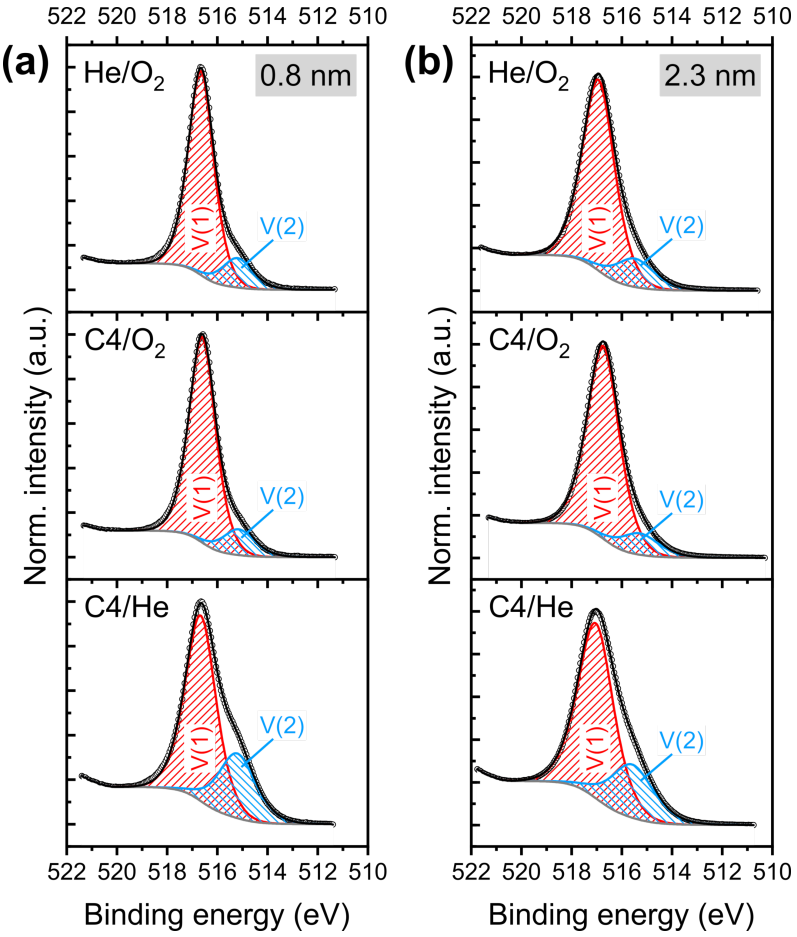

Figure A.4.: Fit of V $2p_{3/2}$ core level of V_2O_{5-x} with two component V(1) (V^{5+}) and V(2) (V^{4+}) after a Shirley background correction in three gas feeds (He/O_2, C_4H_{10}/O_2, C_4H_{10}/He) and at two probing depths **(a)** λ_{IMFP} = 0.8 nm and **(b)** 2.3 nm (400 °C, 25 Pa).

Using this fitting procedure (Table A.1), the average vanadium oxidation state was determined in different gas feeds. The oxidation state of 5.0 was not reached, even in the strongly oxidizing He/O_2 gas feed. A possible explanation is the rather low pressure of the experiment (p_{tot} = 25 Pa) together with the temperature of 400 °C, in view of the known vacuum reduction of vanadium pentoxide at high temperatures.[85,306] In both the He/O_2 and the C_4H_{10}/O_2 atmosphere the V oxidation state was between 4.85 and ~4.90. At the comparatively low total pressure of the NAP-XPS experiments and at a temperature of 400 °C the oxidation state of vanadium seems to be controlled by the partial pressure of oxygen, while the addition of *n*-butane to an oxygen-containing gas feed has only a minor influence.

To identify the surface termination on the V_2O_5 powder sample the surface composition was analyzed in the different gas feeds based on a quantitative analysis of the O 1s, V $2p_{1/2}$ and V $2p_{3/2}$ core levels. A V/O ratio close to the bulk composition of V_2O_5 (V/O ≈ 0.4) was

observed irrespective of the gas atmosphere and the electron inelastic mean free path length, which was presented in the main part of this work. It may be noted that a tentative fit of the O 1s peak taking the contribution of the V $2p_{3/2}$ and V $2p_{1/2}$ satellite features into account already indicates a V/O ratio above 0.40. Small changes in the V/O ratio could still be detected showing a decreasing V/O ratio at the beginning in the He/O_2 gas feed, which can be attributed to a healing of oxygen vacancies, followed by constant values in the C_4H_{10}-containing gas feeds. Coking in the C_4H_{10}/He gas feed, i.e. an increase in the C 1s area, was not observed.

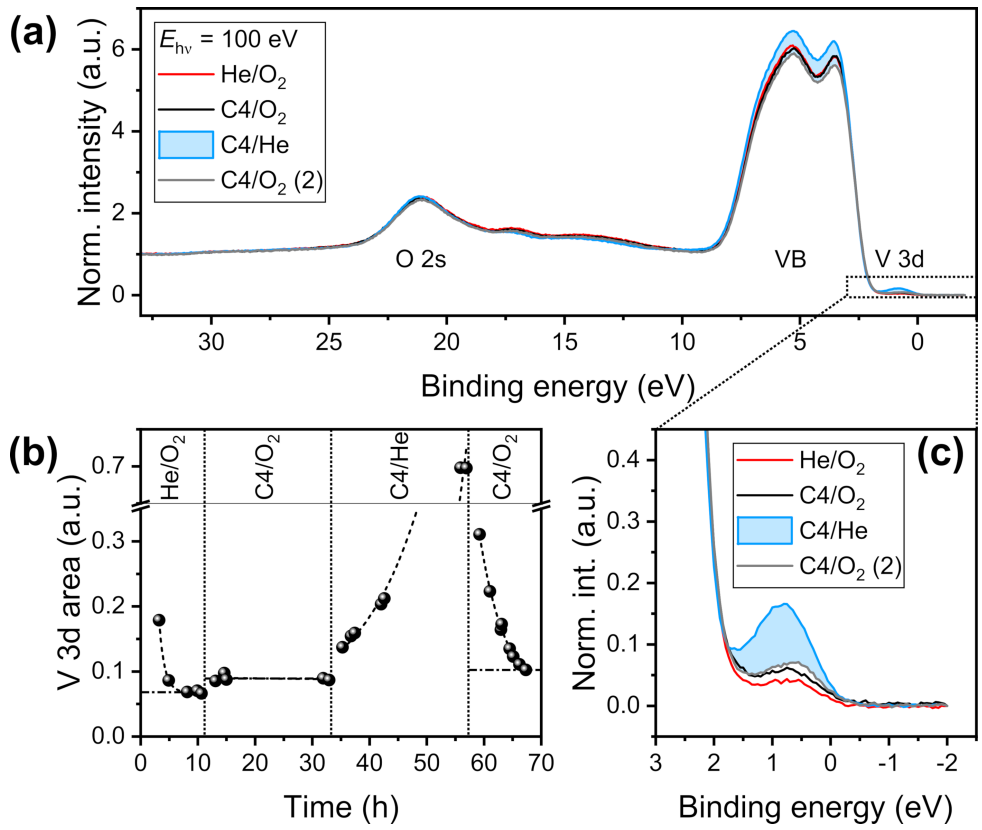

Figure A.5.: **(a)** Valence band and O 2s spectra of V_2O_{5-x} in different gas feeds (400 °C, 25 Pa, $E_{h\nu}$ = 100 eV), **(b)** area of band gap peak "V 3d" from fit with Gaussian curve as a function of time on stream, **(c)** magnification of band gap peak in the binding energy region above 3 eV.

Figure A.5 (a) shows the valence band photoemission spectra of the oxygen-deficient vanadium pentoxide sample in the binding energy range between 0 and 33 eV in the different gas feeds recorded at a photon energy of 100 eV. The spectra were normalized to the background at 33 eV after a linear background correction. In the valence band region between ∼2 to 9 eV two main peaks can be distinguished at binding energies of 3.7 and 5.3 eV. The peak at ∼21 eV in Figure A.5 (a) corresponds to the O 2s level of the sample. In addition, a small feature above the valence band onset can be seen, which is ascribed to occupied V 3d levels (see below in the next section). It can be seen that the valence band spectra were slightly affected by the different gas feeds with a higher intensity in the valence band region in the reducing C_4H_{10}/He gas feed (shown in blue in Figure A.5 (a) and (c)). The spectra in the other gas feeds resembled each other closely. The intensity of the band gap peak increased in the reducing C_4H_{10}/He gas feed, which is clearly shown in Figure A.5 (c). An analysis of the peak area, which was determined

from a fit with a Gaussian peak, is presented in Figure A.5 (b) as time on stream plot in different gas feeds showing reversible changes in the peak area adapting to the different gas atmospheres.

In addition to the changes in the core level spectra, a peak caused by occupied V 3d levels above the valence band maximum of V_2O_{5-x} can be seen with a maximum at ∼1 eV, whose intensity increased in the reducing C_4H_{10}/He gas feed (increased vanadium 3d occupation) and decreased in the oxidizing He/O_2 feed compared to the reaction gas atmosphere. The gas phase-induced changes in the band gap peak area correlated with the average vanadium oxidation state from the V $2p_{3/2}$ core level analysis. An interesting observation, though, is the first recorded V 3d spectrum in He/O_2 (first value after 3.2 h time on stream), which has a rather large area that is not reflected in the average vanadium oxidation state. Here, the seeming ongoing oxidation of the sample in He/O_2 with a continuous decrease in the V 3d occupation is more closely related to the changes in the V/O ratio than to the changes in the vanadium oxidation state.

A.2. NEXAFS Investigation

The redox response of the V_2O_{5-x} sample in different gas feeds was also monitored in changes in the near edge X-ray absorption fine structure (NEXAFS) in the electron yield mode. Figure A.6 presents a comparison of the NEXAFS spectra recorded at the vanadium $L_{2,3}$-edge and oxygen K-edge in the Auger electron yield mode (a) with the total electron yield spectra (b), which are dominated by the π^* resonance of molecular O_2 at 530.8 eV.

Changes in the AEY O K-edge doublet peak around 530 eV in the different gas feeds are illustrated in Figure A.7 showing a decreased splitting Δ or increased intensity between the two peaks upon treating the sample in the reducing C_4H_{10}/He gas feed. It is important to point out that the doublet peak separation Δ of the O K-edge NEXAFS spectra is larger for vanadium oxides with a lower V oxidation state, see the literature spectra e.g. of VO_2[78,188] or of V_6O_{13}.[311] If this seeming decrease in the splitting Δ of the V_2O_{5-x} O K-edge spectra in the C_4H_{10}/He feed is interpreted in terms of a decrease of the ligand field splitting, this might be explained by a weakening of the (σ)-interaction between O 2p and V $3d_{x^2-y^2,z^2}$ upon reduction (filling of V 3d states), because this would lead to a decrease of the bonding σ – antibonding

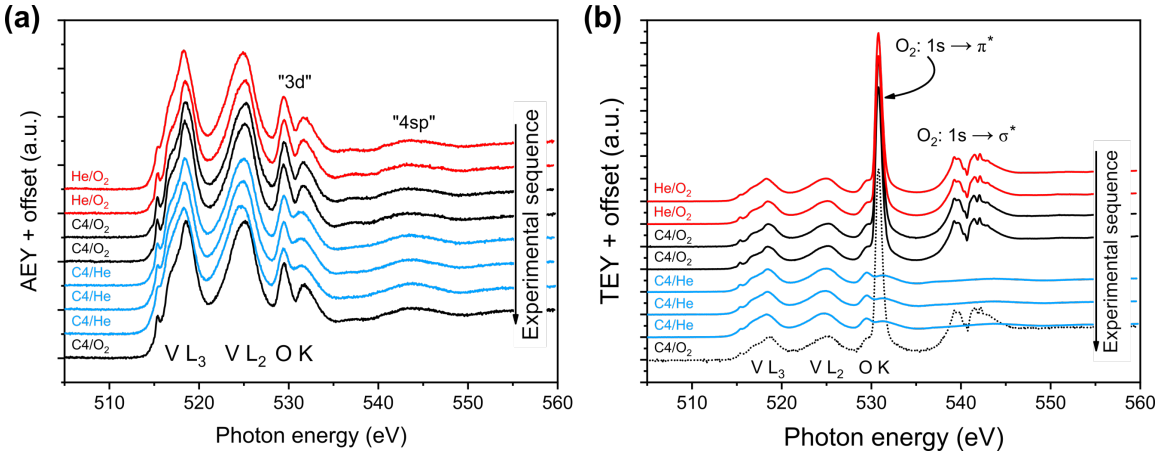

Figure A.6.: Comparison of **(a)** Auger electron yield (AEY) and **(b)** total electron yield (TEY) spectra of the V $L_{2,3}$- and O K-edge of V_2O_{5-x} in different gas feeds (400 °C, 25 Pa).

σ^* separation and hence of the ligand field splitting. The effect of the reducing gas atmosphere on the σ-derived bands should be more pronounced due to the stronger σ-overlap of the O 2p and V 3d orbitals of appropriate symmetry compared to the π-overlap. Indeed, the π^* O K-edge peak was found to exhibit a smaller downward shift in the C_4H_{10}/He feed compared to the σ^* peak, yet both energy shifts were small. A weakening of the O 2p–V 3d σ-overlap would also be seen in increased V-O bond lengths, which agrees with the shift of the V L_3-edge to lower energies (compare to the V L_3-edge spectra of VPP and V_2O_5 in Ref. [183]).

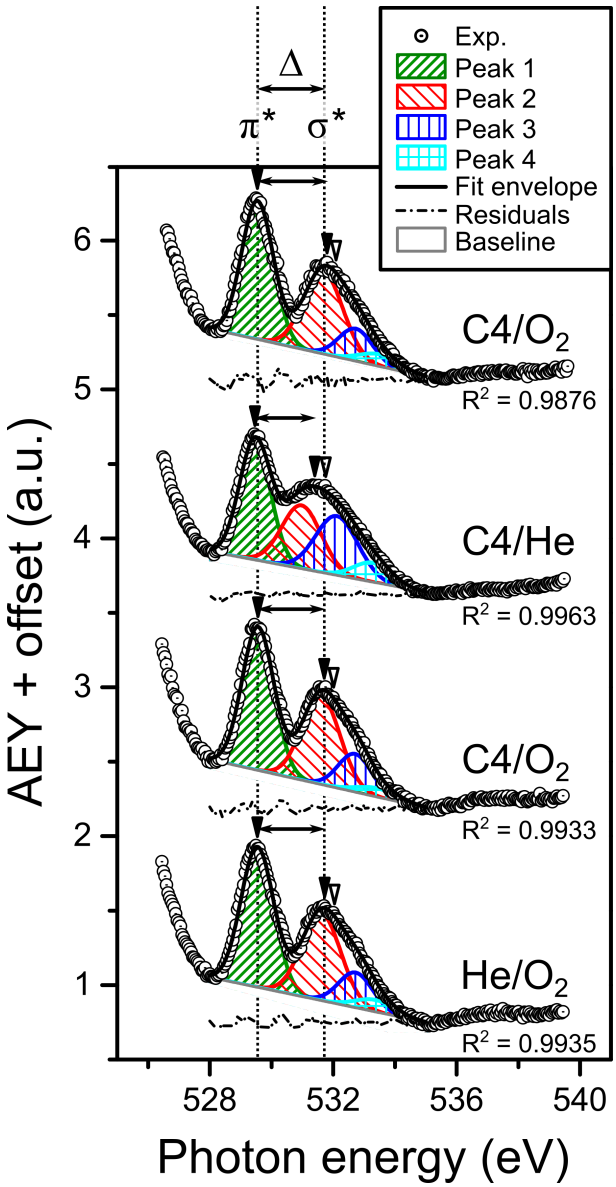

Figure A.7.: V_2O_5 O K-edge spectra (O 2p admixed with V 3d in approx. t_{2g}- and e_g-like symmetry) in different gas feeds.

A.3. Resonant Photoelectron Spectroscopy (resPES)

Valence band spectra of V_2O_{5-x} were recorded at photon energies corresponding to the V L and O K absorption edges ($E_{h\nu}$ = 510 to 551 eV) in two gas atmospheres, *n*-butane/oxygen 1:10 (C_4H_{10}/O_2) and *n*-butane/helium 1:10 (C_4H_{10}/He), at 400 °C and 25 Pa. The resonant

enhancement of valence band features of V 3d character in the V_2O_{5-x} sample and the overlap with Auger peaks was discussed in the main part of this work. This resonant enhancement is not given by the sum of the intensities of the direct photoemission processes and the resonant photoelectron process (or "participant autoionization"[166,167,169,312]), but there is an additional cross-term in case of a coherent superposition of the two processes.[165] If the transition matrix elements of the two processes are of similar magnitude, the cross-terms are large, which leads to a Fano-type line shape when plotting the intensity of a resonantly enhanced valence band feature as a function of photon energy.[165,169,170] Comparing the photoionization cross-sections in the photon energy range of 510 to 551 eV, it is found that the V 3d cross-sections (atomic subshell photoionization cross-section[175,176] σ of 0.02 to 0.01 Mb) are much smaller than the V 2p cross-sections (1.5 to 1.7 Mb). Hence, it is assumed that no interference effects will be observed in the present case for V_2O_{5-x} in terms of a Fano-type line profile. This behavior of early transition metal compounds is generally believed to be different from the one of late transition metal substances.[313]

The contribution of O-$KL_{23}L_{23}$ Auger peaks to the V_2O_{5-x} resPES valence band spectra was observed starting at photon energies close to the O K absorption edge in the spectra recorded at $E_{h\nu}$ of 528.5 eV and above (spectrum "G"). In fact, the valence band spectra of V_2O_{5-x} recorded at the O K-edge is dominated by Auger electron signals. Figure A.8 presents a comparison of the normal Auger electron spectrum of the V_2O_5 sample in C_4H_{10}/O_2 recorded with a photon energy of 860 eV (a) with the resPES valence band spectra as a function of photoelectron kinetic energies (b). The assignment of the Auger electron peaks in Figure A.8 (a) is based on literature on vanadium pentoxide.[82,198] The most intense peak corresponds to the O-$KL_{23}L_{23}$ Auger transition. In the off-resonance valence band spectra of the sample, which are shown in Figure A.8 (c) recorded at photon energies before and after the absorption edges (510 and 551 eV), no overlap with Auger peaks was detected at binding energies above the O 2s level. Indeed, the off-resonance spectra resembled each other closely. At photon energies between 515.9 and 528.7 eV, vanadium $L_{23}M_{45}M_{45}$ Auger peaks moved through the resPES spectra, mainly between the valence band and the O 2s level. The contribution of O-$KL_{23}L_{23}$ peaks to the V_2O_{5-x} resPES valence band spectra was observed starting at photon energies close to the O K absorption edge in the spectra recorded at $E_{h\nu}$ of 528.7 eV and above (cf. Figure A.8 (b), "G–J").

The resPES spectra recorded at photon energies corresponding to the O K-edge X-ray absorption peaks of the V_2O_{5-x} sample of 530 eV ("H", O 1s $\rightarrow$ O 2p-V 3d(π^*) transition), of 532 eV ("I", O 1s $\rightarrow$ O 2p-V 3d(σ^*) transition), and of 536 eV ("J", O 1s $\rightarrow$ O np-V 4sp transition) exhibited the most pronounced increase in intensity (cf. Figure A.8 (b)). The spectral shape of the peaks resembled the one of the normal O-$KL_{23}L_{23}$ Auger transition of the sample shown in Figure A.8 (a). This is further elucidated in Figure A.9, which compares spectra all taken in C_4H_{10}/O_2 but different photon energy namely an Auger spectrum taken off resonance ($E_{h\nu}$= 860 eV) and two resPES spectra taken at the position of the σ^* peak ($E_{h\nu}$= 532 eV) and the π^* peak ($E_{h\nu}$= 530 eV), respectively. The O 2p–V 3d hybridized O K-edge NEXAFS spectrum of the sample is shown in the inset. The prominent peak in spectrum "I" recorded at 532 eV (σ^* peak of the V_2O_{5-x} O K-edge) was found to be overlapping with the normal O-$KL_{23}L_{23}$-Auger electron spectrum. In contrast to this, spectrum "H" ($E_{h\nu}$ = 530 eV, π^* peak of O K-edge

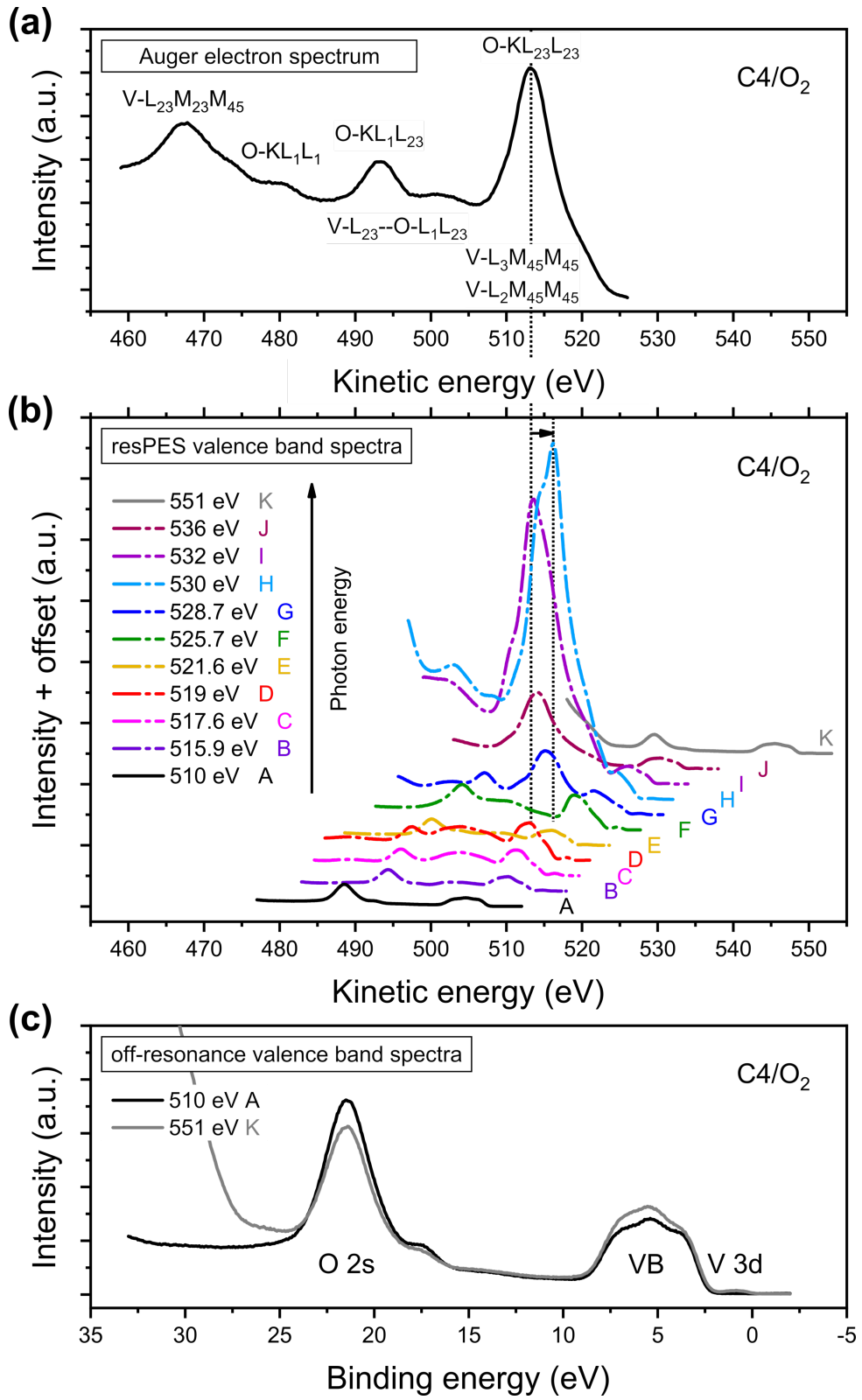

Figure A.8.: Resonant photoelectron spectroscopy of V_2O_{5-x} in C_4H_{10}/O_2 (25 Pa, 400 °C): **(a)** normal Auger electron spectrum at $E_{h\nu} = 860$ eV; **(b)** resPES valence band spectra recorded with $E_{h\nu} = 510$ to 551 eV as a function of photoelectron kinetic energy; **(c)** off-resonance valence band spectra recorded at $E_{h\nu} = 510$ and 551 eV.

doublet) showed a peak shifted to higher kinetic energies by ∼2.9 eV and a shoulder on the low kinetic energy side. This so-called spectator shift to higher kinetic energies in spectrum "H" can clearly be seen compared to the normal Auger electron spectrum. The peak shape indicates an overlap of normal and spectator decay channels. The spectra "I" and "J" recorded at higher photon energies (σ^* O K-edge peak and 4sp hybridized peak, respectively) showed a greater relative contribution of the normal Auger electrons pointing towards intermediate excited states of rather delocalized character, i.e. where the excited electron is not localized in the vicinity of the core hole. Still, also in these spectra an overlap of normal and spectator Auger electrons may occur. Furthermore, it can be seen in Figure A.8 (b) that essentially no resonant enhancement (participant autoionization) occurred in the valence band region of the sample upon excitation at the O K-edge (spectra "G–J").

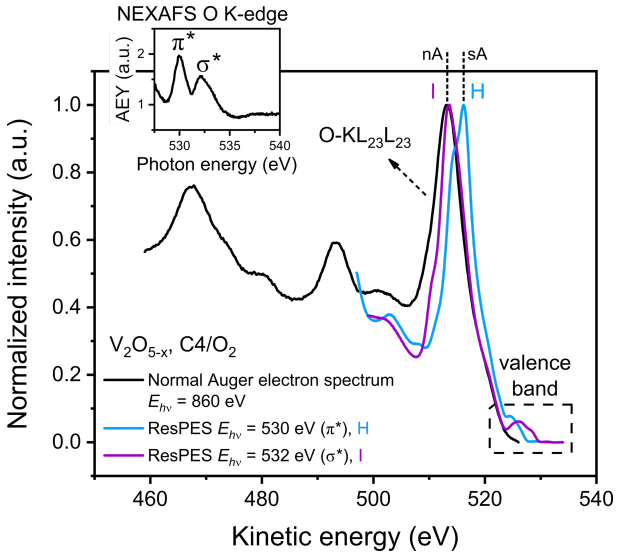

Figure A.9.: Comparison of normalized V_2O_{5-x} resPES spectra recorded at the O K-edge ($E_{h\nu}$ = 530 and 532 eV) with normal Auger electron spectrum of the sample ($E_{h\nu}$ = 860 eV), which is dominated by the O-$KL_{23}L_{23}$ Auger transition, in C_4H_{10}/O_2 (400 °C, 25 Pa). The inset shows the NEXAFS spectrum of the sample with the π^*-σ^* O K-edge doublet peak.

In summary, the excitation at the O K-edge was primarily followed by Auger decay channels, whereas the resonant enhancement of valence band features was negligible. Contributions from both spectator and normal O-$KL_{23}L_{23}$ Auger electrons were observed. In the spectrum recorded at 530 eV corresponding to the π^* peak of the O K-edge doublet, the shift of the most intense Auger peak to higher kinetic energies by ∼2.9 eV is clearly seen compared to the normal Auger electron spectrum of the sample. The peak maximum was therefore labeled as "sA" O-$KL_{23}L_{23}$ Auger line in Figure A.9. This indicates a partially localized character of the intermediate excited state of the O 1s → π^* transition, because the spectator screening depends on the distance of the excited electron from the core hole.[167] At higher photon energies corresponding to the σ^* O K-edge peak, the relative contribution of normal Auger electrons became more pronounced in the spectra of V_2O_{5-x}. Here, the peak maximum coincided with the one of the normal Auger electron spectrum of the sample with E_{kin} of ∼513.2 eV, in agreement with the literature value of 513.4 eV for a V_2O_5 single crystal,[82] which was therefore assigned as "nA" O-$KL_{23}L_{23}$ Auger peak in Figure A.9. The greater contribution of the spectator Auger decay channel in case of the

(more localized) π^* O K intermediate excited state (weaker V 3d–O 2p π-overlap) compared to the excitation at the σ^* or the "4sp" O K-edge peak of V_2O_{5-x} is similar to the observations for $NaNO_2$ measured at photon energies corresponding to the O K absorption edge in terms of a dominant contribution of spectator Auger electrons at excitation energies close to 531 eV, whereas mostly the normal O-KVV Auger electron spectrum was observed at an excitation energy of 536.5 eV.[169] An overlap with Auger electrons was also reported for several systems, for instance in the resPES spectra of various vanadium oxides recorded at the V L-edge,[78,205] in $(V_{1-x}Cr_x)_2O_3$,[206] or in $In_{2-x}V_xO_3$.[207] The spectator Auger decay was found to dominate in V_2O_{5-x} for the excitation at the more localized π^* O K-edge peak compared to the σ^* peak.

B. Supporting Information – *Operando* Electrical Conductivity and Complex Permittivity Study on Vanadia Oxidation Catalysts*

Anna M. Wernbacher, Maik Eichelbaum, Thomas Risse, Sébastien Cap, Annette Trunschke, and Robert Schlögl

B.1. Sample Characterization

A description of the VPP sample preparation can be found elsewhere.[39] The catalyst was pelletized with 1 wt-% graphite and activated in an *n*-butane oxidation gas feed (2% *n*-butane / 3% H_2O in air, 1 ppm triethylphosphate) for about 500 h after a thermal treatment (in air and in N_2/H_2O 1:1), see Eichelbaum *et al.*[39] In the *operando* MCPT measurements a sieve fraction of 100 to 200 μm of the crushed catalyst pellets was investigated.

X-ray fluorescence (XRF) measurements were performed on a Bruker Pioneer S4 Spectrometer. The V_2O_5 sample (SN 22054) was found to consist of 100 wt-% V_2O_5 and the VPP sample (SN 12831) showed 56.4 wt-% V_2O_5 and 43.6 wt-% P_2O_5 (P/V atomic ratio of 1.0).

X-ray powder diffraction (XRPD) measurements were conducted on the Bruker AXS D8 Advance II theta/theta diffractometer (Ni filtered Cu Kα radiation). The powder diffractograms of the VPP samples (SN 12831 and 10449) are shown in Figure B.1 together with the one of a VPP sample (SN 22698) after the *operando* MCPT conductivity measurements, where the main reflections of the vanadyl pyrophosphate crystal structure (ICSD 280777) are indexed. The corresponding powder diffractograms of the fresh (SN 22054) and used V_2O_5 samples after the operando MCPT measurements (SN 24399) and the ICSD entry of α-V_2O_5 (60767) is shown in Figure B.2 together with the assignment of the main reflections.

The peaks below 2θ of 14° in the XRD pattern of the unpretreated VPP samples 12831 and 10449 in Figure B.1 may be ascribed to the hydrated phases $(VO)(HPO_4)(H_2O)_4$ and $(VO)_3(PO_4)_2{\cdot}6H_2O$.

*Reprinted with permission from Wernbacher, A. M.; Eichelbaum, M; Risse, T.; Cap, S.; Trunschke, A.; Schlögl, R. Operando Electrical Conductivity and Complex Permittivity Study on Vanadia Oxidation Catalysts. *J. Phys. Chem. C* **123**, 8005–8017 (2019), DOI: 10.1021/acs.jpcc.8b07417. Copyright 2018 American Chemical Society.

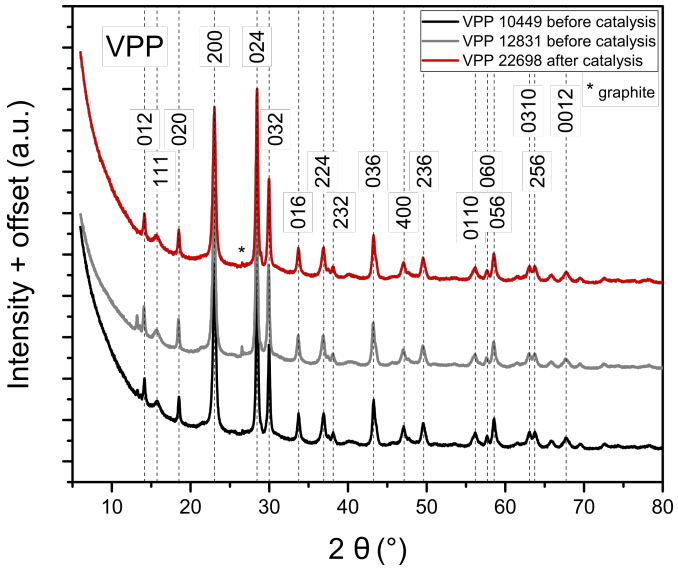

Figure B.1.: X-ray powder diffractograms of VPP samples (SN 12831 and 10449) and of VPP sample after MCPT conductivity measurements (SN 22698).

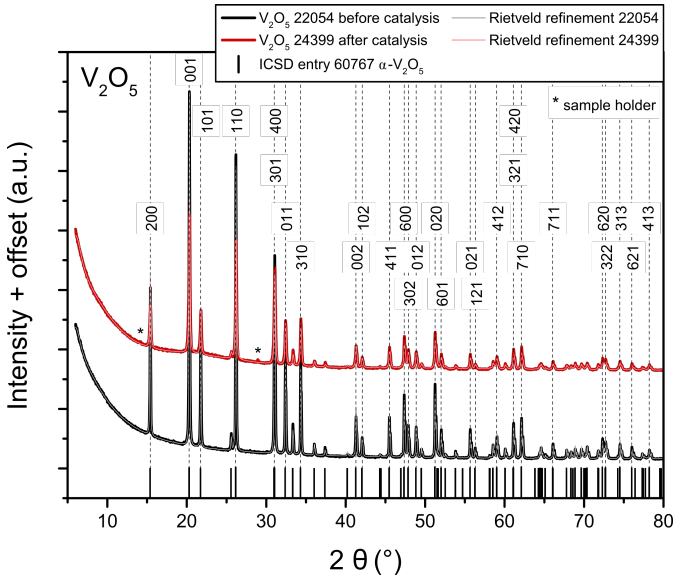

Figure B.2.: X-ray powder diffractograms of V_2O_5 sample (SN 22054) and of V_2O_5 sample after MCPT conductivity measurements (SN 24399). The Rietveld fit of the two samples is shown in gray and in light red on top of the measured diffractograms, respectively.

High-resolution transmission electron microscopy (TEM) imaging of the VPP sample (Figure B.3 (a)) was performed on the JEOL JEM-ARM200F, operated at 200 kV acceleration voltage, using a low dose due to a beam induced sample transformation (electron dose of about 2 $\mu A/cm^2$). In the beginning all VPP particles were crystalline with a very small amorphous part (ca. 1 - 2 nm) on top, which started to grow with prolonged time under the electron beam until the particles became completely amorphous. The V_2O_5 sample likewise showed beam damage effects with an oxygen loss and a transformation to lower vanadium oxides starting from the surface (Figure B.3 (b), JEOL JEM-ARM200F).

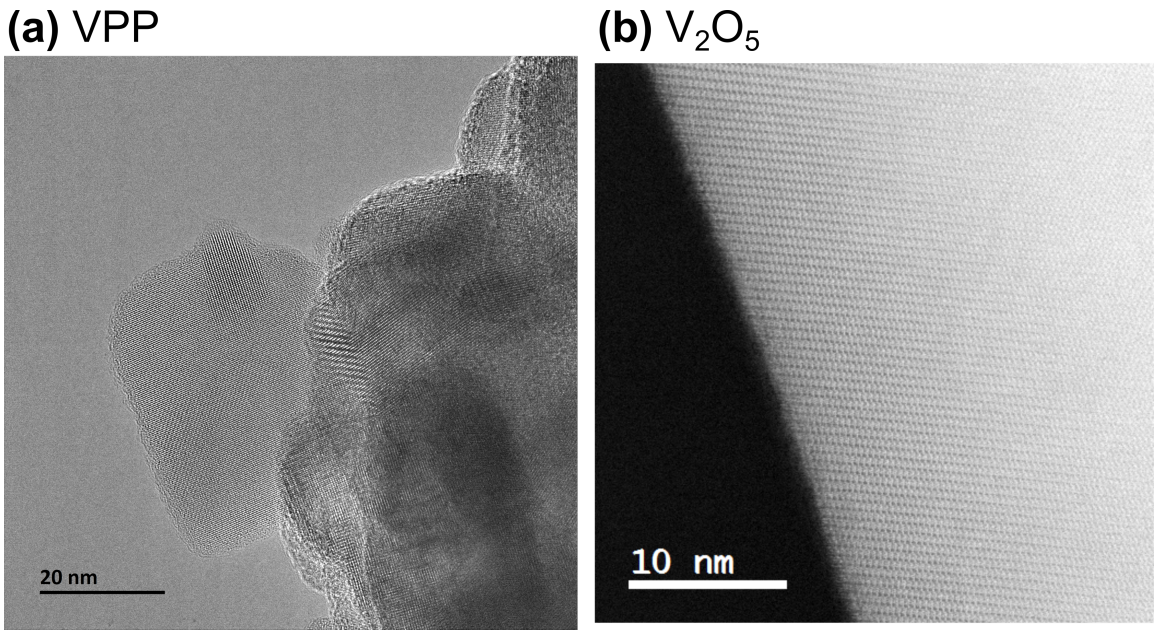

Figure B.3.: (a) High resolution TEM micrograph of the VPP sample (SN 12831, electron dose ∼2 $\mu A/cm^2$); **(b)** annular dark field (ADF) STEM micrograph of the V_2O_5 sample (SN 22054).

B.2. MCPT Conductivity and Permittivity

B.2.1. Correlations between Permittivity/Conductivity and Catalytic Performance

The electrical conductivity and complex permittivity of the vanadium oxide-based catalysts V_2O_5 and vanadyl pyrophosphate (VPP) were investigated during the oxidation of *n*-butane (2% C_4H_{10} / 20% O_2 in N_2) at 400 °C with total gas flows ranging from 2 to 30 ml/min. The response of VPP to different contact times (total gas flows) was tested in three different microwave resonators operating at resonant frequencies from ∼3 to 10 GHz using the TM_{010} and TM_{020} modes. Furthermore, two different VPP samples batches (no. 12831 and no. 10449) were investigated. The electric and magnetic field distributions of the two modes are depicted in Figure B.4.

The results of the repeated contact time variation experiments of VPP are shown in Figure B.5 to Figure B.7. The conductivity changes induced by different reactant conversions in one gas feed were found to be much less pronounced than the changes in between different gas feeds. In order to resolve the small changes of the less conductive VPP at increasing *n*-butane conversion, the measurements had to be conducted in smaller microwave resonators, which exhibit a larger sample/resonator volume ratio (cf. Figure B.5 (c)) and hence a greater perturbation in addition to a higher resonant frequency. Furthermore, the second mode TM_{020} was found to be stable and sensitive to changes of the sample. The absolute conductivity could be influenced by the frequency, which should be considered in a comparison of V_2O_5 with VPP in these contact time variation experiments since V_2O_5 was measured at ∼3 GHz. Nevertheless, the trends of the conductivity changes with *n*-butane conversion (i.e. at different contact times) can be compared in any case.

The conductivity response of the two VPP sample batches in the contact time variation experiments is presented in Figure B.5 (a) as time on stream plot in 2% *n*-butane / 20% oxygen

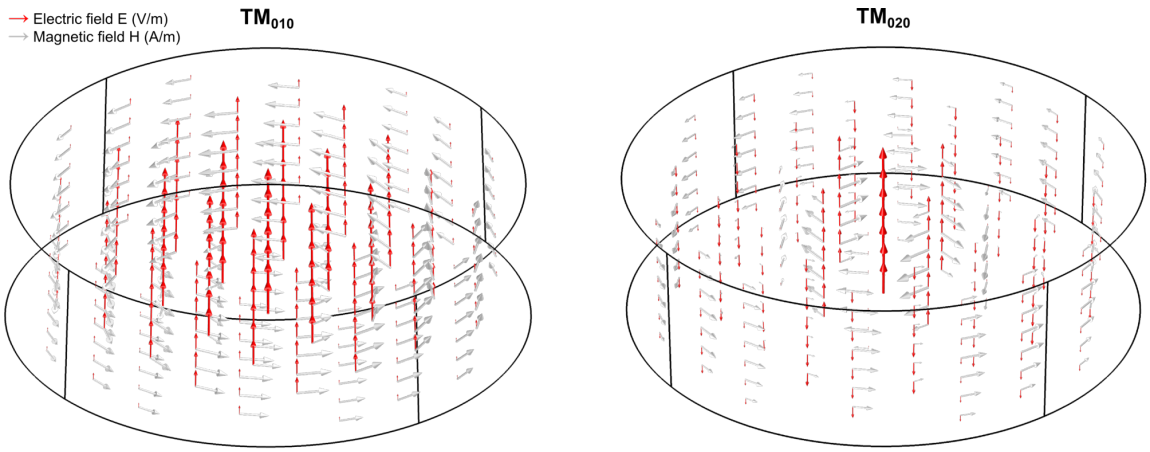

Figure B.4.: Numerically simulated electric field (red arrows) and magnetic field (light gray arrows) inside a cylindrical microwave cavity (left: TM_{010} mode; right: TM_{020} mode) with FEM package COMSOL Multiphysics 5.1, RF module.

in N_2 at 400 °C. The electrical conductivity of VPP was not found to be significantly influenced by the frequency showing an average value of $2.0 \cdot 10^{-2}$ S/m in all the microwave resonators and modes, which were measured over a time period of two years in the *in situ* MCPT setup. This value is also in good agreement with the reported $1.7 \cdot 10^{-2}$ S/m of VPP at 400 °C in 3% propane / 6% oxygen in N_2 (5 GHz, TM_{010} mode),[123] in particular given the expected lower conductivity of the p-type semiconductor VPP in a more reducing gas feed. This finding suggests that also the absolute conductivity of VPP from the contact time variation experiments can be compared to the one of the much more conductive V_2O_5. Still, a seemingly lower conductivity of VPP was observed in one single measurement at 7 GHz shown in gray in Figure B.5 (a), which may be attributed to the usage of a "wrong" microwave mode given the close vicinity of other modes to the intended TM_{020} mode.
In order to show the small conductivity changes of VPP at different contact times, an offset plot of the conductivity as a function of time on stream at 400 °C is presented in Figure B.5 (b). It can be seen in Figure B.5 (b) that hardly any conductivity response could be detected in the ∼3 GHz resonator, which exhibits the smallest sample/resonator volume ratio as shown in Figure B.5 (c). The best signal stability and resolution of the conductivity changes was found in a smaller microwave cavity operating at ∼10 GHz (TM_{020} mode), which was therefore chosen for a further analysis of the correlation between conductivity and catalytic performance.

Figure B.6 shows the response of the real part of the permittivity ε' of VPP in the contact time variation experiments. The inset, which is highlighted in gray, is a magnification of the first three measurements in the 3 GHz and 5 GHz resonators. Interestingly, the real part of the permittivity of VPP showed no changes at different *n*-butane conversions as opposed to the response of ε' of V_2O_5 in the contact time variation experiments. This observation holds generally true, as can be seen in Figure B.6 for the two VPP sample batches (no. 12831 and no. 10449) in the different resonators from ∼3 to 10 GHz and using the TM_{010} and TM_{020} modes. In addition, there seems to be an increase of ε' with increasing operating frequency, disregarding again the 7 GHz "TM_{020}" measurement shown in gray.

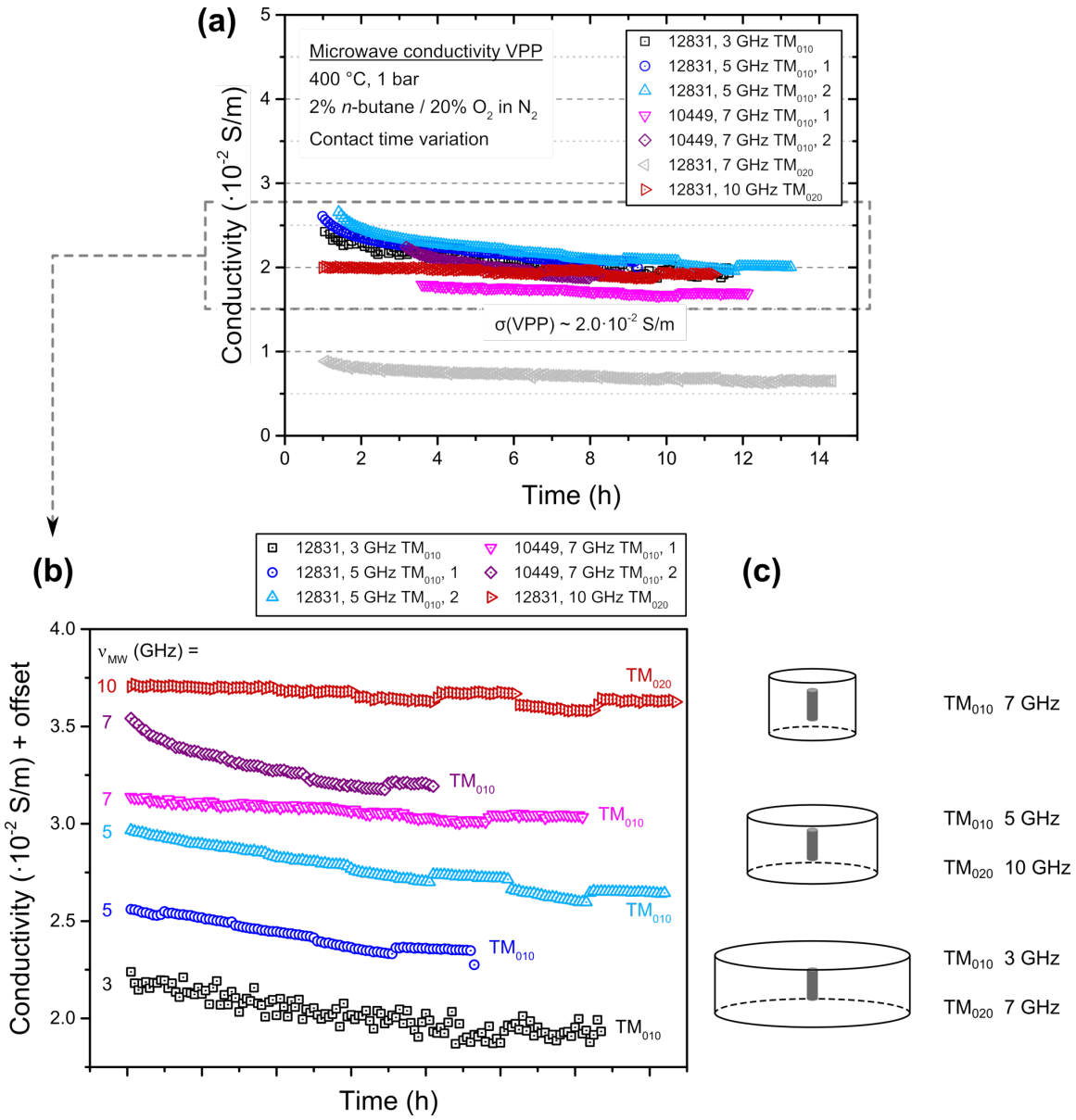

Figure B.5.: **(a)** MCPT contact time variation experiments of VPP at 400 °C in 2% *n*-butane / 20% oxygen in N_2 measured in three different resonators (increasing sample/resonator volume ratio and resonant frequency) using two microwave modes (TM_{010} and TM_{020}) and two different VPP sample batches (no. 12831 and no. 10449); **(b)** offset plot of the conductivity measurements in order to show the small changes at different contact times; **(c)** schematic representation of the different sample-loaded microwave resonators.

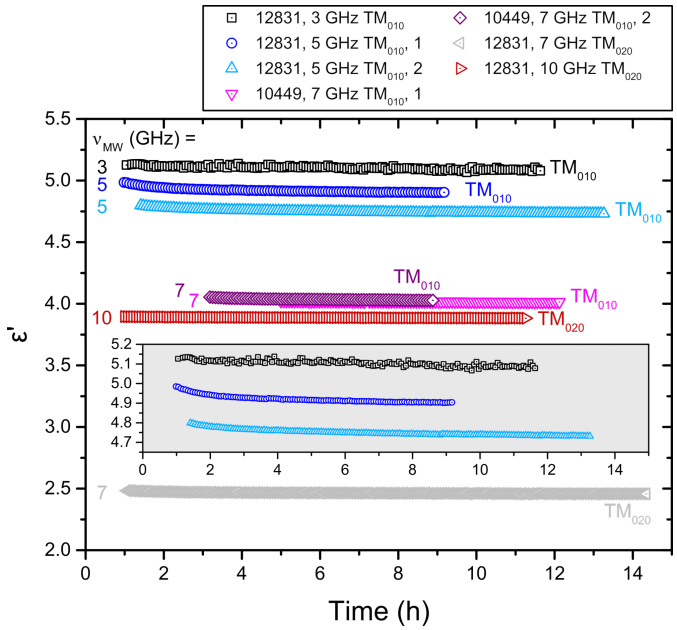

Figure B.6.: Real part of permittivity of VPP from MCPT contact time variation experiments in Figure B.5: measurements using TM_{010} and TM_{020} modes in different resonators of the VPP samples no. 12831 and no. 10449 at 400 °C in 2% *n*-butane / 20% O_2 in N_2.

The catalytic performance of VPP recorded with online GC during the MCPT contact time variation experiments is shown in Figure B.7 in terms of a selectivity-conversion plot. A stable average maleic anhydride selectivity of about 72% was observed over a comparatively wide range of *n*-butane conversions, together with selectivities of approx. 18% and 10% to CO and CO_2, respectively.

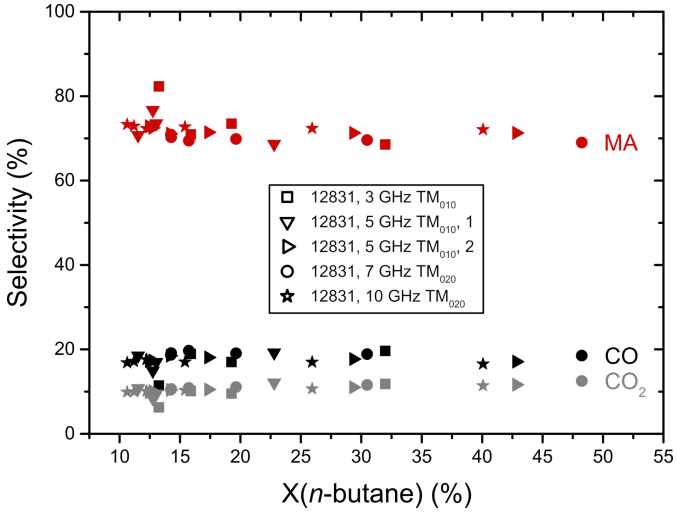

Figure B.7.: Selectivity-conversion (S-X) plot from MCPT contact time variation experiments in Figure B.5: VPP sample no. 12831 at 400 °C in 2% *n*-butane / 20% O_2 in N_2.

B.2.2. Redox Properties

The V_2O_5 sample showed reversible conductivity changes in different gas feeds (2% *n*-butane / 20% O_2 in N_2, 20% O_2 in N_2, 100% N_2, 2% *n*-butane / 20% O_2 in N_2; "redox response"). The

oxidation of V_2O_5 in the 20% oxygen in nitrogen gas feed, which lead to a conductivity decrease due to a consumption of charge carriers,[85]

$$O_2\,(\text{ads}) + 2\ V_O^{\bullet\bullet} + 4\ e' \ \rightarrow \ \ 2\ O_O^x \tag{B.1}$$

proceeded slower and after two hours no steady state of was reached. This was also reported in the literature,[104] where a combination of a fast surface oxidation process and a slower process involving the healing of oxygen vacancies V_O was suggested (see above in Eq. (B.1)).[104] In line with this interpretation, the conductivity and permittivity response can be described by an exponential decay in the O_2/N_2 gas feed with two rate constants.

The 100% nitrogen feed acted slightly reducing compared to the O_2/N_2 gas feed, which may be due to oxygen loss at 400 °C in an O_2-free gas atmosphere. The following treatment of V_2O_5 in the reaction gas feed proved the reversibility and stability of the catalyst.

In non-stoichiometric oxides like V_2O_5 that are prone to oxygen loss ("V_2O_{5-x}"), for instance in reducing gas atmospheres or under ultra-high vacuum at elevated temperatures,[85,86,314–316] the oxygen vacancies are believed to be a source of charge carriers (electrons) and are thus related to the electrical conductivity.[85,222,237] The remaining electrons were shown to be localized at vanadium centers (filled V 3d levels) in the neighborhood of the oxygen vacancies or increasingly freed at higher temperatures.[184,222,232,316–319] Perlstein, however, stated that there is probably no simple relation between the oxygen vacancies and the electrical conductivity in vanadium pentoxide.[238] Similarly, it may be assumed that the situation in vanadyl pyrophosphate is likewise more complicated.

The absorption below 500 to 600 nm in the spectra of V_2O_5 in Figure B.8 (a), which has a band gap of about 2.0 to 2.2 eV,[320,321] is due to O^{2-}–V^{5+} ligand-to-metal charge transfer (LMCT) transitions.[233,322] In addition to the CT transition, also transitions from V^{4+} ($3d^1$) can contribute to the spectra of partially reduced V_2O_5.[232,233] In the literature, the NIR absorption of V_2O_5 is attributed to transitions from $3d^1$ states and their intensity increases with increasing amount of V^{4+}.[232] This can be seen in the present study on V_2O_5 by the increase of the absorption before the CT edge in the region of the "baseline" in the reducing reaction gas feed, see the inset in Figure B.8 (a). In the oxidizing O_2/He gas feed, a decrease of the intensity in this region was observed, which indicates a decrease in the number of the V^{4+} centers.

This effect was also shown in a study on supported V_2O_5 on ZrO_2 in the literature, where an increasing intensity below the absorption edge with increasingly reducing gas feeds at 300 °C was clearly demonstrated,[233] see also the work by Heine *et al.*[104] on V_2O_5 in *n*-butane- and O_2-containing gas atmospheres.[104]

In Figure B.8 (b) the similarity of the MCPT conductivity changes in the different gas feeds at 400 °C to the changes in the intensity at 775 nm in the DR-UV-Vis spectra of V_2O_5 can be seen. Hence, both the increased absorption (Kubelka-Munk function F(R)), which was attributed to V^{4+} centers, and the MCPT conductivity are caused by the same effects, i.e. an increased reduction of the V_2O_5 sample leading to a higher electrical conductivity of the n-type semiconductor in the reaction gas feed. This correlation between the DR-UV-Vis measurements and the MCPT experiments strongly supports the interpretation of the response of the conductivity and of ε'' as due to a change in the number of charge carriers.

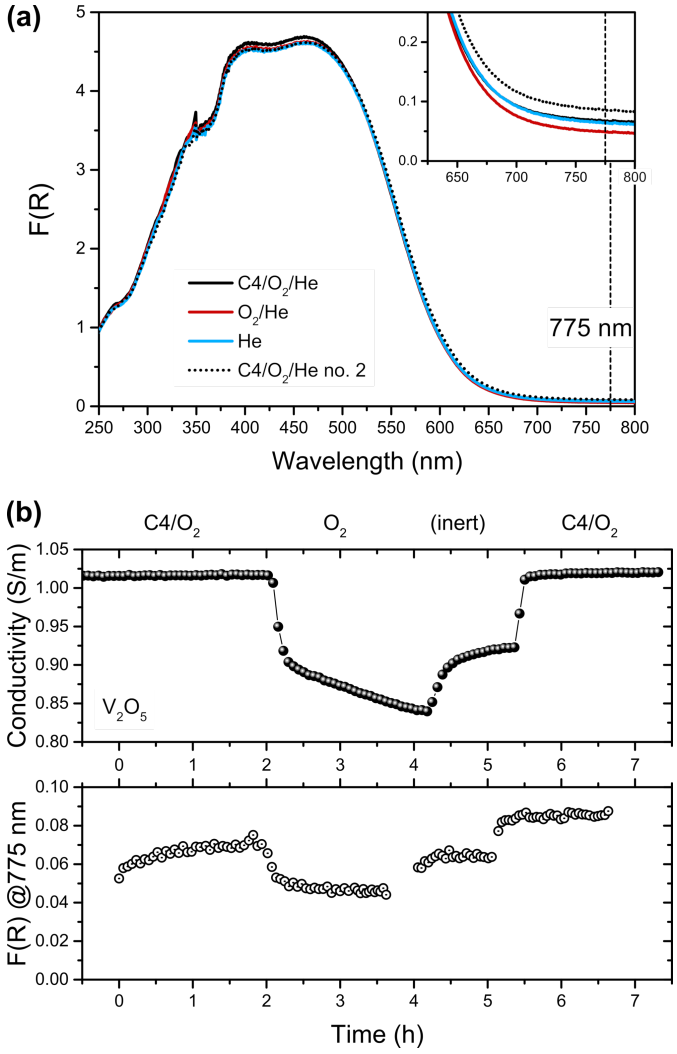

Figure B.8.: **(a)** DR-UV-Vis spectra of V_2O_5 recorded at 400 °C in different gas feeds (average spectra); **(b)** comparison of MCPT conductivity and absorption at 775 nm as time on stream plots in different gas feeds.

The DR-UV-Vis experiments were also extended to the p-type VPP, which has a bulk vanadium oxidation of +4. The DR-UV-Vis spectra of VPP are presented in Figure B.9 (a) at 400 °C. Here, the average spectra in the respective gas feeds are shown and the assignment of the bands according to literature is indicated in the figure. Furthermore, the absorption of VPP at 385 nm (in terms of the Kubelka-Munk function F(R)) is compared to the electrical conductivity response in Figure B.9 (b).

VPP showed the same redox behavior as V_2O_5 in the different gas feeds, except that the conductivity increased in the oxidizing gas feeds (increase of the majority charge carries, i.e. holes)[60]

$$O_2\,(\text{ads}) + 2\,V_O^{\bullet\bullet} \quad \rightarrow \quad 2\,O_O^x + \,4\,h^{\bullet} \tag{B.2}$$

and decreased upon reduction. The trapping of a hole by lattice oxygen can lead to the creation

of a reactive O^- species (or "$O_O^\bullet$").[60,95]

$$O_O^x + h^\bullet \rightleftharpoons O_O^\bullet \quad / \quad V^{5+} + O^{2-} \rightleftharpoons V^{4+} + O^- \tag{B.3}$$

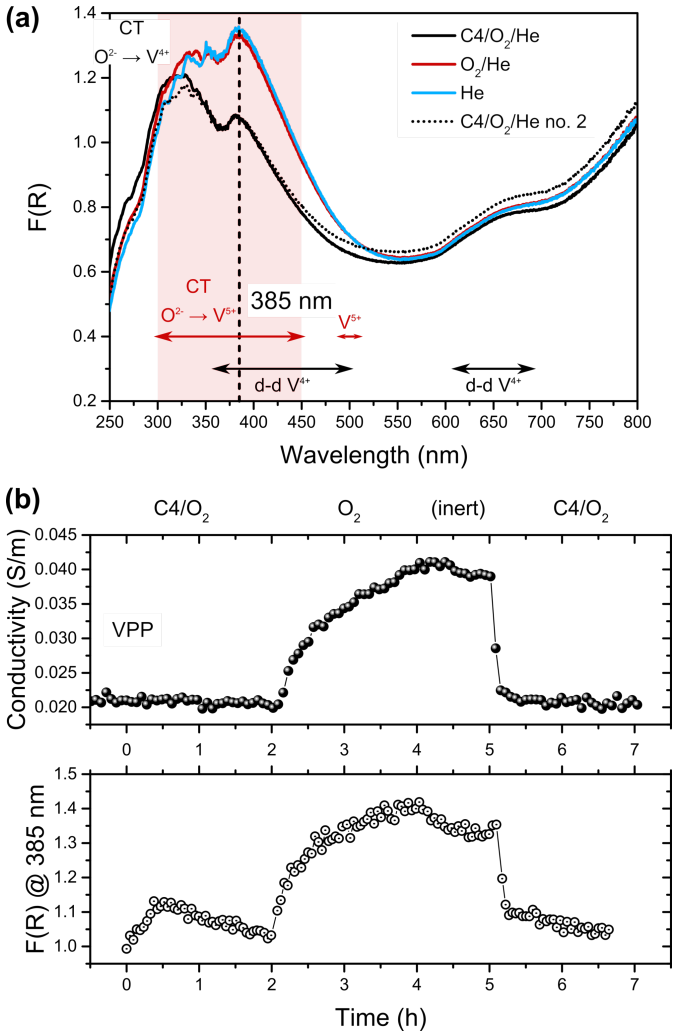

Figure B.9.: **(a)** DR-UV-Vis spectra of VPP recorded at 400 °C in different gas feeds (average spectra); **(b)** comparison of MCPT conductivity and absorption at 385 nm as time on stream plots in different gas feeds.

As was discussed above for V_2O_5, the reduction of VPP in $C_4H_{10}/O_2/N_2$ also proceeded faster than the oxidation in O_2/N_2, where no steady state was reached after two hours. The conductivity of VPP stabilized in the subsequently applied 100% nitrogen gas feed, which stopped the ongoing oxidation. The initial conductivity of $2{\cdot}10^{-2}$ S/m was then reached again by the treatment of VPP in the last reaction gas feed.

The absorption bands of VPP between 250 and 500 nm are due to ligand-to-metal charge transfer transitions. The O^{2-}–V^{4+} CT band occurs below 300 nm[234,323–325] and overlaps with the LMCT band of O^{2-}–V^{5+} that appears at a lower energy[234–236,324] exhibiting a maximum at about 385 nm as indicated in Figure B.9 (a). In addition, some authors have reported a contribution of the energetically highest lying d-d transition of V^{4+} to this region.[236,323] The following d-d transition can also be seen in the spectra between 600 and 700 nm.[235,236,323–325]

The Kubelka-Munk function at 385 nm increased upon oxidation of VPP in the 20% O_2 in He gas feed indicating a higher amount of V^{5+}. The subsequent 100% He feed was found to be inert in line with the 100% nitrogen gas feed in the MCPT conductivity measurements, i.e. no change of the V oxidation state was observed in this gas feed. The redox response of VPP was found to be reversible, which can be seen by the decrease of F(R) at 385 nm (i.e. of the oxidation state) upon returning to the reaction gas feed, see the dotted line in Figure B.9 (a). In Figure B.9 (b) the electrical conductivity of VPP is compared to the Kubelka-Munk function at 385 nm at 400 °C in the different gas feeds. It can be seen that both curves follow the same trends as a function of time on stream. The MCPT conductivity changes can thus be attributed to the reversible oxidation/reduction of vanadium (occupation of V 3d states) like in the case of V_2O_5. This correlation is clearer in the case of VPP, because for V_2O_5 the absorption bands of V^{4+} lie in the IR region and in the DR-UV-Vis spectra only changes in the "baseline" below the absorption edge were detected.

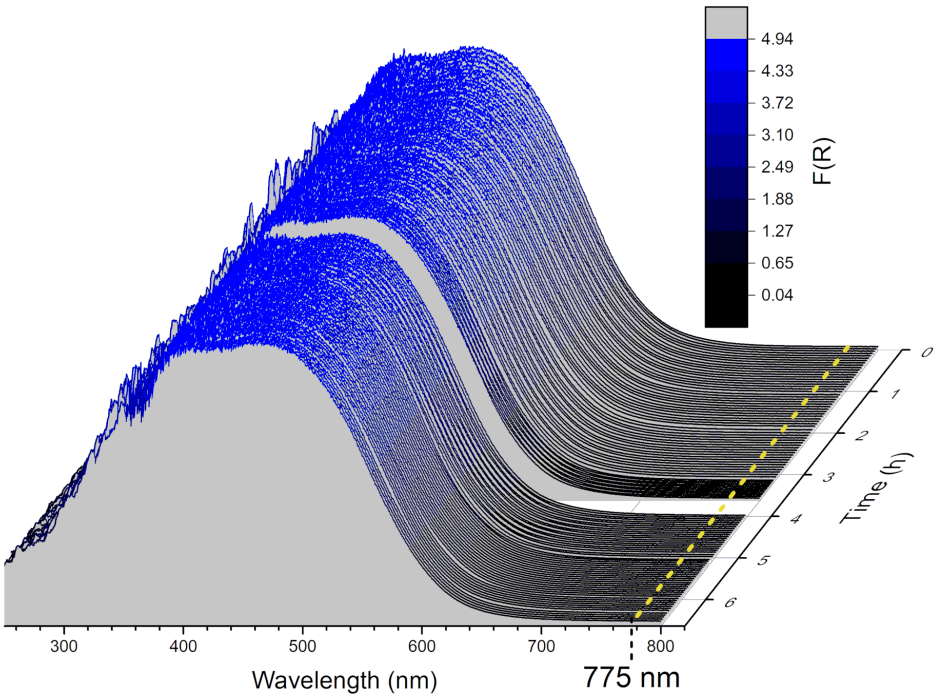

Figure B.10.: DR-UV-Vis spectra of V_2O_5 recorded at 400 °C in different gas feeds (2% C_4H_{10} / 20% O_2 in He, 20% O_2 in He, 100% He, 2% C_4H_{10} / 20% O_2 in He). The evolution of Kubelka-Munk function F(R) at 775 nm is indicated by the dashed line.

The DR-UV-Vis spectra of V_2O_5 in different gas feeds are shown in Figure B.10 as Kubelka-Munk function F(R) with time on stream at 400 °C. The absorption at 775 nm is indicated by the dashed line.

The DR-UV-Vis spectra of VPP as Kubelka-Munk function F(R) with time on stream at 400 °C in different gas feeds are shown in Figure B.11 (a) together with a schematic presentation of the three d-d transitions of the vanadyl ion in approximate local C_{4v} symmetry in Figure B.11 (b).

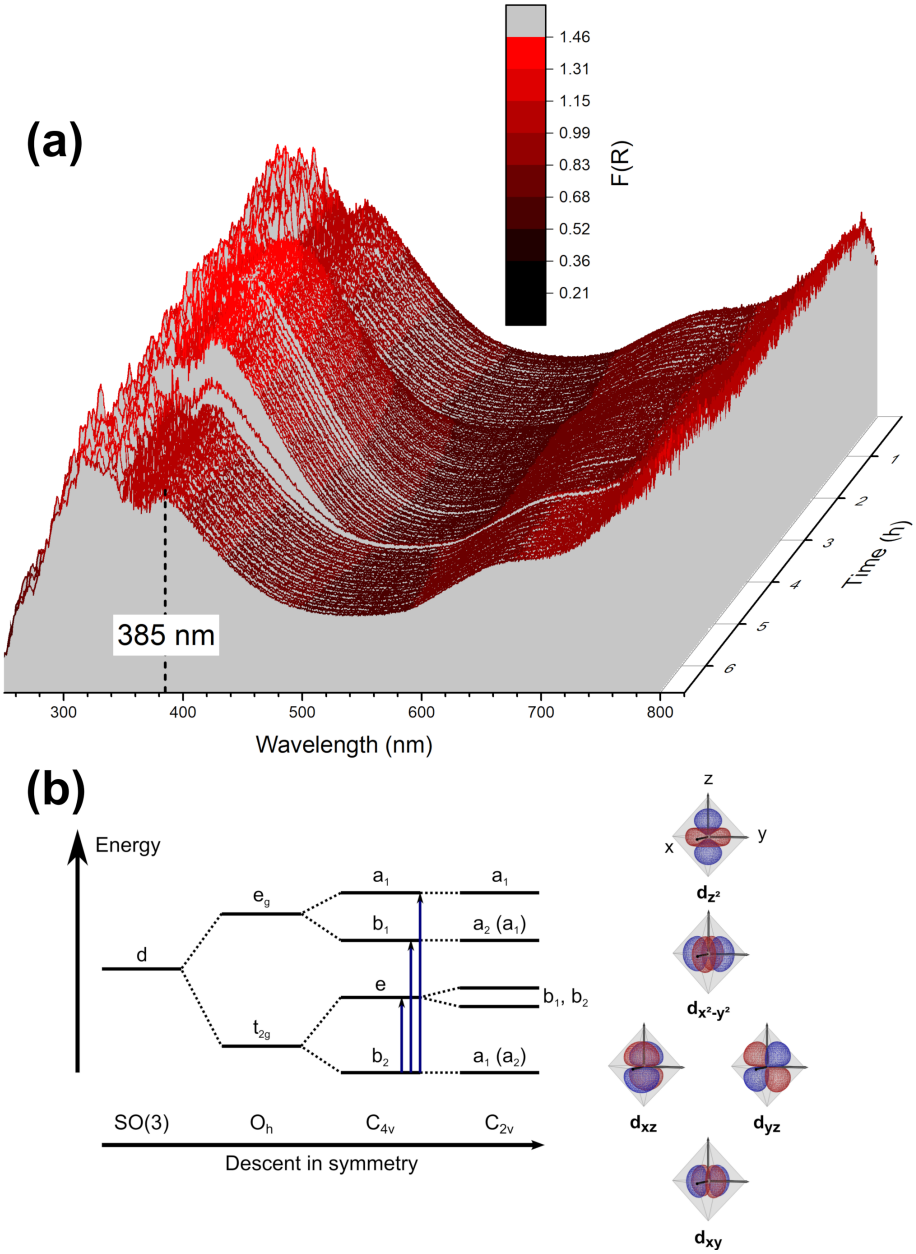

Figure B.11.: **(a)** DR-UV-Vis spectra of VPP recorded at 400 °C in different gas feeds (2% C_4H_{10} / 20% O_2 in He, 20% O_2 in He, 100% He, 2% C_4H_{10} / 20% O_2 in He) and evolution of Kubelka-Munk function F(R) at 385 nm. **(b)** Scheme of the three d-d transitions of the vanadyl ion in approximate local C_{4v} symmetry showing the often-used nomenclature based on the irreducible representations in the C_{4v} group.

B.2.3. Temperature Dependence of Conductivity and Permittivity

The experimental procedure of the temperature-dependent MCPT measurements is shown for the example of V_2O_5 measured in 20% O_2 in N_2 in Figure B.12 in terms of the Q factor change at different temperatures.

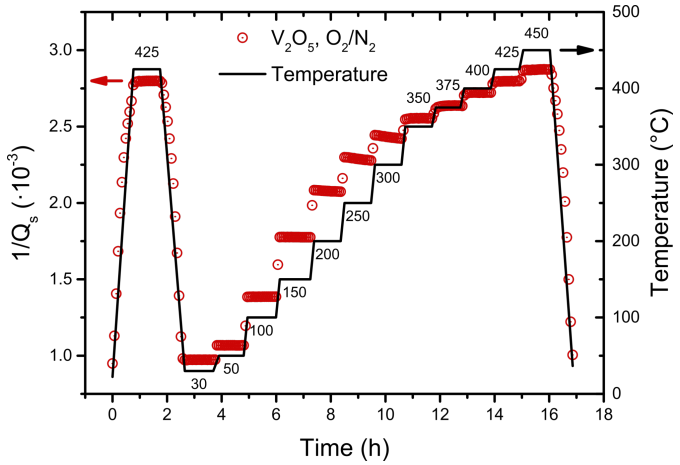

Figure B.12.: Experimental procedure of temperature-dependent MCPT measurements: change of reciprocal Q factor ($1/Q_s$) of V_2O_5-loaded microwave resonator (∼3 GHz; TM_{010}) as a function of time in 20% O_2 in N_2, and corresponding temperatures from 30 to 450 °C, which are also indicated by the numbers.

The temperature-dependent MCPT measurements of V_2O_5 in the different gas feeds (2% *n*-butane / 20% O_2 in N_2, 20% O_2 in N_2, and 100% N_2) are shown in Figure B.13 in terms of the reciprocal Q factor change and the resonant frequency shift compared to the empty cavity measurement.
The corresponding plot of the temperature-dependent MCPT measurements of VPP in the different gas feeds is presented in Figure B.14.

Figure B.13 and Figure B.14 show that the reciprocal Q factor change of V_2O_5 first increased until about 200 °C, but then the increase leveled off, whereas the reciprocal Q factor change of VPP kept rising. The resonant frequency shift of both samples was also increasing with temperature, however, to a smaller extent.
At first glance there seems to be a similarity between the shape of the reciprocal Q factor change of V_2O_5 as a function of temperature and the reported depolarization peak,[138,269] still it should be emphasized that we are showing a plot of $(1/Q_s - 1/Q_0)$ vs. T in contrast to the logarithmic plots as a function of the reciprocal temperature that are found in literature, because, in fact, we observed still rather small changes as compared to the increase in the reciprocal Q factor change over several orders of magnitude (e.g. 10^{-5} to 10^{-2}) that was reported in literature.[138] This is also in line with the finding that neither V_2O_5 nor VPP reached the intrinsic conduction regime in the investigated temperature range (30 to 450 °C), as expected given the rather large band gaps (about 2 eV for V_2O_5).[320,321] In addition, the resonant frequency shift also showed rather small changes with temperature, yet it is not independent of temperature, which would occur upon reaching the high conductivity region above the depolarization crossover.[134]

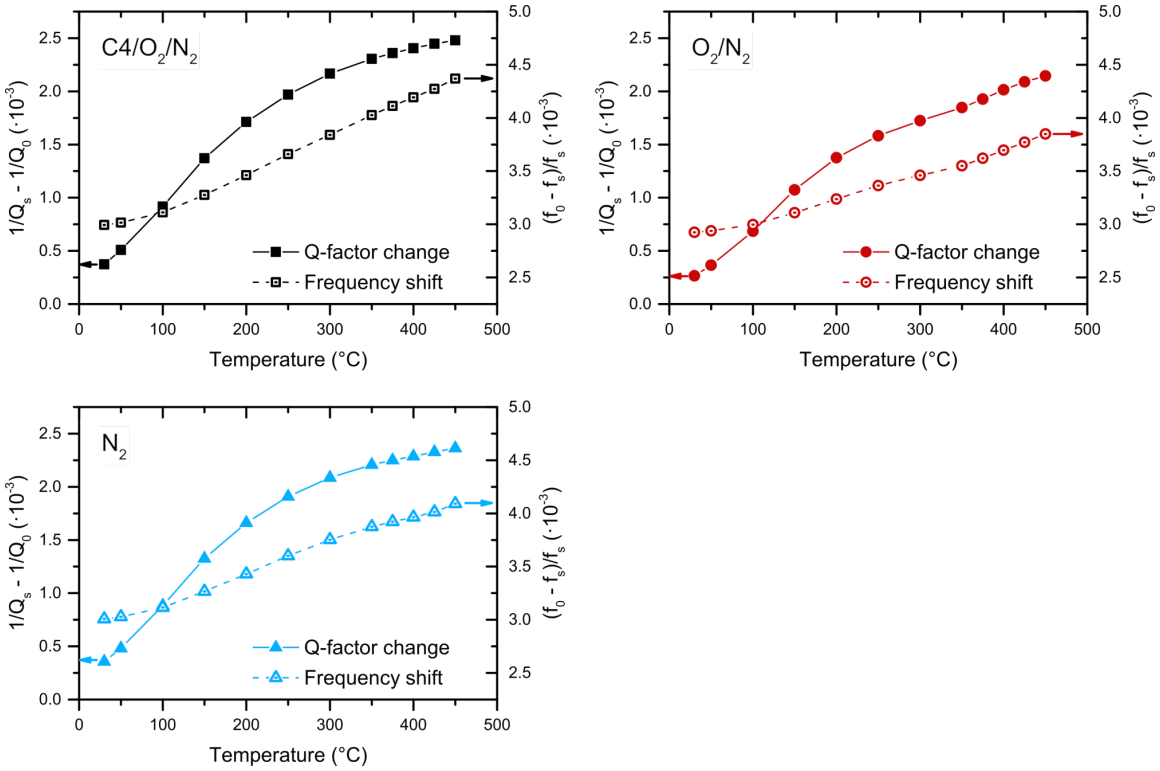

Figure B.13.: MCPT raw data of V_2O_5 (subscript "s") in different gas feeds (2% *n*-butane / 20% O_2 in N_2, 20% O_2 in N_2, 100% N_2) with respect to empty measurement (subscript "0"): change in reciprocal Q factor $(1/Q_s - 1/Q_0)$ and shift in resonant frequency $([f_0 - f_s]/f_s)$ as a function of temperature.

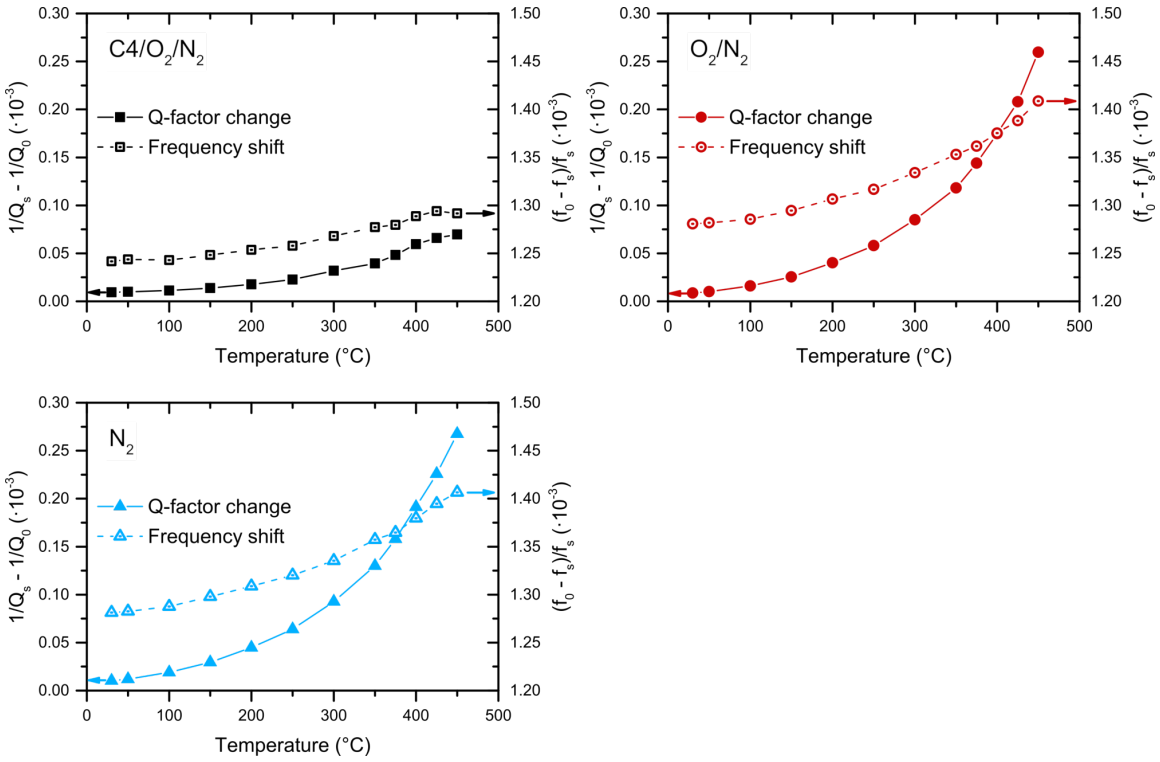

Figure B.14.: MCPT raw data of VPP (subscript "s") in different gas feeds (2% *n*-butane / 20% O_2 in N_2, 20% O_2 in N_2, 100% N_2) with respect to empty measurement (subscript "0"): change in reciprocal Q factor $(1/Q_s - 1/Q_0)$ and shift in resonant frequency $([f_0 - f_s]/f_s)$ as a function of temperature.

In order to be able to better compare our measurements to literature, Figure B.13 is plotted again as semi-logarithmic curve of the temperature-dependent MCPT measurements of V_2O_5 as a function of $1/T$ in Figure B.15.

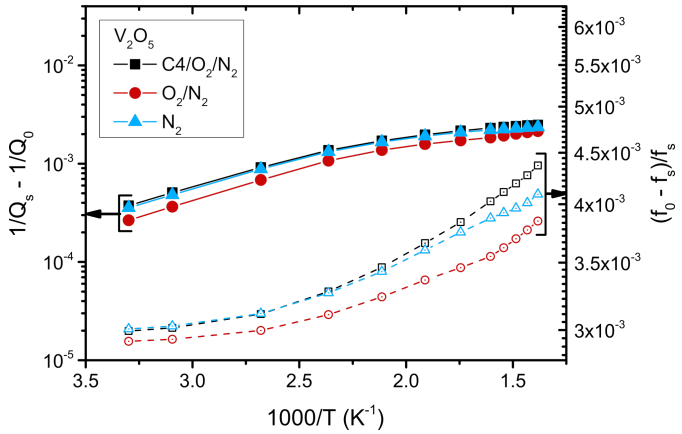

Figure B.15.: Reciprocal Q factor change and resonant frequency shift of V_2O_5 in different gas feeds as semi-logarithmic plot vs. $1/T$.

It is therefore assumed that the measurements of both V_2O_5 and VPP were conducted in the low-conductivity region of the depolarization regime, in which case the resonant frequency shift is proportional to the real part of the sample's permittivity and the change in the reciprocal Q factor is related to the imaginary part of the permittivity.[106,133,138]
Further support for this assumption is given by a comparison of the resonant frequency shift with the cavity filling factor (A (V_s/V_c)) divided by the depolarization factor "N"[138]

$$\frac{f_0 - f_s}{f_0} \ll A\frac{V_s}{V_c}\frac{1}{N} \tag{B.4}$$

which yields a value of $1.8{\cdot}10^{-2}$ with an estimated maximum depolarization factor of 0.1 (for a cylinder of 1.5 mm radius and 10 mm height)[133,134,326] compared to a much smaller frequency shift of V_2O_5 of $3.1{\cdot}10^{-3}$ at 400 °C in 2% n-butane / 20% O_2 in N_2 (~3 GHz, TM_{010}), and of VPP of $1.3{\cdot}10^{-3}$ under the same conditions. It is indeed often assumed that N is close to zero.[327] It may be noted that in this case, with the demonstrated validity of the microwave cavity perturbation equations[106] used in this work, also the condition[133]

$$\varepsilon'' < \varepsilon' - 1 + \frac{1}{N} \tag{B.5}$$

is satisfied with the determined powder conductivities of V_2O_5 and VPP of ε_p'' (V_2O_5) = 0.43 < ε_p' (V_2O_5) = 2.7 (σ_p (V_2O_5) = 0.077 S/m) and of ε_p'' (VPP) = 0.016 < ε_p' (VPP) = 1.7 (σ_p (VPP) = $2.8{\cdot}10^{-3}$ S/m), respectively. The above-mentioned depolarization peak should occur at much higher imaginary permittivities at $\varepsilon'' = \varepsilon' - 1 + 1/N$.[133]
Taken together, there is a strong probability that the resonant frequency shift can be directly related to the real part of the permittivity of V_2O_5 or VPP and hence to dielectric relaxation and the change in the reciprocal Q factor to the imaginary part of the permittivity, which is then used to calculate the conductivity of V_2O_5 or VPP.

The temperature dependence of the thus determined conductivities was then further inves-

tigated. Figure B.16 shows the conductivity and complex permittivity of V_2O_5 and VPP as a function of temperature from 30 to 450 °C in the different gas feeds 2% *n*-butane / 20% O_2 in N_2, 20% O_2 in N_2, and 100% N_2. Both the initial values are shown upon reaching the temperature and the steady-state values, which are average values after 1 hour at the respective temperature. Both samples were previously treated at 425 °C in the different gas feeds in order to remove adsorbates like water.

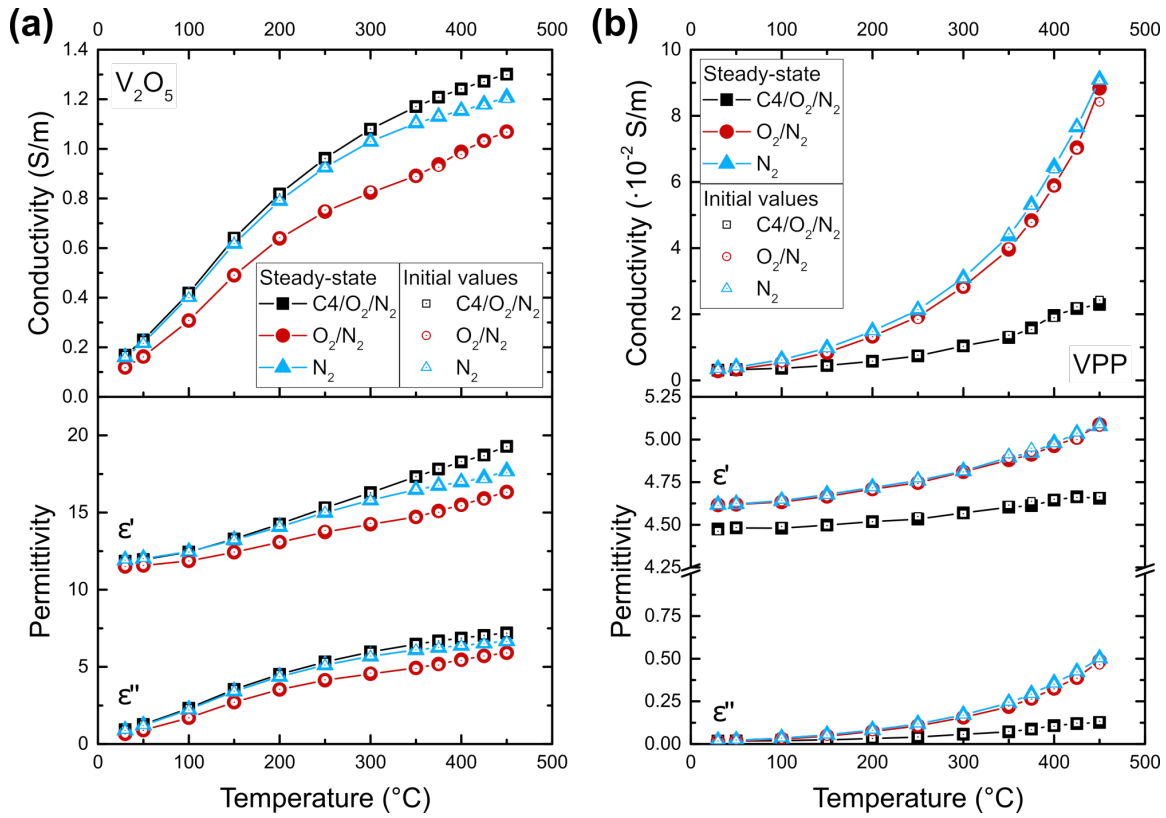

Figure B.16.: Temperature dependence of conductivity and complex permittivity in different gas feeds: **(a)** V_2O_5, **(b)** VPP. Both initial values after reaching a temperature (empty symbols) and steady-state values (filled symbols) are shown.

Already in the conductivity versus temperature curves in Figure B.16, differences between the two samples can be seen. First of all, V_2O_5 exhibited an initial steep increase in conductivity below 200 °C, which leveled off at higher temperatures. In contrast to this, the conductivity of VPP started to increase significantly only above ∼200 °C. Moreover, the comparison of the different gas feeds, $C_4H_{10}/O_2/N_2$, O_2/N_2, and N_2, revealed significant differences for VPP between the reaction gas feed (black squares in Figure B.16 (b)) and the other gas feeds. The conductivity of V_2O_5 in Figure B.16 (a) also followed the trends from before, i.e. a decrease of the conductivity with increasing oxidizing potential of the gas atmosphere $\sigma(C_4H_{10}/O_2/N_2) > \sigma(N_2) > \sigma(O_2/N_2)$. However, these gas-phase-dependent conductivity differences in the high temperature region were much more pronounced in VPP, in particular in the reaction gas feed. This is in line with the generally observed greater relative conductivity changes of VPP in different gas feeds. The initial conductivity (empty symbols in Figure B.16) and steady-state values (filled symbols) were found to be essentially the same. The permittivity of the samples likewise increased with temperature.

In order to investigate the charge transport mechanism in V_2O_5 and VPP, the temperature dependence of their conductivities was analyzed using different conduction models on the basis of semi-logarithmic conductivity vs. $1/T$ plots, which are shown in Figure B.17 for both V_2O_5 and VPP in the different gas feeds.

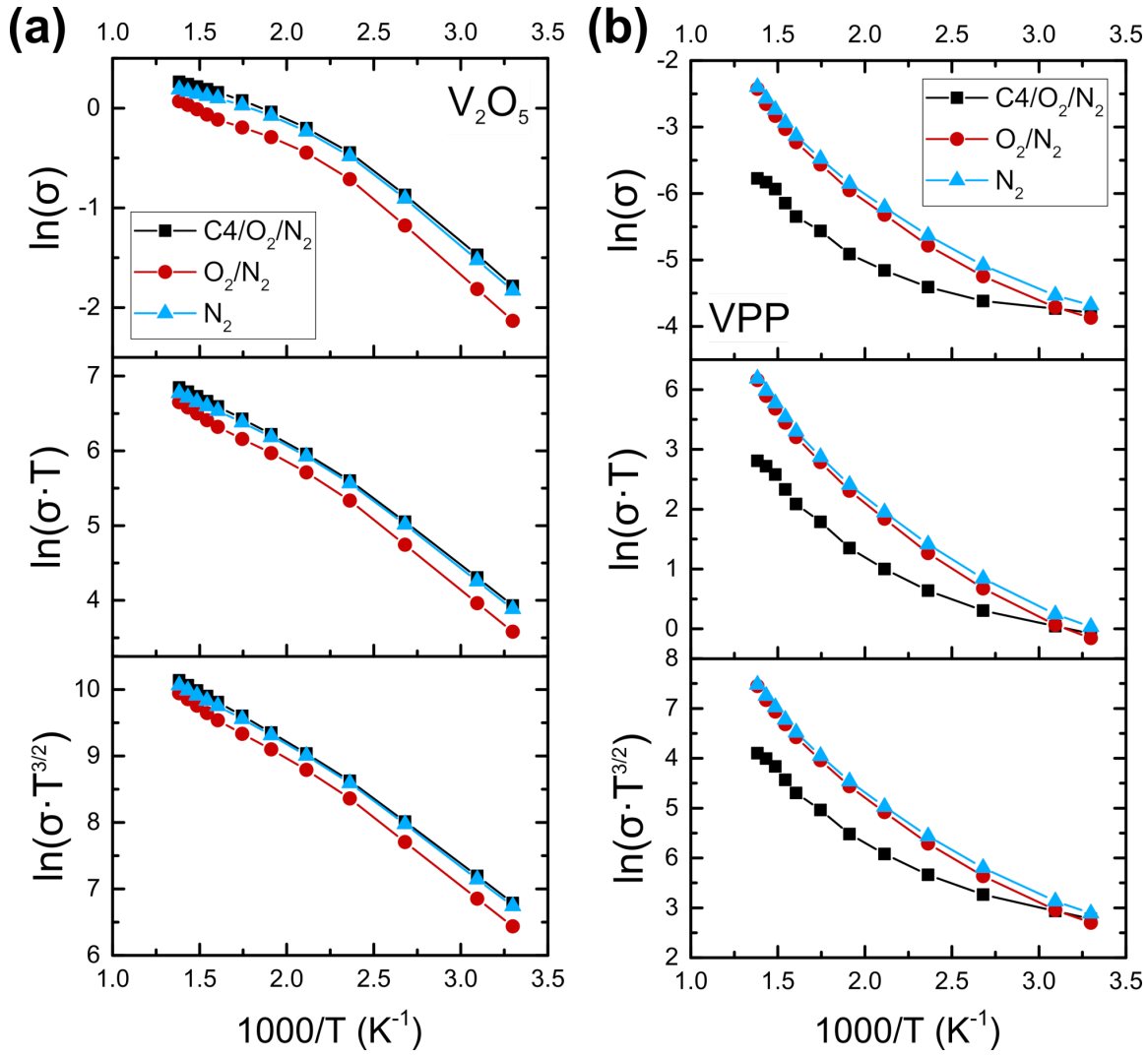

Figure B.17.: Determination of apparent activation energies of conduction of V_2O_5 **(a)** and of VPP **(b)** in different gas feeds (2% *n*-butane / 20% O_2 in N_2, 20% O_2 in N_2, 100% N_2) according to different models (at 3 GHz, TM_{010} mode).

The apparent activation energies of conduction were determined from the slopes in the linear regimes in Figure B.17, where a low-temperature regime ($\leq$ 100-150 °C) and a high temperature regime (350 to 450 °C) was distinguished for V_2O_5 and VPP. The results are presented in Figure B.18. The comparison to absolute literature values for the apparent activation energies of conduction should be read with care given that different samples and methods (single crystals and polycrystalline samples, DC and AC methods until 1 MHz as well as contactless measurements based on the microwave cavity perturbation technique at 3 GHz in the present study) and sometimes different temperature regimes were studied. A lower activation energy should be

measured at higher frequencies ω, as was pointed out by Eichelbaum *et al.*,[103] according to[103,328]

$$\sigma(\omega) = \sigma_{DC} + A\omega^s \quad \Rightarrow \quad E_c = kT \cdot [\ln \sigma_0 - \ln(A\omega^s)] \quad . \tag{B.6}$$

Here, the frequency dependence of the conductivity is given in terms of a frequency-independent part (σ_{DC}) and a second part that shows a power law behavior, where the exponent s is usually close to one, and A is a parameter.[103,328] Still, we found a satisfactory agreement with literature values not only regarding the qualitative trends of the two samples, V_2O_5 and VPP, but also regarding the absolute apparent activation energies when keeping the expected decrease of the apparent activation energy at higher operating frequencies in mind.

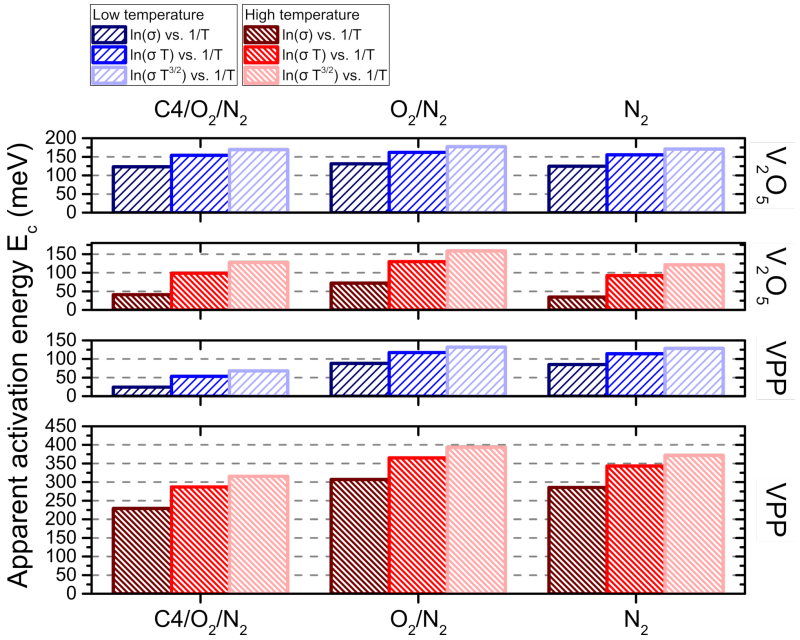

Figure B.18.: Apparent activation energies of conduction of V_2O_5 compared to VPP (from Figure B.17). The activation energies in the low temperature range in blue (30 to 100 °C for VPP or to 150 °C for V_2O_5) and in the high temperature range in red (350 to 450 °C) are shown in different gas feeds (2% *n*-butane / 20% O_2 in N_2, 20% O_2 in N_2, 100% N_2) and using different conduction models.

It can be seen in Figure B.18 that the activation energies increased when using different models, but the trends in the different gas feeds were conserved, i.e. V_2O_5 showed the highest activation energy in both the low temperature and the high temperature regime in the 20% O_2 in N_2 gas feed, which was also observed for VPP, where, however, the lowest activation energy was always found in the reaction gas feed. Figure B.18 also clearly shows the much higher apparent activation energies of conduction of VPP in the catalytically relevant high temperature regime compared to V_2O_5.

In addition to the apparent activation energies of conduction, the temperature dependence of the *n*-butane oxidation over V_2O_5 and VPP was investigated from the *operando* MCPT measurements in 2% *n*-butane / 20% O_2 in nitrogen. Figure B.19 presents the Arrhenius plots of the *n*-butane consumption rates as a function of the reciprocal temperature, where the slopes were used for the determination of the apparent activation energies of the reaction (E_a). The linear fits of the Arrhenius plots yielded apparent activation energies of *n*-butane oxidation of

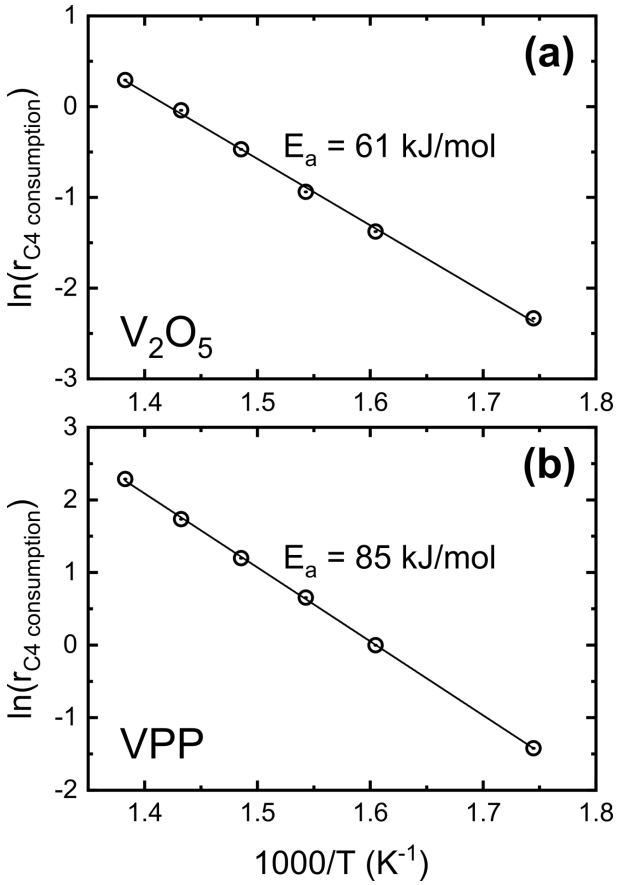

Figure B.19.: Arrhenius plots for determination of apparent activation energies of *n*-butane oxidation E_a **(a)** over V_2O_5 and **(b)** over VPP from temperature-dependent *operando* MCPT measurements in 2% *n*-butane / 20% O_2 in N_2. The natural logarithm of the overall rate of *n*-butane consumption (in mmol g^{-1} h^{-1}) is shown as a function of the reciprocal temperature.

61 kJ/mol or 0.63 eV for V_2O_5 and 85 kJ/mol or 0.88 eV for VPP (R^2 = 0.9982 and 0.9997 for V_2O_5 and for VPP, respectively). For VPO catalysts different values were reported in the literature ranging from ∼54 to 99 kJ/mol with a decreasing activation energy with an oxidation treatment of the catalysts,[329] compare for instance to 71 – 79 kJ/mol found by Zhang-Lin *et al.*[52] or to 88 kJ/mol by Wang & Barteau.[29]

C. Supporting Information – Electronic and Dielectric Properties of MoV-Oxide (M1 Phase) under Alkane Oxidation Conditions*

Anna M. Wernbacher, Pierre Kube, Michael Hävecker, Robert Schlögl, and Annette Trunschke

C.1. MoV-oxide Sample Characterization

The MoV-oxide sample in the orthorhombic M1 phase was characterized with powder X-ray diffraction. The fresh MoV-oxide sample (ID 18075) was measured on a STOE STADI P transmission diffractometer with a DECTRIS MYTHEN 1K position sensitive solid-state detector and using a primary focusing germanium monochromator (Cu Kα_1 radiation) and the used MoV-oxide samples (ID 27238 and 27353) on a Bruker AXS D8 Advance II theta/theta diffractometer using Ni filtered Cu Kα radiation. Figure C.1 depicts the powder X-ray diffractograms of the fresh and used MoV-oxide samples, where the reflections can be assigned to the orthorhombic M1 structure (ICSD 55097).[69,70]

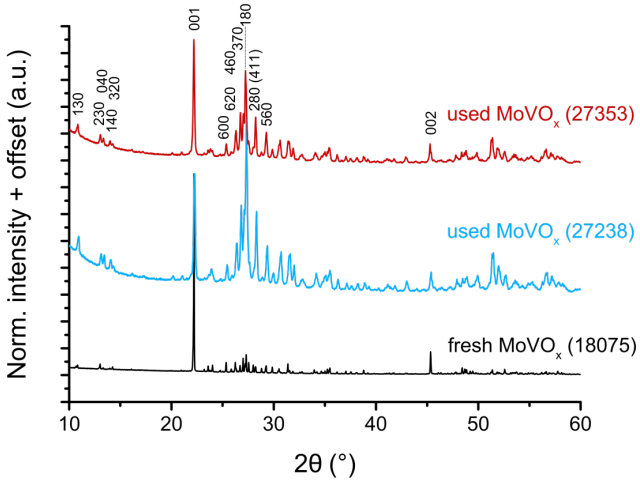

Figure C.1.: Powder X-ray diffractograms of MoV-oxide and indexed main reflections of the orthorhombic M1 structure. The fresh sample (ID 18075) and the used samples after the *operando* MCPT measurements at 270 °C under dry and wet propane oxidation conditions (ID 27238) and under dry ethane/propane/*n*-butane oxidation conditions (ID 27353) are shown.

Scanning transmission electron microscopy (STEM) of MoV-oxide (ID 18075) was performed on a double-corrected JEOL JEM-ARM200F microscope using an acceleration voltage of 200 kV. The STEM image of the sample is shown in Figure C.2.

*Reprinted (adapted) with permission from Wernbacher, A. M.; Kube, P.; Hävecker, M.; Schlögl, R.; Trunschke, A. Electronic and Dielectric Properties of MoV-Oxide (M1 Phase) under Alkane Oxidation Conditions. *J. Phys. Chem. C*, Just Accepted Manuscript, DOI: 10.1021/acs.jpcc.9b01273. Copyright 2019 American Chemical Society.

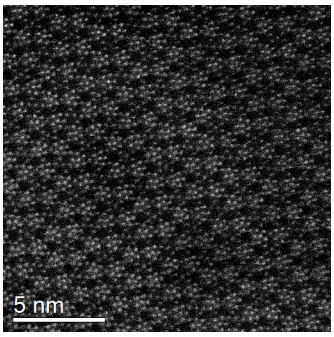

Figure C.2.: STEM image of MoV-oxide M1 phase (ID 18075).

C.2. MCPT Permittivity and Conductivity

The MCPT equations used in the present study apply for samples in the low-conductivity region of the depolarization regime, which occurs for small frequency shifts compared to the so-called filling factor divided by the depolarization factor N.[138]

$$\frac{\omega_0 - \omega_s}{\omega_0} \ll A\frac{V_s}{V_c}\frac{1}{N} \tag{C.1}$$

Assuming a depolarization factor N of 0.1 to 0.2 (for a cylinder of 1.5 mm radius and 7 mm height),[133,134,326] the frequency shift of MoV-oxide was about 3.8 – 3.9·10^{-3} (270 °C, 3% C_3H_8 / 6% O_2 in N_2, W/F of 0.13 to 1.63 g·s/ml), which is much smaller than A (V_s/V_c) $(1/N)$ = 1.4·10^{-2} (for $N = 0.2$) to 2.8·10^{-2} (for $N = 0.1$). In fact, in many cases a depolarization factor close to zero is assumed.[327] Therefore, the used MCPT equations[106,248] should be valid, in which case also the relation[133] $\varepsilon'' < \varepsilon' - 1 + 1/N$ is satisfied with (powder) values for the real and imaginary parts of the permittivity of MoV-oxide of 2.4 and 0.28 (and σ_p of 0.075 S/m), respectively. Hence, it may be assumed that the measurements were indeed carried out in the low-conductivity region of the depolarization regime.

C.2.1. Ethane / Propane / *n*-Butane Oxidation

The conductivity response of MoV-oxide to more or less reducing gas atmospheres was investigated using different propane/oxygen ratios (6% C_3H_8 / 3% O_2 in N_2 → 3% C_3H_8 / 6% O_2 in N_2), which is shown in Figure C.3. Similar to the behavior under the ethane/propane/*n*-butane oxidation conditions, a smaller conductivity in a more reducing gas feed was observed, which is shown in Figure C.3 by switching from 6% propane / 3% O_2 to 3% propane / 6% O_2 in N_2 at the same contact time. Furthermore, the decrease of the conductivity upon changing from a propane/O_2 gas feed to an *n*-butane/O_2 gas feed like in the experiment shown in the main part of the manuscript could be confirmed. The simultaneous increase in the propane conversion upon decreasing the propane/O_2 ratio is in line with the catalytic performance of MoVTeNb-oxide (M1).[72] An alkane-rich gas feed is usually applied in the oxidative dehydrogenation of propane to propene.[330] The reactant conversion increased with the contact time (X(alkane) from 0.4 to 1.4% and from 0.4 to 2.2%, X(O_2) from 0.8 to 3.9% and from 0.5 to 3.2% in C_3H_8/O_2 and in C_4H_{10}/O_2, respectively) and at the same a decrease in the conductivity was observed.

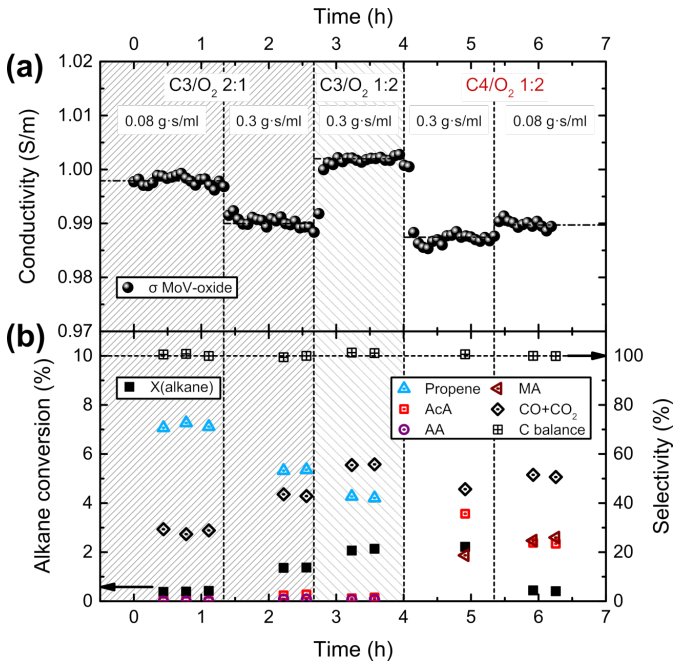

Figure C.3.: **(a)** MCPT conductivity of MoV-oxide (ID 20000) in propane and *n*-butane oxidation at different contact times and propane/O_2 ratios (270 °C); **(b)** simultaneously recorded catalytic data: alkane conversion and product selectivities (propene; acetic acid AcA; acrylic acid AA; maleic anhydride MA; sum of CO and CO_2 selectivities), and carbon balance.

C.2.2. Contact Time Variation Experiments

Contact time variation experiments of MoV-oxide were conducted in 3% alkane, 6% O_2 in nitrogen (alkane = ethane, propane, *n*-butane) at 270 °C, as well as in a dry and a wet propane oxidation gas feed (0% or 5% H_2O). In Fig. C.4 the MCPT conductivity (σ) and complex permittivity ($\tilde{\varepsilon} = \varepsilon' - i\varepsilon''$) of MoV-oxide from the contact time variation experiments are plotted as a function of time on stream. The conductivity and permittivity decreased at higher contact times and hence at higher reactant conversions in all the gas feeds. This decrease was particularly pronounced in the dry propane oxidation gas feed shown in black in Fig. C.4, which may be related to greater changes in the product selectivities with increasing propane conversion in the dry gas feed as discussed in the main part. The influence of steam on the conductivity and permittivity of MoV-oxide is shown in Fig. C.4 (b). The relative changes of both ε' and ε'' (and σ) were greater in the dry propane oxidation feed compared to the wet feed and they also responded more slowly to the different contact times (see Fig. C.4 (b)). The maximum change of ε' was found to be 1.3% and of ε'' and σ 1.5% in the dry feed, whereas in the wet feed smaller relative changes of $\Delta\varepsilon' = 0.7\%$ and of $\Delta\varepsilon''$ or $\Delta\sigma = 0.8\%$ were observed (at the highest contact time compared to the lowest contact time).

In Fig. C.4 (a) and Fig. C.5 (a) the sample mass and volume inside the microwave resonator in the (dry) propane oxidation feed (m = 0.0543 g) is slightly different from the ethane and *n*-butane feed (m = 0.0444 g), because the data correspond to new experiments. The precise absolute value of the real part of the permittivity (ε') depends on many factors and hence differences are observed between different experiments that (slightly) differ e.g. in the sample/resonator volume ratios (sample volume, mass, packing density), in the exact sample position in the

microwave resonator, as well as in the microwave coupling. The data shown are "bulk" values as obtained from the Landau-Lifshitz-Looyenga ansatz, which also corrects for the mass and volume fraction factor.[147–149] Still, small differences in the absolute values may be observed due to the above-mentioned reasons. This may explain the higher value of ε' in the propane oxidation gas feed in Fig. C.4 (a), which was measured in a separate experiment compared to the other two gas feeds (ε' of ~10 to 11). In any case, the *response* to e.g. different contact times in one gas feed is comparable, i.e. the changes of ε' with different conditions. A replication of the experiment using the same sample amount of MoV-oxide (ID 27353) showed a similar absolute value of $\varepsilon' \approx 11.9$ in the different alkane oxidation gas feeds, which will be shown later.

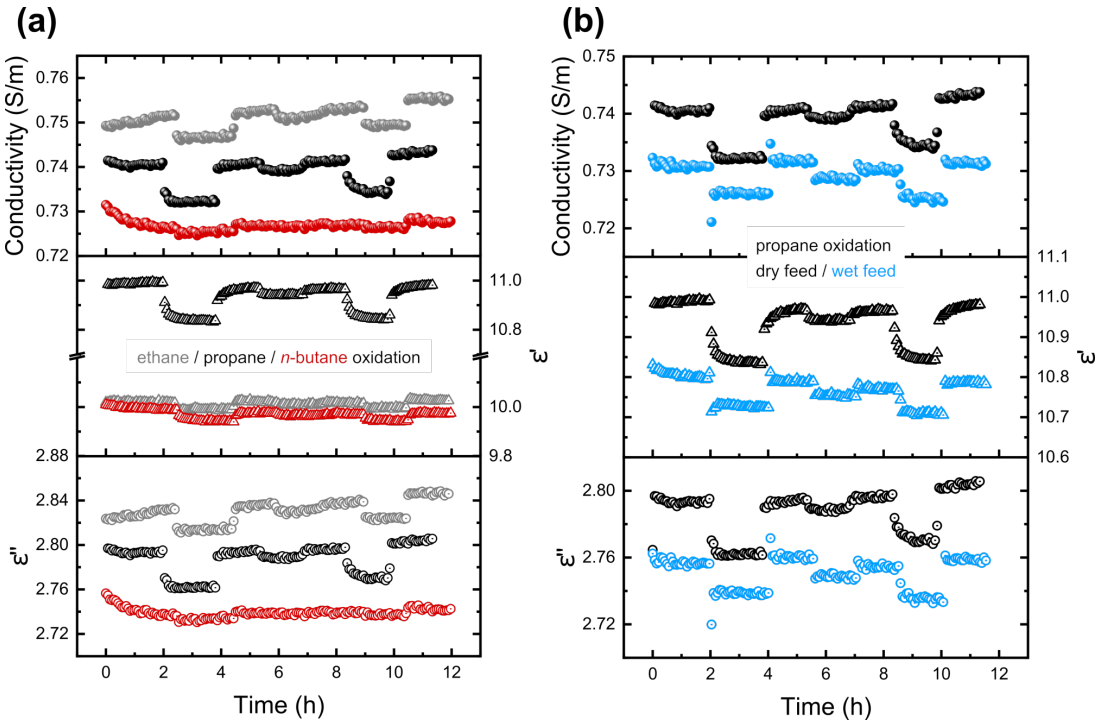

Figure C.4.: Conductivity and complex permittivity of MoV-oxide (ID 18075) under alkane oxidation conditions at 270 °C at different contact times W/F: **(a)** in 3% ethane/propane/*n*-butane, 6% O_2 in nitrogen, **(b)** in 3% propane, 6% O_2, 0% (dry) or 5% (wet) H_2O in nitrogen.

The conductivity decreased not only with the alkane conversion, but also with the oxygen conversion. In Fig. C.5 the average conductivity and permittivity of MoV-oxide at different contact times is plotted as a function of the oxygen conversion. Still, the conductivity decrease was more pronounced as a function of the alkane conversion than as a function of the oxygen conversion.

The greater relative conductivity and permittivity changes may be expressed as greater slopes of the conductivity or permittivity as a function of the reactant conversion, which can be obtained from a linear fit of the data in Fig. 5.3 (main manuscript) and Fig. C.5. The results are presented in Figure C.6. Both the slopes of the conductivity vs. alkane or oxygen conversion curves ($d\sigma/d\mathrm{X}$) are shown and of the permittivity vs. alkane or oxygen conversion curves ($d\varepsilon'/d\mathrm{X}$ and $d\varepsilon''/d\mathrm{X}$).

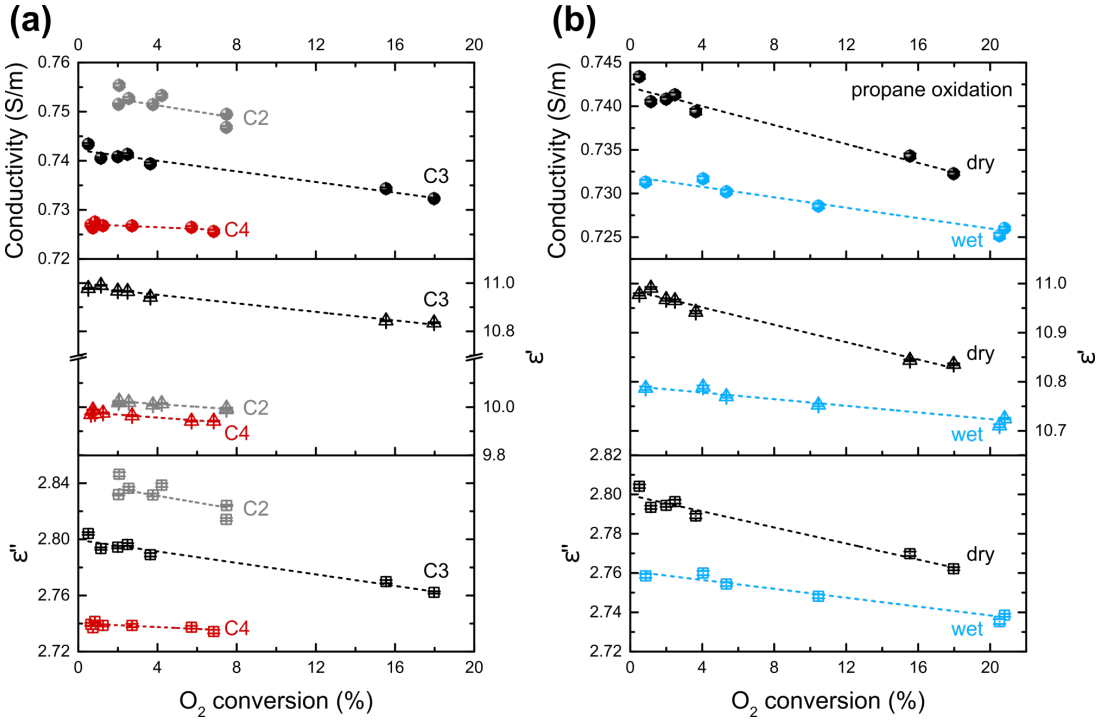

Figure C.5.: Conductivity and complex permittivity of MoV-oxide (ID 18075) as a function of oxygen conversion in different gas feeds (3% ethane/propane/*n*-butane, 6% O_2 in nitrogen; propane oxidation with 0% (dry) and 5% (wet) H_2O) at different contact times W/F at 270 °C.

In all cases a negative slope was observed corresponding to a conductivity or permittivity *decrease* at higher conversions. A maximum was observed in Fig. C.6 (a) in the dry propane oxidation gas feed "C3" or "C3 dry" (highlighted in gray), whereas the conductivity/permittivity decrease with alkane conversion was least obvious in ethane oxidation "C2". The real part of the permittivity was more sensitive to these changes at different contact times ($d\varepsilon'/d\mathrm{X}$) compared to the imaginary part of the permittivity or the conductivity ($d\varepsilon''/d\mathrm{X}$ or $d\sigma/d\mathrm{X}$). Also, the changes with respect to the alkane conversion are greater than the changes with respect to the oxygen conversion (cf. Fig. C.6 (a) and (b)). The difference in the response of ε'' relative to ε' to different contact times is most pronounced in ethane oxidation and least pronounced in *n*-butane oxidation, which is depicted in Fig. C.7 as the ratio of the slopes from the linear fit of the permittivity vs. reactant conversion curves from Fig. C.6 (C2 > C3 wet > C3 dry > C4).

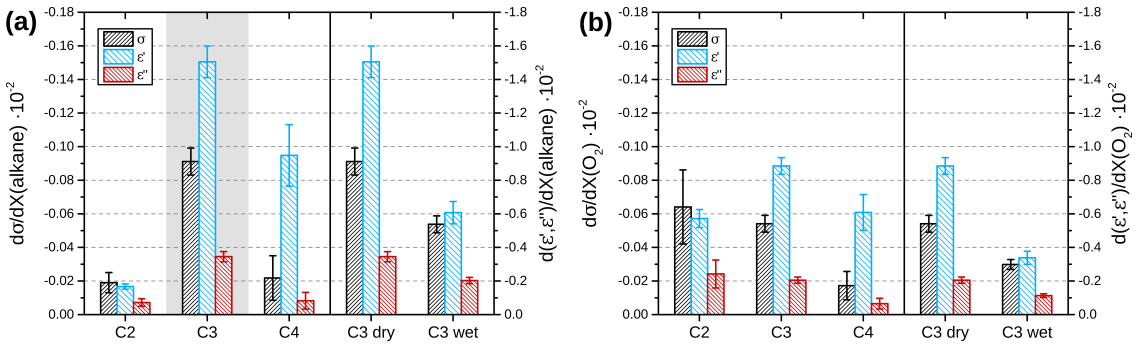

Figure C.6.: Slopes of conductivity (σ) and permittivity ($\tilde{\varepsilon} = \varepsilon' - i\varepsilon''$) changes from the contact time variation experiments **(a)** as a function of the alkane conversion and **(b)** as a function of the oxygen conversion.

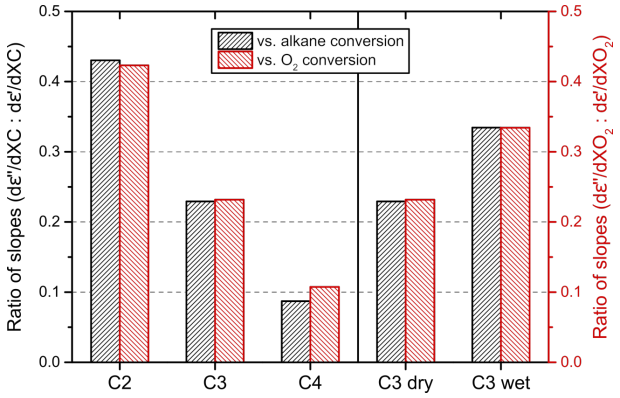

Figure C.7.: Relative response of the real and imaginary parts of the permittivity ($\tilde{\varepsilon} = \varepsilon' - i\varepsilon''$) to different contact times: ratio of slopes from linear fit of permittivity vs. alkane conversion ("XC") and vs. oxygen conversion ("XO_2") curves from Fig. C.6.

The contact time variation experiments in the ethane, propane, and *n*-butane oxidation gas feeds were repeated with a used MoV-oxide sample (ID 27353), which was previously investigated in the dry alkane oxidation feeds at 270 °C. The measurements were conducted with the same mass of MoV-oxide inside the resonator (m = 0.0430 g; W/F of 0.13 to 1.3 g·s/ml). In Fig. C.8 (a) the conductivity and permittivity are shown as a function of the alkane conversion. The corresponding catalytic data recorded during the MCPT experiments are presented in Fig. C.8 (b) as selectivity–conversion (S-X) plots. The conductivity decrease at higher conversions, which was particularly pronounced in the propane oxidation feed, could be confirmed. The same findings were observed when plotting the conductivity or complex permittivity as a function of the oxygen conversion, i.e. the conductivity and permittivity generally decreased at higher reactant conversions.

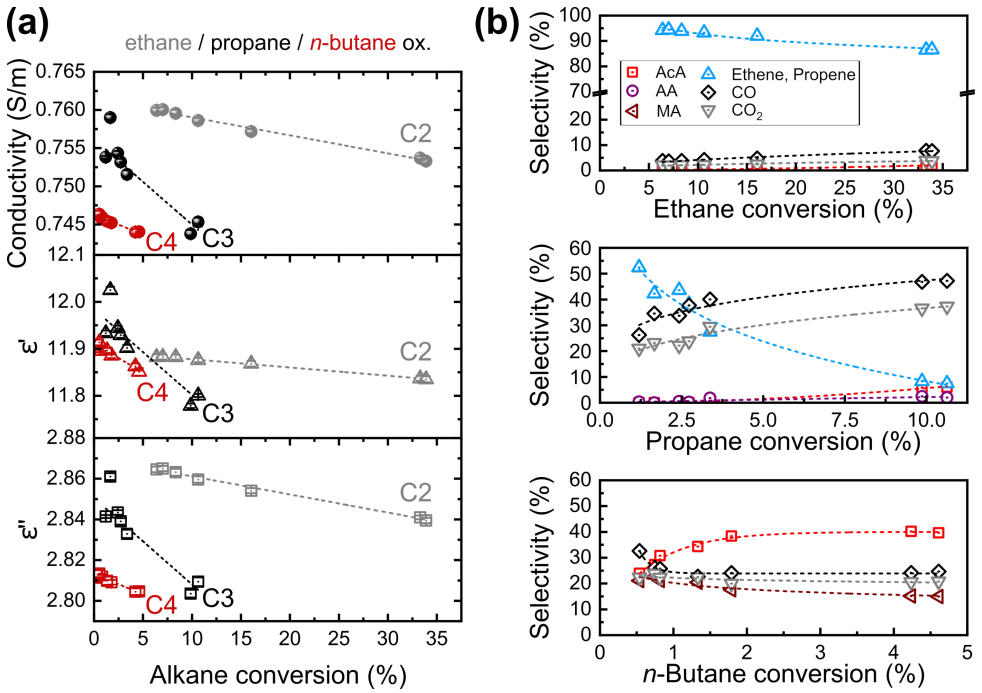

Figure C.8.: **(a)** Conductivity and complex permittivity of MoV-oxide (ID 27353) under alkane oxidation conditions (3% ethane/propane/*n*-butane, 6% O_2 in N_2, 270 °C) at different contact times W/F 0.13 to 1.3 g·s/ml; **(b)** simultaneously recorded catalytic data as S–X plots.

A comparison of the contact time variation experiments of the two MoV-oxide samples (18075 and 27353) in the dry alkane oxidation gas feeds is presented in Figure C.9 showing the slopes from a linear fit of the conductivity and permittivity vs. reactant conversion curves. It can be seen that the same values were obtained for the two samples within the error of the experiment.

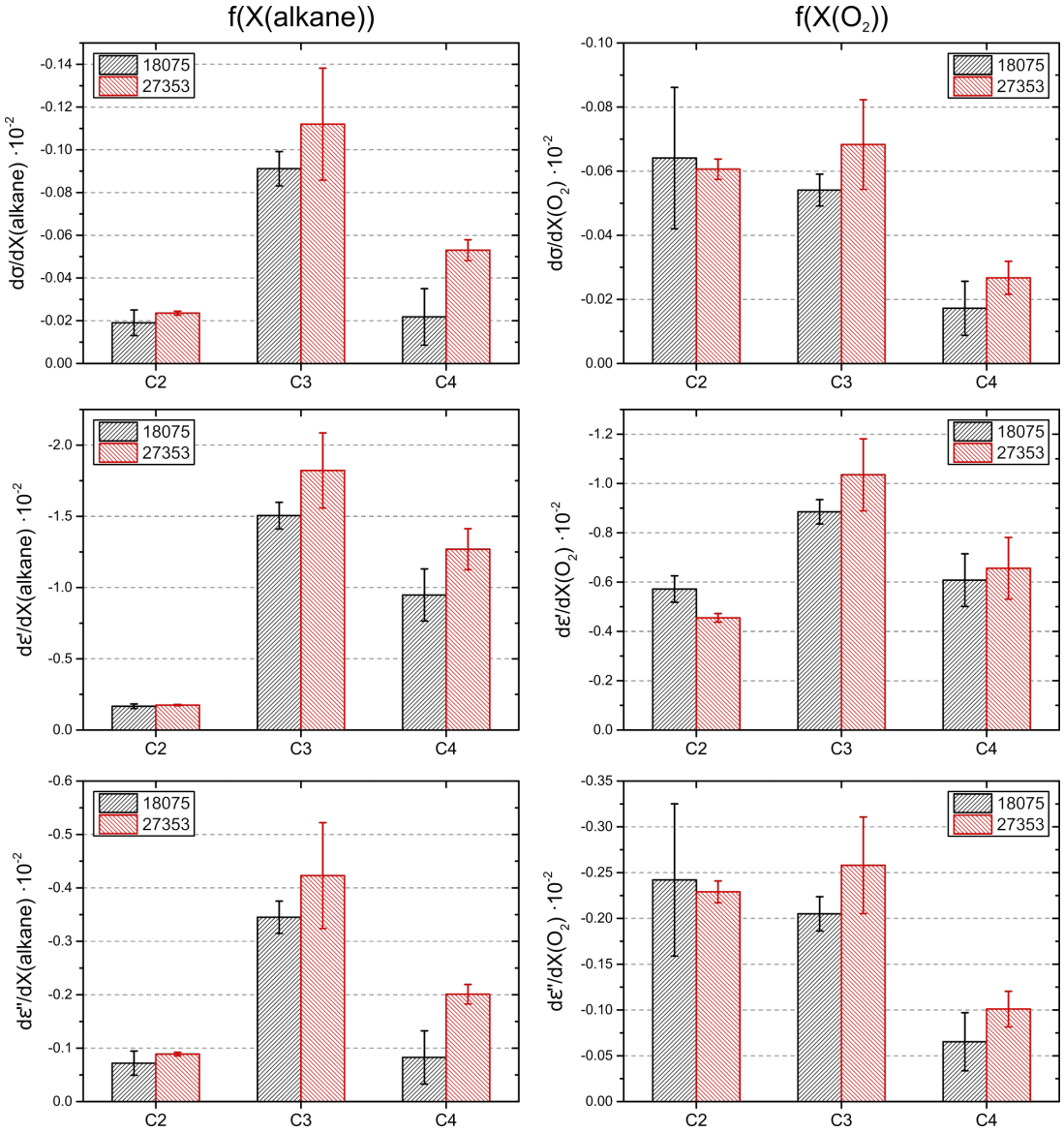

Figure C.9.: Comparison of contact time variation experiments in dry ethane/propane/n-butane oxidation gas feeds of MoV-oxide (M1) samples 18075 and 27353: slopes from linear fit of conductivity (σ) and complex permittivity ($\tilde{\varepsilon} = \varepsilon' - i\,\varepsilon''$) as a function of alkane conversion (on the left) and as a function of oxygen conversion (on the right).

C.2.3. Temperature Dependence of Conductivity

The temperature dependence of the conductivity of MoV-oxide was investigated in the temperature range between 200 and 290 °C in different alkane oxidation gas feeds (3% ethane, propane, n-butane, 6% O_2 in nitrogen). The experimental procedure of the temperature-dependent MCPT measurements is shown in Figure C.10 as a time on stream plot of the raw data (reciprocal Q factor).

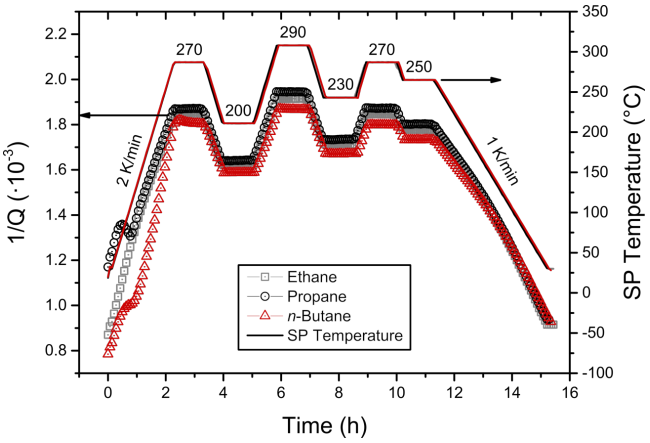

Figure C.10.: Change of reciprocal Q factor ($1/Q_s$) of MoV-oxide-loaded cavity with temperature as a function of time in ethane, propane, and n-butane oxidation gas feeds. The setpoint temperature (measured with a thermocouple in the gas stream before the resonator) is shown on the right axis and the corresponding calibrated temperatures in the center of the resonator are indicated by the numbers.

Figure C.11 shows the cooling curves of MoV-oxide from 290 to 30 °C with 1 K/min in the ethane, propane, and n-butane oxidation gas feeds as well as the steady-state values (at 200 °C, 230 °C, 250 °C, 270 °C (twice), and 290 °C) in terms of the increase in the reciprocal Q factor and the decrease of the resonant frequency. It can be seen in Figure C.11 (a) that differences in the Q factors between the individual gas feeds occurred above ∼100 °C, while the Q factors coincided at lower temperatures. Also, the steady-state values coincided with the values recorded during cooling.

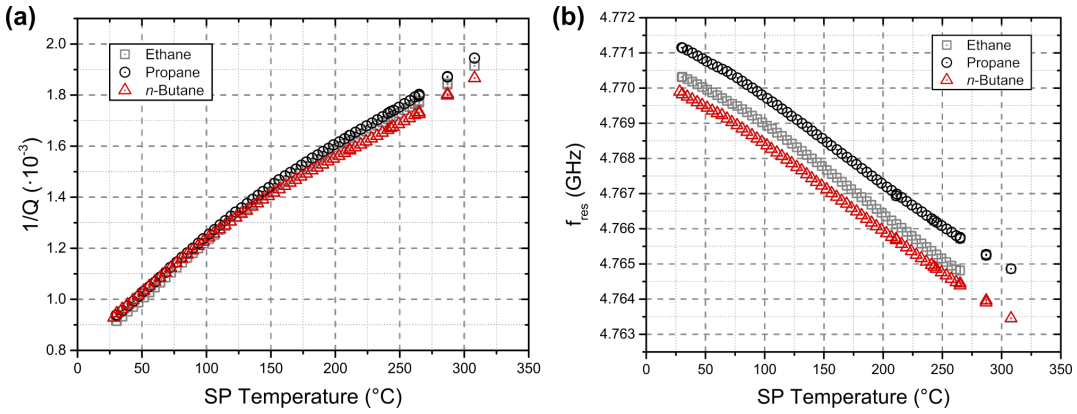

Figure C.11.: MCPT raw data of MoV-oxide in ethane/propane/n-butane oxidation during cooling and steady-state values: **(a)** reciprocal Q factor ($1/Q_s$) and **(b)** resonant frequency f_{res} as a function of the setpoint temperature.

Figure C.12 shows the change in the reciprocal Q factor and the resonant frequency shift of MoV-oxide with respect to the empty cavity measurements as a function of temperature.

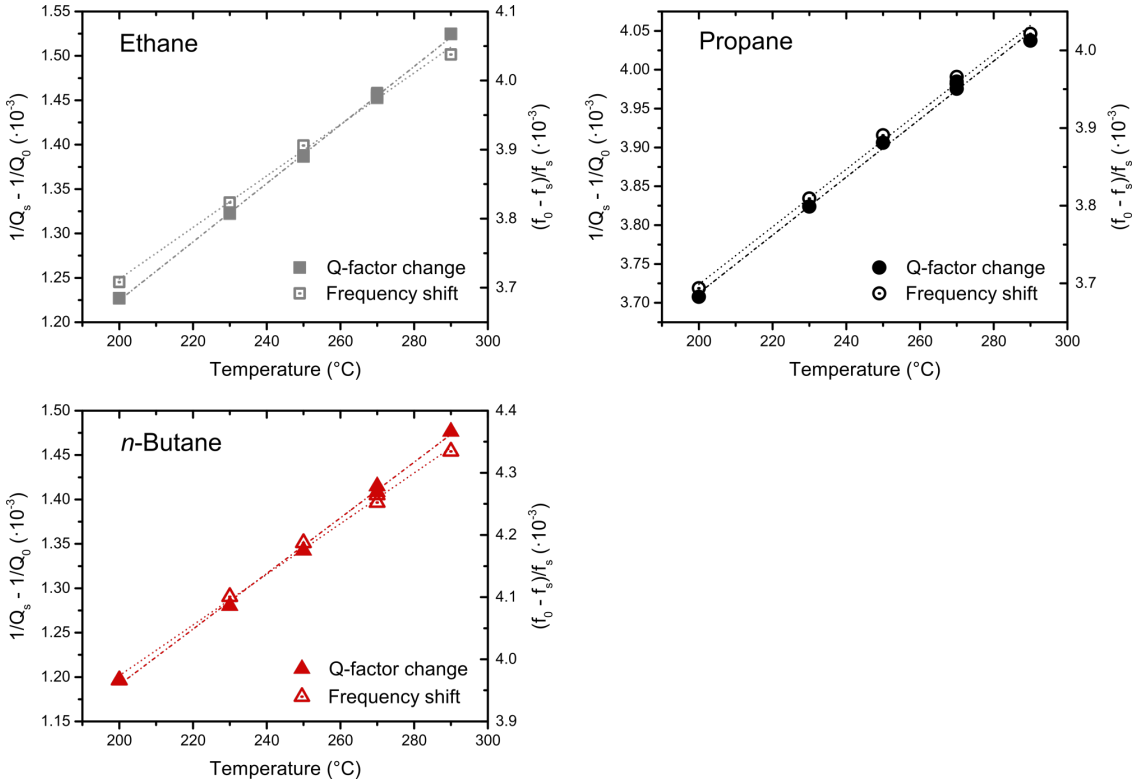

Figure C.12.: MCPT raw data of MoV-oxide in ethane/propane/*n*-butane oxidation (subscript "s") with respect to empty measurement (subscript "0"): change in reciprocal Q factor $(1/Q_s - 1/Q_0)$ and shift in resonant frequency $([f_0 - f_s]/f_s)$ as a function of temperature.

The Arrhenius-type apparent activation energies of conduction of MoV-oxide were discussed in the main part of the present work. Other conduction mechanisms like the contribution of ionic conductivity with both a temperature-dependent diffusion coefficient of the ions and a $1/T$-dependence of the pre-exponential factor[141]

$$\sigma_{\text{ion}} = \frac{\sigma_{\text{ion},0}}{T} \cdot \exp\left(-\frac{E_c}{k\,T}\right) \tag{C.2}$$

or a polaron conduction mechanism[222]

$$\sigma_{\text{polaron}} = \frac{\sigma_{\text{polaron},0}}{T^{3/2}} \cdot \exp\left(-\frac{E_c}{k\,T}\right) \tag{C.3}$$

were considered as well. The apparent activation energies of conduction of MoV-oxide in the different gas feeds were determined from the slope of the logarithmic plot of $\ln(\sigma)$, $\ln(\sigma \cdot T)$ or $\ln(\sigma \cdot T^{3/2})$ versus the reciprocal temperature T^{-1}, which is shown in Figure C.13.

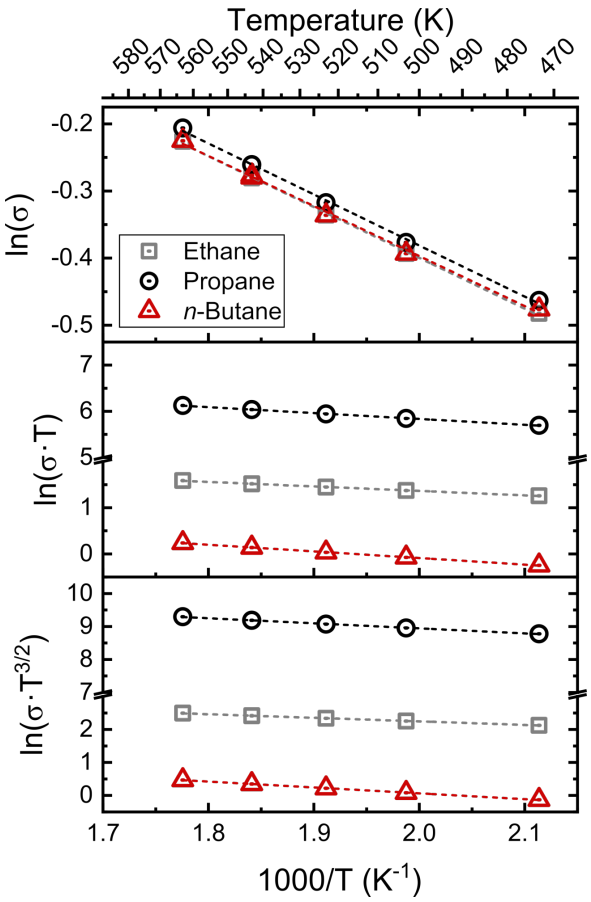

Figure C.13.: Determination of apparent activation energy of conduction of MoV-oxide in ethane, propane, and *n*-butane oxidation gas feeds according to different models. The dashed lines correspond to the linear fits.

C.3. NAP-XPS and NEXAFS

Detailed information on the surface composition and surface electronic structure of MoV-oxide was obtained from near-ambient pressure X-ray photoelectron spectroscopy (NAP-XPS) at 25 Pa and 270 °C in different alkane oxidation gas feeds, which was complemented by near-edge X-ray absorption fine structure (NEXAFS) spectroscopy at the V L-edge and O K-edge.

C.3.1. Core Level Spectra

The core level spectra of MoV-oxide were measured in different gas feeds in order to investigate the redox properties and the surface composition both using different alkanes (alkane/O_2 = 1:2, alkane = ethane, propane, *n*-butane) and in propane/O_2 with and without H_2O(g). This is shown in Figure C.14 for the "surface sensitive" measurements with an estimated electron inelastic mean free path length of 0.6 nm. Major effects were only found by the addition of steam to the gas feed (blue spectra) in the V $2p_{3/2}$ core levels with a peak maximum at a binding energy of about 516.4 to 516.5 eV, where a growing shoulder at the high binding energy side of the peak (∼517.4 to 517.7 eV) was observed, which is ascribed to a higher oxidation state as indicated in Figure C.14 (c). The subsequent treatment of MoV-oxide by a dry propane oxidation gas feed C_3H_8/O_2 did not restore the initial peak shape, i.e. the observed changes

in the V $2p_{3/2}$ core level were irreversible. Minor changes were also observed in the V $2p_{1/2}$ core level and at the high binding energy side of the O 1s peak (∼530.6 eV). In the case of molybdenum (Figure C.14 (a)), no considerable changes in the Mo 3d core levels were found indicating a major molybdenum 6+ oxidation state with a $3d_{5/2}$ binding energy of 232.7 eV and an energy difference between Mo $3d_{3/2}$ and Mo $3d_{5/2}$ of 3.1 eV, in agreement with literature data of the spin-orbit-splitting in Mo-oxides.[331,332] Hence, it is suggested that vanadium is the main redox-active component in MoV-oxide exhibiting changes in the V $2p_{3/2}$ core level related to changes in the relative amounts of V^{4+} and V^{5+}, in agreement with previous findings on the MoV-oxide[77] and on MoVTeNb-oxide (M1 phase).[75]

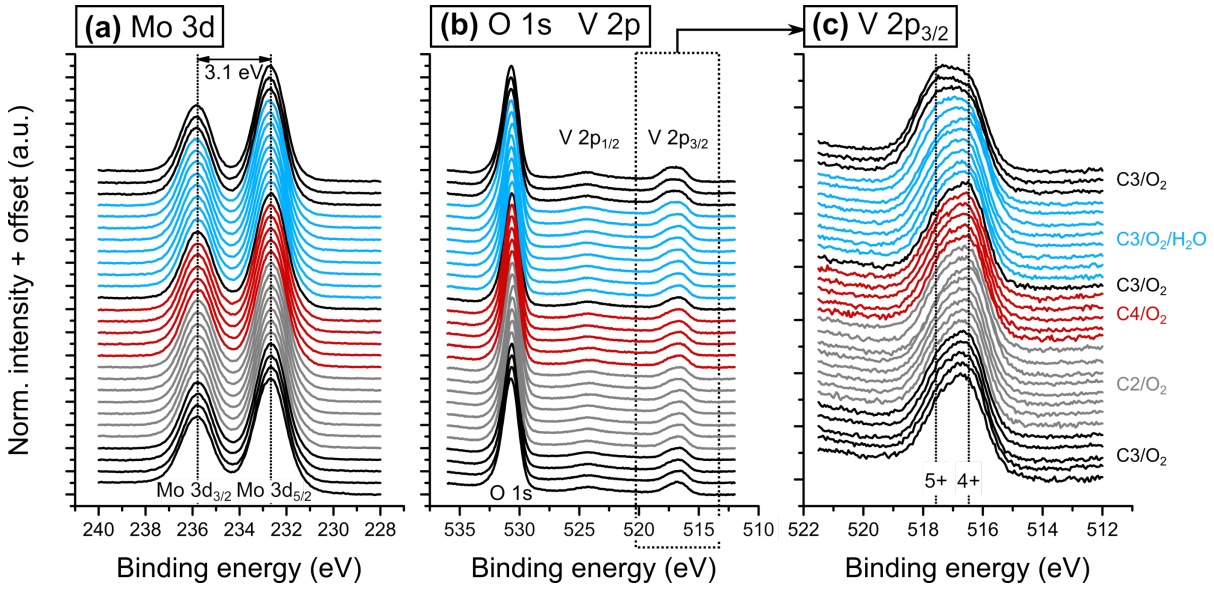

Figure C.14.: Core level spectra of MoV-oxide (Mo $3d_{3/2}$ and $3d_{5/2}$, O 1s, V $2p_{1/2}$ and $2p_{3/2}$) in different gas feeds at 25 Pa and 270 °C (λ_{IMFP} 0.6 nm).

Changes in the vanadium oxidation state were analyzed by a deconvolution of the V $2p_{3/2}$ core level with Gaussian-Lorentzian product functions representing a 4+ and two 5+ components after a Shirley background correction. The fit parameters, which were taken from Ref. [77], are summarized in Table C.1 and example fits are shown in Figure C.15. The positions of the two V^{5+} species were fixed at 1.0 and 1.2 eV higher binding energies than the main V^{4+} component, respectively, and with smaller peak widths, which are expected from literature spectra of vanadium oxides in various oxidation states.[78,185,306–308] The V^{4+} $2p_{3/2}$ binding energy of MoV-oxide of 516.4 to 516.5 eV obtained in this manner was found to be close to, yet a bit higher than, the reported V $2p_{3/2}$ binding energies in VO_2 of 516 eV for a single crystal[308] or of 515.95 eV for a powder sample.[307] The binding energy difference between V^{4+} and the two V^{5+} species of 1.0 and 1.2 eV, respectively, is a bit smaller than the values found in literature for VO_2 and V_2O_5 samples, which range from ΔE_{bind} of 1.20 to 1.36 eV.[184,185,306–309] There exists a spread in the literature values in part caused by different energy calibration schemes,[307] which lead to the suggestion of using the binding energy difference between the O 1s and V $2p_{3/2}$ core levels to distinguish between different vanadium oxidation states.[306] In the present study, an energy difference ΔE_{bind}(O 1s − $V^{4+}2p_{3/2}$) of 14.2 eV was found for MoV-oxide, which lies within the range reported for VO_2 of 14.16 eV[185] to 14.35 eV.[306] In the previous study of MoV-oxide

(M1), Trunschke *et al.*[77] reported a V^{4+} $2p_{3/2}$ binding energy of 516.1 eV similar to the 516.0 to 516.3 eV that were found for MoVTeNb-oxide (M1),[75,252] using the valence band onset for binding energy calibration.[75,77] Others reported V $2p_{3/2}$ binding energies of 516.3 to 516.7 eV for M1 and M2 phases of MoVTeNb-oxide.[274,333,334]

Table C.1.: Fit parameters for V $2p_{3/2}$ core level and constraints (cf. Figure C.15): peak position, full width at half maximum (fwhm), and relative Lorentzian contributions to Gaussian-Lorentzian product functions. A Shirley background was used.

V $2p_{3/2}$	**4+**	**5+ (I)**	**5+ (II)**
Fitted position (eV)	516.4 – 516.5	517.4 – 517.5 (4+) + 1.0	517.6 – 517.7 (4+) + 1.2
fwhm (eV)	1.36 – 1.43	1.22 – 1.28 (4+)·0.9	1.22 – 1.28 (4+)·0.9
Lorentzian contribution	40% L		

In the dry gas feeds a fit with two Gaussian-Lorentzian product functions was possible as well corresponding to a V^{4+} component with a binding energy of 516.5 eV and a V^{5+} component (517.5 eV). However, in the wet feed $C_3H_8/O_2/H_2O$ a second 5+ species was required. This "V^{5+} (II)" species with a slightly higher binding energy by 0.2 eV was suggested to originate from the migration of vanadium from the hexagonal channels in the M1 phase crystal structure (M12 position) to the surface.[77] A similar behavior was recently also found for vanadyl pyrophosphate $(VO)_2P_2O_7$ investigated under dry and wet propane oxidation conditions[123] and for MoVTeNb-oxide (M1).[77] Both catalysts, like MoV-oxide, need a second V^{5+} surface species which is related to the dosing of steam. In the following, the results from this three-component fit model will be discussed. It may be noted that both the position of the V^{4+} component and the vanadium oxidation state are not affected by the choice of the fit model, i.e. both a two-component fit model and the three-component fit model yield the same values, even though the agreement between experimental and fitted spectra is better for the three-component model, particularly in the wet propane oxidation gas feed and the subsequent dry propane oxidation feed.

Typical fit examples in the different gas feeds are shown in Figure C.15, where the changes in the V $2p_{3/2}$ peak profile in the different gas feeds at an electron inelastic mean free path length of ∼0.6 nm become apparent. The last spectrum recorded in the $C_3H_8/O_2/H_2O$ gas feed exhibited the most pronounced high binding energy shoulder. Interestingly, the V^{5+} (II) species became the major 5+ species in the wet feed with a greater relative contribution than V^{5+} (I). Deeper layers recorded at λ_{IMFP} of 1.7 nm (Figure C.15 (b)) showed the same qualitative behavior with an increased V $2p_{3/2}$ shoulder and a change in the relative contributions of the two V^{5+} species upon the addition of steam to the gas feed. This can be caused by the contribution of photoelectrons from the surface region. The relative contribution of the 4+ component to the overall V $2p_{3/2}$ peak area was greater than in the surface sensitive measurements indicating a lower vanadium oxidation state in deeper layers or an oxidized catalyst surface.

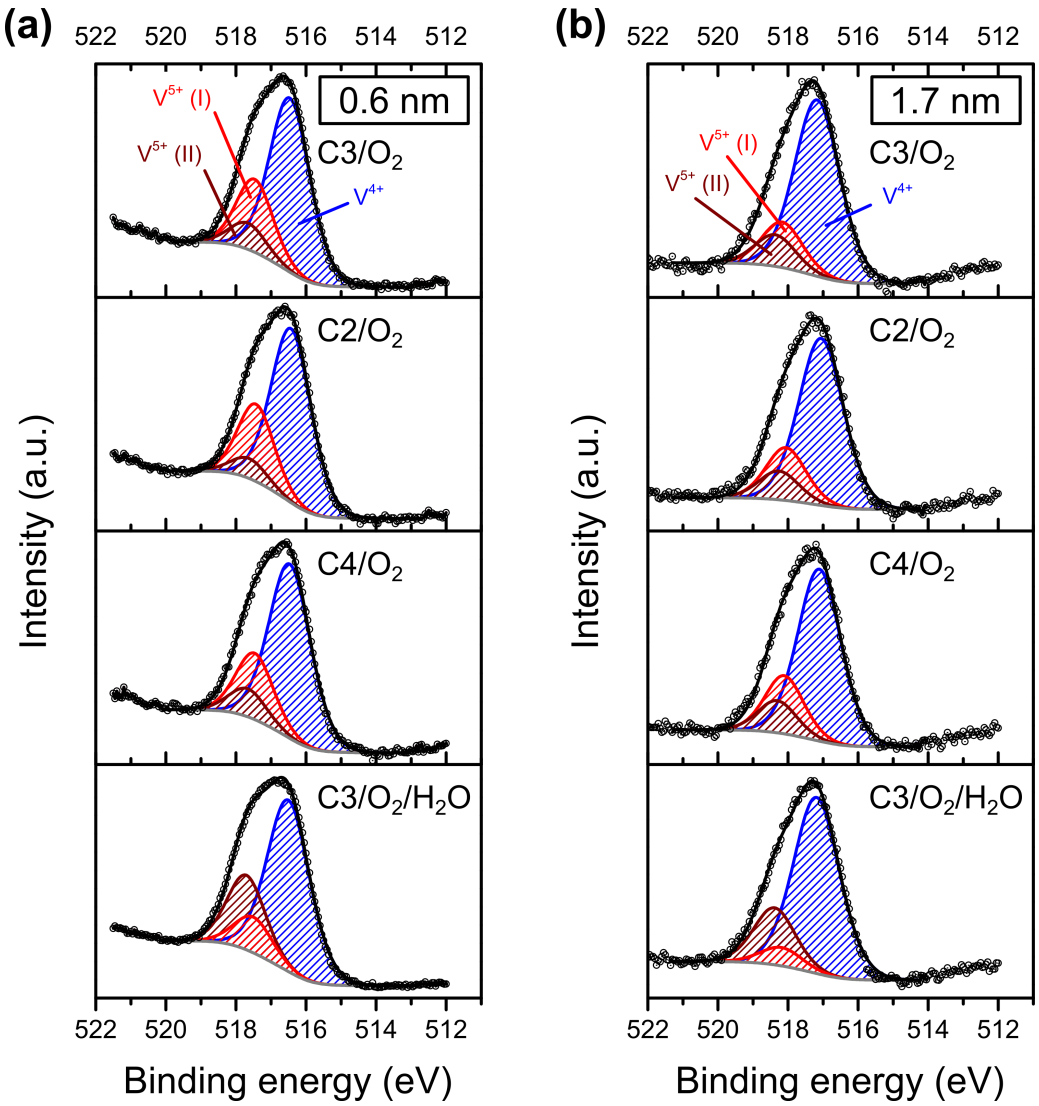

Figure C.15.: Example fits of V $2p_{3/2}$ core level with a 4+ and two 5+ components after a Shirley background correction in the different gas feeds at 25 Pa and 270 °C: **(a)** $\lambda_{\mathrm{IMFP}} = 0.6$ nm, **(b)** $\lambda_{\mathrm{IMFP}} = 1.7$ nm.

The O 1s core level of MoV-oxide was fitted with two components as described in Table C.2, the main peak "O(1)" representing the species from the bulk oxide and the second peak "O(2)" the high binding energy shoulder, which may be caused by surface hydroxyl groups or other oxygen-containing surface species occurring in a similar binding energy range.

Table C.2.: Fit parameters and constraints for O 1s core level (using a Shirley background correction): peak position, full width at half maximum (fwhm), and relative Lorentzian contributions to Gaussian-Lorentzian product functions.

O 1s	**O(1) oxide**	**O(2)**
Position (eV)	530.6	O(1) + 1.2
fwhm (eV)	1.4	1.5 – 1.6
Lorentzian contribution	40% L	

A C 1s peak from surface carbon species on MoV-oxide was observed at the beginning in the

first C_3H_8/O_2 gas feed, which however disappeared with time on stream at 270 °C. An evolution of the area of the C 1s peak was then observed in the wet $C_3H_8/O_2/H_2O$ gas feed. This is shown in Figure C.16.

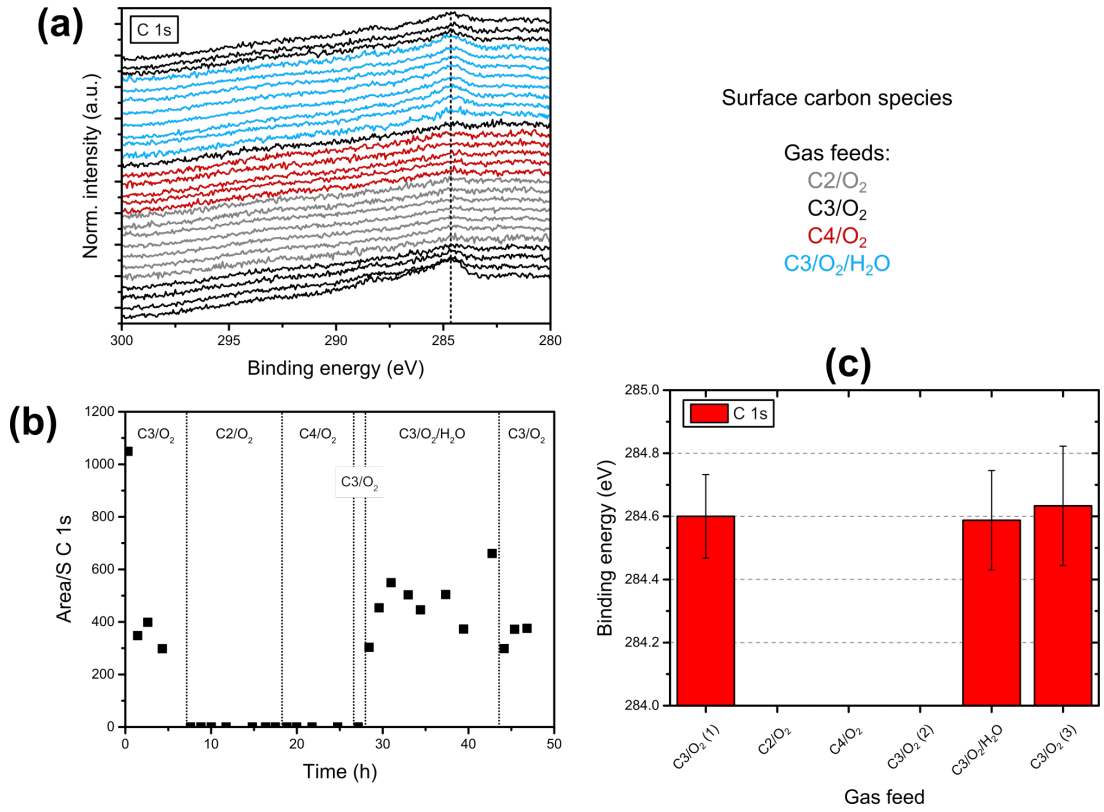

Figure C.16.: Evolution of surface carbon species on MoV-oxide in different gas feeds (25 Pa, 270 °C): **(a)** C 1s core level spectra, **(b)** quantitative analysis, **(c)** average C 1s binding energies (error bar corresponds to one standard deviation).

C.3.2. Valence Band Spectra

The valence band (VB) of MoV-oxide was investigated in the different gas feeds. Figure C.17 shows the valence band spectra recorded at photon energies $E_{h\nu}$ from 100 to 1280 eV (surface sensitive measurements at $E_{h\nu}$ of 100 eV with $E_{\mathrm{kin}} \approx 98.5$ to 89 eV corresponding to λ_{IMFP} of 0.5 nm). The spectra in Figure C.17 were normalized to the maximum intensity of the valence band after a linear background subtraction and set to the same valence band onset for a better comparison. The region between $E_{\mathrm{bind}} \approx 3$ to 10 eV corresponds to the mainly O 2p-constituted valence band, but there is presumably also a hybridization with the transition metal orbitals. A mixing of O 2p and V 3d states in the mid- to high-energy range of the valence band was shown for V_2O_5[78,81,156] and also for $MoVTeNbO_x$.[105] With increasing photon energy, the spectral weight of the valence band spectra in Figure C.17 shifted to the higher binding energy range, where O 2p states are probably hybridized with metal d states, with a relative decrease of the intensity at the valence band onset, which is usually formed by non-bonding O 2p states. This is due to the photon energy dependence of the photoionization cross-sections.[335] Major gas-phase-induced changes in the valence band were observed at a photon energy of 100 eV, i.e. in the surface sensitive measurements, particularly by the addition of steam to the gas feed. An

increase in intensity in the binding energy range below ∼4.5 eV was observed in the wet propane oxidation gas feed $C_3H_8/O_2/H_2O$. The subsequent treatment of MoV-oxide in the C_3H_8/O_2 (3) gas feed lead to a continuous decrease of this valence band shoulder, however, the initial spectral shape of the valence band that was observed in the previous C_3H_8/O_2 gas feeds (or generally in the dry alkane oxidation gas feeds) was not reached within the time frame of the experiment.

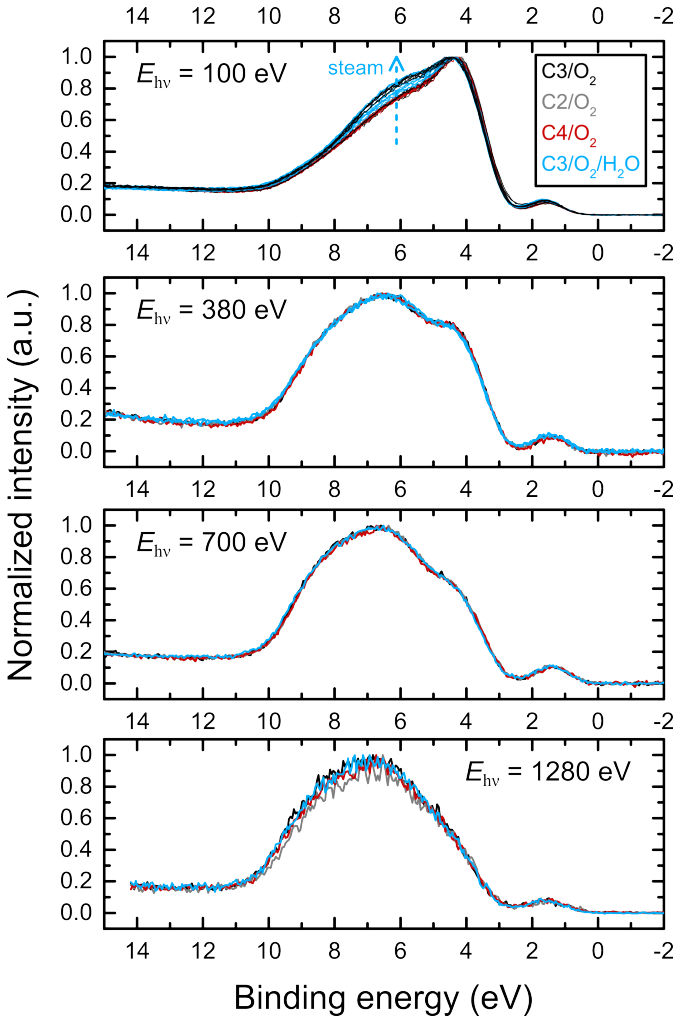

Figure C.17.: Valence band spectra of MoV-oxide in different gas feeds (25 Pa, 270 °C) recorded at photon energies from 100 to 1280 eV.

Figure C.18 shows the extended binding energy range of the valence spectra recorded at 100 eV. The spectra were normalized to the background at 30 eV after a linear background subtraction. The highest binding energy peak at ∼22 eV in Figure C.18 corresponds to the O 2s level. The spectra taken in the different dry alkane oxidation gas feeds resembled each other closely. The decreased intensity in the valence band region in the *n*-butane oxidation gas feed C_4H_{10}/O_2 (see the difference spectra in Figure C.18) might be due to the normalization procedure. The most pronounced effect was observed in the wet propane oxidation gas feed, which can be clearly seen in Figure C.18 in the valence band shoulder around 6 eV as well as in the V 3d(/Mo 4d) states. The effect of steam will be discussed later in more detail.

The valence band (VB) onset of MoV-oxide in different gas feeds was determined from a leading-edge extrapolation, which is shown in Fig. C.19 (a). The results are presented in Fig. C.19

(b) showing a slight increase in the VB onset in the wet propane oxidation feed.

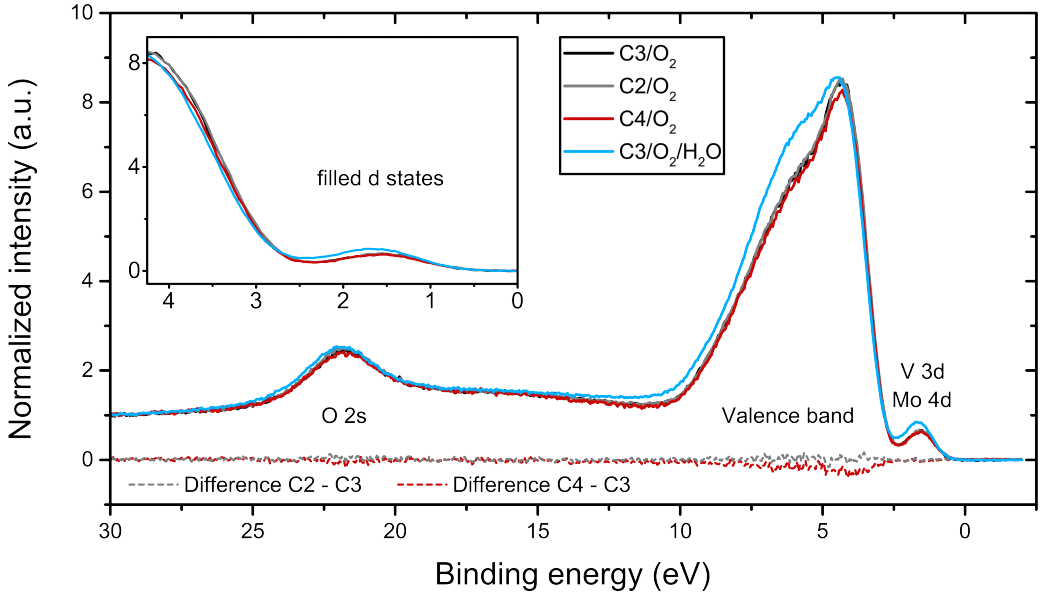

Figure C.18.: MoV-oxide valence band and O 2s spectra in ethane, propane (dry/wet), and *n*-butane oxidation gas feeds ($E_{h\nu}$ = 100 eV). The difference spectra between the dry gas feeds ($Int(C_2H_6/O_2)$ – $Int(C_3H_8/O_2)$ and $Int(C_4H_{10}/O_2)$ – $Int(C_3H_8/O_2)$) are displayed as well and the inset shows the VB onset and the filled d states.

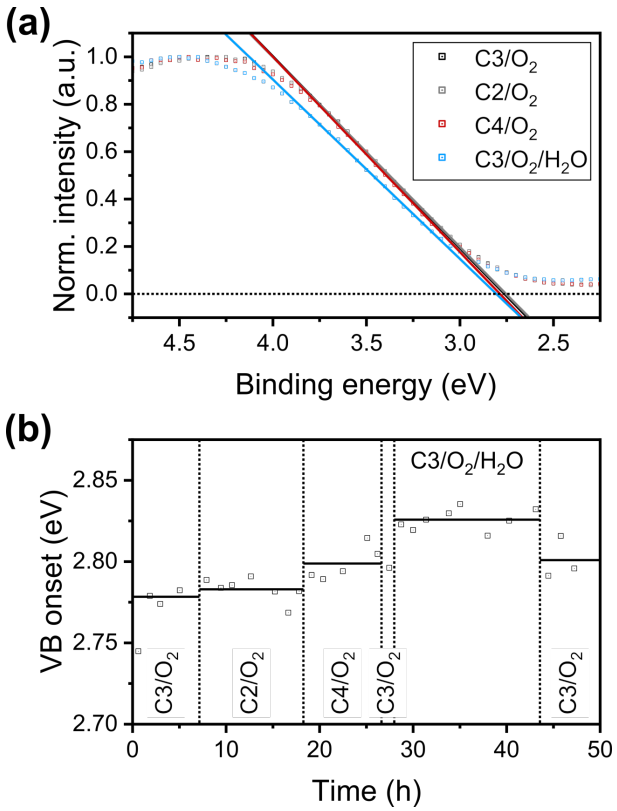

Figure C.19.: **(a)** Leading-edge extrapolation of VB ($E_{h\nu}$ = 100 eV) in different gas feeds (last measurements in respective feed); **(b)** VB onset as a function of time on stream.

C.3.3. The Influence of Steam on the Surface Electronic Structure

The core levels of MoV-oxide were affected by the treatment in the wet propane oxidation gas feed, which is shown in Figure C.20. The Mo 3d, V 2p, and O 1s slightly shifted to higher binding energies, see the difference spectra in Figure C.20, which might be caused by a change in band bending. Furthermore, the V $2p_{3/2}$ and O 1s core levels showed clear changes at the high binding energy side due to an increased average vanadium oxidation state and an increased surface hydroxylation or other surface oxygen species contributing to this binding energy range, respectively.

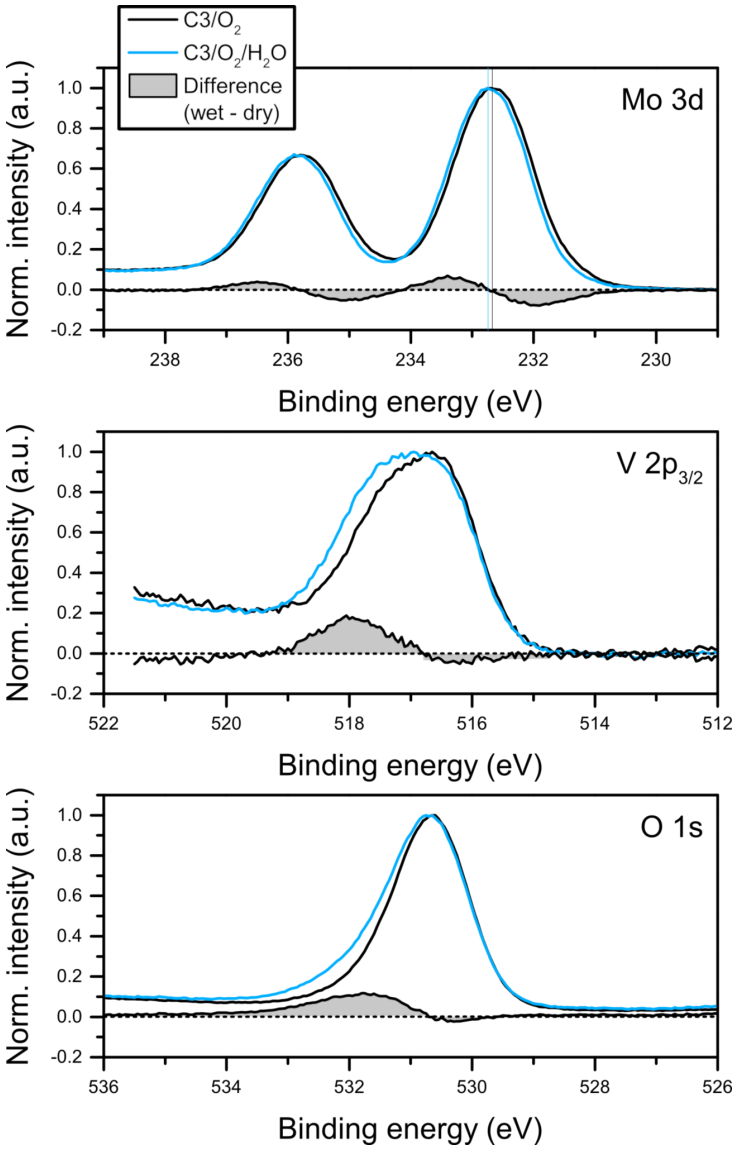

Figure C.20.: Mo 3d, V $2p_{3/2}$, and O 1s core level spectra of MoV-oxide in the first dry propane oxidation gas feed C_3H_8/O_2 and in the wet propane oxidation feed $C_3H_8/O_2/H_2O$ (25 Pa, 270 °C, λ_{IMFP} = 0.6 nm) and their difference spectra Int(wet) – Int(dry).

Figure C.21 demonstrates the steam-induced changes in the O 1s core level with a shoulder around 532 eV and in the valence band spectra with a shoulder at ∼6 eV with increasing time on stream. Furthermore, the inset in Figure C.21 (a) shows a progressive shift of the O 1s peak to higher binding energies by 60 meV. The O 1s peak exhibits a high complexity due to many

overlapping species which occur in this binding energy range between 528.5 and 534 eV. Besides the main peak from the oxide, satellites from the V $2p_{3/2}$ and V $2p_{1/2}$ core levels are expected, together with possible "surface oxygen" species with a slightly differing binding energy, hydroxyl groups, and adsorbed oxygen-containing carbon species.

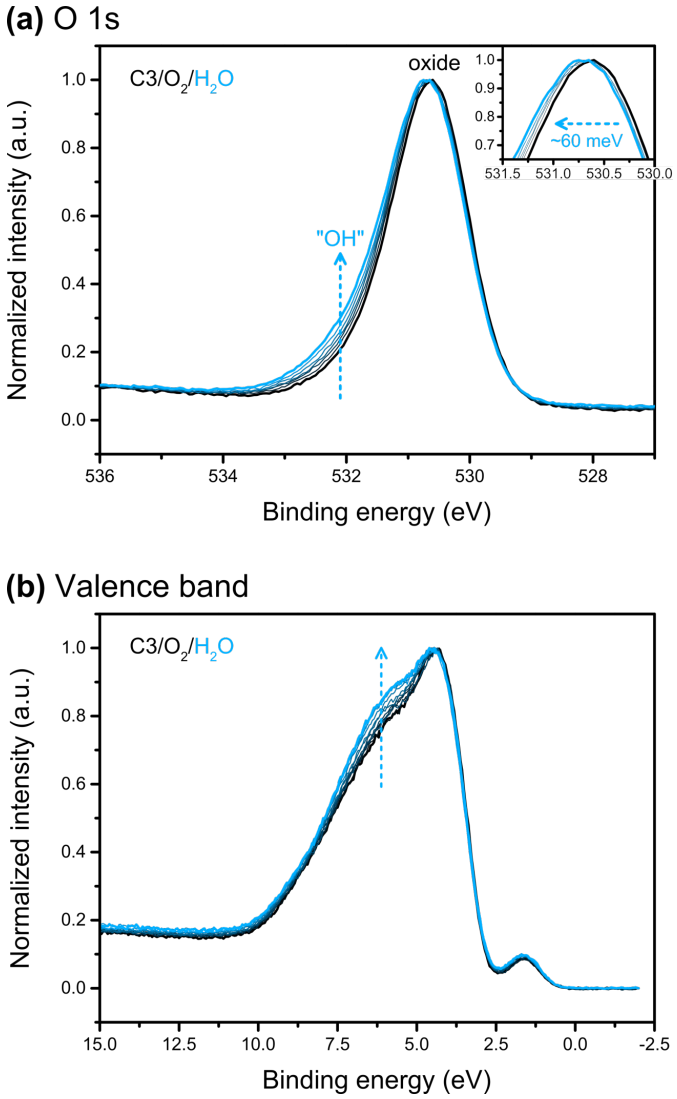

Figure C.21.: Effect of steam on MoV-oxide with time on stream in propane/O_2/H_2O (270 °C, 25 Pa): **(a)** development of O 1s core level shoulder assigned to "OH" or oxygen-species with similar binding energies and **(b)** development of valence band shoulder.

C.3.4. NEXAFS

Additional information on the influence of different alkane oxidation conditions on the electronic structure of MoV-oxide was obtained by probing the unoccupied states with X-ray absorption spectroscopy. The NEXAFS spectra were recorded in the photon energy range of 500 to 560 eV at the V $L_{2,3}$-edge and O K-edge. Figure C.22 shows the corresponding Auger electron yield (AEY) spectra in the different gas feeds. It may be noted that the inelastic mean free path length of an Auger electron with a kinetic energy of ~500 eV is about 1.26 nm, which is in between the "surface sensitive" (λ_{IMFP} of 0.6 nm) and "deeper layers" (λ_{IMFP} of 1.7 nm) XPS measurements.

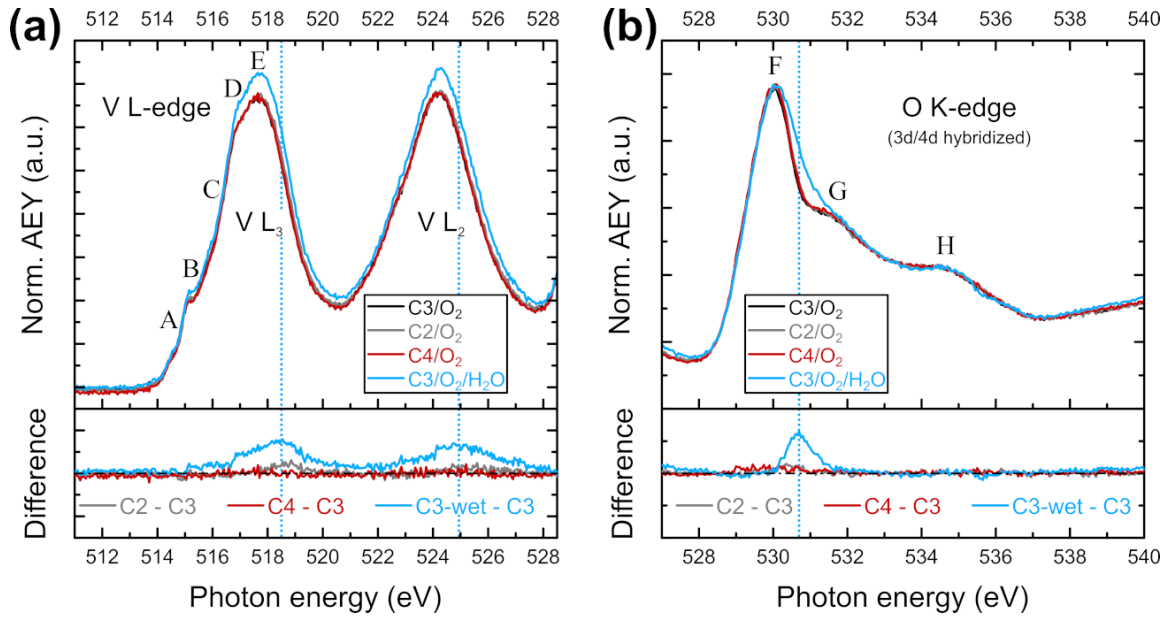

Figure C.22.: Auger electron yield (AEY) NEXAFS spectra of MoV-oxide in different gas feeds: **(a)** V $L_{2,3}$-edge (top) and difference spectra with C_3H_8/O_2 gas feed (bottom); **(b)** "3d/4d hybridized" O K-edge (top) and difference spectra with C_3H_8/O_2 gas feed (bottom).

A closer look at the V L_3-edge spectra in Figure C.22 (a) reveals at least five to six features in the fine structure, which are labeled with the letters "A-E" (corresponding to photon energies of ~514.4, 515.2, 515.9-516, 516.7, and 517.65 eV in the dry gas feeds). These fine structure features are reminiscent of features "I-VI" that were reported for MoVTeNb-oxide.[105] A shoulder at higher energies above the peak maximum "E" around 517.65 eV might occur as well. The fine structure of the V L_3-edge is due to transition from V $2p_{3/2}$ to the ligand field split 3d orbitals in a distorted octahedral environment of vanadium, which is further complicated by multiplet effects.[192,193,336,337] The V L_3-edge spectra of MoV-oxide are similar to the spectra of vanadium oxides with a mixed V^{4+}/V^{5+} oxidation state, but the fine structure is less pronounced than in V_2O_5.[78] The different alkanes did not affect the NEXAFS spectra of MoV-oxide significantly (see the difference spectra at the bottom of Fig. C.22 (a)). In the ethane oxidation feed a small intensity increase at the high energy side was found. Steam had the most pronounced effect on the NEXAFS spectra, in line with the findings from NAP-XPS. The transitions contributing to the mid- to high-energy range of the V L_3-edge were particularly affected by the addition of steam to the gas feed. A comparison to calculated V L-edge X-ray absorption spectra of vanadium oxides in different oxidation states and with a similar local coordination environment around vanadium shows that these energetically highest lying transitions are to final states of V $3d_{x^2-y^2}$ and of V $3d_{z^2}$ character,[189,192] which are characterized by a σ-overlap of V 3d with O 2p orbitals. In addition, it can be seen that the vanadium-related edge-jump intensity increased in the steam-containing feed (cf. Fig. C.22 (a), where the spectra were normalized to the pre-edge and post-edge at 500 and 560 eV, respectively), which could be interpreted as a higher amount of vanadium on the surface and hence an increased concentration of V absorption centers. This would support the results from the core level analysis in terms of an enrichment of vanadium on the surface upon treating MoV-oxide in $C_3H_8/O_2/H_2O$ and is line with observation for MoV-oxide[77] and MoVTeNb-oxide[105] in the literature.

Three to four peaks were observed in the O K-edge spectra of MoV-oxide at ∼530 eV, 531.75 eV, and 534-535 eV, respectively, which are labeled with the letters "F-H" in Fig. C.22 (b). The O K-edge region is due to transitions from O 1s to final states of O 2p character mixed with metal d orbitals. The structure of the O K-edge resembles the spectrum of MoO_3[338–340] more closely than those of V_2O_5 or VO_2.[78,192,194] This can be understood since the majority of the metal sites in MoV-oxide are occupied by molybdenum, which was also pointed out by Heine *et al.*[105] for MoVTeNb-oxide, which exhibits a very similar O K-edge spectrum. Steam affected the O K-edge spectra of MoV-oxide leading to an increase in intensity at ∼530.7 eV, which can clearly be seen in the difference spectrum in Fig. C.22 (b). The energy of this feature is close to the π^* resonance of gas phase O_2 at 530.8 eV[181,182] (cf. the TEY spectra in Fig. C.23 in the SI). It may be due to the lower partial pressure of oxygen in the wet propane oxidation gas feed leading to a higher X-ray transmission in this photon energy range.[180]

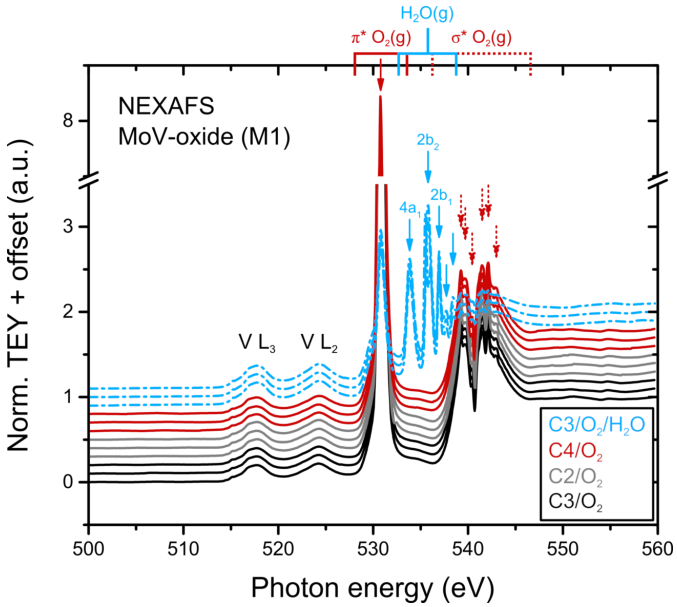

Figure C.23.: Total electron yield (TEY) NEXAFS spectra of MoV-oxide in different gas feeds (25 Pa, 270 °C) and assignment of gas phase signals.

Figure C.23 shows the total electron yield (TEY) NEXAFS spectra of MoV-oxide recorded at the V $L_{2,3}$-edge and O K-edge in different gas feeds. The spectra were normalized to the pre-edge at 500 eV and the post-edge at 560 eV. The dominant contribution of gas phase signals can be seen above 530 eV in the TEY NEXAFS spectra. The most intense peak is due to the O 1s $\rightarrow \pi^*$ excitation of O_2(g). The assignment of the transitions in Figure C.23 is based on literature spectra.[182,341–343] An overlap of the NEXAFS spectra of MoV-oxide with gas phase O_2 excitations was seen in the range of the oxygen absorption in the dry alkane oxidation feeds and with a combination of gas phase O_2 and H_2O signals in the wet propane oxidation feed. The O K-edge absorption spectra of CO and CO_2 were not observed. They occur at higher photon energies with the π^* resonance at approx. 534 eV and 535 eV, respectively.[341,344]

Bibliography

1. Heine, C. *et al.* Work Function, Band Bending, and Microwave Conductivity Studies on the Selective Alkane Oxidation Catalyst MoVTeNb Oxide (Orthorhombic M1 Phase) under Operation Conditions. *J. Phys. Chem. C* **117,** 26988–26997 (2013).
2. Grasselli, R. K. Fundamental Principles of Selective Heterogeneous Oxidation Catalysis. *Top. Catal.* **21,** 79–88 (2002).
3. Ballarini, N. *et al.* VPO catalyst for *n*-butane oxidation to maleic anhydride: A goal achieved, or a still open challenge? *Top. Catal.* **38,** 147–156 (2006).
4. Trivedi, B. C. & Culbertson, B. M. *Maleic Anhydride* (Springer US, New York, 1982).
5. Cavani, F. & Trifirò, F. Some innovative aspects in the production of monomers via catalyzed oxidation processes. *Appl. Catal. A* **88,** 115–135 (1992).
6. Cavani, F. Catalytic selective oxidation: The forefront in the challenge for a more sustainable chemical industry. *Catal. Today* **157,** 8–15 (2010).
7. Cavani, F., Ballarini, N. & Cericola, A. Oxidative dehydrogenation of ethane and propane: How far from commercial implementation? *Catal. Today* **127,** 113–131 (2007).
8. Diercks, R. *et al.* Raw Material Changes in the Chemical Industry. *Chem. Eng. Technol.* **31,** 631–637 (2008).
9. Haber, J. Fifty years of my romance with vanadium oxide catalysts. *Catal. Today* **142,** 100–113 (2009).
10. Schlögl, R. Selective Oxidation: From a Still Immature Technology to the Roots of Catalysis Science. *Top. Catal.* **59,** 1461–1476 (2016).
11. Haber, J. & Witko, M. Oxidation catalysis–electronic theory revisited. *J. Catal.* **216,** 416–424 (2003).
12. Haber, J. *Selectivity in Heterogeneous Catalytic Oxidation of Hydrocarbons* in *Heterogeneous Hydrocarbon Oxidation* (eds Warren, B. K. & Oyama, S. T.) 20–34 (American Chemical Society, Washington, DC, 1996).
13. Haber, J. *Theoretical Basis of the Activation of C-H Bond* in *Catalytic Activation and Functionalisation of Light Alkanes* (eds Derouane, E. G., Haber, J., Lemos, F., Ribeiro, F. R. & Guisnet, M.) 1st ed., 157–187 (Kluwer Academic Publishers, Dordrecht, 1998).
14. Schlögl, R. Heterogeneous Catalysis. *Angew. Chem. Int. Ed.* **54,** 3465–3520 (2015).
15. Schlögl, R. Active Sites for Propane Oxidation: Some Generic Considerations. *Top. Catal.* **54,** 627–638 (2011).

16. Volta, J.-C. Vanadium phosphorus oxides, a reference catalyst for mild oxidation of light alkanes: a review. *C. R. Acad. Sci., Ser. IIc: Chim.* **3,** 717–723 (2000).

17. Centi, G., Trifirò, F., Ebner, J. R. & Franchetti, V. M. Mechanistic aspects of maleic anhydride synthesis from C_4 hydrocarbons over phosphorus vanadium oxide. *Chem. Rev.* **88,** 55–80 (1988).

18. Trifirò, F. & Grasselli, R. K. How the Yield of Maleic Anhydride in *n*-Butane Oxidation, Using VPO Catalysts, was Improved Over the Years. *Top. Catal.* **57,** 1188–1195 (2014).

19. Hodnett, B. K. An overview of recent developments in elucidating the mechanism of selective oxidation of C-4 hydrocarbons over vanadium phosphorus oxide catalysts. *Catal. Today* **1,** 527–536 (1987).

20. Cavani, F. & Trifirò, F. *Selective oxidations of C_4 paraffins* in *Catalysis: Volume 11* (eds Spivey, J. J. & Agarwal, S. K.) 246–317 (The Royal Society of Chemistry, Cambridge, 1994).

21. Millet, J.-M. M. Mechanism of first hydrogen abstraction from light alkanes on oxide catalysts. *Top. Catal.* **38,** 83–92 (2006).

22. Centi, G. Vanadyl Pyrophosphate - A Critical Overview. *Catal. Today* **16,** 5–26 (1993).

23. Wenig, R. W. & Schrader, G. L. Vanadium–phosphorus–oxygen industrial catalysts for *n*-butane oxidation: characterization and kinetic measurements. *Ind. Eng. Chem. Fundam.* **25,** 612–620 (1986).

24. Garbassi, F., Bart, J. C. J., Tassinari, R., Vlaic, G. & Lagarde, P. Catalytic *n*-butane oxidation activity and physicochemical characterization of vanadium-phosphorus oxides with variable P/V ratio. *J. Catal.* **98,** 317–325 (1986).

25. Abon, M., Herrmann, J. M. & Volta, J. C. Correlation with the redox V^{5+}/V^{4+} ratio in vanadium phosphorus oxide catalysts for mild oxidation of *n*-butane to maleic anhydride. *Catal. Today* **71,** 121–128 (2001).

26. Pepera, M. A. *et al.* Fundamental study of the oxidation of butane over vanadyl pyrophosphate. *J. Am. Chem. Soc.* **107,** 4883–4892 (1985).

27. Abon, M., Béré, K. E. & Delichère, P. Nature of active oxygen in the n-butane selective oxidation over well-defined V–P–O catalysts: an oxygen isotopic labelling study. *Catal. Today* **33,** 15–23 (1997).

28. Mars, P. & van Krevelen, D. W. Oxidations carried out by means of vanadium oxide catalysts. *Chem. Eng. Sci.* **3,** 41–59 (1954).

29. Wang, D. & Barteau, M. A. Kinetics of Butane Oxidation by a Vanadyl Pyrophosphate Catalyst. *J. Catal.* **197,** 17–25 (2001).

30. Védrine, J. C. The Role of Redox, Acid-Base and Collective Properties and of Cristalline State of Heterogeneous Catalysts in the Selective Oxidation of Hydrocarbons. *Top. Catal.* **21,** 97–106 (2002).

31. Chen, B. & Munson, E. J. Investigation of the Mechanism of *n*-Butane Oxidation on Vanadium Phosphorus Oxide Catalysts: Evidence from Isotopic Labeling Studies. *J. Am. Chem. Soc.* **124,** 1638–1652 (2002).

32. Bergman, R. I. & Frisch, N. W. *US Patent* US3293268A (1966).

33. Freerks, M. C. & Suda, M. *US Patent* US3832359A (1974).

34. Hodnett, B. K., Permanne, P. & Delmon, B. Influence of P/V ratio on the phase composition and catalytic activity of vanadium phosphate based catalysts. *Appl. Catal.* **6,** 231–244 (1983).

35. Cornaglia, L. M. & Lombardo, E. A. XPS studies of the surface oxidation states on vanadium–phosphorus–oxygen (VPO) equilibrated catalysts. *Appl. Catal. A* **127,** 125–138 (1995).

36. Coulston, G. W., Thompson, E. A. & Herron, N. Characterization of VPO Catalysts by X-Ray Photoelectron Spectroscopy. *J. Catal.* **163,** 122–129 (1996).

37. Hävecker, M. *et al.* In Situ Investigation of the Nature of the Active Surface of a Vanadyl Pyrophosphate Catalyst during *n*-Butane Oxidation to Maleic Anhydride. *J. Phys. Chem. B* **107,** 4587–4596 (2003).

38. Kleimenov, E. *et al.* XPS investigations of VPO catalysts under reaction conditions. *Surf. Sci.* **575,** 181–188 (2005).

39. Eichelbaum, M. *et al.* The Intimate Relationship between Bulk Electronic Conductivity and Selectivity in the Catalytic Oxidation of *n*-Butane. *Angew. Chem. Int. Ed.* **51,** 6246–6250 (2012).

40. Eichelbaum, M. *et al.* Towards Physical Descriptors of Active and Selective Catalysts for the Oxidation of *n*-Butane to Maleic Anhydride. *ChemCatChem* **5,** 2318–2329 (2013).

41. Heine, C. *et al.* Ambient-Pressure Soft X-ray Absorption Spectroscopy of a Catalyst Surface in Action: Closing the Pressure Gap in the Selective *n*-Butane Oxidation over Vanadyl Pyrophosphate. *J. Phys. Chem. C* **118,** 20405–20412 (2014).

42. Eichelbaum, M. *et al.* The Electronic Factor in Alkane Oxidation Catalysis. *Angew. Chem. Int. Ed.* **54,** 2922–2926 (2015).

43. Kiely, C. J. *et al.* Electron microscopy studies of vanadium phosphorus oxide catalysts derived from $VOPO_4{\cdot}2H_2O$. *Catal. Lett.* **33,** 357–368 (1995).

44. Kiely, C. J. *et al.* Characterisation of Variations in Vanadium Phosphate Catalyst Microstructure with Preparation Route. *J. Catal.* **162,** 31–47 (1996).

45. Kiely, C. J. *et al.* Structural transformation sequences occurring during the activation of vanadium phosphorus oxide catalysts. *Faraday Discuss.* **105,** 103–118 (1996).

46. Hutchings, G. J., Kiely, C. J., Sananes-Schulz, M. T., Burrows, A. & Volta, J. C. Comments on the nature of the active site of vanadium phosphate catalysts for butane oxidation. *Catal. Today* **40,** 273–286 (1998).

47. Hutchings, G. J., Desmartin-Chomel, A., Olier, R. & Volta, J.-C. Role of the product in the transformation of a catalyst to its active state. *Nature* **368,** 41–45 (1994).

48. Cavani, F., Centi, G. & Trifirò, F. Structure sensitivity of the catalytic oxidation of n-butane to maleic anhydride. *J. Chem. Soc., Chem. Commun.* 492–494 (1985).

49. Bordes, E. Crystallochemistry of V–P–O phases and application to catalysis. *Catal. Today* **1,** 499–526 (1987).

50. Nguyen, P. T., Hoffman, R. D. & Sleight, A. W. Structure of $(VO)_2P_2O_7$. *Mater. Res. Bull.* **30,** 1055–1063 (1995).

51. Guliants, V. V. *et al.* The effect of the phase composition of model VPO catalysts for partial oxidation of *n*-butane. *Catal. Today* **28,** 275–295 (1996).

52. Zhang-Lin, Y., Forissier, M., Sneeden, R. P., Védrine, J. C. & Volta, J. C. On the Mechanism of *n*-Butane Oxidation to Maleic Anhydride on VPO Catalysts: I. A Kinetics Study on a VPO Catalyst as Compared to VPO Reference Phases. *J. Catal.* **145,** 256–266 (1994).

53. Zhang-Lin, Y., Forissier, M., Védrine, J. C. & Volta, J. C. On the Mechanism of *n*-Butane Oxidation to Maleic Anhydride on VPO Catalysts. II. Study of the Evolution of the VPO Catalysts Under *n*-Butane, Butadiene, and Furan Oxidation Conditions. *J. Catal.* **145,** 267–275 (1994).

54. Abdelouahab, F. B., Olier, R., Guilhaume, N., Lefebvre, F. & Volta, J. C. A study by *in situ* laser Raman spectroscopy of VPO catalysts for *n*-butane oxidation to maleic anhydride I. Preparation and characterization of pure reference phases. *J. Catal.* **134,** 151–167 (1992).

55. Xue, Z.-Y. & Schrader, G. L. *In Situ* Laser Raman Spectroscopy Studies of VPO Catalyst Transformations. *J. Phys. Chem. B* **103,** 9459–9467 (1999).

56. Li, J., Lashier, M. E., Schrader, G. L. & Gerstein, B. C. Oxidation states of vanadium in V-P-O oxidation catalysts ^{31}P NMR by spin-echo mapping. *Appl. Catal.* **73,** 83–95 (1991).

57. Sananes, M. T., Tuel, A. & Volta, J. C. A Study by ^{31}P NMR Spin-Echo Mapping of VPO Catalysts: I. Characterization of the Reference Phases. *J. Catal.* **145,** 251–255 (1994).

58. Brückner, A., Kubias, B. & Lücke, B. In situ-electron spin resonance: a useful tool for the investigation of vanadium phosphate catalysts (VPO) under working conditions. *Catal. Today* **32,** 215–222 (1996).

59. Brückner, A., Kubias, B., Lücke, B. & Stößer, R. In-situ electron spin resonance study of vanadium phosphate catalysts during the selective oxidation of *n*-butane to maleic anhydride. *Colloids Surf., A* **115,** 179–186 (1996).

60. Herrmann, J.-M., Vernoux, P., Béré, K. E. & Abon, M. *In Situ* Study of Redox and of p-Type Semiconducting Properties of Vanadyl Pyrophosphate and of V–P–O Catalysts during the Partial Oxidation of *n*-Butane to Maleic Anhydride. *J. Catal.* **167,** 106–117 (1997).

61. Schuurman, Y. & Gleaves, J. T. A comparison of steady-state and unsteady-state reaction kinetics of *n*-butane oxidation over VPO catalysts using a TAP-2 reactor system. *Catal. Today* **33,** 25–37 (1997).

62. Rodemerck, U., Kubias, B., Zanthoff, H.-W., Wolf, G.-U. & Baerns, M. The reaction mechanism of the selective oxidation of butane on $(VO)_2P_2O_7$ catalysts: The influence of the valence state of vanadium. *Appl. Catal. A* **153,** 217–231 (1997).

63. Wang, D. & Barteau, M. A. Oxidation kinetics of partially reduced vanadyl pyrophosphate catalyst. *Appl. Catal. A* **223,** 205–214 (2002).

64. Cheng, M.-J. & Goddard, W. A. The Critical Role of Phosphate in Vanadium Phosphate Oxide for the Catalytic Activation and Functionalization of *n*-Butane to Maleic Anhydride. *J. Am. Chem. Soc.* **135,** 4600–4603 (2013).

65. O'Leary, W. C., Goddard, W. A. & Cheng, M.-J. Dual-Phase Mechanism for the Catalytic Conversion of *n*-Butane to Maleic Anhydride by the Vanadyl Pyrophosphate Heterogeneous Catalyst. *J. Phys. Chem. C* **121,** 24069–24076 (2017).

66. Ohara, T. *et al. Acrylic Acid and Derivatives* in *Ullmann's Encyclopedia of Industrial Chemistry* 1–18 (Wiley-VCH Verlag GmbH & Co. KGaA, Weinheim, 2012).

67. Penzel, E., Ballard, N. & Asua, J. M. *Polyacrylates* in *Ullmann's Encyclopedia of Industrial Chemistry* 1–20 (Wiley-VCH Verlag GmbH & Co. KGaA, Weinheim, 2018).

68. Grasselli, R. K. *et al.* Active centers in Mo–V–Nb–Te–O_x (amm)oxidation catalysts. *Catal. Today* **91-92,** 251–258 (2004).

69. DeSanto, P. J. *et al.* Structural aspects of the M1 and M2 phases in MoVNbTeO propane ammoxidation catalysts. *Z. Kristallogr. - Cryst. Mater.* **219,** 152–165 (2004).

70. Li, X., Buttrey, D. J., Blom, D. A. & Vogt, T. Improvement of the Structural Model for the M1 Phase Mo–V–Nb–Te–O Propane (Amm)oxidation Catalyst. *Top. Catal.* **54,** 614–626 (2011).

71. Kube, P., Frank, B., Schlögl, R. & Trunschke, A. Isotope Studies in Oxidation of Propane over Vanadium Oxide. *ChemCatChem* **9,** 3446–3455 (2017).

72. Naumann d'Alnoncourt, R. *et al.* The reaction network in propane oxidation over phase-pure MoVTeNb M1 oxide catalysts. *J. Catal.* **311,** 369–385 (2014).

73. Grasselli, R. K., Lugmair, C. G., Volpe, A. F., Andersson, A. & Burrington, J. D. Enhancement of acrylic acid yields in propane and propylene oxidation by selective P Doping of MoV(Nb)TeO-based M1 and M2 catalysts. *Catal. Today* **157,** 33–38 (2010).

74. Cheng, M.-J. & Goddard, W. A. In Silico Design of Highly Selective Mo-V-Te-Nb-O Mixed Metal Oxide Catalysts for Ammoxidation and Oxidative Dehydrogenation of Propane and Ethane. *J. Am. Chem. Soc.* **137,** 13224–13227 (2015).

75. Hävecker, M. *et al.* Surface chemistry of phase-pure M1 MoVTeNb oxide during operation in selective oxidation of propane to acrylic acid. *J. Catal.* **285,** 48–60 (2012).

76. Grasselli, R. K. *et al.* Multifunctionality of Active Centers in (Amm)oxidation Catalysts: From Bi–Mo–O_x to Mo–V–Nb–(Te, Sb)–O_x. *Top. Catal.* **23,** 5–22 (2003).

77. Trunschke, A. *et al.* The Impact of the Bulk Structure on Surface Dynamics of Complex Mo–V-based Oxide Catalysts. *ACS Catal.* **7,** 3061–3071 (2017).

78. Zimmermann, R., Claessen, R., Reinert, F., Steiner, P. & Hüfner, S. Strong hybridization in vanadium oxides: evidence from photoemission and absorption spectroscopy. *J. Phys. Condens. Mat.* **10,** 5697–5716 (1998).

79. Witko, M., Tokarz, R. & Haber, J. Vanadium pentoxide. II. Quantum chemical modeling. *Appl. Catal. A* **157,** 23–44 (1997).

80. Witko, M., Tokarz, R., Haber, J. & Hermann, K. Electronic structure of vanadyl pyrophosphate: cluster model studies. *J. Mol. Catal. A: Chem.* **166,** 59–72 (2001).

81. Khyzhun, O. Y., Strunskus, T., Grünert, W. & Wöll, C. Valence band electronic structure of V_2O_5 as determined by resonant soft X-ray emission spectroscopy. *J. Electron Spectrosc. Relat. Phenom.* **149,** 45–50 (2005).

82. Sawatzky, G. A. & Post, D. X-ray photoelectron and Auger spectroscopy study of some vanadium oxides. *Phys. Rev. B* **20,** 1546–1555 (4 1979).

83. Haber, J. *Electronic Factors in Hydrocarbon Oxidation Catalysis* in *Turning Points in Solid-State, Materials and Surface Science: A Book in Celebration of the Life and Work of Sir John Meurig Thomas* 568–576 (The Royal Society of Chemistry, Cambridge, UK, 2008).

84. Bordes, E. Synergistic effects in selective oxidation catalysis: does phase cooperation result in site isolation? *Top. Catal.* **15,** 131–137 (2001).

85. Haber, J., Witko, M. & Tokarz, R. Vanadium pentoxide I. Structures and properties. *Appl. Catal. A* **157,** 3–22 (1997).

86. Colpaert, M. N., Clauws, P., Fiermans, L. & Vennik, J. Thermal and low energy electron bombardment induced oxygen loss of V_2O_5 single crystals: Transition into V_6O_{13}. *Surf. Sci.* **36,** 513–525 (1973).

87. Hermann, K., Witko, M., Druzinic, R. & Tokarz, R. Oxygen vacancies at oxide surfaces: ab initio density functional theory studies on vanadium pentoxide. *Appl. Phys. A* **72,** 429–442 (2001).

88. Mills, P. L., Randall, H. T. & McCracken, J. S. Redox kinetics of $VOPO_4$ with butane and oxygen using the TAP reactor system. *Chem. Eng. Sci.* **54,** 3709–3722 (1999).

89. Schlögl, R. *Concepts in Selective Oxidation of Small Alkane Molecules* in *Modern Heterogeneous Oxidation Catalysis* (ed Mizuno, N.) 1–42 (Wiley-VCH Verlag GmbH & Co. KGaA, Weinheim, 2009).

90. Ganduglia-Pirovano, M. V. & Sauer, J. Stability of reduced V_2O_5(001) surfaces. *Phys. Rev. B* **70,** 045422 (2004).

91. Wang, Y., Rosowski, F., Schlögl, R. & Trunschke, A. *Molecular oxygen activation on the surface of vanadium pentoxide.* Manuscript, 2018.

92. Bordes, E. Nature of the active and selective sites in vanadyl pyrophosphate, catalyst of oxidation of n-butane, butene and pentane to maleic anhydride. *Catal. Today* **16,** 27–38 (1993).

93. Grasselli, R. K. Genesis of site isolation and phase cooperation in selective oxidation catalysis. *Top. Catal.* **15,** 93–101 (2001).

94. Vol'kenshtein, F. F. *The Electronic Theory of Catalysis on Semiconductors* (ed Birch, E. J. H.) (Pergamon Press, Oxford - London - New York - Paris, 1963).

95. Morrison, S. R. *The Chemical Physics of Surfaces* (Plenum Press, New York, 1977).

96. Zhang, Z. & Yates, J. T. Band Bending in Semiconductors: Chemical and Physical Consequences at Surfaces and Interfaces. *Chem. Rev.* **112,** 5520–5551 (2012).

97. Schwab, G.-M. Mischkatalysatoren mit dotiertem Träger. *Angew. Chem.* **73,** 399–401 (1961).

98. Boudart, M. Electronic Chemical Potential in Chemisorption and Catalysis. *J. Am. Chem. Soc.* **74,** 1531–1535 (1952).

99. Lüth, H. *Solid Surfaces, Interfaces and Thin Films* 5th ed. (Springer Berlin Heidelberg, 2010).

100. Mönch, W. Adsorbate-induced surface states and Fermi-level pinning at semiconductor surfaces. *J. Vac. Sci. Technol., B* **7,** 1216–1225 (1989).

101. Jaegermann, W. *Surface studies of layered materials in relation to energy converting interfaces* in *Photoelectrochemistry and Photovoltaics of Layered Semiconductors* (ed Aruchamy, A.) 195–295 (Kluwer Academic Publishers, Dordrecht, The Netherlands, 1992).

102. Weisz, P. B. Effects of Electronic Charge Transfer between Adsorbate and Solid on Chemisorption and Catalysis. *J. Chem. Phys.* **21,** 1531–1538 (1953).

103. Eichelbaum, M. *et al.* The microwave cavity perturbation technique for contact-free and *in situ* electrical conductivity measurements in catalysis and materials science. *Phys. Chem. Chem. Phys.* **14,** 1302–1312 (2012).

104. Heine, C., Girgsdies, F., Trunschke, A., Schlögl, R. & Eichelbaum, M. The model oxidation catalyst α-V_2O_5: insights from contactless in situ microwave permittivity and conductivity measurements. *Appl. Phys. A* **112,** 289–296 (2013).

105. Heine, C., Hävecker, M., Trunschke, A., Schlögl, R. & Eichelbaum, M. The impact of steam on the electronic structure of the selective propane oxidation catalyst MoVTeNb oxide (orthorhombic M1 phase). *Phys. Chem. Chem. Phys.* **17,** 8983–8993 (2015).

106. Chen, L. F., Ong, C. K., Neo, C. P., Varadan, V. V. & Varadan, V. K. *Microwave Electronics: Measurement and Materials Characterisation* (Wiley, Chichester, West Sussex, England, 2004).

107. Che, R. C., Peng, L.-M., Duan, X. F., Chen, Q. & Liang, X. L. Microwave Absorption Enhancement and Complex Permittivity and Permeability of Fe Encapsulated within Carbon Nanotubes. *Adv. Mater.* **16,** 401–405 (2004).

108. Chen, Y.-J. *et al.* Synthesis, Multi-Nonlinear Dielectric Resonance, and Excellent Electromagnetic Absorption Characteristics of Fe_3O_4/ZnO Core/Shell Nanorods. *J. Phys. Chem. C* **114,** 9239–9244 (2010).

109. Chen, Y. J. *et al.* Synthesis, magnetic and electromagnetic wave absorption properties of porous Fe_3O_4/Fe/SiO_2 core/shell nanorods. *J. Appl. Phys.* **106,** 054303 (2009).

110. Chen, Y. J., Cao, M. S., Wang, T. H. & Wan, Q. Microwave absorption properties of the ZnO nanowire-polyester composites. *Appl. Phys. Lett.* **84,** 3367–3369 (2004).

111. Watts, P. C. P., Hsu, W.-K., Barnes, A. & Chambers, B. High Permittivity from Defective Multiwalled Carbon Nanotubes in the X-Band. *Adv. Mater.* **15,** 600–603 (2003).

112. Zhuo, R. F. *et al.* Multistep Synthesis, Growth Mechanism, Optical, and Microwave Absorption Properties of ZnO Dendritic Nanostructures. *J. Phys. Chem. C* **112,** 11767–11775 (2008).

113. Han, Z. *et al.* Permittivity and permeability of Fe(Tb) nanoparticles and their microwave absorption in the 2–18 GHz range. *J. Appl. Phys.* **107,** 09A929 (2010).

114. Chen, Y.-J. *et al.* Porous Fe_3O_4/SnO_2 Core/Shell Nanorods: Synthesis and Electromagnetic Properties. *J. Phys. Chem. C* **113,** 10061–10064 (2009).

115. Liu, X. G., Geng, D. Y. & Zhang, Z. D. Microwave-absorption properties of FeCo microspheres self-assembled by Al_2O_3-coated FeCo nanocapsules. *Appl. Phys. Lett.* **92,** 243110 (2008).

116. Lee, C.-C. & Chen, D.-H. Ag nanoshell-induced dual-frequency electromagnetic wave absorption of Ni nanoparticles. *Appl. Phys. Lett.* **90,** 193102 (2007).

117. Zhang, X. F. *et al.* Microwave absorption properties of the carbon-coated nickel nanocapsules. *Appl. Phys. Lett.* **89,** 053115 (2006).

118. Du, Y. *et al.* Shell Thickness-Dependent Microwave Absorption of Core–Shell Fe_3O_4@C Composites. *ACS Appl. Mater. Interfaces* **6,** 12997–13006 (2014).

119. McNeal, M. P., Jang, S.-J. & Newnham, R. E. The effect of grain and particle size on the microwave properties of barium titanate ($BaTiO_3$). *J. Appl. Phys.* **83,** 3288–3297 (1998).

120. Viana, R., Lunkenheimer, P., Hemberger, J., Böhmer, R. & Loidl, A. Dielectric spectroscopy in $SrTiO_3$. *Phys. Rev. B* **50,** 601–604 (1994).

121. Shulman, H. S., Damjanovic, D. & Setter, N. Niobium Doping and Dielectric Anomalies in Bismuth Titanate. *J. Am. Ceram. Soc.* **83,** 528–532 (2000).

122. Huang, X., Zhang, H., Lai, Y. & Li, J. The lowered dielectric loss tangent and grain boundary effects in fluorine-doped calcium copper titanate ceramics. *Appl. Phys. A* **123,** 317 (2017).

123. Heenemann, M., Heine, C., Hävecker, M., Trunschke, A. & Schlögl, R. Influence of Steam on a Vanadyl Pyrophosphate Catalyst During Propane Oxidation. *J. Phys. Chem. B* **122,** 695–704 (2018).

124. Dietrich, M., Rauch, D., Porch, A. & Moos, R. A Laboratory Test Setup for *in Situ* Measurements of the Dielectric Properties of Catalyst Powder Samples under Reaction Conditions by Microwave Cavity Perturbation: Set up and Initial Tests. *Sensors* **14,** 16856–16868 (2014).

125. Rauch, D. *et al.* Microwave Cavity Perturbation Studies on H-form and Cu Ion-Exchanged SCR Catalyst Materials: Correlation of Ammonia Storage and Dielectric Properties. *Top. Catal.* **60,** 243–249 (2017).

126. Beulertz, G. *et al.* Microwave Cavity Perturbation as a Tool for Laboratory In Situ Measurement of the Oxidation State of Three Way Catalysts. *Top. Catal.* **56,** 405–409 (2013).

127. Beulertz, G., Votsmeier, M. & Moos, R. Effect of propene, propane, and methane on conversion and oxidation state of three-way catalysts: a microwave cavity perturbation study. *Appl. Catal. B.* **165,** 369–377 (2015).

128. Liu, B. *et al.* Microwaves effectively examine the extent and type of coking over acid zeolite catalysts. *Nat. Commun.* **8,** 1 (2017).

129. Dressel, M., Klein, O., Donovan, S. & Grüner, G. Microwave cavity perturbation technique: Part III: Applications. *Int. J. Infrared Millimeter Waves* **14,** 2489–2517 (1993).

130. Heenemann, M. *Charge Transfer in Catalysis Studied by In-situ Microwave Cavity Perturbation Techniques* PhD thesis (Technischen Universität Berlin, Fakultät II - Mathematik und Naturwissenschaften, 2017).

131. Feynman, R. P., Leighton, R. B. & Sands, M. *The Feynman Lectures on Physics: Mainly Electromagnetism and Matter* New Millennium Edition (Basic Books, Perseus Books Group, New York, 2010).

132. *Handbook of Mathematical Functions with Formulas, Graphs, and Mathematical Tables* (eds Abramowitz, M. & Stegun, I. A.) (Dover Publications, New York, 1972).

133. Klein, O., Donovan, S., Dressel, M. & Grüner, G. Microwave cavity perturbation technique: Part I: Principles. *Int. J. Infrared Millimeter Waves* **14,** 2423–2457 (1993).

134. Shchegolev, I. F. Electric and magnetic properties of linear conducting chains. *Phys. Status Solidi A* **12,** 9–45 (1972).

135. Peligrad, D.-N. *et al.* General solution for the complex frequency shift in microwave measurements of thin films. *Phys. Rev. B* **64,** 224504 (22 2001).

136. Slater, J. C. Microwave Electronics. *Rev. Mod. Phys.* **18,** 441–512 (1946).

137. Waldron, R. A. Perturbation theory of resonant cavities. *Proceedings of the IEE - Part C: Monographs* **107,** 272–274 (1960).

138. Bauhofer, W. Determination of semiconductor energy gaps using the microwave cavity perturbation method. *J. Phys. E: Sci. Instrum.* **14,** 934–938 (1981).

139. Slocombe, D., Porch, A., Bustarret, E. & Williams, O. A. Microwave properties of nanodiamond particles. *Appl. Phys. Lett.* **102,** 244102 (2013).

140. Böttcher, C. J. F. & Bordewijk, P. *Theory of Electric Polarization. Dielectrics in Time-Dependent Fields* 2nd ed. (Elsevier Science, The Netherlands, 1978).

141. Hummel, R. E. *Electronic Properties of Materials* 4th ed. (Springer-Verlag, New York, 2011).

142. Patterson, J. & Bailey, B. *Solid-State Physics. Introduction to the Theory* 2nd ed. (Springer-Verlag, Berlin Heidelberg, 2010).

143. Bruggeman, D. A. G. Berechnung verschiedener physikalischer Konstanten von heterogenen Substanzen. I. Dielektrizitätskonstanten und Leitfähigkeiten der Mischkörper aus isotropen Substanzen. *Ann. Phys.* **24,** 636–664 (1935).

144. Böttcher, C. J. F. *Theory of Electric Polarisation* 1st ed., 415–420 (Elsevier, Amsterdam, 1952).

145. Dube, D. C. & Parshad, R. Study of Böttcher's formula for dielectric correlation between powder and bulk. *J. Phys. D: Appl. Phys.* **3,** 677–684 (1970).

146. Maxwell Garnett, J. C. XII. Colours in metal glasses and in metallic films. *Philos. Trans. R. Soc., A* **203,** 385–420 (1904).

147. Landau, L. D. & Lifshitz, E. M. *Electrodynamics of Continuous Media* (Pergamon Press, New York, 1960).

148. Looyenga, H. Dielectric constants of heterogeneous mixtures. *Physica* **31,** 401–406 (1965).

149. Dube, D. C. Study of Landau-Lifshitz-Looyenga's formula for dielectric correlation between powder and bulk. *J. Phys. D: Appl. Phys.* **3,** 1648–1652 (1970).

150. Shoaib, N. *Vector Network Analyzer (VNA) Measurements and Uncertainty Assessment* 1st ed. (ed Ghione, G.) (Springer International Publishing, Switzerland, 2017).

151. Heine, C. *The Electronic Structure of Vanadium Oxides as Catalysts in the Selective Oxidation of Small Alkanes* PhD thesis (Technischen Universität Berlin, Fakultät II - Mathematik und Naturwissenschaften, 2014).

152. Kajfez, D. *Q Factor Measurements Using MATLAB* (Artech House, Norwood, MA, 2011).

153. Kajfez, D. Linear fractional curve fitting for measurement of high Q factors. *IEEE Trans. Microwave Theory Tech.* **42,** 1149–1153 (1994).

154. Kajfez, D. Random and systematic uncertainties of reflection-type Q-factor measurement with network analyzer. *IEEE Trans. Microwave Theory Tech.* **51,** 512–519 (2003).

155. Rozanska, X., Fortrie, R. & Sauer, J. Oxidative Dehydrogenation of Propane by Monomeric Vanadium Oxide Sites on Silica Support. *J. Phys. Chem. C* **111,** 6041–6050 (2007).

156. Wu, Q.-H., Thissen, A., Jaegermann, W., Schüz, M. & Schmidt, P. Resonant photoemission spectroscopy study of electronic structure of V_2O_5. *Chem. Phys. Lett.* **430,** 309–313 (2006).

157. Haber, J. & Witko, M. Quantum-chemical modelling of hydrocarbon oxidation on vanadium-based catalysts. *Catal. Today* **23,** 311–316 (1995).

158. Brocławik, E., Haber, J. & Piskorz, W. Molecular mechanism of C–H bond cleavage at transition metal oxide clusters. *Chem. Phys. Lett.* **333,** 332–336 (2001).

159. Vuong, T. H. *et al.* Efficient $VO_x/Ce_{1-x}Ti_xO_2$ Catalysts for Low-Temperature NH_3-SCR: Reaction Mechanism and Active Sites Assessed by in Situ/Operando Spectroscopy. *ACS Catal.* **7,** 1693–1705 (2017).

160. Wang, Q. & Madix, R. J. Preparation and reactions of V_2O_5 supported on TiO_2(110). *Surf. Sci.* **474,** L213–L216 (2001).

161. Wang, Q. & Madix, R. J. Partial oxidation of methanol to formaldehyde on a model supported monolayer vanadia catalyst: vanadia on TiO_2(110). *Surf. Sci.* **496,** 51–63 (2002).

162. Andrushkevich, T. V., Kaichev, V. V., Chesalov, Y. A., Saraev, A. A. & Buktiyarov, V. I. Selective oxidation of ethanol over vanadia-based catalysts: The influence of support material and reaction mechanism. *Catal. Today* **279,** 95–106 (2017).

163. Kaichev, V. V. *et al.* Redox mechanism for selective oxidation of ethanol over monolayer V_2O_5/TiO_2 catalysts. *J. Catal.* **338,** 82–93 (2016).

164. Kaichev, V. V. *et al.* Selective oxidation of methanol to form dimethoxymethane and methyl formate over a monolayer V_2O_5/TiO_2 catalyst. *J. Catal.* **311,** 59–70 (2014).

165. Mårtensson, N., Karis, O. & Nilsson, A. Resonant processes in the soft X-ray regime. *J. Electron Spectrosc. Relat. Phenom.* **100,** 379–393 (1999).

166. Tiedje, T., Colbow, K. M., Rogers, D. & Eberhardt, W. Nature of core-electron excited states in CaF_2 determined by high-resolution absorption and electron-emission studies. *Phys. Rev. Lett.* **65,** 1243–1246 (10 1990).

167. Aksela, H. *et al.* Character of F core excitons in alkali fluorides studied by resonant Auger spectroscopy. *Phys. Rev. B* **49,** 3116–3123 (5 1994).

168. Shin, S., Tezuka, Y., Ishii, T. & Ueda, Y. Electronic structure of light transition metal compounds studied by photoemission. *Solid State Commun.* **87,** 1051–1054 (1993).

169. Vinogradov, A. S. *et al.* Nitrogen and oxygen core excitations in solid $NaNO_2$ studied by X-ray absorption and resonant photoemission. *Chem. Phys.* **249,** 249–258 (1999).

170. De Groot, F. Multiplet effects in X-ray spectroscopy. *Coord. Chem. Rev.* **249,** 31–63 (2005).

171. Preobrajenski, A. B. *et al.* Strong participator channels in the non-radiative resonant decay of B 1s excitation in B_2O_3. *Phys. Scr.* **2005,** 1071–1073 (2005).

172. Bluhm, H. *et al. In Situ* X-Ray Photoelectron Spectroscopy Studies of Gas-Solid Interfaces at Near-Ambient Conditions. *MRS Bull.* **32,** 1022–1030 (2007).

173. Vass, E. M. *et al.* The role of carbon species in heterogeneous catalytic processes: an *in situ* soft x-ray photoelectron spectroscopy study. *J. Phys. Condens. Mat.* **20,** 184016 (2008).

174. Blume, R. *et al.* Characterizing Graphitic Carbon with X-ray Photoelectron Spectroscopy: A Step-by-Step Approach. *ChemCatChem* **7,** 2871–2881 (2015).

175. Yeh, J. J. & Lindau, I. Atomic subshell photoionization cross sections and asymmetry parameters: $1 \leq Z \leq 103$. *Atomic Data and Nuclear Data Tables* **32,** 1–155 (1985).

176. Yeh, J. J. *Atomic Calculation of Photoionization Cross-Sections and Asymmetry Parameters* (Gordon & Breach Science Publishers, Langhorne, PE (USA), 1993).

177. Tanuma, S., Powell, C. J. & Penn, D. R. Calculations of electorn inelastic mean free paths. II. Data for 27 elements over the 50–2000 eV range. *Surf. Interface Anal.* **17,** 911–926 (1991).

178. Tanuma, S., Powell, C. J. & Penn, D. R. Calculation of electron inelastic mean free paths (IMFPs) VII. Reliability of the TPP-2M IMFP predictive equation. *Surf. Interface Anal.* **35,** 268–275 (2003).

179. Powell, C. J. & Jablonski, A. *NIST Electron Inelastic-Mean-Free-Path Database - Version 1.2* (National Institute of Standards and Technology, Gaithersburg, MD, 2010).

180. Hävecker, M. *et al.* Methodology for the structural characterisation of V_xO_y species supported on silica under reaction conditions by means of in situ O K-edge X-ray absorption spectroscopy. *Phys. Status Solidi B* **246,** 1459–1469 (2009).

181. Hitchcock, A. P. & Brion, C. E. K-shell excitation spectra of CO, N_2 and O_2. *J. Electron Spectrosc. Relat. Phenom.* **18,** 1–21 (1980).

182. Feifel, R. *et al.* X-ray absorption and resonant Auger spectroscopy of O_2 in the vicinity of the O $1s \rightarrow \sigma^*$ resonance: Experiment and theory. *J. Chem. Phys.* **128,** 064304 (2008).

183. Hävecker, M. *et al.* Influence of the geometric structure on the V L_3 near edge X-ray absorption fine structure from vanadium phosphorus oxide catalysts. *J. Electron Spectrosc. Relat. Phenom.* **125,** 79–87 (2002).

184. Heber, M. & Grünert, W. Application of Ultraviolet Photoelectron Spectroscopy in the Surface Characterization of Polycrystalline Oxide Catalysts. 2. Depth Variation of the Reduction Degree in the Surface Region of Partially Reduced V_2O_5. *J. Phys. Chem. B* **104,** 5288–5297 (2000).

185. Silversmit, G., Depla, D., Poelman, H., Marin, G. B. & Gryse, R. D. Determination of the V2p XPS binding energies for different vanadium oxidation states (V^{5+} to V^{0+}). *J. Electron Spectrosc. Relat. Phenom.* **135,** 167–175 (2004).

186. Mossanek, R. J. O. *et al.* Cluster model and band structure calculations of V_2O_5: Reduced V^{5+} symmetry and many-body effects. *Phys. Rev. B* **77,** 075118 (2008).

187. Hävecker, M. *et al.* Dynamic surface behaviour of VPO catalysts under reactive and non-reactive gas compositions: an in situ XAS study. *Appl. Surf. Sci.* **230,** 272–282 (2004).

188. Abbate, M. *et al.* Soft X-ray absorption spectroscopy of vanadium oxides. *J. Electron Spectrosc. Relat. Phenom.* **62,** 185–195 (1993).

189. Maganas, D. *et al.* L-edge X-ray absorption study of mononuclear vanadium complexes and spectral predictions using a restricted open shell configuration interaction ansatz. *Phys. Chem. Chem. Phys.* **16,** 264–276 (2014).

190. Thole, B. T. *et al.* $3d$ x-ray-absorption lines and the $3d^94f^{n+1}$ multiplets of the lanthanides. *Phys. Rev. B* **32,** 5107–5118 (1985).

191. Zaanen, J. & Sawatzky, G. A. Strong interference between decay channels and valence-electron rearrangements in core-hole spectroscopy. *Phys. Rev. B* **33,** 8074–8083 (1986).

192. Maganas, D. *et al.* First principles calculations of the structure and V L-edge X-ray absorption spectra of V_2O_5 using local pair natural orbital coupled cluster theory and spin-orbit coupled configuration interaction approaches. *Phys. Chem. Chem. Phys.* **15,** 7260–7276 (2013).

193. De Francesco, R., Stener, M., Causà, M., Toffoli, D. & Fronzoni, G. Time dependent density functional investigation of the near-edge absorption spectra of V_2O_5. *Phys. Chem. Chem. Phys.* **8,** 4300–4310 (2006).

194. Velazquez, J. M., Jaye, C., Fischer, D. A. & Banerjee, S. Near Edge X-ray Absorption Fine Structure Spectroscopy Studies of Single-Crystalline V_2O_5 Nanowire Arrays. *J. Phys. Chem. C* **113,** 7639–7645 (2009).

195. Soriano, L. *et al.* The O 1s x-ray absorption spectra of transition-metal oxides: The TiO_2–ZrO_2–HfO_2 and V_2O_5–Nb_2O_5–Ta_2O_5 series. *Solid State Commun.* **87,** 699–703 (1993).

196. Kolczewski, C. & Hermann, K. Identification of oxygen sites at the V_2O_5(010) surface by core-level electron spectroscopy: *Ab initio* cluster studies. *J. Chem. Phys.* **118,** 7599–7609 (2003).

197. Kolczewski, C. & Hermann, K. Ab initio DFT cluster studies of angle-resolved NEXAFS spectra for differently coordinated oxygen at the V_2O_5(0 1 0) surface. *Surf. Sci.* **552,** 98–110 (2004).

198. Fiermans, L. & Vennik, J. Auger electron emission spectroscopy of the V_2O_5(010) and V(100) surfaces. *Surf. Sci.* **24,** 541–554 (1971).

199. Goodman, K. W. & Henrich, V. E. Assignment of a photoemission feature in the O-2s–O-2p band gaps of TiO_2 and V_2O_5. *Phys. Rev. B* **50,** 10450–10456 (1994).

200. Zimmermann, R. *et al.* Electronic structure of 3d-transition-metal oxides: on-site Coulomb repulsion versus covalency. *J. Phys. Condens. Mat.* **11,** 1657–1682 (1999).

201. Eyert, V. & Höck, K.-H. Electronic structure of V_2O_5: Role of octahedral deformations. *Phys. Rev. B* **57,** 12727–12737 (1998).

202. De Groot, F. M. F. *et al.* Oxygen 1s x-ray-absorption edges of transition-metal oxides. *Phys. Rev. B* **40,** 5715–5723 (1989).

203. Huotari, J. *et al.* Separation of valence states in thin films with mixed V_2O_5 and V_7O_{16} phases. *J. Electron Spectrosc. Relat. Phenom.* **211,** 47–54 (2016).

204. Ruzmetov, D., Senanayake, S. D. & Ramanathan, S. X-ray absorption spectroscopy of vanadium dioxide thin films across the phase-transition boundary. *Phys. Rev. B* **75,** 195102 (2007).

205. Eguchi, R. *et al.* Photoemission evidence for a Mott-Hubbard metal-insulator transition in VO_2. *Phys. Rev. B* **78,** 075115 (2008).

206. Mo, S.-K. *et al.* Distortion of V 3d line shape due to Auger emission in resonant photoemission spectra of $(V_{1-x}Cr_x)_2O_3$ at the V 2p $\rightarrow$ 3d absorption edge. *Physica B* **351,** 235–239 (2004).

207. Kobayashi, M. *et al.* Hybridization between the conduction band and 3*d* orbitals in the oxide-based diluted magnetic semiconductor $In_{2-x}V_xO_3$. *Phys. Rev. B* **79,** 205203 (2009).

208. Rihko-Struckmann, L. K. *et al.* Bulk and Surface Properties of a VPO Catalyst Used in an Electrochemical Membrane Reactor: Conductivity-, XRD-, TPO- and XPS-study. *Catal. Lett.* **109,** 89–96 (2006).

209. Sartoni, L. *et al.* Gallium-doped VPO catalysts for the oxidation of n-butane to maleic anhydride. *J. Mater. Chem.* **16,** 4348–4360 (2006).

210. Göbke, D. *et al.* Formaldehyde Formation on Vanadium Oxide Surfaces $V_2O_3(0001)$ and $V_2O_5(001)$: How does the Stable Methoxy Intermediate Form? *Angew. Chem. Int. Ed.* **48,** 3695–3698 (2009).

211. Guimond, S. *et al.* Vanadium oxide surfaces and supported vanadium oxide nanoparticles. *Top. Catal.* **38,** 117–125 (2006).

212. Todorova, T. K., Döbler, J., Sierka, M. & Sauer, J. Vanadium Oxides Supported on a Thin Silica Film Grown on Mo(112): Insights from Density Functional Theory. *J. Phys. Chem. C* **113,** 8336–8342 (2009).

213. Romanyshyn, Y. *et al.* Selectivity in Methanol Oxidation as Studied on Model Systems Involving Vanadium Oxides. *Top. Catal.* **50,** 106–115 (2008).

214. Vyboishchikov, S. F. & Sauer, J. $(V_2O_5)_n$ Gas-Phase Clusters (n = 1–12) Compared to V_2O_5 Crystal: DFT Calculations. *J. Phys. Chem. A* **105,** 8588–8598 (2001).

215. Hermann, K., Witko, M., Druzinic, R. & Tokarz, R. Hydrogen assisted oxygen desorption from the $V_2O_5(010)$ surface. *Top. Catal.* **11,** 67–75 (2000).

216. Hermann, K., Michalak, A. & Witko, M. Cluster model studies on oxygen sites at the (010) surfaces of V_2O_5 and MoO_3. *Catal. Today* **32,** 321–327 (1996).

217. Giannetta, H. M. R., Calaza, C., Lamas, D. G., Fonseca, L. & Fraigi, L. Electrical transport properties of V_2O_5 thin films obtained by thermal annealing of layers grown by RF magnetron sputtering at room temperature. *Thin Solid Films* **589,** 730–734 (2015).

218. Haemers, J., Baetens, E. & Vennik, J. On the electrical conductivity of V_2O_5 single crystals. *Phys. Status Solidi A* **20,** 381–386 (1973).

219. Ioffe, V. A. & Patrina, I. B. Comparison of the Small-Polaron Theory with the Experimental Data of Current Transport in V_2O_5. *Phys. Status Solidi B* **40,** 389–395 (1970).

220. Karakotsou, C., Kalomiros, J. A., Hanias, M. P., Anagnostopoulos, A. N. & Spyridelis, J. Nonlinear electrical conductivity of V_2O_5 single crystals. *Phys. Rev. B* **45,** 11627–11631 (1992).

221. Lányi, Š. Contact-Limited Conduction in V_2O_5 Single Crystals. *Phys. Status Solidi A* **54,** 37–43 (1979).

222. Sanchez, C., Henry, M., Grenet, J. C. & Livage, J. Free and bound polarons in vanadium pentoxide. *J. Phys. C: Solid State Phys.* **15,** 7133–7141 (1982).

223. Allersma, T., Hakim, R., Kennedy, T. N. & Mackenzie, J. D. Structure and Physical Properties of Solid and Liquid Vanadium Pentoxide. *J. Chem. Phys.* **46,** 154–160 (1967).

224. Annamalai, S., Bhatta, R. P., Pegg, I. L. & Dutta, B. Majority charge carrier reversal and its effect on thermal and electron transport in $x\mathrm{V_2O_5}$-$(1-x)$ $\mathrm{As_2O_3}$ glasses. *J. Non-Cryst. Solids* **358,** 1019–1027 (2012).

225. Austin, I. G. & Mott, N. F. Polarons in Crystalline and Non-crystalline Materials. *Adv. Phys.* **18,** 41–102 (1969).

226. Cavani, F. *et al.* Relationship between structural/surface characteristics and reactivity in *n*-butane oxidation to maleic anhydride: The role of $\mathrm{V^{3+}}$ species. *Catal. Today* **61,** 203–210 (2000).

227. Cavani, F. & Trifirò, F. Some aspects that affect the selective oxidation of paraffins. *Catal. Today* **36,** 431–439 (1997).

228. Cavani, F. & Trifirò, F. The characterization of the surface properties of V–P–O-based catalysts by probe molecules. *Appl. Catal. A* **157,** 195–221 (1997).

229. Centi, G. & Trifirò, F. *Selective oxidation of light alkanes: comparison between vanadyl pyrophosphate and vanadium-molybdophosphoric acid* in *Catalytic Science and Technology* (eds Yoshida, S., Takezawa, N. & Ono, T.) **1** (Kodansha, Tokyo, 1991), 225–230.

230. Glaum, R. *et al.* Resource-Efficient Alkane Selective Oxidation on New Crystalline Solids: Searching for Novel Catalyst Materials. *Chem. Ing. Tech.* **84,** 1766–1779 (2012).

231. Bluhm, H. *et al. In Situ* Surface Analysis in Selective Oxidation Catalysis: *n*-Butane Conversion Over VPP. *Top. Catal.* **23,** 99–107 (2003).

232. Clauws, P. & Vennik, J. Optical Absorption of Defects in $\mathrm{V_2O_5}$ Single Crystals: As-Grown and Reduced $\mathrm{V_2O_5}$. *Phys. Status Solidi B* **66,** 553–560 (1974).

233. Gao, X., Jehng, J.-M. & Wachs, I. E. *In Situ* UV–vis–NIR Diffuse Reflectance and Raman Spectroscopic Studies of Propane Oxidation over $\mathrm{ZrO_2}$-Supported Vanadium Oxide Catalysts. *J. Catal.* **209,** 43–50 (2002).

234. Aït-Lachgar, K., Abon, M. & Volta, J. C. Selective Oxidation of n-Butane to Maleic Anhydride on Vanadyl Pyrophosphate. *J. Catal.* **171,** 383–390 (1997).

235. Cavani, F., Centi, G., Manenti, I. & Trifirò, F. Catalytic conversion of $\mathrm{C_4}$ hydrocarbons on vanadium–phosphorus oxides: factors influencing the selectivity in 1-butene oxidation. *Ind. Eng. Chem. Prod. Res. Dev.* **24,** 221–226 (1985).

236. Loukah, M., Coudurier, G., Vedrine, J. C. & Ziyad, M. Oxidative dehydrogenation of ethane on V- and Cr-based phosphate catalysts. *Microporous Mater.* **4,** 345–358 (1995).

237. Naguib, H. M. & Kelly, R. On the increase in the electrical conductivity of $\mathrm{MoO_3}$ and $\mathrm{V_2O_5}$ following ion bombardment. Studies on bombardment-enhanced conductivity–I. *J. Phys. Chem. Solids* **33,** 1751–1759 (1972).

238. Perlstein, J. H. A dislocation model for two-level electron-hopping conductivity in $\mathrm{V_2O_5}$: Implications for catalysis. *J. Solid State Chem.* **3,** 217–226 (1971).

239. Avansi Jr., W., Ribeiro, C., Leite, E. R. & Mastelaro, V. R. Vanadium Pentoxide Nanostructures: An Effective Control of Morphology and Crystal Structure in Hydrothermal Conditions. *Cryst. Growth Des.* **9,** 3626–3631 (2009).

240. Sobrados, L., Goni, S., Sagrera, J. L. & Martinez, M. J. Study of the evolution of $CaCO_3$-V_2O_5 (1:1) mixture at room temperature by thermal analysis. *J. Therm. Anal.* **38,** 997–1004 (1992).

241. Freund, H.-J. *et al.* Model studies on heterogeneous catalysts at the atomic scale: From supported metal particles to two-dimensional zeolites. *J. Catal.* **308,** 154–167 (2013).

242. Ertl, G. & Freund, H.-J. Catalysis and Surface Science. *Phys. Today* **52,** 32–38 (1999).

243. Sauer, J. & Freund, H.-J. Models in Catalysis. *Catal. Lett.* **145,** 109–125 (2015).

244. Grasselli, R. K. & Goddard, W. A. Recent Advances in Selective Oxidation Catalysis. *Top. Catal.* **50,** 1–1 (2008).

245. Ueda, W., Vitry, D. & Katou, T. Structural organization of catalytic functions in Mo-based oxides for propane selective oxidation. *Catal. Today* **96,** 235–240 (2004).

246. Vitry, D., Morikawa, Y., Dubois, J. & Ueda, W. Propane Selective Oxidation Over Monophasic Mo–V–Te–O Catalysts Prepared by Hydrothermal Synthesis. *Top. Catal.* **23,** 47–53 (2003).

247. Helberg, H. W. & Dressel, M. Investigations of Organic Conductors by the Schegolev Method. *J. Phys. I France* **6,** 1683–1695 (1996).

248. Wernbacher, A. M. *et al.* Operando Electrical Conductivity and Complex Permittivity Study on Vanadia Oxidation Catalysts. *J. Phys. Chem. C* **123,** 8005–8017 (2019).

249. Jonscher, A. K. Dielectric relaxation in solids. *J. Phys. D: Appl. Phys.* **32,** R57–R70 (1999).

250. Tahini, H. A. *et al.* Mobile Polaronic States in α-MoO_3: An ab Initio Investigation of the Role of Oxygen Vacancies and Alkali Ions. *ACS Appl. Mater. Interfaces* **8,** 10911–10917 (2016).

251. Anwar, M. & Hogarth, C. A. Effect of film thickness and substrate deposition temperature on the a.c. electrical properties of molybdenum trioxide. *Int. J. Electron.* **66,** 901–912 (1989).

252. Sanfiz, A. C. *et al.* Dynamics of the MoVTeNb Oxide M1 Phase in Propane Oxidation. *J. Phys. Chem. C* **114,** 1912–1921 (2010).

253. Scanlon, D. O. *et al.* Theoretical and Experimental Study of the Electronic Structures of MoO_3 and MoO_2. *J. Phys. Chem. C* **114,** 4636–4645 (2010).

254. Tokarz-Sobieraj, R. *et al.* Properties of oxygen sites at the MoO_3(010) surface: density functional theory cluster studies and photoemission experiments. *Surf. Sci.* **489,** 107–125 (2001).

255. Werfel, F. & Minni, E. Photoemission study of the electronic structure of Mo and Mo oxides. *J. Phys. C: Solid State Phys.* **16,** 6091–6100 (1983).

256. Kröger, M. *et al.* Role of the deep-lying electronic states of MoO_3 in the enhancement of hole-injection in organic thin films. *Appl. Phys. Lett.* **95,** 123301 (2009).

257. Bocquet, A. E. *et al.* Electronic structure of early 3d-transition-metal oxides by analysis of the 2p core-level photoemission spectra. *Phys. Rev. B* **53,** 1161–1170 (1996).

258. Kurtz, R. L. & Henrich, V. E. Surface electronic structure and chemisorption on corundum transition-metal oxides: V_2O_3. *Phys. Rev. B* **28,** 6699–6706 (1983).

259. Flavell, W. R. *et al.* Electronic structure and surface reactivity of $La_{1-x}Sr_xCoO_3$. *Faraday Discuss.* **114,** 407–420 (1999).

260. Ranke, W. Low temperature adsorption and condensation of O_2, H_2O and NO on Pt(111), studied by core level and valence band photoemission. *Surf. Sci.* **209,** 57–76 (1989).

261. Ranke, W. & Kuhr, H. J. Oxygen 2s spectroscopy. *Phys. Rev. B* **39,** 1595–1601 (1989).

262. Ranke, W. & Xing, Y. R. Orientation dependent adsorption on a cylindrical silicon crystal: I. Water. *Surf. Sci.* **157,** 339–352 (1985).

263. Warren, S. *et al.* Adsorption of H_2O on single crystal CuO. *Surf. Sci.* **436,** 1–8 (1999).

264. Ketteler, G. *et al.* The Nature of Water Nucleation Sites on TiO_2(110) Surfaces Revealed by Ambient Pressure X-ray Photoelectron Spectroscopy. *J. Phys. Chem. C* **111,** 8278–8282 (2007).

265. Stoerzinger, K. A. *et al.* Reactivity of Perovskites with Water: Role of Hydroxylation in Wetting and Implications for Oxygen Electrocatalysis. *J. Phys. Chem. C* **119,** 18504–18512 (2015).

266. Yamamoto, S. *et al.* Water Adsorption on α-Fe_2O_3(0001) at near Ambient Conditions. *J. Phys. Chem. C* **114,** 2256–2266 (2010).

267. Biesinger, M. C. *et al.* Resolving surface chemical states in XPS analysis of first row transition metals, oxides and hydroxides: Cr, Mn, Fe, Co and Ni. *Appl. Surf. Sci.* **257,** 2717–2730 (2011).

268. Kendelewicz, T. *et al.* X-ray Photoemission and Density Functional Theory Study of the Interaction of Water Vapor with the Fe_3O_4(001) Surface at Near-Ambient Conditions. *J. Phys. Chem. C* **117,** 2719–2733 (2013).

269. Ong, N. P. Microwave cavity-perturbation equations in the skin-depth regime. *J. Appl. Phys.* **48,** 2935–2940 (1977).

270. Abdullah, M. H. & Yusoff, A. N. Frequency dependence of the complex impedances and dielectric behaviour of some Mg-Zn ferrites. *J. Mater. Sci.* **32,** 5817–5823 (1997).

271. Yusoff, A. N. *et al.* Electromagnetic and absorption properties of some microwave absorbers. *J. Appl. Phys.* **92,** 876–882 (2002).

272. Caldararu, M. *et al.* Electrical conductivity of a MoVTeNbO catalyst in propene oxidation measured in operando conditions. *Catal. Today* **155,** 311–318 (2010).

273. Safonova, O. V., Deniau, B. & Millet, J.-M. M. Mechanism of the Oxidation–Reduction of the MoVSbNbO Catalyst: In Operando X-ray Absorption Spectroscopy and Electrical Conductivity Measurements. *J. Phys. Chem. B* **110,** 23962–23967 (2006).

274. Millet, J., Roussel, H., Pigamo, A., Dubois, J. & Jumas, J. Characterization of tellurium in MoVTeNbO catalysts for propane oxidation or ammoxidation. *Appl. Catal. A* **232,** 77–92 (2002).

275. Lunkenbein, T. *et al.* Direct Imaging of Octahedral Distortion in a Complex Molybdenum Vanadium Mixed Oxide. *Angew. Chem. Int. Ed.* **54,** 6828–6831 (2015).

276. Kawazoe, H. *et al.* P-type electrical conduction in transparent thin films of $CuAlO_2$. *Nature* **389,** 939–942 (1997).

277. Kawazoe, H., Yanagi, H., Ueda, K. & Hosono, H. Transparent p-Type Conducting Oxides: Design and Fabrication of p-n Heterojunctions. *MRS Bull.* **25,** 28–36 (2000).

278. Lany, S. & Zunger, A. Dopability, Intrinsic Conductivity, and Nonstoichiometry of Transparent Conducting Oxides. *Phys. Rev. Lett.* **98,** 045501 (2007).

279. Raebiger, H., Lany, S. & Zunger, A. Origins of the *p*-type nature and cation deficiency in Cu_2O and related materials. *Phys. Rev. B* **76,** 045209 (2007).

280. Robertson, J. & Clark, S. J. Limits to doping in oxides. *Phys. Rev. B* **83,** 075205 (2011).

281. Zhang, K. H. L., Xi, K., Blamire, M. G. & Egdell, R. G. *P*-type transparent conducting oxides. *J. Phys. Condens. Mat.* **28,** 383002 (2016).

282. Lany, S., Osorio-Guillén, J. & Zunger, A. Origins of the doping asymmetry in oxides: Hole doping in NiO versus electron doping in ZnO. *Phys. Rev. B* **75,** 241203 (2007).

283. Rouvet, F., Herrmann, J.-M. & Volta, J.-C. Electrical properties of pure vanadium phosphate phases and of VPO catalysts used in the partial oxidation of *n*-butane to maleic anhydride. *J. Chem. Soc., Faraday Trans.* **90,** 1441–1448 (1994).

284. Deb, S. K. & Chopoorian, J. A. Optical Properties and Color-Center Formation in Thin Films of Molybdenum Trioxide. *J. Appl. Phys.* **37,** 4818–4825 (1966).

285. Guo, Y. & Robertson, J. Origin of the high work function and high conductivity of MoO_3. *Appl. Phys. Lett.* **105,** 222110 (2014).

286. Hanson, E. D. *et al.* Systematic Study of Oxygen Vacancy Tunable Transport Properties of Few-Layer MoO_{3-x} Enabled by Vapor-Based Synthesis. *Adv. Funct. Mater.* **27,** 1605380 (2017).

287. Peelaers, H., Chabinyc, M. L. & Van de Walle, C. G. Controlling *n*-Type Doping in MoO_3. *Chem. Mater.* **29,** 2563–2567 (2017).

288. Ren, G.-K. *et al.* Enhancing thermoelectric performance in hierarchically structured BiCuSeO by increasing bond covalency and weakening carrier–phonon coupling. *Energy Environ. Sci.* **10,** 1590–1599 (7 2017).

289. Grasselli, R. K. Selectivity issues in (amm)oxidation catalysis. *Catal. Today* **99,** 23–31 (2005).

290. Knockaert, G. *Tellurium and Tellurium Compounds* in *Ullmann's Encyclopedia of Industrial Chemistry* 685–695 (Wiley-VCH Verlag GmbH & Co. KGaA, Weinheim, 2012).

291. *Applications of Chalcogenides: S, Se, and Te* (ed Ahluwalia, G. K.) 1st ed. (Springer International Publishing, Switzerland, 2017).

292. Siritanon, T. *et al.* First Observation of Electronic Conductivity in Mixed-Valence Tellurium Oxides. *Chem. Mater.* **21,** 5572–5574 (2009).

293. Chen, Z. *et al.* Electronic Structures and Transport Properties of n-Type-Doped Indium Oxides. *J. Phys. Chem. C* **119,** 4789–4795 (2015).

294. Jiang, X.-h. *et al.* Modulation of electronic and optical properties of ZnO by inserting an ultrathin ZnX (X = S, Se and Te) layer to form short-period $(ZnO)_5/(ZnX)_1$ superlattice. *J. Alloys Compd.* **711,** 581–591 (2017).

295. Liu, Q.-J., Jiao, Z., Liu, F.-S. & Liu, Z.-T. Influences of S, Se, Te and Po substitutions on structural, electronic and optical properties of hexagonal $CuAlO_2$ using GGA and B3LYP functionals. *Phys. Chem. Chem. Phys.* **18,** 14317–14322 (21 2016).

296. Liu, Q.-J., Zhang, N.-C., Liu, F.-S. & Liu, Z.-T. Effects of chalcogen substitution on electronic properties and chemical bondings of delafossite $CuAlO_2$. *Phys. Status Solidi B* **251,** 1630–1634 (2014).

297. Zhu, Y. *et al.* Formation of Oxygen Radical Sites on MoVNbTeOx by Cooperative Electron Redistribution. *J. Am. Chem. Soc.* **139,** 12342–12345 (2017).

298. McCafferty, E. & Zettlemoyer, A. C. Adsorption of water vapour on α-Fe_2O_3. *Discuss. Faraday Soc.* **52,** 239–254 (1971).

299. Farahani, H., Wagiran, R. & Hamidon, M. N. Humidity Sensors Principle, Mechanism, and Fabrication Technologies: A Comprehensive Review. *Sensors* **14,** 7881–7939 (2014).

300. Li, Z., Haidry, A. A., Gao, B., Wang, T. & Yao, Z. The effect of Co-doping on the humidity sensing properties of ordered mesoporous TiO_2. *Appl. Surf. Sci.* **412,** 638–647 (2017).

301. Qu, W. & Meyer, J. A novel thick-film ceramic humidity sensor. *Sens. Actuators, B* **40,** 175–182 (1997).

302. Wang, C., Yin, L., Zhang, L., Xiang, D. & Gao, R. Metal Oxide Gas Sensors: Sensitivity and Influencing Factors. *Sensors* **10,** 2088–2106 (2010).

303. Zang, W., Li, P., Fu, Y., Xing, L. & Xue, X. Hydrothermal synthesis of Co–ZnO nanowire array and its application as piezo-driven self-powered humidity sensor with high sensitivity and repeatability. *RSC Adv.* **5,** 84343–84349 (102 2015).

304. Enjalbert, R. & Galy, J. A refinement of the structure of V_2O_5. *Acta Crystallogr., Sect. C* **42,** 1467–1469 (1986).

305. Eaton, G. R., Eaton, S. S., Barr, D. P. & Weber, R. T. *Quantitative EPR* (Springer-Verlag, Wien, 2010).

306. Mendialdua, J., Casanova, R. & Barbaux, Y. XPS studies of V_2O_5, V_6O_{13}, VO_2 and V_2O_3. *J. Electron Spectrosc. Relat. Phenom.* **71,** 249–261 (1995).

307. Hryha, E., Rutqvist, E. & Nyborg, L. Stoichiometric vanadium oxides studied by XPS. *Surf. Interface Anal.* **44,** 1022–1025 (2012).

308. Demeter, M., Neumann, M. & Reichelt, W. Mixed-valence vanadium oxides studied by XPS. *Surf. Sci.* **454–456,** 41–44 (2000).

309. Silversmit, G., Depla, D., Poelman, H., Marin, G. B. & Gryse, R. D. An XPS study on the surface reduction of $V_2O_5(001)$ induced by Ar^+ ion bombardment. *Surf. Sci.* **600,** 3512–3517 (2006).

310. Tepper, B. *et al.* Adsorption of molecular and atomic hydrogen on vacuum-cleaved V_2O_5(001). *Surf. Sci.* **496,** 64–72 (2002).

311. Goering, E. *et al.* Angular-dependent soft X-ray absorption spectroscopy of V_2O_5 and V_6O_{13}. *Physica B* **208,** 300–302 (1995).

312. Brühwiler, P. A., Karis, O. & Mårtensson, N. Charge-transfer dynamics studied using resonant core spectroscopies. *Rev. Mod. Phys.* **74,** 703–740 (2002).

313. Pollini, I., Mosser, A. & Parlebas, J. C. Electronic, spectroscopic and elastic properties of early transition metal compounds. *Phys. Rep.* **355,** 1–72 (2001).

314. Blum, R.-P. *et al.* Surface Metal-Insulator Transition on a Vanadium Pentoxide (001) Single Crystal. *Phys. Rev. Lett.* **99,** 226103 (2007).

315. Su, D. S. & Schlögl, R. Thermal Decomposition of Divanadium Pentoxide V_2O_5: Towards a Nanocrystalline V_2O_3 Phase. *Catal. Lett.* **83,** 115–119 (2002).

316. Wu, Q.-H., Thissen, A., Jaegermann, W. & Liu, M. Photoelectron spectroscopy study of oxygen vacancy on vanadium oxides surface. *Appl. Surf. Sci.* **236,** 473–478 (2004).

317. Gillis, E. & Boesman, E. E. P. R.-Studies of V_2O_5 Single Crystals. I. Defect Centres in Pure, Non-stoichiometric Vanadium Pentoxide. *Phys. Status Solidi B* **14,** 337–347 (1966).

318. Tokarz-Sobieraj, R., Witko, M. & Gryboś, R. Reduction and re-oxidation of molybdena and vanadia: DFT cluster model studies. *Catal. Today* **99,** 241–253 (2005).

319. Vanhaelst, M. & Clauws, P. EPR Spectrum of the Oxygen Vacancy in Single Crystals V_2O_5. *Phys. Status Solidi B* **87,** 719–723 (1978).

320. Shin, S. *et al.* Vacuum-ultraviolet reflectance and photoemission study of the metal-insulator phase transitions in VO_2, V_6O_{13}, and V_2O_3. *Phys. Rev. B* **41,** 4993–5009 (1990).

321. Wang, L., Maxisch, T. & Ceder, G. Oxidation energies of transition metal oxides within the GGA + U framework. *Phys. Rev. B* **73,** 195107 (2006).

322. Fait, M. J. G., Abdallah, R., Linke, D., Kondratenko, E. V. & Rodemerck, U. A novel multi-channel reactor system combined with operando UV/vis diffuse reflectance spectroscopy: Proof of principle. *Catal. Today* **142,** 196–201 (2009).

323. Bordes, E. & Courtine, P. Some selectivity criteria in mild oxidation catalysis. *J. Catal.* **57,** 236–252 (1979).

324. Cavani, F. *et al.* Transient reactivity of vanadyl pyrophosphate, the catalyst for *n*-butane oxidation to maleic anhydride, in response to *in-situ* treatments. *Appl. Catal. A* **376,** 66–75 (2010).

325. Wang, F., Dubois, J.-L. & Ueda, W. Catalytic performance of vanadium pyrophosphate oxides (VPO) in the oxidative dehydration of glycerol. *Appl. Catal. A* **376,** 25–32 (2010).

326. Osborn, J. A. Demagnetizing Factors of the General Ellipsoid. *Phys. Rev.* **67,** 351–357 (1945).

327. Grabtchak, S. & Cocivera, M. Microwave response due to light-induced changes in the complex dielectric constant of semiconductors. *Phys. Rev. B* **58,** 4701–4707 (1998).

328. Jonscher, A. K. The 'universal' dielectric response. *Nature* **267,** 673–679 (1977).

329. Schuurman, Y. & Gleaves, J. T. Activation of Vanadium Phosphorus Oxide Catalysts for Alkane Oxidation. The Influence of the Oxidation State on Catalyst Selectivity. *Ind. Eng. Chem. Res.* **33,** 2935–2941 (1994).

330. Kube, P. *et al.* Functional Analysis of Catalysts for Lower Alkane Oxidation. *ChemCatChem* **9,** 573–585 (2017).

331. Brox, B. & Olefjord, I. ESCA Studies of MoO_2 and MoO_3. *Surf. Interface Anal.* **13,** 3–6 (1988).

332. Cruz, T. G. S., Gorenstein, A., Landers, R., Kleiman, G. G. & deCastro, S. C. Electrochromism in MoO_x films characterized by X-ray electron spectroscopy. *J. Electron Spectrosc. Relat. Phenom.* **101,** 397–400 (1999).

333. Botella, P., López Nieto, J. M., Solsona, B., Mifsud, A. & Márquez, F. The Preparation, Characterization, and Catalytic Behavior of MoVTeNbO Catalysts Prepared by Hydrothermal Synthesis. *J. Catal.* **209,** 445–455 (2002).

334. Concepción, P., Hernández, S. & López Nieto, J. M. On the nature of active sites in MoVTeO and MoVTeNbO catalysts: The influence of catalyst activation temperature. *Appl. Catal. A* **391,** 92–101 (2011).

335. Hüfner, S. *Photoelectron Spectroscopy. Principles and Applications* 2nd ed. (ed Cardona, M.) (Springer-Verlag, Berlin Heidelberg, 1995).

336. Bagus, P. S., Freund, H., Kuhlenbeck, H. & Ilton, E. S. A new analysis of X-ray adsorption branching ratios: Use of Russell–Saunders coupling. *Chem. Phys. Lett.* **455,** 331–334 (2008).

337. De Groot, F. M. F. *et al.* Differences between L_3 and L_2 x-ray absorption spectra of transition metal compounds. *J. Chem. Phys.* **101,** 6570–6576 (1994).

338. Cavalleri, M. *et al.* X-ray spectroscopic fingerprints of reactive oxygen sites at the MoO_3(010) surface. *Catal. Today* **124,** 21–27 (2007).

339. Purans, J., Kuzmin, A., Parent, P. & Laffon, C. X-ray absorption study of the electronic structure of tungsten and molybdenum oxides on the O K-edge. *Electrochim. Acta* **46,** 1973–1976 (2001).

340. Sato, H. *et al.* Soft X-ray absorption and emission study on anisotropic electronic structure of MoO_3. *J. Electron Spectrosc. Relat. Phenom.* **181,** 211–214 (2010).

341. Coreno, M. *et al.* Vibrationally resolved oxygen $K \rightarrow \Pi^*$ spectra of O_2 and CO. *Chem. Phys. Lett.* **306,** 269–274 (1999).

342. Fransson, T. *et al.* Requirements of first-principles calculations of X-ray absorption spectra of liquid water. *Phys. Chem. Chem. Phys.* **18,** 566–583 (2016).

343. Schirmer, J. *et al.* K-shell excitation of the water, ammonia, and methane molecules using high-resolution photoabsorption spectroscopy. *Phys. Rev. A* **47,** 1136–1147 (1993).

344. Yang, B., Kirz, J. & Sham, T. Oxygen K-edge absorption spectra of O_2, CO and CO_2. *Phys. Lett. A* **110,** 301–304 (1985).